13 January 2012 | $10

Science

AAAS

CONTENTS continued >>

page 158

page 169

COVER

A young wandering albatross (*Diomedea exulans*) glides smoothly over the Southern Ocean swell during a calm day. Albatrosses take advantage of ocean winds to travel more efficiently. Recent changes in Southern Ocean wind conditions have allowed wandering albatrosses to travel more rapidly and shift their foraging range southward, with positive influences on reproduction and potential contributions to albatross conservation. See page 211.

Photo: Paul Tixier

DEPARTMENTS

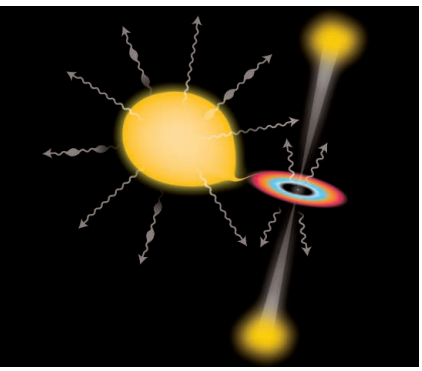

pages 175 & 189

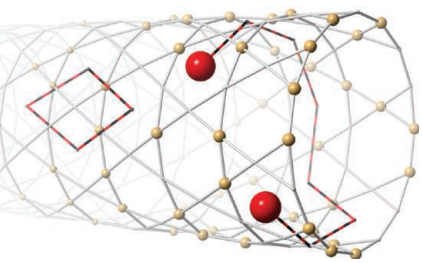

page 193

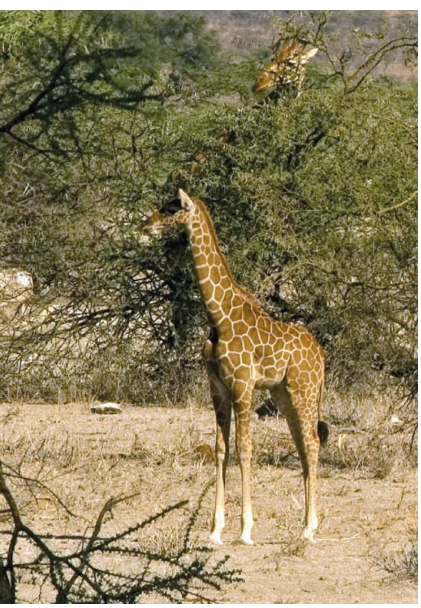

pages 174 & 214

BREVIA

RESEARCH ARTICLE

REPORTS

Published by AAAS

SCIENCEONLINE

SCIENCEXPRESS
www.sciencexpress.org

Female Leadership Raises Aspirations and Educational Attainment for Girls: A Policy Experiment in India
L. Beaman et al.
The effects of female leaders on girls occur via policy changes in the short run and parental aspirations in the longer run.
10.1126/science.1212382
>> Science *Podcast*

Innate Response Activator B Cells Protect Against Microbial Sepsis
P. J. Rauch et al.
A specialized population of B lymphocytes is important for controlling bacterial infections and preventing sepsis.
10.1126/science.1215173

Revealing the Superfluid Lambda Transition in the Universal Thermodynamics of a Unitary Fermi Gas
M. J. H. Ku et al.
Thermodynamic quantities for the superfluid transition of a strongly interacting atomic Fermi gas were measured.
10.1126/science.1214987

High-Latitude Forcing of the South American Summer Monsoon During the Last Glacial
L. C. Kanner et al.
High-latitude processes in the Northern and Southern Hemispheres both influence the South American Summer Monsoon.
10.1126/science.1213397

TECHNICALCOMMENTS

Comment on "Late Mousterian Persistence near the Arctic Circle"
N. Zwyns et al.
Full text at www.sciencemag.org/cgi/content/full/335/6065/167-b

Response to "Comment on Late Mousterian Persistence near the Arctic Circle"
L. Slimak et al.
Full text at www.sciencemag.org/cgi/content/full/335/6065/167-c

SCIENCENOW
www.sciencenow.org
Highlights From Our Daily News Coverage

New CO_2 Sucker Could Help Clear the Air
A plastic sponge may eventually make its way into artificial trees.
http://scim.ag/Clear-Air

A Guide to the Dark Side
Astronomers create the largest-ever map of dark matter.
http://scim.ag/Dark_Matter

Meat-Eating Plant Traps Victims Underground
A Brazilian species catches worms with leaves buried in the sand.
http://scim.ag/Plant-Worms

SCIENCESIGNALING
www.sciencesignaling.org
The Signal Transduction Knowledge Environment
10 January issue: http://scim.ag/ss011012

EDITORIAL GUIDE: Focus Issue—Wnt and β-Catenin Signaling in Development and Disease
N. R. Gough
Research reveals new functions for Wnt in cancer, tooth development, and neuronal pathfinding.

RESEARCH ARTICLE: Wnt/β-Catenin Signaling and AXIN1 Regulate Apoptosis Triggered by Inhibition of the Mutant Kinase $BRAF^{V600E}$ in Human Melanoma
T. L. Biechele et al.

PODCAST
T. L. Biechele et al.
Exploiting crosstalk between signaling pathways may lead to more effective melanoma therapies.

RESEARCH ARTICLE: A Wnt-Bmp Feedback Circuit Controls Intertissue Signaling Dynamics in Tooth Organogenesis
D. J. O'Connell et al.
Computational and genetic analyses reveal a Wnt and Bmp circuit in developing teeth in mice.

PROTOCOL: A Dual Array-Based Approach to Assess the Abundance and Posttranslational Modification State of Signaling Proteins
K. Luckert et al.
Combining two strategies enables simultaneous quantification of multiple signaling proteins.

PRESENTATION: Wnt-Induced Calcium Signaling Mediates Axon Growth and Guidance in the Developing Corpus Callosum
B. I. Hutchins et al.
Wnt-mediated axon repulsion requires the calcium- and calmodulin-dependent protein kinase II.

SCIENCETRANSLATIONAL MEDICINE
www.sciencetranslationalmedicine.org
Integrating Medicine and Science
11 January issue: http://scim.ag/stm011112

PERSPECTIVE: Magnetic Resonance Metabolic Imaging of Glioma
P. Metellus and D. Figarella-Branger
Noninvasive spectroscopic imaging of mutated enzymes and their metabolites could represent a new paradigm in glial tumor management.

RESEARCH ARTICLE: Detection of 2-Hydroxyglutarate in *IDH*-Mutated Glioma Patients by In Vivo Spectral-Editing and 2D Correlation Magnetic Resonance Spectroscopy
O. C. Andronesi
A metabolite overproduced in *IDH*-mutated brain tumors can be detected noninvasively in patients by spectroscopic imaging.

RESEARCH ARTICLE: Magnetic Resonance of 2-Hydroxyglutarate in *IDH1*-Mutated Low-Grade Gliomas
A. Elkhaled et al.
Metabolites can be detected ex vivo in biopsy tissue from *IDH1*-mutant gliomas using proton NMR spectroscopy.

RESEARCH ARTICLE: Alcohol Consumption Induces Endogenous Opioid Release in the Human Orbitofrontal Cortex and Nucleus Accumbens
J. M. Mitchell et al.
Endogenous opioids are released in reward-related brain areas after an alcoholic drink to a greater extent in heavy drinkers than in control subjects.

SCIENCECAREERS
www.sciencecareers.org/career_magazine
Free Career Resources for Scientists

Science in Northeastern Brazil
S. Gaidos
Outside Brazil's major scientific hubs, progress requires a mix of patience and impatience.
http://scim.ag/NE_Brazil

Shifting Sands in Northeastern Brazil
S. Gaidos
Physician-scientist Selma Jeronimo is looking for ways to control the spread of leishmaniasis.
http://scim.ag/Selma_Jeronimo

Brazil's Science Culture Shock
S. Gaidos
Physicist Mauro Copelli is working to foster a sustainable research culture in northeastern Brazil.
http://scim.ag/MauroCopelli

Building Up Brazilian Brain Research
S. Gaidos
Miguel Nicolelis is harnessing science as an agent of social change in northeastern Brazil.
http://scim.ag/MiguelNicolelis

SCIENCEPODCAST
www.sciencemag.org/multimedia/podcast
Free Weekly Show

On the 13 January *Science* Podcast: cost-effectively combating climate change, female leadership's effect on young girls, peopling the Aleutian Islands, and more.

SCIENCEINSIDER
news.sciencemag.org/scienceinsider
Science Policy News and Analysis

SCIENCE (ISSN 0036-8075) is published weekly on Friday, except the last week in December, by the American Association for the Advancement of Science, 1200 New York Avenue, NW, Washington, DC 20005. Periodicals Mail postage (publication No. 484460) paid at Washington, DC, and additional mailing offices. Domestic individual membership and subscription (51 issues): $149 ($74 allocated to subscription). Domestic institutional subscription (51 issues): $990; Foreign postage extra: Mexico, Caribbean (surface mail) $55; other countries (air assist delivery) $85. First class, airmail, student, and emeritus rates on request. Canadian rates with GST available upon request, GST #1254 88122. Publications Mail Agreement Number 1069624. **Printed in the U.S.A.**

Change of address: Allow 4 weeks, giving old and new addresses and 8-digit account number. **Postmaster:** Send change of address to AAAS, P.O. Box 96178, Washington, DC 20090–6178. **Single-copy sales:** $10.00 current issue, $15.00 back issue prepaid includes surface postage; bulk rates on request.

AAAS
ADVANCING SCIENCE, SERVING SOCIETY

EDITED BY STELLA HURTLEY

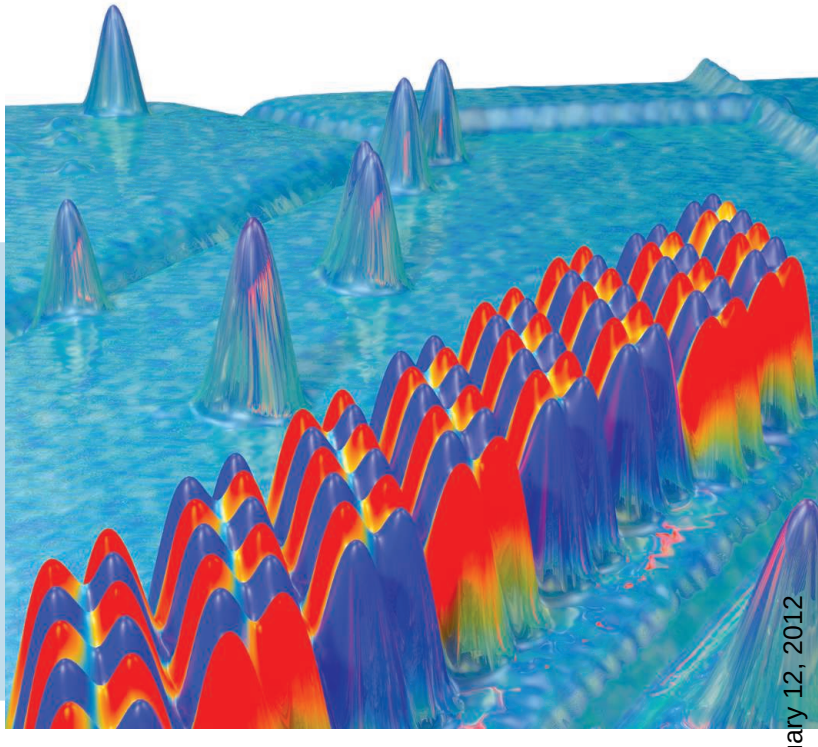

Structured Memories >>

High-density magnetic memory is generally produced by using ferromagnetic materials. As the density increases and the memory elements become closer together, stray fields can result in cross-talk and a corruption of the stored information. Antiferromagetic structures, however, are expected to be relatively insensitive to magnetic fields and so should, in principle, allow the elements to be packed in even closer. **Loth *et al.*** (p. 196) carried out low-temperature experiments to construct antiferromagnetic structures atom by atom. Electrical switching of the magnetic states was observed, and data could be robustly stored on the structure for several hours, albeit at low temperature.

Why Wait?

Tropospheric ozone can be dangerous to human health, can be harmful to vegetation, and is a major contributor to climate warming. Black carbon also has significant negative effects on health and air quality and causes warming of the atmosphere. **Shindell *et al.*** (p. 183) present results of an analysis of emissions, atmospheric processes, and impacts for each of these pollutants. Seven measures were identified that, if rapidly implemented, would significantly reduce global warming over the next 50 years, with the potential to prevent millions of deaths worldwide from outdoor air pollution. Furthermore, some crop yields could be improved by decreasing agricultural damage. Most of the measures thus appear to have economic benefits well above the cost of their implementation.

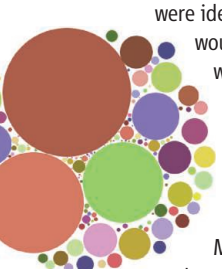

TACE Trafficking

The cytokine tumor necrosis factor (TNF) is a major driver of inflammation and contributes to the immune pathology seen in a variety of diseases, including inflammatory bowel disease, rheumatoid arthritis, and sepsis. Soluble TNF is produced by cleavage of its ectodomain by the ADAM family metalloprotease, TNFα-converting enzyme (TACE). However, the molecular regulation of TACE is not understood (see the Perspective by **Lichtenthaler**). **Adrain *et al.*** (p. 225) and **McIlwain *et al.*** (p. 229) now show that the rhomboid family member iRhom2 interacts with TACE in macrophages and is required for its proper intracellular trafficking and activation. In the absence of iRhom2, TACE was not released from the endoplasmic reticulum, and active protease did not reach the cell surface. Because of an inability to produce TNF, iRhom2-deficient mice were more resistant to lipopolysaccharide-induced septic shock but could not adequately control a *Listeria monocytogenes* infection.

Binary Revelation

Binary star systems that contain a neutron star or a black hole are expected to emit gamma rays. These gamma-ray binaries are a rare class of objects, which are also expected to emit x-rays. Indeed, several such systems were initially detected through their x-ray emission. The **Fermi LAT Collaboration** (p. 189; see the Perspective by **Mirabel**) reports the detection of a gamma-ray binary that was previously unknown as an x-ray source. Follow-up observations reveal that the system is also a source of x-rays and that the companion star is a class O star, a type that is very hot and very luminous.

Breaking Up the Indivisible

The famous Millikan oil drop experiment demonstrated that electric charge is quantized and cannot be divided into parts smaller than that of an electron. Decades later, the fractional quantum Hall effect was discovered that could only be explained through the existence of quasiparticles of fractional charge. Now, **Isakov *et al.*** (p. 193) numerically demonstrate the existence of an even more exotic object, a fractionalized quantum critical point (QCP), in the so-called Kagome lattice of bosons. Quantum Monte Carlo simulations were used to measure the critical exponents and revealed the fractionalization by comparison with a QCP of real bosons.

Dispersal in 3D

The fabrication of composites containing small proportions of nanoparticles is limited by the ability to disperse the particles uniformly in all three dimensions. **Erb *et al.*** (p. 199; see the Perspective by **Fratzl**) describe a process for creating nanoparticle composites in which a magnetic field is used to align the nanoparticles. Surprisingly, the magnetic alignment of iron-oxide functionalized nanorods and discs was enabled using very small magnetic fields and low-volume fractions of magnetic nanoparticles, which allowed control of the orientation of the nanorods and discs three-dimensionally.

Fluoride Riboswitch

Riboswitches are found in prokaryote and eukaryote messenger RNAs (mRNAs), where they regulate expression of the linked mRNA through ligand binding and conformational change. **Baker *et al.*** (p. 233, published online 22 December) analyzed the binding properties of the "*crcB* motif" found in the noncoding RNA at the 5′ end of a diverse collection of prokaryotic genes. A *crcB* motif from *Pseudomonas syringae* was capable of selectively sensing the very small and highly charged fluoride ion. Some of the *crcB* and *eriC* genes associated with the fluoride riboswitch showed evidence of being fluoride transporters. The bacterium *Methylobacterium extorquens* DM4, which can use halogenated hydrocarbons as an energy source, was found to encode at least 10 fluoride riboswitches in its genome.

Criegee Sighting

Standard mechanistic models for the reaction of ozone with unsaturated hydrocarbons implicate

CREDITS (TOP TO BOTTOM): SEBASTIAN LOTH/IBM RESEARCH ALMADEN; SHINDELL *ET AL.*

Published by AAAS

a transient carbonyl oxide compound, termed the "Criegee intermediate," which has largely eluded detection. **Welz *et al.*** (p. 204; see the Perspective by **Marston**) have now detected the compound by using mass spectrometry, following the low-pressure photolytic reaction of oxygen with diiodomethane, and measured its decay kinetics in the presence of nitric oxide, nitrogen dioxide, and sulfur dioxide. Reaction rates were higher than expected, suggesting that the intermediate may play a more prominent role in atmospheric chemistry than previously assumed.

Riding the Wind

Pelagic seabirds rely on wind to move between breeding and foraging areas, and albatrosses—which travel thousands of kilometers over sea—are well-known wind riders. **Weimerskirch *et al.*** (p. 211; see the cover) monitored foraging and reproduction in wandering albatrosses over 40 years and found that a change in wind patterns, probably induced by climate change, had a notable impact on important life history traits. Greater wind strength increased the rate of travel for the birds and shortened their foraging trips. These shorter trips improved breeding success and resulted in an increase in adult mass. Thus, over the past half-century, environmental changes have improved conditions for the albatross.

Parasite Invasion Strategy

Exocytosis is essential to the lytic cycle of apicomplexan parasites and is required for the pathogenesis of toxoplasmosis and malaria. DOC2 proteins recruit the membrane fusion machinery required for exocytosis in a Ca^{2+}-dependent fashion. **Farrell *et al.*** (p. 218) describe the phenotype of a *Toxoplasma gondii* conditional mutant impaired in host cell invasion and egress. The phenotype was explained by a defect in secretion of the micronemes, an apicomplexan-specific organelle that contains adhesion proteins. A *T. gondii* Doc2 gene was identified, by whole-genome sequencing, to be involved in the secretion defect, and a conditional allele of the orthologous gene engineered into the malaria parasite, *Plasmodium falciparum*, also caused defects in microneme secretion.

That Sweet Sensation

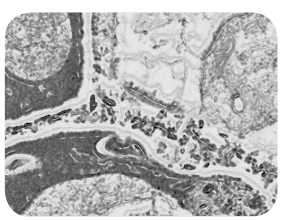

Photosynthesis in the leaf generates sucrose that must be transported via the phloem to other parts of the plant in order, for example, to be incorporated into harvestable produce. Studying *Arabidopsis* and rice, **Chen *et al.*** (p. 207, published online 8 December; see the Perspective by **Braun**) identified the SWEET family of sucrose efflux transporters that are responsible for carrying sucrose out of the leaf cells. When the transporters were disabled, sucrose accumulated in the leaves. Functioning properly, the SWEET transporters carry sucrose across the plasma membrane and other transporters move it further into the phloem.

Doing the Side Step

The molecular motor, dynein, contains two ring domains responsible for its movement along the microtubule. However, how the rings move relative to each other during processive motility and whether dynein processivity requires interhead coordination are unclear. To directly observe how dynein "walks" along microtubules, **DeWitt *et al.*** (p. 221, published online 8 December) performed advanced fluorescence-imaging studies to follow both motor domains of a single dynein motor at nanometer resolution. The data suggest that the two heads do not cooperate during movement, which suggests a fundamentally different mechanism of motility from that observed for other microtubule-based motors.

Long-Lasting Pain Killers

Opioids are among the most widely used and extensively studied drugs in the world. A continuous application of relatively low opioid doses is thought to be necessary to maintain synaptic depression in pain pathways. **Drdla-Schutting *et al.*** (p. 235) found that a single opioid application could produce lasting reversal of synaptic long-term potentiation in pain pathways. Chronic pain is often associated with synaptic potentiation in nociceptive pathways. A brief, high-dose application of opioids depotentiated long-term potentiation in spinal pain pathways. The same dose also reversed hyperalgesia in behaving animals. Thus, opioids not only attenuate pain but also may eradicate a significant cause for chronic pain.

CREDIT: DAVIDE SASSO AND WOLF B. FROMMER/CARNEGIE INSTITUTION FOR SCIENCE, STANFORD CA

It's the Teachers

John E. Burris is president of the Burroughs Wellcome Fund, Research Triangle Park, NC. E-mail: jburris@bwfund.org.

THE POOR PERFORMANCE OF U.S. STUDENTS ON INTERNATIONAL MEASURES OF SCIENCE AND MATH has been bemoaned by everyone from the president to concerned parents. The first Trends in International Mathematics and Science Study (TIMSS) results were released in 1995 and the first Program for International Student Assessment (PISA) test results in 2000. The education reforms that they helped to motivate have had little impact on U.S. performance, and the country continues to hope for a simple solution that will miraculously turn the tide. But there are no quick fixes in the world of education. Instead, the United States must commit to the laborious task of improving the teachers we train and the environment in which they teach, while providing teachers with a respect and trust commensurate with their critical societal roles.

The U.S. education system has methods at its disposal to improve science and math education, such as inquiry-based learning, collaborative problem-solving, and exciting and timely curricula. But no approach can be successfully sustained without bright, well-prepared, and well-supported teachers. Finland has scored near the top of the PISA examinations for the past decade, and the lessons of its success are simple: Recruit the best and the brightest to be teachers, and train them extensively and well.* Give them the freedom to develop teaching skills, independence from centralized authority, and ample time to prepare lessons and to interact with peers and students outside the classroom. And as I discovered on a recent visit there, Finland acknowledges the central role of teachers in society, as demonstrated by the respect accorded teachers and the high demand of young people to be teachers, despite salaries at the national average.

This approach is radically different from what happens in the United States, where the brightest are often not recruited into teacher education. Many U.S. colleges and universities provide substandard training, focused on methods classes to the exclusion of rigorous education in the disciplines that many will teach. Future teachers are educated only through the bachelor's degree level, in contrast to Finland, where all teachers must have a master's degree. Unlike Finnish teachers, U.S. teachers are on the treadmill of teaching to endless standardized tests, and there is little recognition of the importance of time spent with peers or participating in professional development. Most importantly, society does not give teachers the respect they deserve as professionals.

So what should the United States and other nations struggling with similar problems do? It took Finland decades to change its learning environment. Every change was initially opposed, but it now has one of the best educational systems in the world. The United States can start by raising the bar for acceptance into teacher education (Finland accepts only about 1 in 10 applicants for teacher training). We must also rigorously train teachers not only in pedagogy but in subject matter. Much of the high turnover rate of U.S. math and science teachers is due to inadequate professional development and limited classroom autonomy,† so in addition to improving training, it is critical to change the work environment in schools.

The United States is a large, diverse country, and a federal mandate to implement such changes is impractical and unrealistic. But many states have centralized funding and certification practices. States can close down underperforming teacher training and certification programs, reduce standardized testing, and recognize excellence in teaching, just as they now help to ensure quality textbooks and curricula.

As Finland has shown, the answer to the problem that beleaguers many nations is a straightforward commitment to both value and trust the most important part of any successful educational system—the teacher.

– John E. Burris

10.1126/science.1218159

*P. Sahlberg, *Finnish Lessons* (Teachers College Press, New York, 2011).
†R. Ingersoll, H. May, The *Magnitude, Destinations and Determinants of Mathematics and Science Teacher Turnover* (Consortium for Policy Research in Education, University of Pennsylvania, Philadelphia, 2010).

Published by AAAS

ECONOMICS

Speaking Up Saves Lives

Each year, almost twice as many people die as a result of injuries suffered in road traffic accidents as from malaria. Most of these deaths occur in developing countries, and inexpensive and easy-to-implement measures to reduce this toll could offer a big payoff. Habyarimana and Jack describe a simple nudge applied to the minibus-based long-distance transport system linking major towns to Nairobi, Kenya. Stickers encouraging passengers to speak up if they were subject to bad driving and a lottery to discourage drivers from removing the stickers combined to halve the number of insurance claims at a cost of less than 6 USD per year of life saved, which is comparable to the cost of childhood vaccinations. — GJC

J. Public Econ. **95**, 1438 (2011).

PLANT SCIENCES

To Grow or Not to Grow

A pollen grain that lands on a compatible pistil (the central female reproductive organ of flowering plants) still has a ways to go before it can achieve successful fertilization. Pollen grains contain plant sperm cells, but must also grow a tube through which the sperm cells migrate from the pistil surface to the more distant ovule. The factors that regulate this process are not well defined. Qin *et al*. have now identified a small diffusible compound from the *Arabidopsis* pistil that encourages pollen germination. After mass spectrometry analysis identified the key compound, the authors synthesized structural mimics: *N*-methanesulfinyl 1- and 2-azadecalins. Although flavonols can trigger germination of tobacco pollen, they do not have that effect on *Arabidopsis* pollen. *Arabidopsis* pollen germination instead seems to be enhanced by the sulfinylated azadecalins, which have no such effect in tobacco. These findings, along with quantitative differences in responses of pollen from Columbia and Landsberg accessions of *Arabidopsis*, hint at some level of divergence and specificity in how these signals interact with pollen of diverse species. — PJH

Plant J. **68**, 800 (2011).

BIOMEDICINE

A Recipe for Brain Injury

Type 2 diabetes, hypertension, heart disease, stroke, osteoarthritis, cancer. In case the list of health issues associated with a poor diet and obesity is not daunting enough, new research has uncovered another candidate—brain injury. Studying rodent models susceptible to diet-induced obesity, Thaler *et al*. examined the effect of a high-fat diet on a brain region called the hypothalamic arcuate nucleus, which has a well-established role in feeding and energy balance. Consumption of a high-fat diet caused a spike in hypothalamic inflammation and was accompanied by gliosis, an activation of astrocytes and microglia that normally occurs in response to brain injury. In contrast to high-fat diet–induced peripheral tissue inflammation, which primarily occurs in response to weight gain, brain inflammation occurred rapidly upon high-fat diet initiation. Although initially transient, hypothalamic inflammation reappeared with prolonged consumption of a high-fat diet along with other indicators of brain injury such as increased abundance of neuronal stress proteins, increased neuronal autophagy, and ultimately neuronal loss. In a preliminary analysis, the authors saw radiologic evidence of gliosis in the hypothalamus of obese but not lean humans, consistent with the rodent studies. One hypothesis is that the hypothalamic injury caused by a high-fat diet actively contributes to the progression of obesity and its associated metabolic disorders, but this remains to be experimentally established. — PAK

J. Clin. Invest. **122**, 153 (2012).

DEVELOPMENT

Methylate for Males

For some fish and reptiles, the genetic sex of an individual can be overridden by extreme temperature shifts, an effect that results in skewed sex ratios. One such species, the European sea bass, shows a male-biased sex ratio in response to high temperatures experienced before gonad development. How temperature affects sex ratios at a molecular level, however, is not well understood. Navarro-Martín *et al*. investigated this and found enhanced methylation of the promoter of the *cyp19a* gene in males as compared to females. *cyp19a* encodes gonadal aromatase, the enzyme that converts male hormones into the female hormones that are required for ovarian development. Increased methylation of the aromatase promoter was associated with reduced expression of the aromatase enzyme in males. Temperature increases resulted in increased methylation of the aromatase promoter in females, which was accompanied by a decrease in gene expression. On the basis of these results, the authors conclude that aromatase probably controls temperature sex determination in the European sea bass. Whether these results have implications for sex determination in other species remains to be determined. — LMZ

PLoS Genet. **7**, e1002447 (2011).

CREDITS (TOP TO BOTTOM): FLICKR/CARLOS FERNANDEZ; GEORGES JANSOONE

AROUND THE WORLD

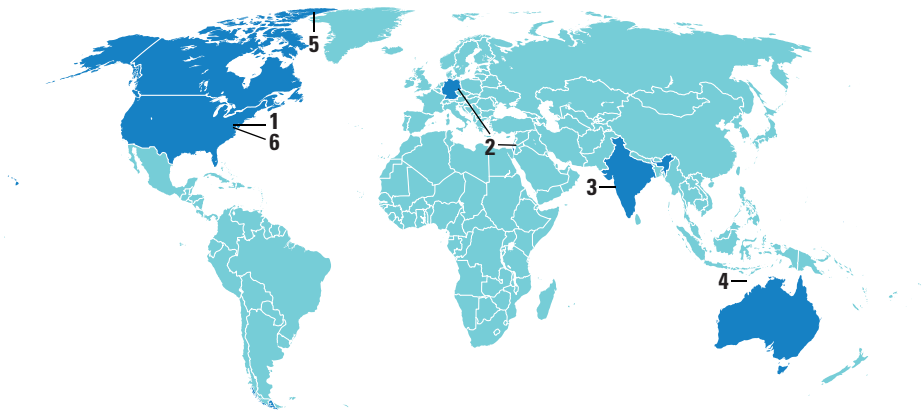

Bethesda, Maryland **1**

Acting Director Discusses New Translational-Science Center

This month, the National Institutes of Health (NIH) launched a new $575 million center that aims to tackle bottlenecks in drug development and speed the translation of basic discoveries into therapies. In an interview with *Science*Insider, Thomas Insel, the acting director of the National Center for Advancing Translational Sciences (NCATS), discussed the aims, structure, and temporary leadership of the controversial new center.


Insel

Insel dismissed reports that industry is skeptical: Industry leaders told NIH that they would "love to have help" with improving their R&D efforts, Insel said. Insel also clarified that he is not a candidate to become NCATS's permanent director. **http://scim.ag/TomInsel**

Rehovot, Israel, and Leipzig, Germany **2**

Joint German-Israeli Research Center Planned

The Munich-based Max Planck Society is teaming up with Israel's Weizmann Institute of Science to create a joint center devoted to studying archaeology and human evolution, to be based in both Rehovot, Israel, and Leipzig, Germany. The center will focus on questions such as the timing of cultural change over the past tens of thousands of years and the nature of coexistence between Neandertals and modern humans.

On 11 January, Max Planck President Peter Gruss, and Daniel Zajfman, president of the Weizmann Institute in Rehovot, signed a contract to create the new Max Planck Weizmann Center for Integrative Archaeology and Anthropology, worth about €5 million over the next 5 years. It will be funded by the Max Planck's Minerva Foundation, which has supported German-Israeli collaborations since the 1960s.

The money will fund up to 10 postdocs or graduate students in each city, says anthropologist Jean-Jacques Hublin of the Max Planck Institute for Evolutionary Anthropology in Leipzig. It will also support infrastructure and equipment. Hublin and archaeologist Steve Weiner of the Kimmel Center for Archaeological Science at the Weizmann will co-direct the new center.
http://scim.ag/PlanckCenter

Bhubaneswar, India **3**

Singh Promises Windfall for India's Scientists

India's Prime Minister Manmohan Singh has vowed to more than double his nation's spending on R&D over the next 5 years and build two major research facilities. The pledge, made 3 January at the annual Indian Science Congress, is expected to be a highlight of the government's new 5-year plan being finalized before its submission to parliament in March or April.

Singh said he will seek to boost the country's R&D expenditures to at least 2% of gross domestic product by 2017, up from the current 0.9%. According to his target for the central government, over the next 5 years public R&D spending would rise to about $8 billion per year, up from $3 billion spent in 2011. The R&D windfall stems in part from Singh's belief that Indian scientists are not keeping pace with peers in China and elsewhere. "Over the past few decades, India's position in the world of science has been declining, and we have been overtaken by countries like China. Things are changing, but we cannot be satisfied with what has been achieved," Singh said. "We need to do much more to change the fate of Indian science."
http://scim.ag/Indiaresearch

Ashmore Reef, Australia **4**

Dwindling Sea Snakes

Sea snakes could be going missing from a haven in the Pacific Ocean. Ashmore Reef, a colorful marine community off the coast of western Australia, has long been considered a hotbed of sea snake diversity. Here, 17 species, including three endemics, ply the waters. In surveys conducted throughout the 1990s, Michael Guinea of Australia's Charles Darwin University found up to 70 snakes per hectare in this reef; now there is less than 1 snake per 10 hectares, he reported last week at the annual meeting of the Society for Integrative and Comparative Biology in Charleston, South Carolina. Anecdotal evidence suggests the loss may extend at least 1000 kilometers down the northern coast of western Australia. The reef still looks pristine, with coral and sea grass intact. So it seems unlikely that climate change or increases in reef-side human activity are solely to blame. Guinea suggests seismic surveys in the area may have contributed to the decline of the sea snakes—possibly through damaging sound waves because the snakes seem to be very sensitive to minor changes in the environment—but that idea has yet to be tested.


Snake shortage. Sea snakes like this Stokes' sea snake (*Astrotia stokesii*) are becoming rarer in parts of the Pacific Ocean.

CREDITS (LEFT TO RIGHT): NIH; EVA BOOGAARD/LOCHMAN TRANSPARENCIES

Published by AAAS

Astronomy in the cold. The Canadian High Arctic could make a good site for space viewing.

Ellesmere Island, Canada **5**

Astronomy in the High Arctic

Move over, Antarctica: A new study suggests that the Canadian High Arctic is also a good spot for ground-based optical astronomy. Both locations offer frigid temperatures, dry air, and endless nights, but the Great White North has some practical advantages over the Antarctic, according to the study, in press at *Publications of the Astronomical Society of the Pacific*.

The paper describes data collected by an all-sky wide-field camera mounted under a Plexiglas dome on the roof of Canada's Polar Environment Atmospheric Research Laboratory at 80° north latitude. The Arctic site, the study found, has very clear, dark skies, making it good for high-quality photometry. It also appears not to suffer from strong low-level atmospheric turbulence found on the Antarctic plateau, which can distort images. And unlike Antarctica, the Canadian site is accessible via road and has an all-weather airstrip large enough for jet aircraft. Overall, the study found that spectroscopy can be done at the Arctic site 68% of the time and high-precision photometry about half the time. **http://scim.ag/HighArctic**

Washington, D.C. **6**

Report Challenges Ambitious U.S. Climate Research Plan

A National Research Council (NRC) committee has chided a federal climate change research program. The panel, which advises the 21-year-old U.S. Global Change Research Program (USGCRP), criticized the program for planning to broaden its climate activities without the expertise, governance structure, or prospect of sufficient funding to make it work.

In its report, the NRC committee commended the USGCRP, an interagency coordinating group, for the general idea of broadening its program beyond basic climate change science. In its recent draft 10-year strategic plan, program officials write that they intend to coordinate research that would support society's efforts to reduce greenhouse warming and to adapt to any unavoidable global change.

But, according to the report, "the USGCRP and its member agencies and programs are lacking in capacity to achieve the proposed broadening of the Program." They're missing in-house expertise to integrate the needed social and ecological sciences or to develop the capacity to support decision makers. USGCRP officials counter that they are already working on involving social scientists and similar experts in their work and reworking the governance structure. **http://scim.ag/USGCRP**

NEWSMAKERS

That's 'Professor Sir' to You

In a New Year's tradition dating back to the days of Queen Victoria, the British monarch handed out 27 knighthoods on 31 December. This year, a number of scientists can now address themselves as "Sir" or "Dame." The new knights include three Nobel laureates: University of Manchester physicists **Andre Geim** and **Konstantin Novoselov,** who received the 2010 physics Nobel Prize for their work on graphene, and struc- >>

Rhesus Pieces

Rhesus monkeys Roku and Hex are two of the world's first lab-generated chimeric primates—each is composed of cells representing as many as six distinct genomes. Irresistible cuteness aside, the experiments that produced these monkeys are helping researchers better understand primate embryonic stem (ES) cells. For decades, scientists have used mouse ES cells to make chimeras. They add a few of these nondifferentiated cells into an early mouse embryo. The animal develops normally, incorporating the new cells into its tissues. When Shoukhrat Mitalipov and his colleagues at the Oregon National Primate Research Center in Beaverton tried the same test with rhesus ES cells, they found that the ES cells were unable to incorporate into the host embryo; the developing fetuses contained no trace of the added cells. The only way the researchers were able to make chimeric monkeys was to fuse several very early stage embryos into one. That is consistent with a growing body of evidence that primate ES cells—including human ES cells—may represent a slightly later stage of development than mouse ES cells. That may help explain why recipes that turn mouse ES cells into specific tissues don't work as well with human cells.

Published by AAAS

Random Sample

Better Networking Through Chemistry on Fakebook

If you asked hydrogen what its job is, what would it say? According to hydrogen's "Fakebook" profile, its job is to be "rocket-ship fuel." Furthermore, its relationship status is "bonded." And carbon, nitrogen, and oxygen are its friends.

Fakebook (http://classtools.net/fb/home/page) is a Facebook-look-alike Web site created in January 2011 by Russel Tarr, a teacher at the International School of Toulouse, France. The Web site is rapidly becoming a popular teaching tool for science, history, and other school subjects, with a quarter of a million hits per week, Tarr says. In December alone, 14 Hydrogen profiles appeared on the site. "Kids love Facebook, and you always have to latch on to what they're enthused about and channel it into the classroom," he says.

Each of the students in Forest Grove, Oregon, teacher Tammy Johnson's biology class wrote a profile for a different cell organelle—and then Johnson had them post on one another's walls as a way to think about how the cell parts interact. "It puts it into a context that they're more familiar with," Johnson says.

Students in Lee Ferguson's Advanced Placement (AP) biology class in Allen, Texas, meanwhile, made profiles for animals. Gerald the giraffe, for example, notes that he sleeps only 20 minutes a night—"sort of like an AP student." Writing on Gerald's wall, an acacia tree complains about being eaten. "I'm really stressed," the tree writes. "I've just got a lot of things eating at me right now."

Other Fakebook friends run to the geometric. The rectangle laments that its birthday is "disputed" because it doesn't know if it was invented or discovered. It also notes, ruefully, that it "can be a bit square sometimes."

>>NEWSMAKERS

tural biologist Venki Ramakrishnan of the MRC Laboratory of Molecular Biology in Cambridge, who shared the 2009 Nobel Prize in physiology or medicine for discovering the structure of the ribosome. Queen Elizabeth II will also be knighting American-born climate researcher Robert Watson, who formerly headed the Intergovernmental Panel on Climate Change and now serves as scientific advisor for the U.K. Department for Environment, Food and Rural Affairs, as well as several clinical researchers and a mathematician. Royal Society of Chemistry President David Phillips and two other scientific researchers are receiving a different honor, Commander of the Order of the British Empire. The knighting ceremonies will take place later this year.

FINDINGS

More Than Just a Pretty Face

Monkeys can tell a lot about their neighbors from their colorful facial patterns. In South America, the faces of these tree-swingers come in all shapes and colors. Some differences give the animals an edge in their environment: Brown fur is better than white for camouflage, for instance. But many monkeys sport complicated, multicolored patterns that might not suit those sneaky needs. To get to the bottom of these appearances, researchers created facial recognition software to map out the faces of 129 species of

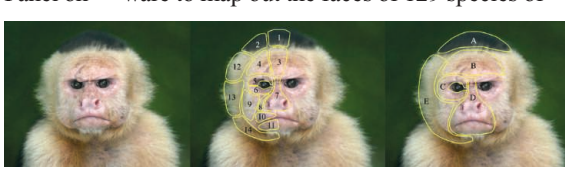

New World monkeys (above) and rated them by the complexity of their color patterns. Monkeys who live in smaller groups or alone tended to have more complex color patterns than those who live in larger groups. Monkeys with many colors, such as the spider monkey, may need to be more conspicuous to quickly recognize others from the same species, the researchers hypothesize this week in the *Proceedings of the Royal Society B,* as such encounters may be few and far between. **http://scim.ag/MonkeyFace**

BY THE NUMBERS

15% Improvement in cars' average gas mileage from 1980 to 2006. Although average fuel efficiency increased by 60% in that time, bigger and more powerful cars account for the disparity, according to a report in *American Economic Review.*

54% Percentage of clinical trials that were still unpublished 30 months after they ended, according to a survey of 635 trials described last week in the *British Medical Journal.*

16% Increase in toxic chemicals released into the environment from 2009 to 2010, reversing a previous downward trend since 2006, according to a 5 January report by the U.S. Environmental Protection Agency.

CREDITS (TOP TO BOTTOM): COURTESY OF RUSSEL TARR; S. E. SANTANA *ET AL., PROCEEDINGS OF THE ROYAL SOCIETY B* (ADVANCED EDITION, 2012)

Published by AAAS

What a drag. China is home to 300 million smokers—the world's largest total—and a newly minted academician who studies "low-tar" cigarettes.

CREDITS (TOP TO BOTTOM): STEPHEN SHAVER/AFP/NEWSCOM; ADAPTED FROM GLOBAL ADULT TOBACCO SURVEY, CHINA 2010 COUNTRY REPORT, CHINESE CENTER FOR DISEASE CONTROL AND PREVENTION

CHINA

Tobacco Scientist's Election Tars Academy's Image

BEIJING—Within hours of the election of Xie Jianping to the prestigious Chinese Academy of Engineering (CAE) on 8 December, the Internet here was buzzing with wild accusations. On the popular microblog Tencent Weibo, Liu Zhifeng got an early jump, questioning the anointment of a scientist whose research, he charged, is used "to more effectively kill people."

Prominent researchers weighed in, too. "I feel ashamed," CAE academician and food-safety expert Chen Junshi declared on his blog. Former health vice minister Wang Longde hinted to the *Beijing Times* that Xie, a deputy director of the Zhengzhou Tobacco Research Institute (ZTRI) who studies "low-tar" cigarettes, was complicit in deceptive tobacco marketing—in clear violation of the Framework Convention on Tobacco Control (FCTC), an international treaty that China ratified in 2005. And Wang Ke'an, director of the Think Tank Research Center for Health Development here and former president of the Chinese Academy of Preventive Medicine, penned an angry letter to CAE. Xie's research, Wang told *Science*, "lacks a scientific foundation and misleads the public." Xie did not respond to phone or e-mail requests for comment.

Xie's election has become a touchstone for broad unease over the Chinese tobacco industry's encroachment in science. Tensions are running high over the government's support for tobacco research centers—ZTRI is owned by China National Tobacco Corp. (CNTC)—and for its backing of research papers on low-tar and "reduced-harm" products.

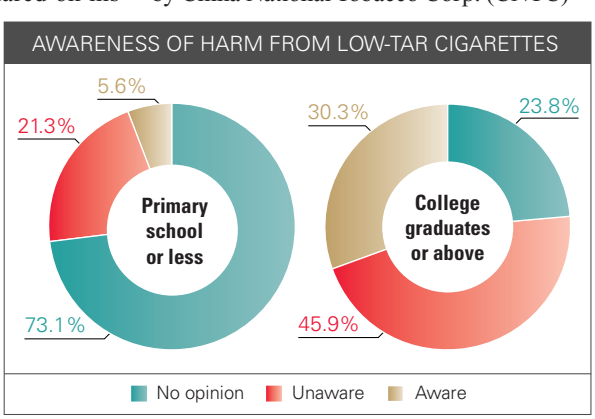

Knowing the risks? Critics allege that industry research has especially misled educated Chinese about the health effects of "low-tar" cigarettes.

In some ways, China is restaging a battle that has already played out in the West. "This is not new," says epidemiologist Armando Peruga of the World Health Organization's (WHO's) Tobacco Free Initiative. For decades, he says, "the tobacco industry has been researching ways to make their products appear less harmful than they are." In the United States, leaked documents and a Justice Department lawsuit against the major tobacco companies in the 1990s put researchers and universities accepting tobacco money in the hot seat (*Science*, 26 April 1996, p. 488). A decade later, controversy flared over research into "reduced-harm" products, again because of industry involvement (*Science*, 7 January 2005, p. 36). "That's exactly what's happening in China now," says cardiologist Stanton Glantz of the University of California, San Francisco.

This time the stakes are higher. China is home to 300 million smokers—more than any other country in the world. In 2010, fully 53% of men aged 15 to 69 smoked. Here, the same entity responsible for tobacco control—the government—is also the country's largest cigarette manufacturer. CNTC is operated by the State Tobacco Monopoly Administration, and together the two bodies produce hundreds of cigarette brands, from the ubiquitous Double Happiness to the upmarket Chunghwa. They have also jointly spearheaded industry investment in science. "In other countries," Wang says, governments "do not set aside money for this sort of research."

While China's ratification of the FCTC was a milestone, sources say the government is increasingly torn between concern over the health and economic costs of smoking and allegiance to the tobacco industry, which pulled in $79 billion in revenue in 2010. "The industry holds tremendous clout because of the economics of tobacco in China," says Jonathan Samet, director of the Institute for Global Health at the University of Southern California in Los Angeles. And CNTC's influence has allowed it to outdo even the powerful multinationals in some aspects of its campaign. Says Glantz: "The claims that are being made [in China] are way, way, way more aggressive than anything that have been made in the U.S."

Published by AAAS

Assault on science

In a cramped second-floor office tucked in an alley here, Yang Gonghuan glares at photos of scientists on her computer screen—scientists she believes have all accepted funding or favors from the tobacco industry. The tireless former deputy director of the Chinese Center for Disease Control and Prevention, now a professor at Peking Union Medical College's School of Basic Medicine, has become a critical figure in the controversy over Xie's election. Last month, she published two lengthy blog posts retracing the history of tobacco-industry funding of science in China. CNTC and the tobacco administration, she says, "have spent a lot of effort doing this sort of public relations."

Now Yang's trying to counteract what she sees as an assault on science. Yang is no stranger to the Chinese tobacco industry. She had spent years looking at secondhand smoke and other issues before setting out to probe its research investments. Still, she was surprised at the brazenness of what she dredged up. "Abroad, companies know these activities are illegal, so they do it in secret," Yang says. "Here, all of the materials are made public."

She knew that CNTC and its provincial affiliates had long used questionable marketing tactics, such as sponsoring elementary schools and university scholarships. (A 2010 Chinese CDC report found that more than 100 elementary schools bore the names of tobacco companies.) But until recently, such tactics didn't extend to research. Then in 1996, in anticipation of the release of a WHO study on the health effects of secondhand smoke, Philip Morris organized representatives of the major Asian tobacco companies into the Asian Regional Tobacco Industry Scientists Team. The Asian companies "were mostly state monopolies and had a different attitude than the Western multinationals had about what they could and couldn't say in terms of science," Glantz says. "While they generally didn't go around saying smoking was killing people, the multinationals were afraid that they might admit that smoking was bad."

But the real impetus for industry funding of research, Yang discovered, came in 2001, as China considered signing the FCTC. Much as the publication of a paper linking smoking to cancer prompted the U.S. tobacco industry to set up the Council for Tobacco Research in 1954, the convention prodded China's tobacco industry to mobilize. Over the next 5 years, a working group centered at Yunnan Tobacco Science Research Institute in Kunming held regular conferences to develop a counterattack. In 2003, the tobacco administration adopted the China Cigarette Science and Technology Outline, which recommends supplementing the funding of institutes like ZTRI. The following year, the administration hosted a forum on low-tar and "low-hazard" cigarettes that drew attendees from the Chinese Academy of Sciences (CAS).

By then, the industry had formulated research goals. Yang brandishes a copy of a 442-page report published by the Kunming institute soon after the FCTC took effect in January 2006, which details "countermeasures" to the convention. In reaction to Article 11, which bans labeling such as "low-tar" and "light," the group recommended that industry-funded research develop separate standards.

Crusader. Former Chinese Center for Disease Control and Prevention deputy director Yang Gonghuan has spent years probing the tobacco industry's investments in science.

CREDIT: YANG GONGHUAN

Such prescriptions have come with hefty increases in funding and research output. In 2009, the state-owned industry spent over $48 million on research. In the meantime, Glantz and Gan Quan, then a postdoc at the University of California, Santa Cruz, searched PubMed, Web of Science, and China National Knowledge Infrastructure for papers on tobacco and smoking by authors in mainland China. Papers published or sponsored by tobacco companies, they found, more than quadrupled from 576 between 1982 and 1987 to 4810 between 2002 and 2007. More tellingly, over the same period the proportion of those papers involving academic researchers leapt from 6% to 48%. And because many Chinese journals don't require conflict-of-interest disclosures, says Gan, now an adviser to the International Union Against Tuberculosis and Lung Disease here, "this could be a serious underestimate."

Among those engaging with the industry are some of China's leading science institutes. CAS, for example, operates a joint Ph.D. program with ZTRI on tobacco chemistry. Also on the list is the University of Science and Technology in Hefei; its Tobacco and Health Research Center has close ties to CNTC. The Chinese Academy of Agricultural Sciences, meanwhile, jointly administers the Qingzhou Tobacco Research Institute with CNTC.

Yang believes the proliferation of industry-backed research has influenced public perceptions. In China's 2010 Global Adult Tobacco Survey, which was conducted by the Chinese CDC for WHO, 86% of adults interviewed either did not know or did not properly understand that low-tar cigarettes are just as harmful as regular cigarettes. For Yang, who was the survey's principal investigator, the breakdown of that data is even more revealing: Adults with a college education or higher were more than twice as likely to have an incorrect understanding of the health effects of low-tar cigarettes as those who had attended primary school or less. "They've been exposed to misleading propaganda," Yang explains.

Such ideas resurfaced in the debate over Xie's election. "Low-tar and harm reduction [research] is a necessary step in resolving our smoking problem," CAE member Wei Fusheng told *Nanjing Daily* in explaining why he voted for Xie. And yet, Yang says, the uproar gives cause for hope. In 1997, when CAE elected Xie's mentor—ZTRI scientist Zhu Zunquan—no one publicly objected, she points out. Now, she says, awareness is growing. She opens an e-mail from Liu, the blogger who kicked off the election debate. "He's just an average Netizen," she says with approval.

Yang and others are prodding CAE to strip Xie of his academician title. Although CAE has never taken that step, CAS has twice struck academicians from its rolls. Regardless of how Xie's drama plays out, Yang hopes that the outcry will spur the Chinese government to honor its FCTC commitment.

–MARA HVISTENDAHL

GROUND-BASED ASTRONOMY

Pleading Poverty, NSF Delays Plans for Giant Telescope

An aerial view of the Carnegie Observatories in Pasadena, California, shows a flowerlike pattern of seven large circles painted next to the parking lot. The picture represents the mirror design for the Giant Magellan Telescope (GMT), a 24.4-meter instrument that a consortium led by Carnegie wants to build in Las Campanas, Chile. If only making the real thing were as simple as drawing lines on asphalt.

The architects of GMT and the Thirty Meter Telescope (TMT), a rival project planned for a Hawaiian mountaintop, have long expected the U.S. National Science Foundation (NSF) to bear a significant part of the sizable cost of the two instruments: GMT's price tag stands at $700 million and TMT's at $1.1 billion. But last month, NSF announced that it would not be able to support construction of either project in this decade. The best the agency can offer right now, according to a funding solicitation posted on 30 December, is a chance at $1.25 million over 5 years to continue their planning.

No money in sight. Both TMT (*left*) and GMT are counting on significant federal funding.

"We are not committing to constructing anything," says James Ulvestad, head of NSF's astronomy division. "It's just a consequence of budget realities."

NSF's decision means that the two projects are on their own for the indefinite future, even as overseas rivals are moving forward quickly with an even bigger instrument. The European Space Observatory has begun the formal approval process for funding the 39.2-meter European Extremely Large Telescope, which ESO expects to build at a cost of €1.1 billion over the next decade.

Although the lack of support from NSF is an obvious setback for both projects, GMT officials say it won't alter their plans. Astrophysicist Wendy Freedman, director of the GMT board, says that the consortium still intends to start construction in 2013. "NSF cannot provide construction funding until 2020 at earliest; therefore, we must begin construction without their funding," Freedman says.

TMT officials also see reason for optimism. "It's a great pity that NSF does not have enough money to contribute right now," says Richard Ellis, an astronomer at the California Institute of Technology (Caltech) in Pasadena and a member of the TMT board. "But it is good news that NSF has realized that it must begin discussions to see how it can contribute later. It does provide a first step in ensuring that U.S. astronomers will one day have access to this telescope."

Both teams hatched their plans after the 2000 decadal survey by the U.S. National Academies recommended the construction of a giant segmented mirror telescope (GSMT) as a top priority for U.S. astronomy. TMT's 30-meter-wide primary mirror is made up of 492 pieces, whereas GMT features seven 8.4-meter-wide mirrors. Initial attempts to merge the two projects were unsuccessful because of differences in technological approach and personality clashes (*Science*, 23 October 2009, p. 512).

Each team has invested millions of dollars in developing the necessary technologies, from the actuators that will control the positions of the mirrors to the processes by which light collected by the mirrors will be converted into images. Funding from private donors and foreign partners was expected to supplement NSF's contribution.

The TMT collaboration has received commitments of $350 million, which includes a $250 million pledge from the Gordon and Betty Moore Foundation and a $100 million pledge from Caltech and the University of California. Japan and Canada are each expected to chip in 20% of the overall cost, and China and India are both considering a 10% share, Ellis says. GMT has so far garnered $250 million in gifts and commitments, including 10% commitments from Australia, South Korea, and the Carnegie Institution. Both teams have already fabricated some components of their proposed instruments, and this month GMT plans to begin casting the second of its seven primary mirrors.

Both teams have lobbied for federal support. Six weeks ago, an impatient Congress directed NSF to avoid any further delay in picking "a viable GSMT project." The language, tucked into the 2012 appropriations bill for NSF and several other agencies, urged that the selection be made "expeditiously and utilize a fully competitive process, with a solicitation issued no later than the end of calendar year 2011 and a result announced no later than July 31, 2012."

That kick in the pants forced NSF to put out last month's solicitation. "The intent is to find the best option for a project that would have community participation in the future," Ulvestad says. The federal agency is asking for proposals for combining private and public funds to build a large segmented mirror telescope, including details about how U.S. astronomers will be able to share the facility. Ulvestad adds that NSF expects to make one award, not two, in effect picking a winner between GMT and TMT.

GMT officials declined to say whether they intend to submit a proposal by the 12 April deadline. But TMT appears ready to go after the award. "Some of my colleagues have said it is a lot of work to write a 250-page proposal for just $250,000 a year, but that's not the point," Ellis says. "The point is that this is a beginning of an engagement with the federal government."

–YUDHIJIT BHATTACHARJEE

CREDITS (LEFT TO RIGHT): COURTESY OF TMT OBSERVATORY CORP.; GMTO CORP.

Published by AAAS

GLOBAL CHANGE

A Quick (Partial) Fix for an Ailing Atmosphere

The world's air could use a quick scrubbing. So a group of scientists has come up with 14 practicable approaches to doing just that. The researchers say the selected cleaning methods, described on page 183, would more than pay for themselves in lives saved and crop yields increased while cutting global warming to boot. "Technically, it can be done," says atmospheric scientist Mark Jacobson of Stanford University in Palo Alto, California, who was not involved in the work. "It's a question of will power."

Scientists and policymakers alike have long known how, in principle, to get a quick start on cleaning up the atmosphere: Stop the gush of short-lived pollutants. Carbon dioxide will remain in the atmosphere for centuries, warming the world all the while, but pollutants like soot and methane remain airborne just a few weeks and a decade or so, respectively. Stop their emissions and their concentrations would promptly start dropping, sharply.

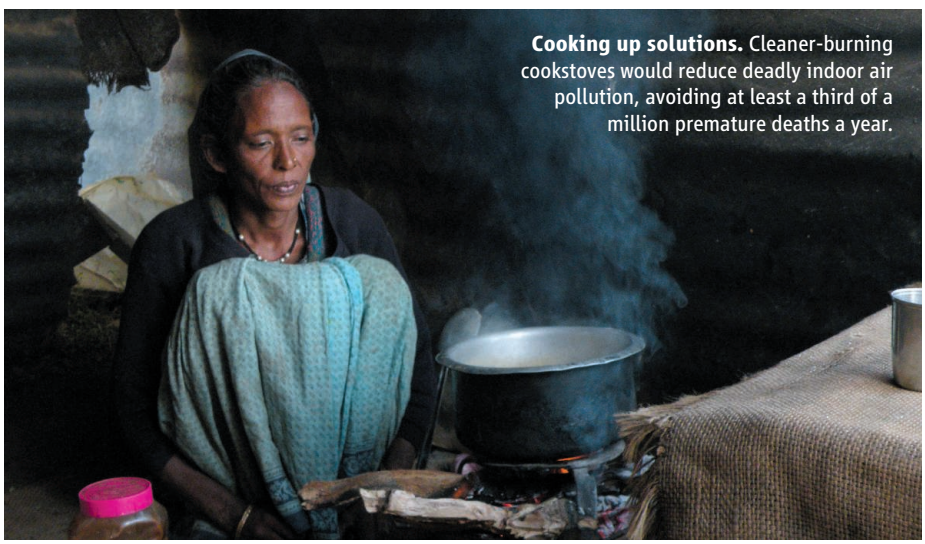

Cooking up solutions. Cleaner-burning cookstoves would reduce deadly indoor air pollution, avoiding at least a third of a million premature deaths a year.

CREDIT: V. RAMANATHAN, SCRIPPS INSTITUTION OF OCEANOGRAPHY

And that would be a good thing. Inhaled soot, also called black carbon, kills or debilitates millions of people each year, while soot in the atmosphere tends to warm climate, mainly by absorbing more sunlight. Methane is a powerful greenhouse gas that also acts like a catalyst to produce ozone in the lower atmosphere, where it damages crops and people's lungs.

But how exactly should methane and soot pollution be controlled to do the most good at the least cost? Twenty-four researchers came together to get the best answer possible with today's science and existing technology. Led by climate modeler Drew Shindell of NASA Goddard Institute for Space Studies in New York City, the group included scientists from five different specialties located in 13 organizations in a half-dozen countries.

Using a relatively simple model, the group of 24 screened about 400 tried-and-true pollution control methods for methane and soot that would both reduce warming and improve air quality. Ranked by how much they reduced warming, the top 14 included seven methane reduction methods targeting sources ranging from coal mining and landfills to livestock manure and rice paddies. The soot-controlling methods target processes in which fuel is not completely burned. They would improve diesel engines, increase the efficiency of wood- or dung-burning cookstoves, and ban the burning of agricultural wastes, among other methods.

Next, the researchers looked at how much good their top-performing pollution control methods would do if phased in around the world from 2010 to 2030. They selected two scenarios describing how much greenhouse-stoking carbon would be emitted over coming decades: a business-as-usual case assuming no new carbon controls and a low-carbon future featuring stringent new controls. Various combinations of the methane and soot controls were also combined with the business-as-usual and low-carbon scenarios. Each resulting scenario then served as input to two different complex computer models. They calculated what chemical composition of the atmosphere—including soot and ozone—would result and what the climate effects would be. These results were then used to estimate health and agricultural impacts.

The benefits of controlling methane and soot emissions turned out to be considerable. Largely thanks to reduced methane emissions, global warming by 2050 would be reduced by about half a degree; global warming so far has amounted to about 0.8°C. The additional controls also ensure that the low-carbon scenario holds warming below the danger level of 2°C of warming, at least for the next 60 years. Methane controls would also keep ozone low enough to avoid annual crop losses of 30 million to 135 million metric tons in 2030.

The drop in outdoor air pollution, due largely to soot emission reductions, would avoid 700,000 to 4.7 million premature deaths each year. Indoors, more than one-third of a million lives would be saved annually in India and China alone. A total of at least a million lives saved a year compares with the 600,000 premature deaths from tuberculosis expected in 2030 or the 2.1 million deaths due to traffic accidents.

And the costs of all these benefits would be more than reasonable, the study finds. While on average it would cost less than $250 to prevent the emission of a metric ton of methane, the benefits for not emitting that ton of methane would run from $700 to $5000. The benefits of soot reduction are more uncertain, but "the bulk of the [soot] measures could probably be implemented with costs substantially less than the benefits given the large valuation of the health impacts," the authors write. And the health benefits of soot reduction would largely fall to the countries that spent to control their emissions. All in all, fully implementing these controls in the next 20 years may be ambitious, says lead author Shindell, and there are uncertainties. But "by showing the potential, [the study] highlights what could be done if society puts its mind to it."

Outside experts agree. Professor of environmental engineering and international affairs Denise Mauzerall of Princeton University finds that the study "makes a compelling case for higher controls. It's much more comprehensive than what has been done before. Giving specific recommendations on cost-effective controls is very instructive for policymakers." And "they're doing as good a job as you can do," says atmospheric scientist Joyce Penner of the University of Michigan, Ann Arbor. "The whole approach is exactly what we need." The trick, of course, will be convincing governments of that.

–RICHARD A. KERR

NEWSMAKER INTERVIEW: C. N. R. RAO

Top Indian Chemist Helps Make the Case for Science Windfall

BANGALORE, INDIA—At the Indian Science Congress last week, Prime Minister Manmohan Singh surprised his audience with a promise to more than double central government R&D spending from $3 billion in 2011 to $8 billion by 2017. If the windfall appears in India's next 5-year plan, expected to be released in March or April, credit Singh's science advisory council. In a report to Singh last month, the panel, chaired by eminent chemist C. N. R. Rao, warned that Indian laboratories are rife with mediocrity and its universities are in decay. Worried that India's scientific community is losing ground to China and other nations, the council urged Singh to take "steps in a warlike fashion," including dispatching hundreds of students abroad for training and creating centers of excellence around top-shelf investigators.

Singh's embrace of science comes at a critical juncture for India, says Rao, Singh's science adviser. With 45 books and more than 1500 research papers to his name, India's most-cited scientist's latest fascination here at the Jawaharlal Nehru Centre for Advanced Scientific Research is the wonder-material graphene. In an interview with *Science*, Rao, 77, bemoaned the deterioration of India's academic institutions and its tendency to steer talented individuals into information technology. He also worried that scientists are losing ground to activists. For instance, Rao pointed to a decision in 2010 by India's environment minister to reject a scientific panel's advice and ban commercialization of what would have been the country's first genetically modified food crop: varieties of eggplant, called brinjal in India, equipped with a protein from the bacterium *Bacillus thuringiensis* (Bt) that's toxic to insect pests. The following comments have been edited for clarity and brevity. **–PALLAVA BAGLA**

CREDIT: © PALLAVA BAGLA

"The crisis we are facing is how to create a large, measurable, sizable, or critical mass of very capable scientists in different areas."

—C. N. R. RAO

Q: Is there a crisis in Indian science?
C.N.R.R.: There are serious concerns. In any given area of science or engineering, the number of experts is rather small in India. The other day somebody asked, "How many people work in graphene?" I thought, "We have enough people." We found only five or six.

We have been short of high-level talent for some time, and we are also short of leaders. The crisis we are facing is how to create a large, measurable, sizable, or critical mass of very capable scientists in different areas. India is the biggest supplier of technocoolies for the information technology industry but produces only 25 Ph.D.s in computer science. What an irony!

Q: Is India's bureaucracy killing science?
C.N.R.R.: Oh yeah, partly. Suppose you are the head of an institution and we want to give you another 3-year term. The procedure is so terrible. It will take 1 year! That is not how science is done. People should be treated better as individuals, and you can demand results if you have treated them well.

I don't think a professor in a university in any state in India has the freedom even to think properly because he is completely cowed by the atmosphere.

Q: Is India obsessed with big science and funding space and nuclear research?
C.N.R.R.: This obsession we have with big science, I am a bit unhappy about that. Science is not just atomic energy, science is not just space. Real science is done in small laboratories.

Q: India is looking at a mission to Mars and sending humans to the moon. Is this the thrust India should have?
C.N.R.R.: I am more worried about people on Earth. I am a very simple-minded person. There is so much to be done for this country in terms of infectious diseases and other social and living conditions.

Q: Why hasn't an Indian won a science Nobel since C. V. Raman's physics prize in 1930?
C.N.R.R.: I don't see any potential Nobel laureates in most subjects in India. Maybe we should create new opportunities for young people to perform in such a way that they become potential Nobel laureates.

Q: What does one need to succeed as a scientist in India?
C.N.R.R.: Stamina, tenacity, doggedness, and perseverance. Also a little intelligence is useful.

Q: In the past 1 or 2 years, the general feeling I am getting is that respect for science in India has gone down.
C.N.R.R.: Yes. We have to be very sure to educate our young people much better. Otherwise, the rabble-rousers and social activists will mislead the country. This is where the government has to also show maturity by taking proper scientific advice.

Q: You are talking about Bt brinjal [a genetically modified eggplant]?
C.N.R.R.: Bt brinjal was only the starting point; they will eventually take a decision which is based on either so-called popular opinion or opinion that goes along with the feelings of certain groups of people. Politics should never enter this kind of decision-making; unfortunately, it does. All over the world it does, but in India it is much more so. Being a democracy, there will be several views. That may be a problem.

Q: Colleagues say you still have a childlike excitement about science.
C.N.R.R.: I love it. Science is like that. If you are not childlike, you cannot be a scientist.

Q: Do you have any regrets over having never left India for a position abroad?
C.N.R.R.: I have suffered, I have agonized, but have no regrets.

Q: Any big message for India?
C.N.R.R.: I wish in 20 years India will be in the top three or four countries in the world in science. I really want to see India shine.

Published by AAAS

The Peopling Of the Aleutians

Few Aleuts still live in their ancestral homeland, but their genetics and archaeology offer a rare glimpse into one of humanity's last great migrations—and into the mysterious peopling of the Americas

ADAK ISLAND, ALASKA—Clam Lagoon, at the northern edge of this volcanic island, is a peaceful refuge from the wind-ravaged tides of the Bering Sea. Sea otters do the backstroke in its tranquil waters, and puffins and murrelets roost on the treeless shores. About 7000 years ago, kayak-paddling humans arrived here, setting up housekeeping on a bluff overlooking both the lagoon and the sea. Exceptionally well-adapted to maritime life, these first colonists promptly set about exploiting the local riches: They ate the otters and the birds, as well as seals and sea lions. They fished for cod and greenlings with hooks made from the birds' wing bones, and they made tools using obsidian brought from another island hundreds of kilometers away. Before long, a smaller group left Adak to colonize yet more islands to the west.

These people, the ancient Aleuts, began exploring the 2000-kilometer Aleutian archipelago—the world's longest—at least 9000 years ago. Because they had the islands to themselves for thousands of years, researchers say the archipelago is a living laboratory for studying human migratory behavior. "I don't think there is a better model than the Aleutians," says geneticist Michael Crawford of the University of Kansas, Lawrence.

Online
sciencemag.org
Podcast interview with author Michael Balter.

Sadly, most of the Aleuts were evacuated from their ancestral islands during World War II, never to return. And yet Adak today has become the center of intense exploration into when, how, and why the Aleutians were peopled. Many of today's Aleuts can trace their ancestry back to the islands' first inhabitants, so "the Aleutians are a perfect storm of deep time depth," says Anna Kerttula de Echave, director of the National Science Foundation's (NSF's) Arctic Social Sciences Program, which funds much of the work in the islands. "Only in a few places on the globe do you find such a continuous record of human occupation."

The Aleuts' story also opens a window into the peopling of the Americas as a whole. The Aleuts descend from ancestors who lived in Asia at least 13,000 years ago, making them part of the great migrations across the now-submerged Bering Strait land bridge into North America. Their history is obviously distinct from that of the groups who continued farther south into continental North and South America. But because the Aleuts have been relatively isolated for so long, researchers can more clearly read their ancient prehistory from their genes and archaeology, a task more difficult farther south where internal migrations may have blurred the earliest records.

To some, the Aleuts' maritime adaptations strengthen the idea that the first Americans were sea travelers (*Science*, 4 March 2011, p. 1122). "The Aleutians show that a coastal route is entirely reasonable," says archaeologist Lucy Johnson of Vassar College in Poughkeepsie, New York. Others counter that the Aleutians were settled too late to have a bearing on the land-versus-sea debate. "I have great difficulty with this notion," says archaeologist Don Dumond of the University of Oregon, Eugene.

Either way, the story of the Aleutians reveals how maritime migrations work. "We are coming to understand the dynamics of island colonization," Crawford says.

Two waves

The written history of the Aleutians starts in 1741, when Russian explorers led by Vitus Bering discovered the Aleuts and changed their lives forever. At the time, the Aleuts were hunting sea mammals and living in rectangular huts. The Russians turned the Aleutians into a fur factory, pressing the Aleuts into servitude and moving them from island to island. Historians estimate that they numbered up to 16,000 in 1740, but by 1900, disease, starvation, and suicide had slashed

CREDIT: MASAYUKI TORII

Published by AAAS

Refuge from the winds. A narrow isthmus separates Adak's Clam Lagoon (*left*) from the stormy Bering Sea.

Digging deep. Archaeologists are finding clues across the Aleutians, including at Adak's Clam Lagoon (*left*) and on Kiska, where Veronica Lech of the Memorial University of Newfoundland holds an ancient sea cow rib.

their population by up to 90%.

The Americans who took over in 1867 were apparently more benign: By 1920, Aleut numbers began to bounce back, and they grew from about 3000 to 8000 by 1980.

Beginning in the late 1800s, scientists began to visit the Aleutians, and in the 1930s famed Smithsonian anthropologist Aleš Hrdlička gathered dozens of skeletons. Hrdlička concluded that the Aleutians had been settled by two consecutive groups: the original settlers, the Paleo-Aleuts, who had high and narrow skulls (dolichocranic), and the Neo-Aleuts, who had wider, rounder skulls (brachycranic).

That basic idea has been confirmed by more recent research. In new studies of 86 of Hrdlička's skeletons, ranging from 3400 to 380 years old, anthropologist Joan Brenner Coltrain of the University of Utah in Salt Lake City found that the skulls did indeed separate into these two groups, and that all skulls older than 1000 years were dolichocranic. The groups "appear genetically distinct," Coltrain says. "Paleo-Aleut [skulls] are typical of the earliest people to occupy the New World, like the Kennewick Man and the Spirit Cave Woman. They all look more European than Asian, perhaps because they descend from European populations that occupied the Siberian region."

Recent genetic work confirms the distinction: Mitochondrial DNA (mtDNA) from 69 of Hrdlička's skeletons showed that Neo-Aleuts, like most modern Aleuts, descend from a common ancestor that carried genetic markers known as haplogroup D, according to recent work by University of Utah geneticist Dennis O'Rourke. But most Paleo-Aleuts were members of haplogroup A, as are most groups now living in Arctic North America.

Hrdlička argued that the Neo-Aleut populations came from the Alaskan mainland and replaced the Paleo-Aleuts. But Coltrain and others have found that the newcomers in fact coexisted with the original settlers. "The long-headed Paleo-Aleuts were still very much around" for several hundred more years, says anthropologist Richard Davis of Bryn Mawr College in Pennsylvania. About two-thirds of living Aleuts belong to haplogroup D and one-third to haplogroup A, according to work by Crawford and his co-workers, and they are presumed to be the result of admixture between Paleos and Neos. Crawford's research with modern Aleuts also suggests that they carry some Paleo-Aleut DNA, because their ancestors branched off from other Arctic peoples about 13,000 years ago—long before they colonized the islands, perhaps when they were still in Asia or Beringia.

The Neo-Aleuts were not only physically but also culturally distinct. For example, Davis says, after 1000 years ago, the archaeological record reflects a shift to more sophisticated stone tool types as well as changes in house styles from single to multiroomed structures. The Neo-Aleuts ate more big marine mammals such as sea lions and seals, while Paleo-Aleuts dined more on smaller animals such as birds and sea otters, according to an isotopic study of their bones that Coltrain published in the journal *Arctic* in 2010. "The Neo-Aleuts may have been more sophisticated technologically or more hierarchical in social organization," Coltrain says, possibly because they came from a "more complex and populous Alaskan peninsula setting."

Archaeologists are working all across the islands, and additional burials that might yield more ancient DNA are turning up as climate change accelerates coastal erosion, says archaeologist Debra Corbett of the U.S. Fish and Wildlife Service in Alaska. However, the Aleuts, like other Native American groups, are sometimes hesitant to allow research on skeletons (*Science*, 8 October 2010, p. 166). "Our policy is that if human remains are found, they must be immediately reburied," says Melvin Smith, archaeology coordinator for the Anchorage-based Aleut Corp., which represents native interests.

Nevertheless, Smith, who grew up on two of the islands, says archaeology helps native Aleuts to "better understand our own history and culture." And sometimes the corporation makes exceptions. For example, in a new edited volume, Corbett and her colleagues report on the 350-year-old remains of a child from one of the central islands, who was a member of haplogroup D like the Neo-Aleuts. Isotopic studies show that the child ate shellfish and sea birds and was infected with roundworms and tapeworms that often contaminate sea mammal meat.

Island arc. The Aleutian archipelago, the world's longest, stretches for 2000 kilometers.

From east or west?

Such recent burials offer clues to the lives of the Neo-Aleuts, but what of the ancient Paleo-Aleuts? Where did they come

CREDITS (TOP LEFT TO RIGHT): LYN GUALTIERI; COURTESY OF VERONICA LECH

Published by AAAS

Bounty from the sea. With kayaks, the Aleuts colonized islands and exploited maritime riches, as seen in this 19th century painting by Henry Wood Elliott.

from, and when did they get here? For much of the 20th century, such questions went unanswered, as few researchers reached the remote archipelago. Then in 1942, after the attack on Pearl Harbor, the Japanese invaded the western islands of Attu and Kiska and put the inhabitants in concentration camps in Japan. In response, the Americans built a military base on Adak and evacuated nearly all the Aleuts to abandoned canneries in southeast Alaska. Only a few dozen families subsequently made it back to their native islands. "The Aleuts suffered tremendously," says archaeologist Dixie West of Kansas State University, Manhattan.

Investigations into Aleut prehistory came to a standstill. Then after WWII, the islands were caught up in the Cold War. Adak housed up to 6000 soldiers and sailors, and civilian access to the island was limited.

Finally, in the late 1990s, the base closed. Although no Aleuts had lived on Adak since the 1800s, some now settled there. Beginning in 1998, Corbett, West, and other archaeologists began to visit, eager to uncover the story of one of the last great peoplings of the world.

They began to tackle one of the most basic and yet controversial questions about the settling of the Aleutians: Were they colonized from west to east, or the reverse? If they came westward from Alaska, then they must first have crossed the Beringian land bridge to the Americas, making them part of that great migration. But if they came from Russia, then their southerly shortcut across the Bering Sea may have been independent of the larger Beringian migrations.

Some Russian archaeologists had argued that the first Aleuts entered the archipelago from the west, via the Commander Islands near Russia's Kamchatka Peninsula. (The far-western Commander Islands belong to Russia, while the rest of the Aleutians are U.S. territory.) But American archaeologists pointed out that the earliest known Aleutian archaeological site was radiocarbon-dated to 9000 years ago—and it is located in the east, on Anangula Island.

The old ways. Colonization disrupted Aleut culture (seen in painting, *left*), and WWII forced the children in this 1938 photo to leave their island. But some traditions, such as dancing regalia (*right*), have been preserved.

To resolve the issue, West, Corbett, and a handful of others began excavations and radiocarbon dating on the islands. They found that the western islands were first occupied about 3500 years ago, relatively late. Then in 2005, dates from radiocarbon and volcanic ash put fish bones on Adak, at site ADK-171 overlooking Clam Lagoon, at nearly 7000 years ago. This demonstrated a clear east-west pattern of migration. "It looks as though the Aleutians were occupied from the east," agrees paleoecologist Arkady Savinetsky of the A. N. Severtsov Institute of Ecology and Evolution in Moscow.

Recent genetic studies bolster the archaeological evidence. Despite the fact that few today live in the islands of their grandparents, Aleuts remember where they came from, and their memories have helped create a remarkably sharp portrait of geography and genes. Each island community had distinctive dance regalia, and an Aleut's origins can still be identified from the ceremonial costumes he or she wears today, explains Mike Swetzof, who was born on St. George Island and is now mayor of Adak.

Crawford's team has now analyzed mtDNA from more than 250 Aleuts from 11 islands as well as displaced Aleuts living in Anchorage and compared them with mtDNA from people elsewhere in the Arctic. The Aleuts bear little genetic resemblance to people of the Kamchatka Peninsula, as might have been expected had the islands been colonized from west to east. And the data show a striking correlation between the island that families originally came from and their maternally inherited mtDNA. "The Aleut populations are distributed spatially like beads on a necklace," Crawford and his co-workers wrote in 2010 in *Human Biology*. Indeed, the mtDNA haplogroups can be further subdivided into three groups, corresponding to the eastern, central, and western Aleutians, regions that also differ somewhat in cultural traditions, according to recent archaeological work. "This really blew my mind when you consider everything that has happened to the Aleuts," Crawford said. "The correlation between genetics and geography was phenomenal."

Ripan Malhi of the University of Illinois, Urbana-Champaign, agrees that there is a "very clear pattern from east to west in the mtDNA haplogroup" profiles. But he questions whether that is a relic of migrations that

CREDITS: (TOP) NATIONAL ANTHROPOLOGICAL ARCHIVES, SMITHSONIAN INSTITUTION [IMAGE 7119_13]; (BOTTOM LEFT TO RIGHT) PHOTO BY HULTON ARCHIVE/GETTY IMAGES; V. B. SCHEFFER/LIBRARY OF CONGRESS; LAURA GRABHORN

Published by AAAS

took place as early as 9000 years ago or perhaps reflects more recent movements along the Aleutian chain. (The paternally inherited Y chromosomes don't show such a clear geographic pattern, probably because Russian men had children with Aleut women, researchers agree.)

Who are the Aleuts' closest relatives today? To date, no one has sequenced the whole genome of an Aleut, although researchers are working on it. But the mtDNA data cluster them with Siberians and the people of Russia's northern Chukchi Peninsula, which was once part of the Bering Strait land bridge. Aleuts show little mtDNA resemblance to Alaskan Eskimos, possibly refuting earlier assumptions that these groups separated relatively late, Crawford says. Comparisons of mtDNA from Aleuts, Eskimos, and Asian groups suggest that the Aleuts and Eskimos originally shared a common ancestor in Asia but went their separate genetic ways at least 11,000 years ago, probably while still in Asia; they may even represent separate migrations. "This suggests that there have been a lot of population expansions out of Beringia" and into the Americas, Malhi says (*Science*, 23 September 2011, p. 1692). "These populations had a dynamic history of extinction, admixture, and expansion."

Colonizing by kayak

One foggy Thursday last June, a team of archaeologists led by Diane Hanson of the University of Alaska, Anchorage, boarded the 3.5-hour flight to Adak, only to circle the island and turn back to Anchorage because of low visibility. They made it out the following Sunday, then hopped aboard the U.S. Fish and Wildlife Service ship the *Tiglax*—which provides a ferry service for researchers in the Aleutians—to a remote spot in western Adak, where they camped for 2 months, excavating prehistoric Aleut houses. This latest work, at an inland site, provides new evidence that the versatile ancient Aleuts exploited habitats all over the islands, not just on the coasts.

But there's no denying the power of the sea in Aleut life. And there's no doubt that whoever came to the Aleutians, and when, must have done it by boat. During glacial times, the easternmost islands were part of Beringia. But the rest of the Aleutians, including Adak, have been in open sea for more than 20,000 years.

The Aleuts encountered by the Russians were traveling between islands in kayaks and umiaks (larger open boats) made from driftwood or whalebone frames and covered with seal skins. Remains of such boats have been found at numerous Aleutian sites dating back about 2000 years; researchers assume that the first Aleuts had similar boats, although the evidence does not preserve over time. "The fact that we find obsidian on Adak that comes from an island 1000 kilometers to the east indicates that these folks were moving around and they weren't doing this by swimming or walking between the islands," West says. "Those seas were treacherous."

It's no surprise that the Aleutians were colonized after the rest of the Americas: Massive ice sheets blocked the way from the Alaskan peninsula to the Aleutians until about 9000 years ago, according to work in the 1970s. The Paleo-Aleuts "probably could have landed on glacial shores and spent the night," Johnson says. "But it wasn't a place they could live." Once the sea route was clear, however, the ancient Aleuts moved swiftly. "The earliest inhabitants we know of, at Anangula, camped virtually right on top of glacial till," Davis says. "This suggests that as soon as those small islets were clear of ice, hunters from the mainland came to exploit available resources right away." Indeed, some researchers say, the islands' abundant maritime resources might have provided sustenance as good as or better than that available on the mainland. "The Aleuts became adapted to a kind of life that was quite rich, richer than most of the terrestrial areas," Dumond says. "As the population grew, it dug itself in to that way of living."

New evidence suggests that the pulse of migrations from east to west may correlate with times when the sea was coldest and most productive. Three western Aleutian islands were apparently first occupied during a long cold spell that started 3350 years ago, according to a paper by Savinetsky in a 2010 edited volume. In a second volume just published, Savinetsky, West, and others report that about 13% of the fish species at Adak's 7000-year-old ADK-171 site were cold-loving saffron cod. This suggests that Adak, too, was first settled during a cold period.

Cold periods might also have dampened the wicked winds of the Bering Sea, say Savinetsky and West, who point to earlier work suggesting that cooling in the north Pacific may have occurred during periods of weakened cyclonic activity. "Did cooler temperatures mean weakened cyclonic activity, thus less high waves, and greater marine productivity?" West asks. If so, she says, "then perhaps folks were more likely to explore and find new places."

When the ancient Aleuts did go exploring, Crawford says, they probably did so in family groups, splitting off from larger island populations and setting up residence on islands farther west.

But why did they keep trekking westward, exploring new territory? No one knows for sure. Some researchers chalk it up to human nature—our "constant search for new lands and endless curiosity," says archaeologist Christine Lefevre of the National Museum of Natural History in Paris. Corbett says she wonders about it all the time. "I was on Adak one cloudless, sunny day. I climbed a mountain where I could look out at the other islands. I imagined all those villages and the people living in them, boats on the water, smoke coming out of the houses. This was really a populated landscape. And yet there was lots of elbow room on the Alaskan peninsula and in the eastern Aleutians. But people still kept aiming for the horizon. They kept moving forward." **–MICHAEL BALTER**

Frigid waters. Cold-loving cod (*inset*) hint that the Aleutians were colonized during cold spells.

CREDITS: MASAYUKI TORII; (INSET) KITTY MECKLENBURG/NOAA

Additional Reading

D. West *et al.*, Eds. *The People Before: The Geology, Paleoecology and Archaeology of Adak Island, Alaska.* British Archaeological Reports, Oxford (2012).

D. Corbett *et al.*, Eds. *The People at the End of the World: The Western Aleutians Project and the Archaeology of Shemya Island.* Aurora, Anchorage (2010).

Published by AAAS

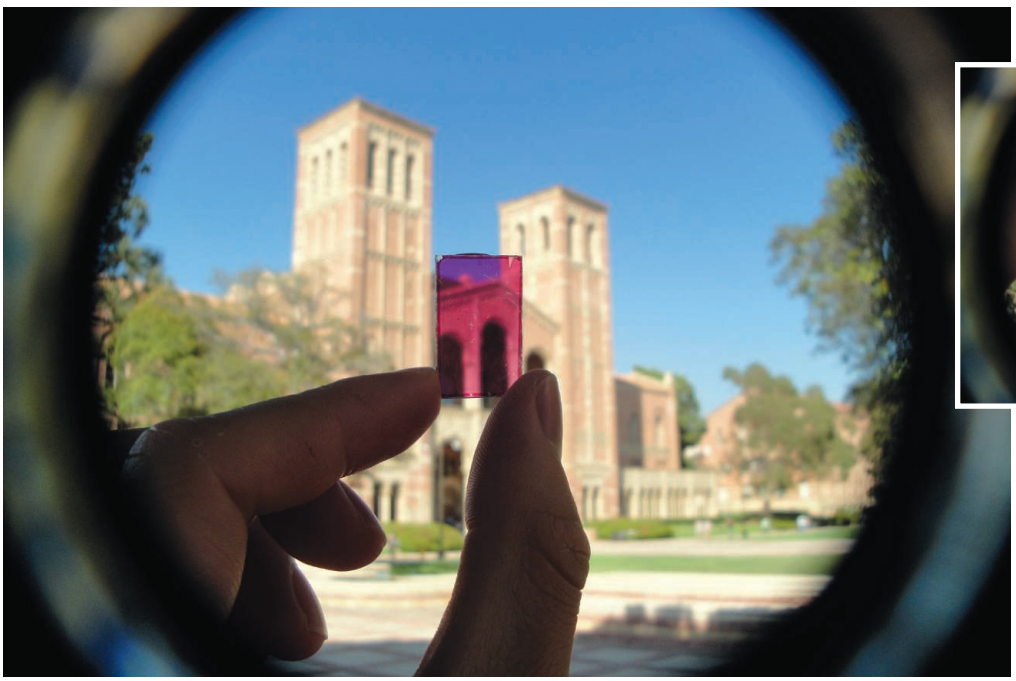

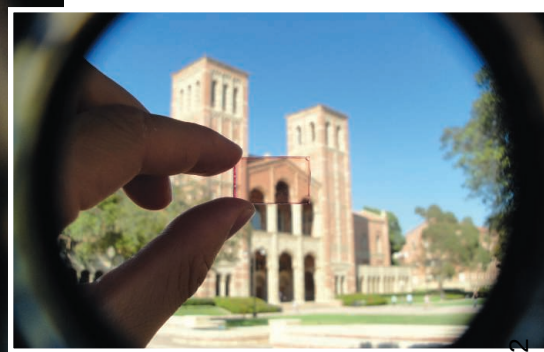

Solar harvest. Light shines through two polarizing filters oriented parallel to each other (*above*). But most is blocked when one is turned 90 degrees (*left*).

New Lease for Leftover Light

Today's thin TVs and computer monitors have the cool factor, but they're energy hogs. The most common monitors, liquid crystal displays (LCDs), waste about 75% of the backlight they use to light the screen. Most of it is absorbed by polarizing filters that control how much light passes through each point on the screen in order to produce the desired image. Researchers in California reported at the meeting, however, that they've devised polarizing filters made from organic solar cells that recycle some of this absorbed light. With further improvements, energy captured by the new solar cell filters could noticeably improve lifetimes of cell phones, laptops, and other battery-driven technologies that rely heavily on displays.

LCDs take advantage of the fact that the electromagnetic waves that make up light oscillate in different directions. Unlike waves in the ocean that rise and fall vertically, light waves can oscillate side to side as well. To control what light comes through a screen, LCDs use two polarizing filters. The first blocks all the light waves except those that oscillate up and down, and the other blocks all the light waves except those that oscillate left and right. Virtually all light that encounters both filters is absorbed, and the spot remains black.

In between these filters sits a layer of liquid crystals, rod-shaped molecules that stack like logs in a pile all oriented in the same direction. When given a jolt of electricity, the rods in the pile twist like a spiral staircase so that the rods at the top of the pile are perpendicular to those at the bottom. This helical twist rotates the polarization of photons of light passing through, allowing them to emerge from the display.

This technology is more energy-efficient than many rival technologies, but it's still wasteful: In many modern electronic devices, 80% of the total energy they use goes to lighting the display. But researchers led by Yang Yang, a chemist at the University of California, Los Angeles (UCLA), thought they might be able to recapture some of this lost energy, much as the regenerative brakes in a hybrid car reclaim energy to recharge the car's battery. They replaced the two conventional polarizing filters with organic solar cells. At the heart of these cells are rod-shaped polymers made from the most common organic light absorber, known as P3HT. Yang and his colleagues oriented these rods in the same direction in each solar cell by simply brushing them with a soft cloth. They added additional material films to help convert the captured light to electrical charge and shuttle the charges to wires that could be connected to a battery.

They then oriented the two solar cells so that their light-absorbing polymers were perpendicular to one another. These polarizers absorbed 90% of the light, converting about 3% of it to electricity, which in a real device would be used to recharge the battery. Even better, the new solar cell filters continue to harvest light even when the LCD screen is not in use. So such displays could serve not only as an energy saver but also as an energy supply. The UCLA results were also reported in the 22 September 2011 issue of *Advanced Materials*.

Marc Baldo, an organic solar cell expert at the Massachusetts Institute of Technology in Cambridge, calls the new work "a good thing." But Baldo and Yang point out that to be useful commercially, organic polarizing filters would need to block more than 99% of the light in order to create black on the screen. "That's an all-around big issue for organics" because organic light absorbers typically don't do a good job of blocking red light. But at the meeting, Yang reported that his group has developed a novel polymer that absorbs red and infrared light. The group is currently using it to make solar cells. Yang notes that if the new IR polymer pans out, it might improve not only future displays but also plastic solar cells in general. Because the polymers absorb IR light but let visible light pass through them, they could be layered atop conventional visible light–absorbing cells to boost the amount of light captured and converted to electricity. That could add an extra cool factor to solar cells as well. **–ROBERT F. SERVICE**

CREDITS: YANG YANG LAB/UCLA

Published by AAAS

Snapshots From the Meeting >>

Organic PVs break the 10% barrier. Researchers from Mitsubishi Chemical Group Science and Technology Research Center in Yokohama, Japan, reported that they've created the first organic photovoltaic device that's more than 10% efficient at converting sunlight to electricity, but they offered few details on the new device.

Stretchable electronics beat the heat. Researchers would love to use flexible organic-based integrated circuits (ICs) as implantable electronics for sensors and other health-monitoring devices. But they've had trouble making them robust enough to withstand the high temperatures needed to sterilize them. At the meeting, a team from the University of Tokyo reported that it has now created heat-stable organic ICs.

Lookie here. Researchers at the University of California, Berkeley, have created a new nanowire-based optical probe able to peer within individual cells.

Large-scale nanocarbons. Researchers in Japan reported that a new pilot-scale production plant is producing 100 grams of carbon nanotubes per hour and said they're on track to open a commercial-scale facility in 2014 capable of producing 50 tons per year. Another team, meanwhile, reported being able to synthesize single-atom-thick carbon sheets of graphene in a roll-to-roll setup like those used in printing.

Can you see me now? Researchers in California reported using a light-sensitive protein to turn a transistor on and off. The proteins in this case were ion channels able to ferry protons from one side of a cell membrane to another when exposed to light. They were embedded in a lipid coating around a nanowire electrode in the device; when light hit the proteins, they pumped protons away from the nanowire, thereby changing the pH nearby and triggering the transistor to turn on. Down the road, arrays of such devices might be used to make an artificial retina. **–R.F.S.**

Al Bids to Vie With Li In Battery Wars

We love our rechargeable lithium-ion batteries. They drive our cell phones, laptops, power tools, electric cars, and countless other gadgets. And their numbers are rising. The global market for lithium-ion batteries has risen fivefold to $10 billion a year over the past decade. Still, lithium-ion batteries may face tough times ahead. Lithium supplies are limited, and the cost of the metal has skyrocketed in recent years. So researchers are on the lookout for novel battery chemistries. At the meeting, researchers from New York described materials that could pave the way for making rechargeable batteries from aluminum. Because aluminum is one of the most abundant elements on the planet, and is less prone to catching fire than lithium is, it could pave the way to cheaper and safer rechargeables.

Batteries work by shuttling ions back and forth through an electrolyte that sits between two electrodes. At the electrodes, the ions either give away extra electrons during discharge or sop them up during recharging. Numerous researchers have dabbled in making aluminum batteries before. But aluminum ions are larger than lithium ions, and they tend to clump together inside batteries. These aluminum clumps move more slowly between electrodes than lithium ions do, which reduces their conductivity. So in the past, research teams ran their aluminum-ion cells at high temperatures to boost their conductivity. But high-temperature cells aren't useful for most applications that run at or near room temperature.

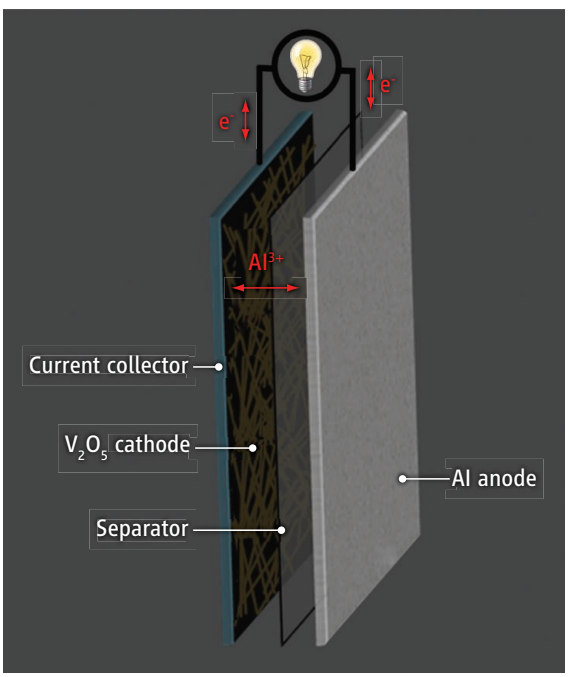

Cheaper rechargeables? New aluminum-ion batteries store about the same amount of energy as lithium-ion versions, and they should be safer.

CREDIT: ADAPTED FROM L. ARCHER/CORNELL UNIVERSITY

In 2010, researchers at Cornell University, led by chemical engineer Lynden Archer, began searching for a way to boost the room-temperature conductivity of aluminum-ion cells. Previous aluminum-ion batteries had used conventional ion-conducting electrolytes, which were poor aluminum-ion conductors. So Archer and his colleagues turned to an electrolyte made from an ionic liquid that sped up the shuttle time for the aluminum ions. They also synthesized vanadium-oxide nanowires for their cathode that were able to harbor more aluminum ions during charging. At the meeting, Archer's postdoctoral assistant Navaneedhakrishnan Jayaprakash reported that the new cells made with these improvements were rechargeable at room temperature at typical recharge times. After 20 charge-discharge cycles, they had a capacity of 273 milliamp-hours per gram, on par with lithium-ion cells sold today. The results were also published online on 3 November in *Chemical Communications*.

"It's quite intriguing," says Paul Braun, a chemist and battery expert at the University of Illinois, Urbana-Champaign. One advantage, Braun says, is that each aluminum ion can ferry three electrons every time it moves between electrodes, whereas lithium ions can carry only one electron. That could help boost the energy-storage capacity of aluminum batteries. But both Braun and Archer note that the new aluminum-ion cells aren't ready to go up against lithium cells. The ionic liquid electrolyte is too expensive for commercial use. And the anode in the new battery is pure aluminum metal, which after repeated charge-discharge cycles can form tiny metal spears that can damage key parts of the battery. Archer says he and his colleagues are now turning to these and other challenges in hopes of turning one of the most abundant metals into a better battery. **–R.F.S.**

Published by AAAS

Fishing for ever more
169

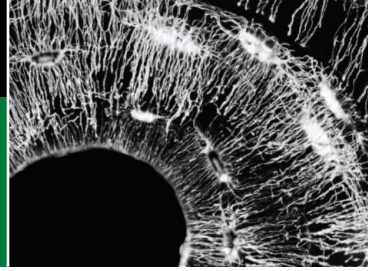

Boning up on materials design
177

LETTERS | BOOKS | POLICY FORUM | EDUCATION FORUM | PERSPECTIVES

LETTERS

edited by Jennifer Sills

Single-Sex Education: Results One-Sided

IN THEIR EDUCATION FORUM "THE PSEUDOSCIENCE OF SINGLE-SEX schooling" (23 September, p. 1706), D. F. Halpern *et al*. claim that there is no evidence to support positive effects of single-sex education. They acknowledge that "without blind assessment, randomized assignment to treatment or control experiences, and consideration of selection factors, judging the effectiveness of innovations is impossible," yet they cite only those studies that support their thesis.

Absent from their analysis were studies such as "Public and Catholic schooling: The effects of gender context policy" (*1*), which indicates that it was the single-sex system that accounted for the outperformance by Catholic schools of public schools in an earlier study (*2*). They also overlooked a longitudinal study conducted in New Zealand indicating that single-sex education resulted in different and more favorable outcomes in terms of gender equity than did coeducation (*3*).

Halpern *et al*. seemed to question whether males and females respond differently to stress, despite abundant research that has been done in this area (*4*). They also claim that "boys who spend more time with other boys become increasingly aggressive" and "girls who spend more time with other girls become more sex-typed," yet the source they cite as support studied children whose mean age was 52 months (*5*). Proponents of single-sex schools are not arguing for single-sex preschools, and a study of preschool children is not applicable to children in elementary, middle, and upper-school students.

Anecdotally, having taught in both single-sex and coeducational middle and upper schools, I have observed that sex-role stereotyping is more evident in a coeducational environment. The onset of adolescence seems to create enormous pressure on many boys and girls to appear and behave as true to their gender stereotype as possible, especially in the presence of the opposite sex.

It is interesting that the authors argue that there is no study using blind assessment and randomized assignments to support the idea that single-sex education leads to stronger outcomes. This is similar to the arguments that the tobacco industry used for years to argue that there was no causal (experimental) evidence to support the notion that cigarette smoking was harmful to one's health. Although it would make for better science to randomly select experimental and control groups for single-sex and coed conditions, I do not know any proponent of single-sex education that wishes to force who model on any student or parent.

OLEN ANTHONY KALKUS

Princeton Academy, 1128 Great Road, Princeton, NJ 08540, USA. E-mail: okalkus@princetonacademy.org

References

1. C. Riordan, *Am. J. Ed.* **93**, 518 (1985).
2. J. Coleman, T. Hoffer, S. Kilgore, "Public and private schools" (National Center for Education Statistics, National Opinion Research Center, Chicago, 1981).
3. S. J. Gibb, D. M. Fergusson, L. J. Horwood, *Aust. J. Ed.* **52**, 301 (2008).
4. S. E. Taylor *et al*., *Psychol. Rev.* **107**, 411 (2001).
5. C. L. Martin, R. A. Fabes, *Dev. Psychol*. **37**, 431 (2001).

Single-Sex Education: Positive Effects

IN THEIR EDUCATION FORUM "THE PSEUDOscience of single-sex schooling" (23 September, p. 1706), D. F. Halpern *et al*. correctly point out the challenges inherent in assessing the causal effects of single-sex schooling: Because in most contexts, students (or their families) choose between single-sex and coeducational schools, differences between the groups may reflect variations in unobserved characteristics (such as motivation or ability) that contributed to school selection. However, Halpern *et al*.'s assertion that "there is no well-designed research showing that single-sex education improves students' academic performance" is incorrect.

We took advantage of a unique setting in Seoul, South Korea, to assess causal effects of single-sex schools (*1*). Until 2009, students in Seoul were randomly assigned to high schools within school districts regardless of whether schools are single-sex or coeducational. Observed socioeconomic student backgrounds are well balanced between the two types of schools, confirming randomness of school assignment. Noncompliance with random assignment is at most very limited. Our analysis shows that single-sex schools produce higher 4-year college attendance and better national university entrance exam scores than coeducational schools for both boys and girls. Although we do not argue that our finding is conclusive and can be generalized to other contexts, this study and others (*2*, *3*) provide data and statistical support for positive impacts of single-sex schooling.

Meanwhile, to support their conclusion that single-sex schools perpetuate sex-typed behaviors and sexism, Halpern *et al*. cite observational studies of small samples (*4*, *5*). They also cite an observational study

CREDIT: ZORAN IVANOVICH/ISTOCKPHOTO.COM

Published by AAAS

to show that single-sex schooling increases divorce (*6*), but they ignore the results in the same work showing positive educational outcomes of single-sex schools.

The literature shows that, in contrast to the claims of Halpern *et al*., systematic analyses of the impacts of single-sex schools have found significant positive effects on educational outcomes, whereas equally systematic investigations of the impacts of single-sex schools on sex-typed behaviors and sexism are not yet available.

HYUNJOON PARK,[1]* JERE R. BEHRMAN,[2] JAESUNG CHOI[2]

[1]Department of Sociology, University of Pennsylvania, Philadelphia, PA 19104–6299, USA. [2]Department of Economics, University of Pennsylvania, Philadelphia, PA 19104–6297, USA.

*To whom correspondence should be addressed. E-mail: hypark@sas.upenn.edu

References

1. H. Park, J. Behrman, "Causal effects of single-sex schools on college attendance: Random assignment in Korean high schools" (PSC Working Paper Series 10-01, University of Pennsylvania, Philadelphia, 2010).
2. L. Sax *et al*., "Women graduates of single-sex and coeducational high schools: Differences in their characteristics and the transition to college" (The Sudikoff Family Institute for Education & Information Studies, Los Angeles, 2009).
3. A. Sullivan *et al*., *Am. Educ. Res. J*. **47**, 6 (2010).
4. L. J. Hilliard, L. S. Liben, *Child Dev*. **81**, 1787 (2010).
5. C. L. Martin, R. A. Fabes, *Dev. Psychol*. **37**, 431 (2001).
6. D. Leonard, "Single-sex and coeducational secondary schooling: Life course consequences?" [Economic and Social Research Centre (ESRC) Report (RES-000-22-1085 ESRC), Swindon, UK, 2007].

Single-Sex Education: Unequal to Segregation

IN THEIR EDUCATION FORUM "THE PSEUDOscience of single-sex schooling" (23 September, p. 1706), D. F. Halpern *et al*.'s premise that racial segregation and single-sex schools are equivalent is unfounded. Racially segregated schools were a function of a reprehensible belief that people of color were different from and, hence, inferior to whites, and that inferiority warranted inequality on any count, including education. Those beliefs and behaviors were destructive and detrimental not only to the people required by law to go to inferior schools, but to our entire society. Single-sex education has no such damaging intention or outcome. Most important, it is a choice made willingly by students and parents, because of the value they recognize in the academic and social development that single-sex schools provide for their children, not only in the short term (test scores and college admission), but also for life.

BURCH FORD

President, National Coalition of Girls' Schools, 50 Leonard Street, Belmont, MA 02478, USA. E-mail: burchford@ncgs.org

Single-Sex Education: Parameters Too Narrow

IN THEIR EDUCATION FORUM "THE PSEUDOscience of single-sex schooling" (23 September, p. 1706), D. F. Halpern *et al*. evaluate school success solely by standardized test scores. They make no attempt to do or cite research that measures parameters such as self-confidence, self-reliance, and leadership qualities. These are the attributes that parents look to single-sex schooling to foster in their children.

The authors also cite divorce statistics in a survey done of adults who went through single-sex schooling in the United Kingdom. Are these data applicable to our American experience? How are they relevant in a time when divorce is so common? Is "not getting divorced" a positive social value? In whose judgment? Is "not getting divorced" in and of itself a sign of responsible, educated adult behavior?

Halpern *et al*. reason that studies of stereotyping caused by single-type schools for racial and ethnic minorities are applicable to single-sex schools. However, gender is balanced numerically and cuts across race, income, region, and education. Given the extreme prejudice that blacks and Hispanics have faced historically, it is inappropriate to equate the experience of same-gender schools with same-race schools.

THOMAS G. PALAIMA

Department of Classics, University of Texas at Austin, Austin, TX 78712, USA. E-mail: tpalaima@mail.utexas.edu

Response

WE APPRECIATE THE LETTER WRITERS' responses to our Education Forum and reply to their concerns in turn. The Letters by Kalkus and by Park *et al*. argue that we neglected to cite certain studies showing the benefits of single-sex education. Our conclusion was based on several large research reviews and data syntheses of thousands of extant studies. Aggregated findings provide more meaningful evidence than any single selected report.

The U.S. Department of Education's review (*1*) included the cohorts studied by two of Kalkus's references—Riordan (*2*) and Gibb *et al*. (*3*)—in arriving at its conclusion of "equivocal" evidence for differences between single-sex and coeducational outcomes. Thus, unlike the tobacco industry's response to data on smoking and health, we cite multiple comprehensive reviews that fail to find an association between single-sex education and educational benefits. Kalkus also cites a paper on stress responses by Taylor *et al*. (*4*) as a rationale for separating boys and girls and teaching them differently. This study is largely theoretical, whereas recent research finds no difference between boys' and girls' levels of the stress hormone cortisol (*5*); no difference between the levels of α-amylase, a salivary enzyme whose release is triggered by the central sympathetic nervous system (*6*); nor any difference in the balance of sympathetic and parasympathetic control of heart rate variability, another measure of stress response (*7*). When found, sex differences in children's neurobehavioral measures tend to be small, with much more variance within each sex than difference between them, making such group differences unsuitable for sorting students into different schools or classrooms.

Contrary to Kalkus's assertion, studies of young children are relevant. Single-sex classrooms are being established in U.S. kindergartens (*8*) and pre-kindergartens (e.g., Princeton Academy). Peers influence children at all ages (*9*). Furthermore, a recent meta-analysis found support for the intergroup contact hypothesis—that is, segregation of groups promotes stereotyping and prejudice toward the other group, whereas intergroup contact reduces such stereotyping and prejudice, among children, adolescents, and adults (*10*).

Regarding Kalkus's points about aggression, a recent longitudinal study found that adolescent boys were less aggressive in schools characterized by high levels of cross-gender interactions (*11*). Similarly, a large analysis of gender "dosage" reported that the lower the proportion of girls in a classroom, the more disruption and violence (*12*). These studies thus agree with findings on younger children that male aggression is associated with the proportion of boys in the group.

Sexism and stereotyping may be found in both coeducational and single-sex class-

Letters to the Editor

Letters (~300 words) discuss material published in *Science* in the past 3 months or matters of general interest. Letters are not acknowledged upon receipt. Whether published in full or in part, Letters are subject to editing for clarity and space. Letters submitted, published, or posted elsewhere, in print or online, will be disqualified. To submit a Letter, go to www.submit2science.org.

Published by AAAS

rooms (*13*). However, the most efficient and effective solution lies not in segregating boys and girls, but in fostering a favorable school climate that encourages mutual respect and positive, productive gender interactions, a conclusion supported by a recent social policy report from the Society for Research on Child Development (*14*).

We thank Park *et al*. for pointing us to their working paper (*15*), which exploits randomized school assignment to assess single-sex versus coeducational outcomes in South Korea. However, because their study does not directly assess demographic variables and includes only two coarse measures of school quality, it is impossible to determine whether the different college outcomes are due to gender composition or to other differences between types of schools. In fact, the study found that boys' advantage could be attributed exclusively to the higher proportion of male faculty in all-boys schools, which the authors note can be implemented in coeducational schools. Furthermore, another analysis of the same randomized population (*16*), found that girls from single-sex schools were significantly less likely to be admitted to the nation's premier university than girls from coeducational schools, a puzzling finding given that Park *et al*. report that these single-sex educated girls earned better national university entrance exam scores. Another recent study involving semirandomized assignment of students in Trinidad and Tobago (*17*) found that most students performed no better in single-sex schools, compared with coeducational schools, and that girls in single-sex schools took fewer science courses and more traditionally female subjects than girls in coeducational schools.

We agree with Park *et al*. that systematic reviews have yet to address the potential harm of single-sex schooling in increasing gender stereotyping and sexism. However, we cited several individual studies demonstrating the negative effects on children when adults use attributes such as gender to organize the learning environment and also provide evidence for negative gender intensification when children are limited to same-sex peer interactions. We also note that increased gender stereotyping was a prominent finding in a study of the failed California experiment to implement single-sex public schooling (*18*). In addition, although the UK study addressing men's divorce rates did find a benefit of single-sex schooling on girls' self-concept in math and science, this did not translate into greater female participation in STEM careers or even overall labor market participation (*19*), suggesting that the all-girls' environment, which other research indicates may foster a "pernicious" sexism (*13*), does not buffer against real-world sexism.

Ford and Palaima reject the analogy between gender segregation and racial segregation. We stand by our argument. Over 50 years of psychological research has shown that people who are sorted into groups based on either biological (e.g., eye color, sex, or skin color) or arbitrary (e.g., shirt color) traits develop favoritism toward the in-group and stereotypes of the out-group (*20*). We also note that, similar to children of color, girls were historically denied an education equal to boys, and that women, like racial minorities, have been subject to intrinsic bias in hiring and promotion, which is exacerbated in gender-segregated workplaces (*21*). Racial segregation was legal in U.S. schools until social scientists and others testified in court regarding its harmful consequences and worked to change the law.

Palaima is wrong in his assertion that we examined only "standardized test scores." The U.S. Department of Education review we cited (*1*) examined a wide range of outcome variables in addition to school achievement, including self-concept, delinquency, attitudes toward school, school completion, choice of college major, eating disorders, career aspirations, attitudes toward women, and opportunities for leadership roles.

We do not advocate value judgments regarding divorce. However, data showing

CORRECTIONS AND CLARIFICATIONS

***Science* Prize Essay:** "Lessons from a science education portal" by D. Micklos *et al*. (23 December 2011, p. 1657). Errors were made during galley corrections. On page 1657, two words were substituted for the authors': In the first line of column two, "experimental" for "exponential" and, in the last sentence of the second paragraph in column three, "visualization" for "visitation." The first corrected sentence is: "Search engines became de facto arbiters of an exponentially expanding Web, periodically directing 'robots,' or 'spiders,' to build a searchable index of a site." The second corrected sentence is: "Additional efforts in spring 2011 increased visitation 20.5% in June to November." The sentences have been corrected in both the PDF and HTML versions online.

Perspectives: "A correlation for the 21st century" by T. Speed (16 December 2011, p. 1502). Owing to a production error, the name J. Wishart was mistakenly included as a coauthor in reference 7. H. O. Hirschfeld is the sole author.

News of the Week: "An elemental process nears its end" (9 December 2011, p. 1329). The story incorrectly stated that the official name for element 116 will be flerovium. Element 116 will be named livermorium, and element 114 will be flerovium.

Reports: "Pathogen effectors target *Arabidopsis* EDS1 and alter its interactions with immune regulators" by S. Bhattacharjee *et al*. (9 December 2011, p. 1405). In both the PDF and HTML versions online, the figures have been upgraded to remove white lines in color blocks.

News Focus: "Where does the time go?" by A. Cho (2 December 2011, p. 1200). The story stated that neutrino pulses take 2.43 microseconds to travel from the CERN laboratory in Switzerland to a detector at Gran Sasso in Italy. The correct figure is 2.43 milliseconds.

Perspectives: "Warburg effect and redox balance" by R. B. Hamanaka and N. S. Chandel (2 December 2011, p. 1219). In the figure, PMK2 should be PKM2.

Perspectives: "True performance metrics in electrochemical energy storage" by Y. Gogotsi and P. Simon (18 November 2011, p. 917). On page 918, in panels A and B of the figure, for the vertical axis (power density), the units should be W/kg and W/liter instead of Wh/kg and Wh/liter, respectively.

TECHNICAL COMMENT ABSTRACTS

Comment on "Late Mousterian Persistence near the Arctic Circle"

Nicolas Zwyns, Wil Roebroeks, Shannon P. McPherron, Adam Jagich, Jean-Jacques Hublin

Slimak *et al*. (Reports, 13 May 2011, p. 841) reanalyzed the lithic assemblage from the northern site of Byzovaya (Russia) and concluded that it was Mousterian and produced by Neandertals. The previous interpretation of this assemblage as falling within Early Upper Paleolithic variability remains the most parsimonious explanation; pending additional fossil discoveries, there is no evidence supporting the occurrence of Neandertals at these high latitudes.

Full text at www.sciencemag.org/cgi/content/full/335/6065/167-b

Response to Comment on "Late Mousterian Persistence near the Arctic Circle"

Ludovic Slimak, John Inge Svendsen, Jan Mangerud, Hugues Plisson, Herbjørn Presthus Heggen, Alexis Brugère, Pavel Yurievich Pavlov

Contrary to what Zwyns *et al*. claim on a bibliographical basis, the lithic industry of Byzovaya cannot belong to the Streletskayan complex or be considered as Upper Palaeolithic (UP). Direct analysis of northern assemblages and of Streletskayan technologies reveal incompatible features between these industries. Byzovaya is structured on specific Mousterian technologies and does not show any unique features of the UP.

Full text at www.sciencemag.org/cgi/content/full/335/6065/167-c

that men in their 40s were more likely to be divorced if they attended single-sex schools than if they attended coeducational schools (*18*) provide support for the theory that when girls and boys work and play cooperatively in structured, supportive environments, they develop the skills needed for working and living together. In light of compelling counterarguments to the critiques offered in the preceding letters, we reaffirm the conclusions in our original article.

DIANE F. HALPERN,[1]* LISE ELIOT,[2] REBECCA S. BIGLER,[3] RICHARD A. FABES,[4] LAURA D. HANISH,[4] JANET HYDE,[5] LYNN S. LIBEN,[6] CAROL LYNN MARTIN[4]

[1]Claremont McKenna College, Claremont, CA 91711, USA. [2]Rosalind Franklin University, North Chicago, IL 60064, USA. [3]University of Texas, Austin, TX 78712, USA. [4]Arizona State University, Tempe, AZ 85287, USA. [5]University of Wisconsin, Madison, WI 53706, USA. [6]The Pennsylvania State University, University Park, PA 16802, USA.

*To whom correspondence should be addressed. E-mail: diane.halpern@cmc.edu

References

1. U.S. Department of Education, "Single-sex versus coeducational schooling: A systematic review" (Department of Education, Washington, DC, 2005).
2. C. Riordan, *Am. J. Ed.* **93**, 518 (1985).
3. S. J. Gibb, D. M. Fergusson, L. J. Horwood, *Aust. J. Ed.* **52**, 301 (2008).
4. S. E. Taylor *et al*., *Psychol. Rev.* **107**, 411 (2001).
5. D. S. Jessop, J. M. Turner-Cobb, *Stress,* ***11,*** 1 (2008).
6. J. Strahler, A. Mueller, F. Rosenloecher, C. Kirschbaum, N. Rohleder, *Psychophysiology* **47**, 587 (2010).
7. Y. Fukuba *et al*., *J. Phys. Anthropol.* **28**, 269 (2009).
8. E. Weil, *The New York Times Magazine,* 2 March 2008, p. 38.
9. M. J. Prinstein, K. A. Dodge, *Understanding Peer Influence in Children and Adolescents* (Guilford, New York, 2008).
10. T. F. Pettigrew, L. R. Tropp, *J. Pers. Soc. Psychol.* **90**, 751 (2006).
11. R. Faris, D. Felmlee, *Am. Sociol. Rev.* **76,** 48 (2011).
12. V. Lavy, A. Schlosser, *NBER Working Paper* No. 13292 (August 2007).
13. V. E. Lee, H. M. Marks, T. Byrd, *Sociol. Ed.* **67**, 92 (1994).
14. M. Killen, A. Rutland, M. D. Ruck, "Promoting equity, tolerance, and justice in childhood" (Society for Research in Child Development, Social Policy Report, Volume 25, Number 4, Ann Arbor, MI, 2011).
15. H. Park, J. Behrman, "Causal effects of single-sex schools on college attendance: Random assignment in Korean high schools" (PSC Working Paper Series 10-01, University of Pennsylvania, Philadelphia, 2010).
16. S. Han, T.-H. Kim, B. Seo, "The effects of high school features on high track students' academic achievement in Korea" (2011); www.econ.hokudai.ac.jp/~kinkei/HahnNo4.pdf.
17. C. K. Jackson, *J. Public Econ*. **96**, 173 (2012).
18. A. Datnow, L. Hubbard, E. Woody, "Is single-gender learning viable in the public sector? Lessons from California's pilot program" (Ontario Institute for Studies in Education, Toronto, 2001); http://eric.ed.gov/PDFS/ED471051.pdf.
19. D. Leonard, "Single-sex and coeducational secondary schooling: Life course consequences?" [Economic and Social Research Centre (ESRC) Report (RES-000-22-1085 ESRC), Swindon, UK, 2007].
20. M. Hewstone, M. Rubin, H. Willis, *Annu. Rev. Psychol.* **53**, 575 (2002).
21. B. Mintz, D. H. Krymkowski, *Sociol. Quart.* **51**, 20 (2010).

Comment on "Late Mousterian Persistence near the Arctic Circle"

Nicolas Zwyns,[1]* Wil Roebroeks,[2] Shannon P. McPherron,[1] Adam Jagich,[2] Jean-Jacques Hublin[1]

Slimak *et al*. (Reports, 13 May 2011, p. 841) reanalyzed the lithic assemblage from the northern site of Byzovaya (Russia) and concluded that it was Mousterian and produced by Neandertals. The previous interpretation of this assemblage as falling within Early Upper Paleolithic variability remains the most parsimonious explanation; pending additional fossil discoveries, there is no evidence supporting the occurrence of Neandertals at these high latitudes.

The recent paper by Slimak *et al*. (*1*) makes two large claims. First, based on their reanalysis of the small (n = 313 on 550 m^2), previously excavated (*2*) lithic assemblage from Byzovaya (Russia) (Fig. 1), they claim that the assemblage is now best attributed to the Mousterian. Second, they use this Mousterian attribution to claim that the Byzovaya assemblage was produced by Neandertals. This inferred Neandertal presence near the Arctic Circle is the northernmost one claimed thus far and is at least 7000 ^{14}C years younger than any other unambiguous and directly dated Neandertal skeletal remains (*3*). If substantiated, their claim would considerably expand the geographical range of Neandertals and possibly demonstrate the existence of northern refugia before their disappearance.

The problem with their claims is that there is a more parsimonious explanation for the Byzovaya assemblage. When considered in its regional context, this assemblage fits within the variability displayed by Early Upper Paleolithic (EUP) assemblages. This conclusion, reached by previous studies of the very same assemblage [(*2*, *4*, *5*), which included one of us (W.R.), who handled the material] is not refuted by the Slimak *et al*. paper. So, for example, Byzovaya shares many features with the EUP Streletskaya technocomplex [36, 000 to 27,000 ^{14}C years before the present (yr B.P.)] (*4*), which is present at the contemporaneous site of Garchi (*6*) (Fig. 1). Most of the features described by Slimak *et al*. as Mousterian, such as discoid technology and sidescrapers with scalar retouch, are well documented in Streletskayan EUP assemblages at Kostenki (Fig. 2) that date to roughly the same time period (*7*). EUP laminar elements are known to be rare in Streletskayan assemblage, and previous publications of Byzovaya (*2*, *4*) report the presence of a few of them. The Byzovaya leaf points, interpreted by Slimak *et al*. as showing a connection to the eastern European Mousterian, are also identical to some from the EUP of Kostenki.

Zaozer'e, dated 5000 ^{14}C years older than Byzovaya and with an assemblage recovered in primary archaeological context (*2*), is an important regional point of comparison. This assemblage contains a pronounced EUP component that includes points on large prismatic blades, blades with steep retouch, and retouched and simple burins on truncations or breaks. Additionally, Zaozer'e includes UP elements such as bone and antler points, perforated pendants, and beads (*6*). In Zaozer'e, however, there is also a strong Middle Paleolithic (MP) component dominated by small plano-convex bifacial tools, similar to those found in the eastern European Mousterian but, importantly, also similar to the reported Keilmesser of Byzovaya. The fact that the archaeological level in Byzovaya is in secondary context raises questions regarding the assemblage composition. As indicated by the low frequency of small stone artifacts, sorting processes likely occurred and could explain the absence of UP elements such as small blades, pendants, or antler points that sometimes occur within similar assemblages in primary context.

One of the key arguments for the Mousterian attribution is Levallois blank production. The Levallois component noted by Slimak *et al*. consists of four reported cores and an unknown quantity of unillustrated Levallois flakes. However, given that the Byzovaya bifacial technology can produce flakes highly similar to Levallois flakes, demonstration requires some illustration of these artifacts. The one illustrated Levallois core [figure 3 in (*1*)] lacks a clear preparation of the flaking surface and, as such, stretches the limits of the definition of the Levallois method (*8*). A more complete description of the reported Levallois technology is required because Levallois is a highly variable technique that also appears in so-called MP to UP transitional assemblages and in initial UP assemblages across Eurasia (*9*, *10*).

With regard to the Neandertal refugium argument, it is important to note that so far no archaeological material older than the Mamontovaya (*11*)/Zaozer'e sites (i.e., before about 35,000

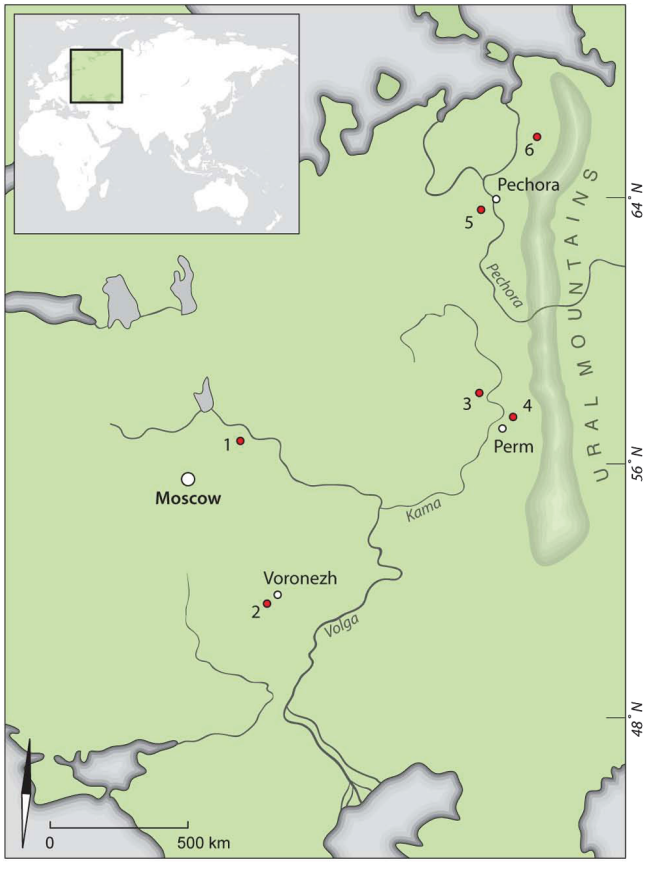

Fig. 1. The geographical distribution of the sites mentioned in the text. (**1**) Sungir. (**2**) Kostenki. (**3**) Garchi I. (**4**) Zaozer'e. (**5**) Byzovaya. (**6**) Mamontovaya Kurya.

[1]Department of Human Evolution, Max Planck Institute for Evolutionary Anthropology, Deutscher Platz, 04103, Leipzig, Germany. [2]Faculty of Archaeology, Leiden University, Post Office Box 9515, 2300RA Leiden, Netherlands.

*To whom correspondence should be addressed. E-mail: nicolas_zwyns@eva.mpg.de

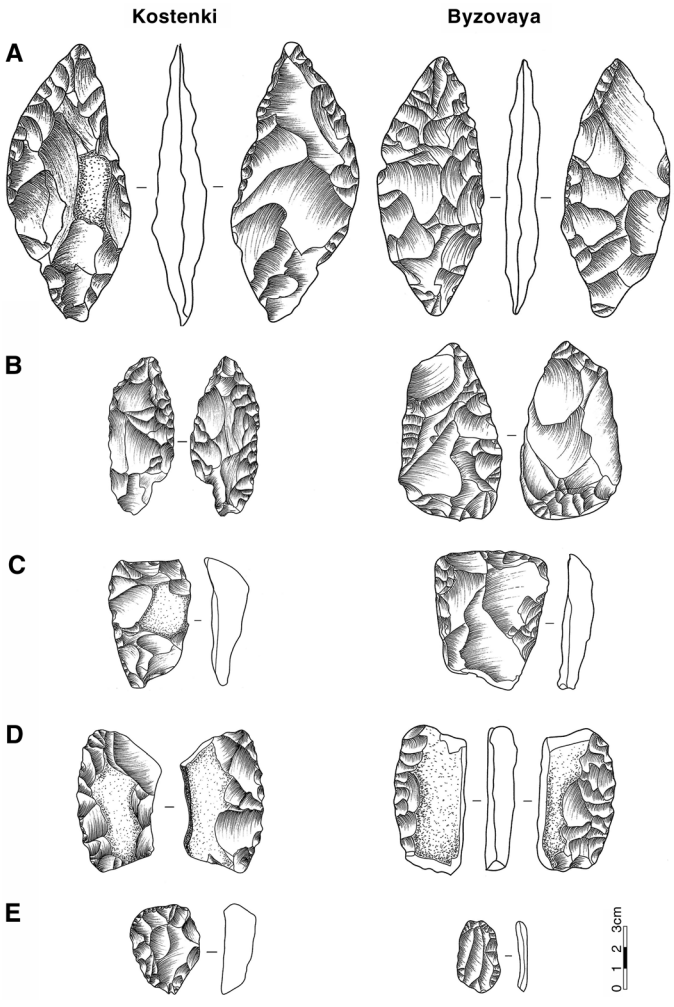

Fig. 2. Comparison between Streletskayan assemblages from Kostenki 1 level V (A), Kostenki 12 level III (B to E), and Byzovaya. All Mousterian tools described by Slimak *et al.* occur in Streletskayan assemblages. Given this context, they are insufficient to support an attribution to Mousterian. (**A**) Leaf point. (**B**) Bifacial knife (with scalar retouch). (**C**) Mousterian scrapers. (**D**) Quina-type side-scrapers. (**E**) End-scrapers. Redrawn from previous publications [e.g., (*5*, *15*)].

^{14}C yr B.P.) has been found in this region, despite the fact that finding MP sites has been a goal of fieldwork over the past decade (*6*). Further south in the lower Don River basin, the absence of Mousterian assemblages from the Kostenki site complex (21 sites, several including multiple layers) suggests that between 38,000 and 20,000 ^{14}C yr B.P., only UP assemblages were produced there and shows, based on skeletal remains and mitochondrial DNA (mtDNA), that anatomically modern humans were present in the region by at least 31,000 ^{14}C yr B.P. (*12*). At the still closer site of Sungir, the oldest dates on two modern human skeletons and on a Streletskayan assemblage are comparable with the dates for Byzovaya (*13*). Accepting the Slimak *et al.* interpretation of Byzovaya implies that the makers of the Mousterian entered—and then remained constrained to—the northern latitudes before 38,000 years ago, shared the region for at least 5000 years with the EUP makers of the Zaozer'e assemblage, and remained otherwise invisible in the archaeological record for about 10,000 years.

Slimak *et al.*'s paper again raises the question of whether specific types of lithic assemblages can be linked to hominin species in the absence of skeletal remains. Western and Central Europe are for now the only regions where the Mousterian and/or the Levallois technologies are indeed exclusively associated with Neandertal fossils, whereas in Africa and the Levant they are also associated with early modern humans. Given that the local EUP retains numerous MP features, the small Byzovaya assemblage cannot be used to determine the hominin taxon that made it. Fossils are needed to settle the important issues regarding the former distribution of extinct hominins and to document a hypothetical expansion of Neandertals in the far north. Such fossil remains can consist of morphologically diagnostic skeletal remains and/or of DNA signals retrieved from skeletal remains. Analysis of mtDNA from otherwise undiagnostic skeletal remains from Okladnikov (eastern Russia) extended the Neandertal range a spectacular 1500 km to the east (*14*). In contrast, Slimak *et al.*'s claim for a similarly spectacular expansion of the Neandertal chronological and geographical range is not supported by any type of evidence, neither skeletal nor archaeological. The previous interpretation of the Byzovaya assemblage remains the best interpretation. It is Upper Paleolithic.

References and Notes

1. L. Slimak *et al.*, *Science* **332**, 841 (2011).
2. P. Pavlov, W. Roebroeks, J. I. Svendsen, *J. Hum. Evol.* **47**, 3 (2004).
3. R. Pinhasi, T. F. G. Higham, L. V. Golovanova, V. B. Doronichev, *Proc. Natl. Acad. Sci. U.S.A.* **108**, 8611 (2011).
4. B. I. Guslitzer, P. Y. Pavlov, in *From Kostenki to Clovis*, O. Soffer, N. D. Praslov, Eds. (Plenum Press, New York & London, 1993), pp. 175–187.
5. P. Pavlov, *Archaeol. Ethnol. Anthropol. Eurasia* **33**, 33 (2008).
6. J. I. Svendsen *et al.*, *Quat. Sci. Rev.* **29**, 3138 (2010).
7. V. P. Chabai, in *The Chronology of the Aurignacian and of the Transitional Technocomplexes. Dating, Stratigraphies, Cultural Implications*, J. Zilhao, F.D. D'Errico, Eds. (Trabalhos de Arqueologia, Lisboa, 2003), pp. 71–86.
8. E. Boëda, *Le Concept Levallois: Variabilité des Méthodes* (CNRS Editions, Paris, 1994).
9. V. I. Usik, Y. E. Demidenko, *Paleorient* **19**, 5 (1993).
10. P. J. Brantingham *et al.*, in *The Early Upper Paleolithic Beyond Western Europe*, P. J. Brantingham S. Kuhn, K. Kerry, Eds. (University of California Press, London, 2004), pp. 223–241.
11. P. Pavlov, J. I. Svendsen, S. Indrelid, *Nature* **413**, 64 (2001).
12. J. Krause *et al.*, *Curr. Biol.* **20**, 231 (2010).
13. Y. V. Kuzmin *et al.*, *Nucl. Instrum. Methods Phys. Res.* **2004**, 223 (2004).
14. J. Krause *et al.*, *Nature* **449**, 902 (2007).
15. M. V. Anikovich, N. K. Anisyutkin. L. B. Vishnyatsky (Nestor-Historia, St. Petersburg, 2007).

Acknowledgments: We are grateful to A. A. Sinitsyn for providing us documentation and to T. Kivell for her helpful comments.

16 June 2011; accepted 28 November 2011
10.1126/science.1209908

Response to "Comment on Late Mousterian Persistence near the Arctic Circle"

Ludovic Slimak,[1]* John Inge Svendsen,[2] Jan Mangerud,[2] Hugues Plisson,[3] Herbjørn Presthus Heggen,[2] Alexis Brugère,[4] Pavel Yurievich Pavlov[5]

Contrary to what Zwyns *et al*. claim on a bibliographical basis, the lithic industry of Byzovaya cannot belong to the Streletskayan complex or be considered as Upper Palaeolithic (UP). Direct analysis of northern assemblages and of Streletskayan technologies reveals incompatible features between these industries. Byzovaya is structured on specific Mousterian technologies and does not show any unique features of the UP.

The main criticism by Zwyns *et al*. (*1*) is that they think that the Byzovaya assemblage "fits within the variability displayed by Early Upper Paleolithic....Streletskaya technocomplex." They support their view by making a comparison with some selected artifacts from the UP sites of Zaozer'e, Garchi, and Kostenki farther to the south. We previously performed an in-depth analysis of all these industries and disagree with their assertion that the Byzovaya material offers several points of resemblance with these and other UP sites. Our direct analyses reach the conclusion that three distinct Palaeolithic Boreal traditions existed over a period covering at least 7 millennia (*2*).

In all, 2437 lithic elements were available from the Zaozer'e site, including our 2008 field campaign. This includes 107 tools, as compared with 80 from Byzovaya. Zwyns *et al*. claim that in Zaozer'e "there is also a strong Middle Paleolithic component dominated by small plano-convex bifacial tools, similar to those found in the eastern European Mousterian but, importantly, also similar to the reported Keilmesser of Byzovaya." Zaozer'e is dominated by retouched blades, representing 28 of the 107 tools. We found 14 plano-convex elements that represent an original category: bifacial end-scrapers presenting a regular circular front, for which no Mousterian equivalence is known (Fig. 1). Zwyns *et al*. further assume that "low frequency of small stone artifacts" at Byzovaya would explain the "absence of UP elements such as small blades, pendants, or antler points that sometimes occur within similar assemblages in primary context." This is not substantiated by the facts, as small elements (<2 cm) are even more frequent from Byzovaya (20.8%) than from Zaozer'e (16.3%). The Zaozer'e collection also presents a variety of large tools and subproducts on bone, antler, and ivory, which is typically UP (Fig. 1).

As many as 5000 lithic elements have been uncovered from Garchi. This includes many characteristic triangular points with a concave base that is considered diagnostic of the Streletskayan industry. The remaining artifacts are for the most part subproducts of this point production. Finally, a few small end-scrapers that are shaped directly from siliceous pebbles are present, and none of the lithic elements at Garchi share any technological similarities with the artifacts from either Byzovaya or Zaozer'e.

Direct technological data show that Byzovaya, Zaozer'e, and Garchi represent three different technical traditions that are not related to each other. The Garchi lithics are typical of UP Streletskayan industries, and it seems clear that Zaozer'e also belongs to a UP complex. These sites present incompatible technologies, corroborating our previous conclusion that they present no technical relation with Byzovaya.

Zwyns *et al*. discuss the Levallois technology of Byzovaya. They argue that the core shown in our figure 3 (*3*) would lack a clear preparation of the flaking surface that would be typical for this technology. We lean on the explanation provided by Bordes (*4*): "the expression 'facetted butt,' taken in the sense of the Levallois technique, is absolutely erroneous, because there are many flakes with facetted butts that are non-Levallois, and there exist Levallois flakes with a flat butt" (*5*). Their position is hardly understandable because they refer to a major publication giving the Levallois diagnostic features that absolutely fit with the Byzovaya elements (*6*). The less-disputed way to demonstrate a Levallois technology is based on the core geometry and structure that demonstrate that at Byzovaya, Levallois technologies illustrate the preferential method, the most diagnostic feature of the Mousterian.

Zwyns *et al*. assume that "Comparison between Streletskayan assemblages from Kostenki 1 level V (A), Kostenki 12 level III (B to E), and Byzovaya" would demonstrate that tools described as typically Mousterian by us occur in Streletskayan complexes. However, they do not compare the full "assemblages" but illustrate their view from drawings of five selected objects from Byzovaya and five others from two different sites of Kostenki. In our opinion, this approach is misleading because it: (i) is based on second-hand data, (ii) focuses on a handful of selected objects, (iii) mixes elements from different sites, and (iv) isolates objects from their specific technological context. Any lithic element belongs to a coherent system that has to be examined as an entity. In this case, their supposed similarities are very vague. For making this clear, we added five tools from a French final Neolithic site to figure 2 in (*1*) (Fig. 3), illustrating the danger of such analogic methods.

Before our original paper (*3*) was published, we performed a first-hand technological comparison with Streletskayan assemblages from the well-known UP sites Kostenki 6 (the eponymous Streletskayan) and Biryuchya Balka, which offers the richest collection of such an industry. We could not find a single element reflecting a real Mousterian technology. We suspect that the so-called archaic structure is the frequent occurrence of retouched flakes whose blanks occur from the bifacial shaping of the concave-base points as at Garchi (Fig. 2). However, it is noteworthy that none of the 50,000 artifacts from Biryuchya Balka could be confused with a Levallois or discoid artifact by any experienced lithicist.

Zwyns *et al*. interpret the elements from Kostenki and Byzovaya shown in figure 2A in (*1*) as a "leaf point" (Blattspitzen). The artifact from Kostenki is more than 2 cm thick and has very irregular edges and two differently shaped faces—one with flat covering retouch, the other scalar, showing that it represents an unfinished and undiagnostic bifacial element. We are much in doubt about this classification. In contrast, their selected artifact from Byzovaya is much thinner and more regular but bears a plano-convex construction. To be precise, such tool is no more compatible with the leaf-point definition but appears classically among Mousterian technologies [see (*4*), plate 49].

Figure 4 shows a Blattspitzen from Byzovaya, symmetric across all axes, with indisputable regular edges. Flat retouch covers each face, and the tool is only few millimeters thick. We consider it a classic example of its category, typical for the Central and Eastern European Mousterian industries and distinctively different from the unconvincing example from Kostenki.

The given samples of "Quina-type side-scrapers" [figure 2D in (*1*)] are no more relevant; the one from Byzovaya is an artifact struck from a natural slate and shaped by a bifacial flat retouch [compare with figure S6 in (*3*)].

[1]CNRS, UMR 5608, TRACES, Université de Toulouse le Mirail, Maison de la Recherche, 5 Allées Antonio Machado, 31058 Toulouse Cedex 9, France. [2]Department of Earth Science and Bjerknes Centre for Climate Research, University of Bergen, Allégaten 41, N-5007, Bergen, Norway. [3]CNRS, UMR 5199, PACEA, IPGQ, Université Bordeaux 1, Bâtiment B18, Avenue des Facultés, 33405 Talence Cedex, France. [4]CNRS, USR 3225, and UMR 7041, ArScAn, "Archéologies Environnementales," Maison de l'Archéologie et de l'Ethnologie René Ginouvès, CC023, 21, Allée de l'Université, 92023 Nanterre Cedex, France. [5]Department of Archaeology, Institute of Language, Literature and History, Komi Science Centre, Russian Academy of Sciences, Kommunisticheskaya Street 26, 167000 Syktyvkar, Komi, Russia.

*To whom correspondence should be addressed. E-mail: slimak@univ-tlse2.fr

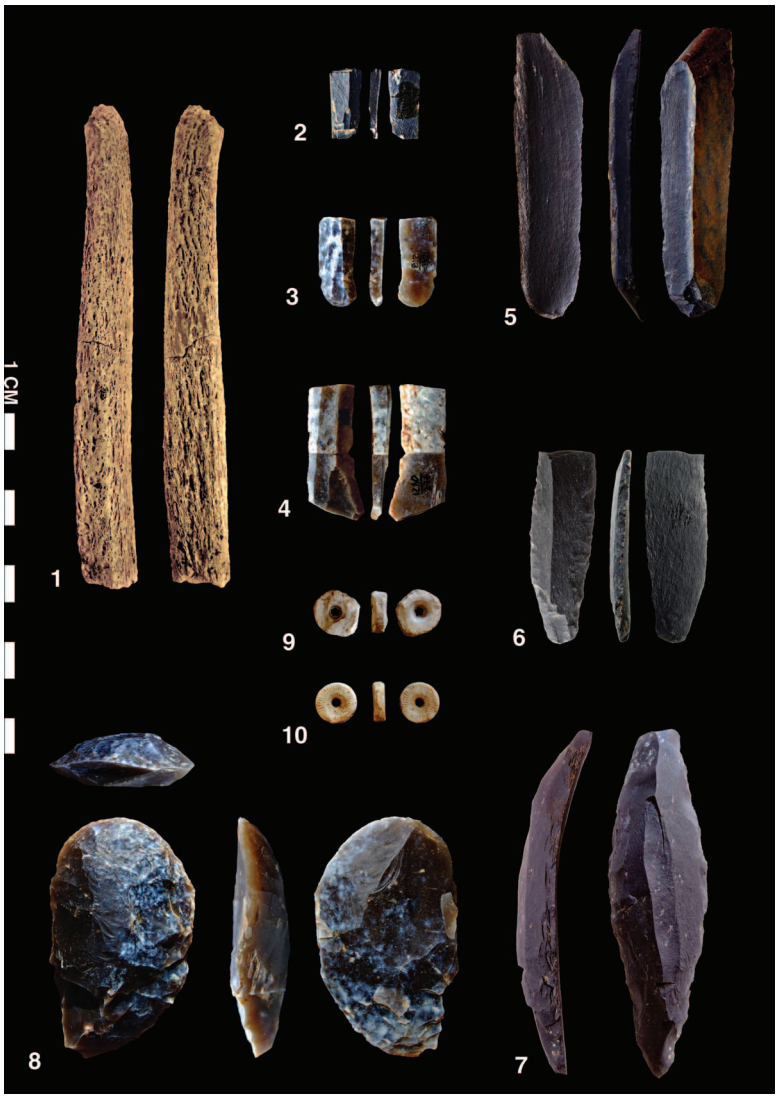

Fig. 1. Zaozer'e industry is, like any other UP industry, based on blade and bladelets technology. The plano-convex tools are 14 very specific end-scrapers. Moreover, the industry contains various evidence of bone, ivory, and antler technology, including ornaments. None of these elements is present in Byzovaya, and their combination is unknown in the Mousterian industries of Eurasia. (**1**) Antler tool. (**2** to **4**) Bladelets. (**5** to **7**) Blades. (**8**) Zaozer'e end-scraper shaped from plano-convex blank. (**9** and **10**) Fossil pendants. [Photos by L. Slimak]

Finally, the commenters argue for the lack of Middle Palaeolithic sites previously found in the region. We underline that, since the 19th century, Palaeolithic research has been conducted there by only three archaeologists, in an area bigger than France and where Pleistocene discoveries are restricted to eroded river banks. We therefore warn against conclusions based on negative evidence.

Such debate cannot stay at such a binary level and within a closed frame that would exclude any new data. First-hand analyses reveal the existence of at least three distinct traditions, illustrating concretely the complexity of the High Latitudes colonization.

Byzovaya is typically Mousterian according to its original definition (*4*), which does not depend on the biological identity of the knapper or on other aspects of hominin social organization. In Europe, Mousterian industries have so far always been associated with Neandertals, a reality that could be dismissed, but only by concrete facts. From current knowledge, the Byzovaya technologies probably reveal a Neandertal Arctic persistence, although we still stick to our statement from our original paper; "whether Byzovaya represents a Neandertal site or not cannot be demonstrated beyond doubt until human bones or DNA are found" (*3*).

References and Notes

1. N. Zwyns *et al.*, *Science* **335**, 167 (2012); www.sciencemag.org/cgi/content/full/335/6065/167-b.
2. P. Pavlov, *Archaeol. Ethnol. Anthropol. Eurasia* **33**, 33 (2008).
3. L. Slimak *et al.*, *Science* **332**, 841 (2011).
4. F. Bordes, *Typologie du Paléolithique Ancien et Moyen* (Delmas, Bordeaux, France 1961).
5. In the original French: "L'expression 'talon à facettes,' prise dans le sens de technique Levallois, est de plus parfaitement erronée, car il y a bien des éclats à talons facettés qui ne sont pas Levallois et il existe des éclats Levallois à talon lisse."
6. E. Boeda, *Le Concept Levallois: Variabilité des Méthodes* (CNRS Editions, Paris, 1994).

Acknowledgments: We thank A. E. Matyukhin for the opportunity to access the Biryuchya Balka collections in 2007 and J. E. Lewis for improving the English.

14 July 2011; accepted 28 November 2011
10.1126/science.1210211

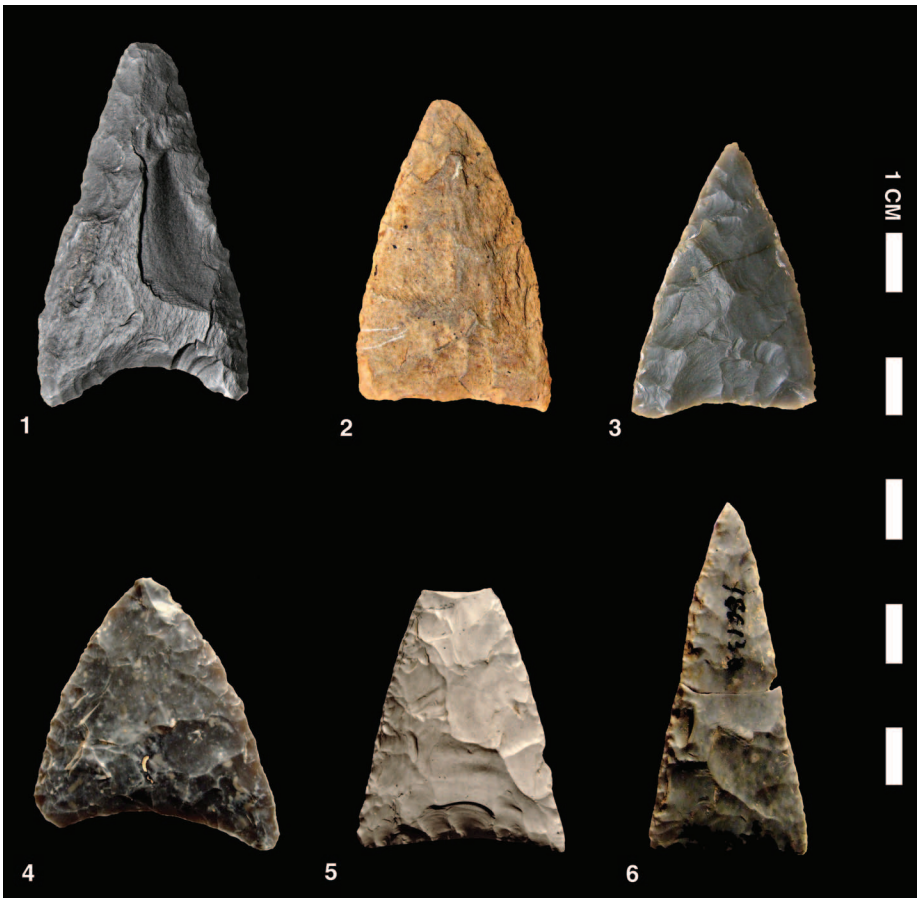

Fig. 2. Small concave base-point production represents the main diagnostic feature of the Streletskayan industries. It is based on precise technological criteria easily recognizable both in the structure of these projectiles points and in the numerous subsequent subproducts. (**1** to **3**) Garchi. (**4** to **6**) Biryuchya Balka. [Photos by H. Plisson and L. Slimak]

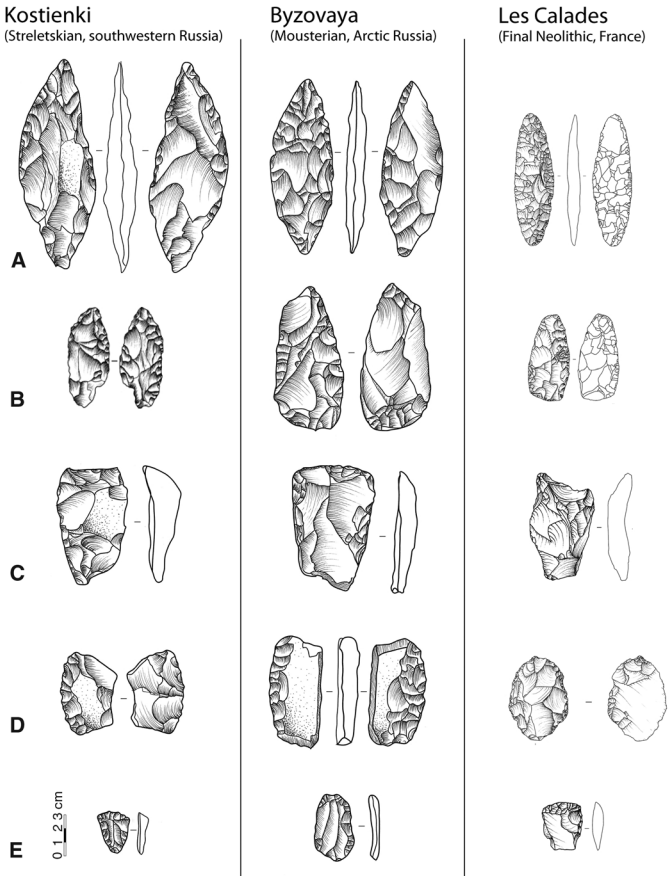

Fig. 3. Tools from Les Calades shown alongside the drawings from figure 2 in (*1*). The comparison of morphological traits out of their specific technological and archaeological context is misleading. Designations from (*1*) are misleading because they are extracted from their specific archeological context and their precise technological background: "(**A**) Leaf point. (**B**) Bifacial knife (with scalar retouch). (**C**) Mousterian scrapers. (**D**) Quina-type side-scrapers. (**E**) End-scrapers." [Drawings from Les Calades sites by R. Furestier]

Fig. 4. Byzovaya. Real Blattspitzen. [Photos by Ludovic Slimak]

OCEANS

Maxing Out Our Take

Carl Safina

Maximum sustainable yield (MSY) is, for its detractors, an idea that has outlived a usefulness it never had. The idea: A wild population can withstand human extraction, without harm, in perpetuity, up to some maximum amount. MSY's flaws include its nonconsideration of food webs and its fixation on "maximum." Quantifying MSY requires data that many fisheries lack. And political exigencies frequently cause fisheries managers to simply set catch limits far higher than the scientifically recommended, formally calculated MSY. But rather than blaming fishery failures at least partly on managers' frequent refusal to apply the principle, some put all the blame on the principle itself. The author of *All the Fish in the Sea* is among them.

Pieter Bruegel the Elder's *Big Fish Eat Little Fish* (16th century).

Carmel Finley (a historian at Oregon State University) dismisses MSY as unscientific: "MSY is, and always has been, policy disguised as science" and "a straitjacket on the ability of scientists to incorporate new scientific understandings." She also claims that the adoption of MSY set off "a free-for-all to catch the world's fish stocks."

Is MSY guilty as charged? Since the 1970s, Alaska's fisheries managers have generally held catches to scientifically quantified estimates of sustainable yields. Meanwhile, New England's managers routinely ignored scientists' recommendations. Alaska maintained robust fisheries. New England's fisheries collapsed. U.S. law recently limited catch quotas to MSY-based calculations, facilitating some significant recoveries. Perhaps MSY can be useful despite its flaws. The free-for-all that Finley blames on MSY was, in my view, the near-inevitable result of a technological explosion in a competitive world that hadn't found the limits to ocean resources. Fishing nations were simply racing to the fish.

Yet, cutting MSY no slack, Finley dismisses the modest notion that MSY represented an implied acknowledgment that resources have limits. Finley's finger of blame even lands upon Garrett Hardin. She holds that his "'Tragedy of the Commons' paper … implied that it was impossible to control the 'commons.' This in turn provided justification for those who opposed … international regulatory regimes. Moreover, by persuading scientists that overuse of resources was virtually a law of nature, Hardin's analysis drew attention away from the conscious government policies that had helped to produce the prevailing situation." Well—I doubt many ecologists agree.

All the Fish in the Sea
Maximum Sustainable Yield and the Failure of Fisheries Management
by Carmel Finley
University of Chicago Press, Chicago, 2011. 222 pp. $35. ISBN 9780226249667.

The book's most interesting, tragic, road-not-taken figure is Michael Graham, a Quaker, soldier, farmer, and human ecologist who, after World War II, became Britain's chief fisheries scientist. Having independently deduced the precautionary principle, he articulated his "great law of fishing: 'Fisheries that are unlimited become unprofitable.' "

The timing was superb. War had devastated fishing fleets, allowing fish to recover from earlier depletion. Graham correctly saw a go-slow opportunity for "rational fishing." But the mood was wrong. The United States and other developed nations wanted to stop poorer countries from defensively extending territorial claims seaward. Governments hurriedly expanded fishing fleets to project their nations' dominance. Foremost was the United States.

As Finley sets it up, Graham's ideological rival was Wilbert M. Chapman, the U.S. State Department's fisheries undersecretary, who propounded MSY with evangelical zeal and self-deceiving jingoism. MSY was then merely a concept accompanied by a qualitative curve, with no quantitative parameters and no supporting data. At the curve's low end, fish were wasted by leaving them in the sea; at its high end, excess fishing drove the population down. But finding that sustainable maximum meant that fishing would not be restricted until the stocks were overfished. Chapman never believed that fishing could deplete a fish population. Others held that bankruptcy following depletion would prevent fish extinction—and they expected MSY to work automatically, in this self-regulating way. Chapman asserted that his policies would "make possible the maximum production of food from the sea on a sustained basis year after year." His MSY was not really a limit, but a goal to be reached.

Chapman, the American policy-maker, emphasized "maximum." Graham, the British scientist, believed that "the primary objective of fishery conservation is to control man's activities" and that "an intermediate rate of fishing gives the best result." But events drove policy. Latin nations extending territorial claims up to 200 miles from their coasts infuriated American tuna fishermen and, in turn, Chapman and the State Department. The territorial claims were "morally … unjustifiable," railed Chapman. He saw the Latin Americans as selfish because they would not allow U.S. fishermen to catch the fish.

Chapman's bluster trumped Graham's precautions. During a contentious 1955 inter-

The reviewer is at the School of Marine and Atmospheric Science and Center for Communicating Science, Stony Brook University, Stony Brook, NY 11794, USA. E-mail: csafina@blueocean.org

Published by AAAS

national fisheries conference in Rome, delegates voted that "conservation measures should be applied when scientific evidence shows that fishing activity adversely affects … the resources." But they intended conservation "to increase, or at least maintain, the average sustainable yield" and "to secure a maximum supply of food." Thus, wealthy nations granted themselves permission to take vastly more.

Graham had his "great law of fishing." Chapman had a grand delusion: "There is a crop to be taken in the international common. Each takes according to his ability. When the safe crop is taken, all stop the harvest."

Finley correctly observes that once fishing power sufficient to catch the maximum sustainable yield has been built, it generates pervasive political pressures that make dialing it back nearly impossible. By the 1970s, over a thousand Communist-bloc ships were fishing off North America. Americans watched helplessly as the policy they championed took their fish. Global fishing capacity far overshot what the fish could bear, and many great fisheries crumbled. Graham's words resonate most: "I am still teaching this: 'Find what direction to go in and take a small step that way.' "

10.1126/science.1215443

BIOETHICS

Institutionalizing Ethical Research

Charles W. Lidz

How did we get here? Seeking to answer that question for institutional review boards (IRBs), Laura Stark's *Behind Closed Doors* challenges the historical mythology of bioethics.

IRBs are supposed to evaluate proposed research to "assess risks and safeguard participants' rights" in human experimentation. Yet it is hard to see how this protection will be ensured by having the research institution's senior managers choose some subordinates to meet on a regular basis to look at some paper plans for what will happen in a particular project. Don't committee members have a serious conflict of interest? Working for the investigator's institution, they presumably have an interest in its success and thus in approving the protocols. Why should such reviews be done on a local basis? Research ethics in San Diego should not differ from those in Chicago. Why should 15 or 20 people, whose time is valuable and expensive, regularly sit in a room and listen to others report their findings about plans submitted by investigators (or more typically, by investigators' research assistants)? Does this procedure guarantee ethical treatment of research participants and, if not, what other purposes could it serve? Stark (a sociologist at Wesleyan University) clarifies how we came to settle on the particular answers that we have to these questions.

Behind Closed Doors
IRBs and the Making of Ethical Research
by Laura Stark
University of Chicago Press, Chicago, 2012. 237 pp. $85. ISBN 9780226770864. Paper, $27.50. ISBN 9780226770871. Morality and Society.

There is a conventional account for how our current system of research review got started. It is the story that those of us who teach bioethics regularly recount to our students. It begins with the atrocities of Nazi "medical research" in the concentration camps before and during World War II. The subsequent Nuremberg trials built the basis for modern bioethics, including the key role of informed consent. Over the following decades, a series of severely unethical research studies occurred, such as the notorious Tuskegee syphilis study, the Jewish Chronic Disease Hospital case (which involved injecting live cancer cells into elderly demented patients without consent), and the Willowbrook experiments (randomly choosing institutionalized severely developmentally delayed people to be given hepatitis). Public outrage over these events and intensive pressure from bioethicists led to our current procedures for research review.

The most important contribution of this interesting, slim book is Stark's demonstration that the conventional version of the origin of IRBs is a very partial story. Everyone knows that the IRB regulations were developed and promulgated by the U.S. National Institutes of Health (NIH). What Stark learned through a detailed review of hundreds of NIH documents is that the concept was built on the NIH Clinical Center's internal process called "group consideration." The Clinical Center developed that largely as a means of preserving its researchers' autonomy, especially in choosing how consent was to be documented. Although the reviews were not primarily focused on ethics, group consideration was intended to assure Congress and other outsiders that the Clinical Center's researchers were behaving ethically.

Two things led NIH to push its internal system for ethical review onto all medical and behavioral scientists at institutions receiving federal funding: The Tuskegee and Jewish Chronic Disease Hospital scandals increased attention from both Congress and the media. And the growth of NIH's external research funding increased concerns that NIH could be held liable for the ethical and legal violations of outside researchers. NIH wanted to distance itself legally from the experimentation that it funded. The IRB system of local review provided that protection while demonstrating NIH's concern for the ethics of the research it supported.

There is, of course, considerable irony in this history. What started out as a means of protecting research from intrusive regulation (and particularly the requirement that subjects sign detailed consent forms) has evolved into precisely what the group consideration process was meant to prevent: an intensive regulatory process that researchers resent as an intrusion on their autonomy. All applications for NIH funding for research involving humans now require a detailed description of how the subjects are to be treated and informed consent obtained. Thus, even the local nature of ethical review is increasingly limited.

Along with the historical account, Stark offers several chapters based on her ethnographic observation of two IRBs at different universities. Some of this interesting material contributes substantially to our understanding of how IRBs make decisions: She describes how committee members persuade one another of their expertise to critique a protocol. She provides a plausible account of why different IRBs generate conflicting reviews even though they have the same basic ethical commitments. And she explores the role of staff-written summaries of reviews in allowing IRBs to develop critical reviews of the ethics of their colleagues' research.

This book is not without its difficulties. The reader is jolted from ethnography to the historical material with only modest clues concerning how the two sections are connected. Only in the conclusion does the author effectively tie them together. Nonetheless, *Behind Closed Doors* makes an important contribution to our understanding of IRBs and the ethical regulation of research.

10.1126/science.1214711

The reviewer is at the Center for Mental Health Services Research, University of Massachusetts Medical School, 55 Lake Avenue North, Worcester, MA 01655, USA. E-mail: chuck.lidz@umassmed.edu

EDUCATION

Better Research Needed on the Impact of Charter Schools

Randomized trials, although a promising approach, reflect impacts of only a limited subset of highly sought-after schools.

Julian R. Betts[1,2]† and Richard C. Atkinson*

Charter schools have been promoted as a solution to what many view as the public school malaise in the United States. Charter schools, although publicly funded, can operate fairly independently of large district bureaucracies and teacher unions, for instance, by setting their own curriculum and teaching methods and by avoiding the system that grants the most senior teachers first choice of job openings, regardless of their classroom effectiveness. Proponents hope that the semi-independent governance structure of charters will encourage these schools to generate fresh ideas. President Obama has followed Presidents Bush and Clinton in identifying charter schools as a key element of school reform.

Are charter schools boosting achievement? Is there variation across charter schools in effectiveness? These are key policy questions, as failing charter schools should be shut down, and successful charter schools replicated (*1*). Unfortunately, most studies of charter schools' impact on student achievement use unsophisticated methods that tell us little about causal effects. We highlight below some key problems, and suggest policies and practices that could improve research and, we hope, education.

Lotteries: Promising, But Not Perfect

A recent meta-analysis discarded roughly 75% of studies because they failed to account for differences between the background and academic histories of students attending charter schools and those attending traditional public schools (*2*). Most studies simply take a snapshot of student performance at a single point in time. Such studies cannot disentangle school quality from the preexisting achievement level and trajectory of students who decide to attend a given school. The potential for student self-selection into charter schools is great, which makes naïve comparison of student outcomes at charter schools and traditional public schools misleading. Parents may not apply to a charter school because of the distance to the school or lack of time to fulfill volunteer work that such schools sometimes request. Families that apply may be unusually motivated. The decision by charter school operators about where to locate also influences who attends, which makes simple comparisons with traditional public schools difficult. More often than not, the difference in average test scores between charter schools and traditional public schools reflects who enrolls at the schools more than the quality of education being provided (*3*, *4*).

But rigorous research on charters is beginning to appear, and much of this takes advantage of the way in which charter schools admit students. State laws dictate that if a charter is oversubscribed, then an admissions lottery must be held. Because only chance distinguishes who does and does not receive admission, the students who lose the lottery represent the ideal control group. Lottery-based studies of charter schools have been done in Boston (Massachusetts); New York City; a small national sample of middle schools; and a few schools in Chicago (Illinois), San Diego (California), and Lynn (Massachusetts). These studies tend to find that charter schools either outperform or perform at the same level as traditional public schools (*5*–*12*). These studies, however, cover only about 90 charter schools, roughly 2% of charter schools nationally (*13*).

We strongly support the wider use of randomized controlled trials of the impact of charter schools on student outcomes. At the same time, we acknowledge that this approach has limitations. Foremost among these is that most charter schools are not oversubscribed. For example, the U.S. Department of Education released a lottery-based study of charter middle schools that found that only 130 out of 492 such schools nationwide used admission lotteries (*10*). This raises the possibility that a study of oversubscribed charters will not tell us anything about the effectiveness of the majority of charter schools that are not sufficiently popular to be oversubscribed. The natural targets for research, districts with many oversubscribed charter schools, may have unusually good charter schools. Indeed, one study showed that parents in Texas are more likely to remove their children from underperforming charter schools than from charter schools that outperform nearby traditional public schools (*14*). Lottery-based studies of middle- and high-school charter schools in Boston produced among the highest estimates of impacts on reading and math achievement in studies of those grade spans (*5*). Another lottery-based study of New York City charter schools produced the largest estimated impacts among studies of elementary and middle schools in combination (*8*). In contrast, a lottery-based national study of charter middle schools that did not solely seek districts with the greatest demand for charter school slots found no significant gains from winning a lottery (*10*).

For several reasons, it will be important to study the many charter schools that are not oversubscribed, using the best research designs possible. In addition to obtaining a more representative portrait of charter schools, studying the qualitative features of a broad set of schools will allow both theoretical insight and institutional knowledge that can help to separate causation from correlation.

Essential to studies of undersubscribed charters schools is to account for individual students' past achievement. Even with this, it will be difficult to estimate the causal effects of attending a charter school because of unobserved factors that influence who attends charter schools. We have three locations in which to compare results of lottery-based and careful non–lottery-based studies (*15*, *16*). The two approaches produce somewhat similar results, although the non–lottery-based studies have sometimes produced lower estimated effects, perhaps because of inadequate controls for unobservable characteristics of students and their families.

Better Policy, Better Data, Better Research

Research on charter schools must evolve in several other ways. Because charter schools have freedom to experiment, not all of them will perform equally well. Thus, research should estimate the impact of specific charter schools (or, at the very least, types of charter

[1]Department of Economics, University of California, San Diego, La Jolla, CA 92093, USA. [2]Bren Fellow, Public Policy Institute of California, San Francisco, CA 94111, USA.

*R. C. Atkinson is President Emeritus of the University of California and former Director of the National Science Foundation. †Author for correspondence. E-mail: jbetts@ucsd.edu

Published by AAAS

schools). Once we have identified the most successful models, in order to replicate them, we need better information on what aspects of these schools lead to better performance. Do pedagogical or curricular approaches, or the qualifications of teachers, explain any of the differences? Does it matter whether charters are organized locally or are affiliated with charter management (nonprofit) or educational management (for-profit) organizations? Do aspects of the policy environment, such as state law and approaches taken by local authorizers, matter? It will be increasingly important for the literature to report not just "average" effects of charter schools but effects of individual schools, while getting inside the "black box" to learn more about distinctive educational features of each charter school.

There are other roadblocks to the use of admission lottery data for analyzing effects of charters. Fortunately, individual states could remove most of these barriers by overhauling the laws governing charter schools, charter school authorizers, and the bureaucracy that can limit the availability of student test score data to the research community.

First, in most states, individual school districts are the main agencies that can authorize the opening of a charter school. In a few states, public universities or a state agency can directly charter schools as well. State laws typically do not require that charter schools share lottery information with the authorizing entity or the state. This is shortsighted. The aforementioned national study found that of the 130 charter middle schools that used lotteries, only 77 agreed to participate by sharing their lottery data (*10*). Lottery data should not be viewed as the property of the charter school; rather, it is incumbent upon authorizers to gather and scrutinize these data, not least to verify that the lotteries are being done in a fair manner. States should thus require each charter school to share its lottery data with the authorizing authority and also with the state's department of education, subject to standard safeguards to avoid release of individuals' identities.

Second, for researchers to conduct a successful evaluation of charter schools, either an observer needs to be present or detailed characteristics of the lottery process need to be reported (*17*). If some lottery winners turn down the admission offer, it is crucial that researchers understand how the school admitted students from its wait list of students who were not initially admitted in the lottery. If the school admits students from the wait list on a nonrandom basis, showing favoritism toward certain students, all pretense of randomization is lost. As another example, researchers need to know whether students were placed into separate lotteries by grade, or were given preferences; for instance, if a sibling already attended the school. Such information allows researchers to preserve an experimental analysis by stratifying the data. Charter schools should be required to submit not only a list of lottery winners and those who did not win the lottery, but details on how students were admitted from wait lists, whether separate lotteries were held for different groups of students, and what preferences were applied.

Finally, with a few exceptions, most states make it difficult if not impossible to obtain student-level test-score data for research purposes. States should routinely authorize researchers from academic institutions to obtain longitudinally linked student test-score data. This would raise all education research, not just on charter schools, to a more rigorous level by enabling researchers to use rigorous nonexperimental approaches in the many cases where schools are not oversubscribed. This would also open up the possibility of supplementing analyses of test-score gains with longer-term outcomes such as high school graduation and college attendance (*18*). These are likely to be better predictors of long-term adult success of students than test scores alone. Such studies are much needed, because of concerns that states' achievement tests focus on a fairly narrow set of skills, e.g., making it difficult to reveal differences between charter schools and other schools on measures of learning higher-order reasoning and writing ability.

It may seem like a tall order for so many states to enact these reforms independently. The federal government could play an important role in encouraging states to follow through. Federal initiatives such as the No Child Left Behind Act and the Race to the Top fund have made federal financial support for states' education systems contingent upon states enacting certain reforms. The federal government could tie funds to support charters or other schools to these reforms, and thus help identify and replicate the most successful schools, then shut down the schools that underperform.

References and Notes

1. B. H. Obama, Remarks by the President to the Hispanic Chamber of Commerce on a Complete and Competitive American Education (Office of the Press Secretary, White House, 10 March 2009).
2. J. R. Betts, Y. E. Tang, *The Effect of Charter Schools on Student Achievement: A Meta-Analysis of the Literature* (National Charter School Research Project, Center on Reinventing Public Education, Bothell, WA, 2011); www.crpe.org/cs/crpe/download/csr_files/pub_NCSRP_BettsTang_Oct11.pdf.
3. For an example of how simple comparison of test scores between charter and traditional public schools reflects initial student achievement but not actual gains in performance, see (*4*).
4. J. R. Betts, Y. E. Tang, A. C. Zau, in *Taking Measure of Charter Schools: Better Assessments, Better Policymaking, Better Schools*, J. R. Betts and P. T. Hill, Eds. (Rowman & Littlefield, Lanham, MD, 2010), chap. 2.
5. A. Abdulkadiroglu *et al.*, *Informing the Debate: Comparing Boston's Charter, Pilot and Traditional Schools* (The Boston Foundation, Boston, 2009); www.tbf.org/uploadedFiles/tbforg/Utility_Navigation/Multimedia_Library/Reports/InformingTheDebate_Final.pdf.
6. J. D. Angrist, S. M. Dynarski, T. J. Kane, P. A. Pathak, C. R. Walters, *Am. Econ. Rev. Pap. Proc.* **100**(2), 1 (2010).
7. W. Dobbie, R. Fryer Jr., *Are High Quality Schools Enough to Close the Achievement Gap? Evidence from a Social Experiment in Harlem* [Working Paper 15473, National Bureau of Economic Research (NBER), Cambridge, MA, 2009].
8. C. M. Hoxby, S. Murarka, J. Kang, *How New York City's Charter Schools Affect Achievement, August 2009 Report* (Charter Schools Evaluation Project, Cambridge and New York, 2009); www.nber.org/~schools/charterschoolseval/how_NYC_charter_schools_affect_achievement_sept2009.pdf.
9. C. M. Hoxby, S. Murarka, *New York City's Charter Schools Overall Report* (NBER, Cambridge, MA, 2007); www.nber.org/~schools/charterschoolseval/.
10. P. Gleason, M. Clark, C. C. Tuttle, E. Dwoyer, *The Evaluation of Charter School Impacts: Final Report* (NCEE 2010-4029, National Center for Education Evaluation and Regional Assistance, Institute of Education Sciences, U.S. Department of Education, Washington, DC, 2010); http://ies.ed.gov/ncee/pubs/20104029/pdf/20104029.pdf.
11. C. M. Hoxby, J. E. Rockoff, *Findings from the City of Big Shoulders* (Education Next, Cambridge, MA, 2005); http://educationnext.org/files/ednext20054_52.pdf.
12. L. McClure, B. Strick, R. Jacob-Almeida, C. Reicher, *The Preuss School at UCSD: School Characteristics and Students' Achievement* (The Center for Research on Educational Equity, Assessment and Teaching Excellence, Univ. of California, San Diego, San Diego, CA, 2005); http://create.ucsd.edu/_files/publications/PreussReportDecember2005.pdf.
13. R. J. Lake, Ed., *Hopes, Fears and Reality: A Balanced Look at Charter Schools in 2008* (National Charter School Research Project, Center For Reinventing Public Education, Univ. of Washington, Bothell, WA, 2008), p. vi; www.crpe.org/cs/crpe/view/csr_pubs/255.
14. E. A. Hanushek, J. F. Kain, S. G. Rivkin, G. F. Branch, Charter school quality and parental decision making with school choice. *J. Public Econ.* **91**, 823 (2007).
15. Both lottery-based and nonexperimental estimates for Boston are provided in (*5*). In three of four cases, the nonexperimental estimate is lower than the corresponding lottery-based estimate. Lottery-based estimates for New York City are provided in (*8*). A nonexperimental replication of the New York City results is provided in (*16*), and the authors obtain the same estimate for math but an estimate for reading that is two-thirds of the lottery-based estimate. An attempt to replicate the lottery-based results in (*12*) without lottery data yields similar results, but only if each student's past achievement is controlled for (*4*).
16. Center for Research on Educational Outcomes, *Charter School Performance in New York City* (Stanford Univ., Stanford, CA, 2010); http://credo.stanford.edu/reports/NYC%202009%20_CREDO.pdf.
17. P. J. McEwan, R. B. Olsen, in *Taking Measure of Charter Schools: Better Assessments, Better Policymaking, Better Schools*, J. R. Betts and P. T. Hill, Eds. (Rowman & Littlefield, Lanham, MD, 2010), chap. 6.
18. J. R. Betts, *Taking Measure of Charter Schools: Better Assessments, Better Policymaking, Better Schools*, J. R. Betts and P. T. Hill, Eds. (Rowman & Littlefield, Lanham, MD, 2010), chap. 4.

10.1126/science.1205418

PLANT SCIENCE

SWEET! The Pathway Is Complete

A protein moves sucrose out of leaf cells prior to entry into the plant vascular system.

David M. Braun

Photosynthesis in plants leads to the accumulation of carbohydrates (e.g., sugars, starch), upon which all terrestrial life depends. In most plants, sucrose is the principal carbohydrate transported long-distance in the veins to support the growth and development of roots, flowers, fruits, and seeds. Sucrose can be directly stored in specialized tissues, such as fruits or the stems of sugarcane and sweet sorghum, or it can be converted into starch in cereal seeds and potato tubers. Thus, proper control of carbohydrate partitioning is fundamental to crop yield and human nutrition and to the development of plant-based biofuels. Given the importance of this process, it may come as a surprise that until now, we did not understand the entire pathway for the export of sucrose from leaves. On page 207 of this issue, Chen *et al*. (*1*) identify and characterize the long-sought missing player in sucrose transport, the sucrose effluxer.

Carbon assimilation in mature leaves results in a surplus of carbohydrates, which are exported through the veins to nonphotosynthetic tissues (*2*–*7*). Sucrose is synthesized in leaf mesophyll cells and diffuses cell-to-cell through plasmodesmata (conduits spanning the cell wall and connecting adjacent cells) toward the vein (see the figure). Within the veins, the phloem is the specialized tissue involved in long-distance sucrose transport. The phloem contains three cell types: parenchyma cells, companion cells, and sieve elements. In the majority of crop plants, the companion cells and sieve elements are not connected by plasmodesmata to the other cells in the leaf; therefore, sucrose must be effluxed from the phloem parenchyma cell to the cell wall space (apoplast) before being imported into the companion cells and/or sieve elements by sucrose transporters located on their plasma membranes (*2*–*7*). The portions of the sucrose transport pathway from the mesophyll cell to the phloem parenchyma cell, and from the apoplast into the companion cell and sieve element, have been well characterized. However, the mechanism of sucrose efflux into the apoplast, the last unresolved step in the sucrose phloem loading pathway, remained a mystery (*8*). The sucrose effluxer was finally identified by Chen *et al*. through an elegant approach that combined cell biology, biochemistry, genomics, and genetics.

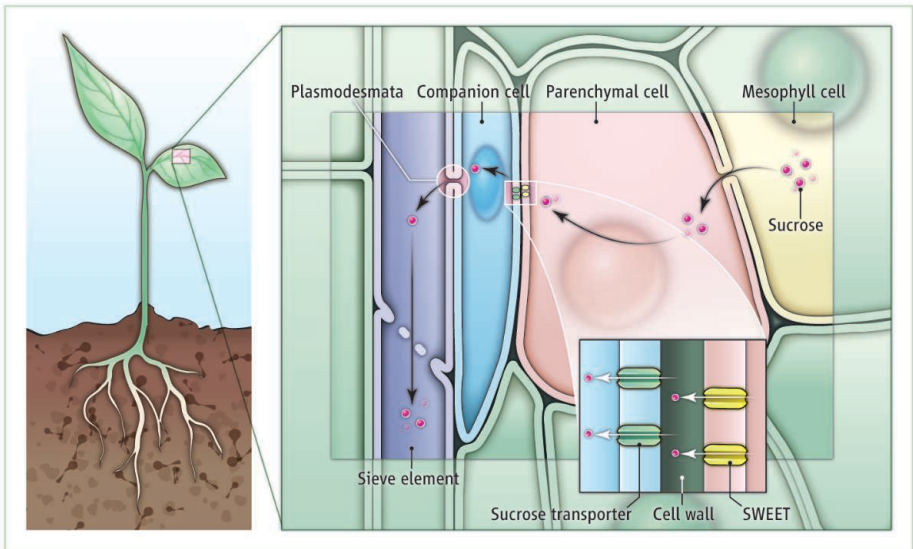

Sucrose partitioning in plants. Sucrose is synthesized in leaf mesophyll cells and diffuses through plasmodesmata into phloem parenchyma cells. SWEET proteins facilitate sucrose efflux into the cell wall (apoplast). Sucrose transporters import sucrose into companion cells and/or sieve elements. Sucrose is transported through sieve elements out of leaves to nonphotosynthetic tissues, such as roots, stem, and fruits.

A key that enabled this breakthrough was the development of fluorescence resonance energy transfer (FRET) optical sensors that could be used in cells to report the sugar concentration in the cytoplasm (*9*, *10*). A sugar-binding protein domain was placed between variants of cyan fluorescent protein and yellow fluorescent protein. When the sensor protein binds sugar, it undergoes a conformational shift that alters the fluorescence, such that a change in the amount of fluorescence emitted can be used to monitor changes in sugar concentration. By expressing such an optical sensor for glucose or sucrose, root cells were observed to rapidly transport the sugars across cellular membranes in response to concentration gradients (*11*). This led to the hypothesis that novel membrane proteins mediate sugar transport because the expression patterns and biochemical transport properties observed were inconsistent with known sugar transporters.

To identify these unknown proteins, Chen *et al*. previously used a human cell line to coexpress the glucose sensor and a collection of *Arabidopsis* proteins containing multiple membrane-spanning domains (*12*). The authors found that a specific SWEET protein could take up glucose from the cell culture medium. SWEETs are membrane proteins that transport glucose molecules across a membrane down a concentration gradient. Phylogenetic analysis revealed that *SWEET* genes are evolutionarily conserved from plants to humans. There are 17 *SWEET* genes in *Arabidopsis* and 21 in rice. Intriguingly, different bacterial or fungal pathogens obtain carbohydrates from plants by increasing the expression of different plant *SWEET* genes (*12*).

Chen *et al*. determined that AtSWEET11 and 12 (and OsSWEET11 and 14 in rice) transport sucrose in *Arabidopsis* (*1*). Both transporters localize to the plasma membrane and are expressed in a subset of leaf phloem parenchyma cells, proximal to the companion cells and sieve elements. Mutations in either the *AtSWEET11* or *12* genes produced no obvious phenotypes, but double mutants (*atsweet11;12*) showed moderate defects in sucrose phloem transport and an excessive accumulation of carbohydrates in the leaves. A third gene, *AtSWEET13*, showed increased expression in the *atsweet11;12* double mutant background and may partially compensate for

Division of Biological Sciences, Interdisciplinary Plant Group, Missouri Maize Center, University of Missouri, Columbia, MO 65211, USA. E-mail: braundm@missouri.edu

CREDIT: Y. HAMMOND/*SCIENCE*

Published by AAAS

their function. Hence, these *SWEET* genes are genetically redundant, which likely explains why earlier genetic screens failed to identify the efflux step. Collectively, the data demonstrate that the *AtSWEET11* and *12* genes encode the missing link in sucrose phloem loading, the sucrose effluxer.

The identification of SWEET proteins as sucrose facilitators raises a number of questions. Are the regulation and localization of SWEETs and sucrose transporters coordinated to maximize phloem loading efficiency and minimize any potential loss of sucrose to the apoplast (and thereby to pathogens)? Additionally, *AtSWEET11* and *12* are expressed in most *Arabidopsis* tissues; what other roles beyond phloem loading might they play? One possibility is that they may function in sucrose efflux to seeds (*13*). Another is that during long-distance transport, SWEETs may facilitate the "leakage" of sucrose from the phloem to nourish adjacent stem tissues (*14*). If so, manipulating *SWEET* expression could enhance carbohydrate delivery to developing seeds to increase yield, or it could increase the sucrose concentration in the storage cells of sugarcane or sweet sorghum stems to improve biofuel production.

References

1. L.-Q. Chen *et al.*, *Science* **335**, 207 (2012); 10.1126/science.1213351.
2. T. L. Slewinski, D. M. Braun, *Plant Sci.* **178**, 341 (2010).
3. B. G. Ayre, *Mol. Plant* **4**, 377 (2011).
4. E. A. Ainsworth, D. R. Bush, *Plant Physiol.* **155**, 64 (2011).
5. C. Kühn, C. P. L. Grof, *Curr. Opin. Plant Biol.* **13**, 287 (2010).
6. S. Lalonde, D. Wipf, W. B. Frommer, *Annu. Rev. Plant Biol.* **55**, 341 (2004).
7. N. Sauer, *FEBS Lett.* **581**, 2309 (2007).
8. D. M. Braun, T. L. Slewinski, *Plant Physiol.* **149**, 71 (2009).
9. I. Lager, L. L. Looger, M. Hilpert, S. Lalonde, W. B. Frommer, *J. Biol. Chem.* **281**, 30875 (2006).
10. B.-H. Hou *et al.*, *Nat. Protoc.* **6**, 1818 (2011).
11. B. Chaudhuri *et al.*, *Plant J.* **56**, 948 (2008).
12. L.-Q. Chen *et al.*, *Nature* **468**, 527 (2010).
13. W. -H. Zhang *et al.*, *Funct. Plant Biol.* **34**, 314 (2007).
14. P. E. H. Minchin, M. R. Thorpe, *J. Exp. Bot.* **38**, 211 (1987).

10.1126/science.1216828

ECOLOGY

Biodiversity and Ecosystem Function

A study of drylands across the world highlights the importance of species richness for ecosystem function.

Guy F. Midgley[1,2]

How is the biodiversity within an ecosystem related to the ecosystem's function? Quantifying and understanding this relationship—the biodiversity-ecosystem function (BEF) (*1*)—is important because socio-economic development is almost always accompanied by the loss of natural habitat and species (*2*). Short-term economic gains may thus trump longer-term benefits for human society, creating vulnerabilities that could be avoided or corrected with enough knowledge about the role of biodiversity. Erosion of biodiversity at local and regional scales may also reduce resilience at larger spatial scales as a result of degradation of ecosystem function (*3*). On page 214 of this issue, Maestre *et al*. (*4*) report an important step toward extending our understanding of BEF to globally important ecosystems.

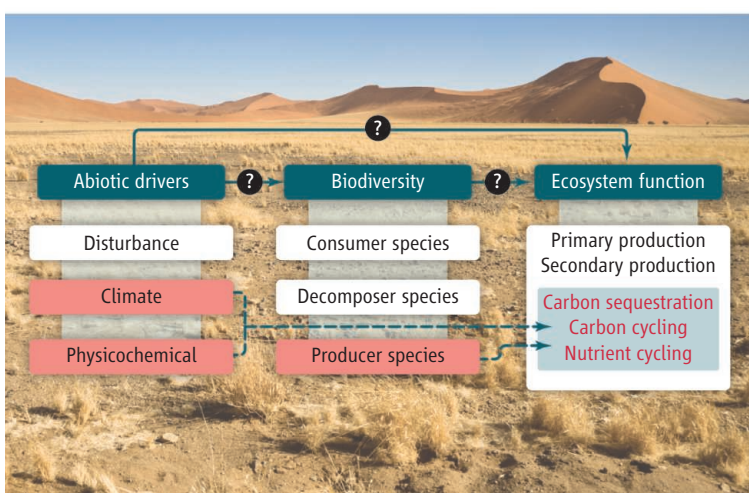

A framework for testing the BEF. Biodiversity and abiotic drivers determine ecosystem function individually and in concert (blue boxes). How they do so cannot be fully answered without assessing the roles of multiple elements within these categories (indicative elements elaborated below blue boxes). The elements included in Maestre *et al*.'s test of the BEF are shown in red; dashed blue lines and arrows denote the relationships tested by the authors.

Concern about the loss of biodiversity and its consequences is motivating the development of an Intergovernmental Platform on Biodiversity and Ecosystem Services (*5*), which aims to address the gaps in the science–policy interface on biodiversity and ecosystem services. Yet despite this level of attention, understanding of the BEF is far from complete (*5*), and is biased toward a small number of ecosystems amenable to experimental manipulation (*6*). Far-reaching preliminary conclusions about the critical importance of biodiversity thus rest on a small and unrepresentative knowledge base.

Maestre *et al*. ask whether the plant species richness in semi-arid ecosystems (drylands) enhances their multifunctionality (the ability of ecosystems to maintain multiple functions, such as carbon gain, carbon storage, and nutrient cycling). The authors employ a natural experiment approach, which uses quantifiable variables measured under field conditions as explanatory and response variables, to assess 14 functions in the carbon, nitrogen, and phosphorus cycles in the soil. In a massive global effort, they collected data on these functions by analyzing the soils of 224 dryland ecosystems sampled from all continents except Antarctica. From this they evaluated how biodiversity (quantified as the species richness of perennial vascular plants growing in those soils) relates to ecosystem multifunctionality across dryland ecosystems globally. This is a useful new angle and a particularly stringent test of the BEF hypothesis, according to which increasing biodiversity enhances ecosystem function. Most previous

[1]Climate Change and Bioadaptation, South African National Biodiversity Institute, Rhodes Drive, Cape Town 7735, South Africa. [2]School of Agricultural, Earth, and Environmental Sciences, University of Kwazulu-Natal, Pietermaritzburg Campus, Pvt Bag X101, Scottsville 3209, South Africa. E-mail: g.midgley@sanbi.org.za

work assessed functions individually and did not address dryland systems, which, as Maestre *et al*. point out, cover 41% of Earth's land surface and support over 38% of the global human population.

Human society needs ecosystems to provide multiple services effectively, especially as we increase pressure on ecosystems from local impacts such as extractive harvesting to global impacts such as climate change (*4*). In drylands, critical ecosystem services include the conversion of solar energy, atmospheric CO_2, and water to plant biomass (net primary productivity), carbon storage, and provision of nutrient pools. This suite of services is vital for arresting desertification trends and sequestering carbon.

Maestre *et al*.'s test of the BEF hypothesis is stringent because they test for a relationship between species richness of primary producer species (perennial plants) and ecosystem functions expressed in soils. Soil functions are subject both to abiotic drivers and many biotic effects other than those due to perennial plants. Confirmation of the BEF hypothesis under these constraints would therefore imply robust general support for it. They also did not shy away from the confounding influence of human management impacts, given that their field sites around the world represent a wide range of intensity of human use, barring major soil disturbances such as farming or mining.

Maestre *et al*. report that perennial plant species richness is a statistically significant explanatory variable for ecosystem multifunctionality both on its own and when considered together with several abiotic explanatory variables. Indeed, only two abiotic variables, mean annual temperature and soil sand content, were more important than plant species richness in explaining ecosystem multifunctionality (hotter, more sandy sites had lower multifunctionality), in a set of variables that included mean annual rainfall.

Maestre *et al*. find that the relationship between species richness and ecosystem multifunctionality rises steeply with fewer than five species and then increases incrementally with the addition of more species. This implies that ecosystem multifunctionality as defined by Maestre *et al*. is well established by relatively few species in these dryland ecosystems, in contrast with results from temperate grasslands (*5*). However, the large spread in Maestre *et al*.'s data suggests that, apart from uncontrolled effects such as land-use history mentioned above, there may be important individual species effects (including keystone species effects) that are not quantified in this natural experimental approach. That is, the stringency and generality of their test have the unfortunate consequence of obscuring important details that seem better revealed by the experimental approaches followed in the temperate grassland studies (*6*).

Given the acknowledged limitations of the experimental design used by Maestre *et al*., future work should focus on teasing out how much variation is explained by plant species richness when potentially powerful factors such as land-use history and intensity of herbivory are controlled for. This will be important in assessing the value of biodiversity in real-world settings and may suggest how rapidly ecosystem multifunctionality could be enhanced under different land management practices aimed at ecosystem restoration.

All considered, Maestre *et al*.'s conclusion that perennial plant species richness matters for ecosystem function in dryland systems is robust. This answer has global relevance, and is especially valuable for many developing and least-developed countries facing desertification trends. Neither Maestre *et al*.'s approach nor the experimental approaches undertaken in temperate grasslands or earlier experimental work (*7*) have yet fully addressed the multilayered question of how biodiversity across trophic levels, in conjunction with abiotic drivers, determines ecosystem function (see the figure).

References

1. J. E. Duffy, *Front. Ecol. Environ* **7**, 437 (2009).
2. A. Duraiappah *et al*., Eds., *Ecosystems and Human Well-Being: Biodiversity Synthesis* (Island Press, Washington, DC, 2005).
3. S. Díaz, J. Fargione, F. S. Chapin III, D. Tilman, *PLoS Biol.* **4**, e277 (2006).
4. F. T. Maestre *et al*., *Science* **335**, 214 (2012).
5. C. Perrings, A. Duraiappah, A. Larigauderie, H. Mooney, *Science* **331**, 1139 (2011).
6. F. Isbell *et al*., *Nature* **477**, 199 (2011).
7. F. S. Chapin III *et al*., *Science* **277**, 500 (1997).

10.1126/science.1217245

ASTRONOMY

Gamma-Ray Binaries Revealed

The Fermi Large Area Telescope is unveiling a large population of otherwise hidden sources of gamma rays.

I. F. Mirabel[1,2]

Recent ground- and space-based telescopes that detect high-energy photons from a few up to hundreds of gigaelectron volts (GeV) have opened a new window on the universe. However, because of the relatively poor angular resolution of these telescopes, a large fraction of the thousands of sources of gamma rays observed remains unknown. Compact astrophysical objects are among those high-energy sources, and in the Milky Way there is a particular class called gamma-ray binaries. These are neutron stars or black holes orbiting around massive stars (*1*). On page 189 of this issue, the Fermi Large Area Telescope Collaboration (*2*) use the correlated orbital modulation at gamma-ray, x-ray, and radio-wave wavelengths to show that the source 1FGL J1018.6–5856 is a new gamma-ray binary, demonstrating the potential of searches for periodic modulation at gamma rays and other wavelengths to unveil new populations of gamma-ray binaries.

This area of high-energy astronomy presents several challenges: identifying the gamma-ray source with a source observed at other wavelengths; determining the properties of the binary system; and understanding the physical mechanisms by which gamma-rays are produced. In the Milky Way, only a handful of binaries radiating at gamma rays have been unambiguously identified (Cygnus X-3; PSR B1259–63; LSI +61° 303; LS 5039; HESS J0632+057). However, models of the evolution of massive stellar binaries suggest a much larger population of gamma-ray binaries.

The Large Area Telescope (LAT) on board the Fermi satellite has cataloged more than 1400 high-energy sources. Many of them are in the Milky Way, but because of the uncertain positions in the sky provided by the gamma-ray telescope (typically a few arc-min), and the complexity of the star-formation regions where gamma-ray binaries are usually located, the association of these high-energy sources with objects observed at other wavelengths is usually uncertain. The observation of correlated

[1]Instituto de Astronomía y Física del Espacio, IAFE-Conicet, Buenos Aires, Argentina. [2]Institut de Recherche sur les lois Fondamentales de l'Univers, Commissariat à l'Énergie Atomique et aux Énergies Alternatives (IRFU-CEA), Saclay, France. E-mail: felix.mirabel@cea.fr

Science
AAAS

Gamma-Ray Binaries Revealed

I. F. Mirabel

Science **335**, 175 (2012);
DOI: 10.1126/science.1215895

Science (print ISSN 0036-8075; online ISSN 1095-9203) is published weekly, except the last week in December, by the American Association for the Advancement of Science, 1200 New York Avenue NW, Washington, DC 20005.

work assessed functions individually and did not address dryland systems, which, as Maestre *et al*. point out, cover 41% of Earth's land surface and support over 38% of the global human population.

Human society needs ecosystems to provide multiple services effectively, especially as we increase pressure on ecosystems from local impacts such as extractive harvesting to global impacts such as climate change (*4*). In drylands, critical ecosystem services include the conversion of solar energy, atmospheric CO_2, and water to plant biomass (net primary productivity), carbon storage, and provision of nutrient pools. This suite of services is vital for arresting desertification trends and sequestering carbon.

Maestre *et al*.'s test of the BEF hypothesis is stringent because they test for a relationship between species richness of primary producer species (perennial plants) and ecosystem functions expressed in soils. Soil functions are subject both to abiotic drivers and many biotic effects other than those due to perennial plants. Confirmation of the BEF hypothesis under these constraints would therefore imply robust general support for it. They also did not shy away from the confounding influence of human management impacts, given that their field sites around the world represent a wide range of intensity of human use, barring major soil disturbances such as farming or mining.

Maestre *et al*. report that perennial plant species richness is a statistically significant explanatory variable for ecosystem multifunctionality both on its own and when considered together with several abiotic explanatory variables. Indeed, only two abiotic variables, mean annual temperature and soil sand content, were more important than plant species richness in explaining ecosystem multifunctionality (hotter, more sandy sites had lower multifunctionality), in a set of variables that included mean annual rainfall.

Maestre *et al*. find that the relationship between species richness and ecosystem multifunctionality rises steeply with fewer than five species and then increases incrementally with the addition of more species. This implies that ecosystem multifunctionality as defined by Maestre *et al*. is well established by relatively few species in these dryland ecosystems, in contrast with results from temperate grasslands (*5*). However, the large spread in Maestre *et al*.'s data suggests that, apart from uncontrolled effects such as land-use history mentioned above, there may be important individual species effects (including keystone species effects) that are not quantified in this natural experimental approach. That is, the stringency and generality of their test have the unfortunate consequence of obscuring important details that seem better revealed by the experimental approaches followed in the temperate grassland studies (*6*).

Given the acknowledged limitations of the experimental design used by Maestre *et al*., future work should focus on teasing out how much variation is explained by plant species richness when potentially powerful factors such as land-use history and intensity of herbivory are controlled for. This will be important in assessing the value of biodiversity in real-world settings and may suggest how rapidly ecosystem multifunctionality could be enhanced under different land management practices aimed at ecosystem restoration.

All considered, Maestre *et al*.'s conclusion that perennial plant species richness matters for ecosystem function in dryland systems is robust. This answer has global relevance, and is especially valuable for many developing and least-developed countries facing desertification trends. Neither Maestre *et al*.'s approach nor the experimental approaches undertaken in temperate grasslands or earlier experimental work (*7*) have yet fully addressed the multilayered question of how biodiversity across trophic levels, in conjunction with abiotic drivers, determines ecosystem function (see the figure).

References

1. J. E. Duffy, *Front. Ecol. Environ* **7**, 437 (2009).
2. A. Duraiappah *et al*., Eds., *Ecosystems and Human Well-Being: Biodiversity Synthesis* (Island Press, Washington, DC, 2005).
3. S. Díaz, J. Fargione, F. S. Chapin III, D. Tilman, *PLoS Biol.* **4**, e277 (2006).
4. F. T. Maestre *et al*., *Science* **335**, 214 (2012).
5. C. Perrings, A. Duraiappah, A. Larigauderie, H. Mooney, *Science* **331**, 1139 (2011).
6. F. Isbell *et al*., *Nature* **477**, 199 (2011).
7. F. S. Chapin III *et al*., *Science* **277**, 500 (1997).

10.1126/science.1217245

ASTRONOMY

Gamma-Ray Binaries Revealed

The Fermi Large Area Telescope is unveiling a large population of otherwise hidden sources of gamma rays.

I. F. Mirabel[1,2]

Recent ground- and space-based telescopes that detect high-energy photons from a few up to hundreds of gigaelectron volts (GeV) have opened a new window on the universe. However, because of the relatively poor angular resolution of these telescopes, a large fraction of the thousands of sources of gamma rays observed remains unknown. Compact astrophysical objects are among those high-energy sources, and in the Milky Way there is a particular class called gamma-ray binaries. These are neutron stars or black holes orbiting around massive stars (*1*). On page 189 of this issue, the Fermi Large Area Telescope Collaboration (*2*) use the correlated orbital modulation at gamma-ray, x-ray, and radio-wave wavelengths to show that the source 1FGL J1018.6–5856 is a new gamma-ray binary, demonstrating the potential of searches for periodic modulation at gamma rays and other wavelengths to unveil new populations of gamma-ray binaries.

This area of high-energy astronomy presents several challenges: identifying the gamma-ray source with a source observed at other wavelengths; determining the properties of the binary system; and understanding the physical mechanisms by which gamma-rays are produced. In the Milky Way, only a handful of binaries radiating at gamma rays have been unambiguously identified (Cygnus X-3; PSR B1259–63; LSI +61° 303; LS 5039; HESS J0632+057). However, models of the evolution of massive stellar binaries suggest a much larger population of gamma-ray binaries.

The Large Area Telescope (LAT) on board the Fermi satellite has cataloged more than 1400 high-energy sources. Many of them are in the Milky Way, but because of the uncertain positions in the sky provided by the gamma-ray telescope (typically a few arc-min), and the complexity of the star-formation regions where gamma-ray binaries are usually located, the association of these high-energy sources with objects observed at other wavelengths is usually uncertain. The observation of correlated

[1]Instituto de Astronomía y Física del Espacio, IAFE-Conicet, Buenos Aires, Argentina. [2]Institut de Recherche sur les lois Fondamentales de l'Univers, Commissariat à l'Énergie Atomique et aux Énergies Alternatives (IRFU-CEA), Saclay, France. E-mail: felix.mirabel@cea.fr

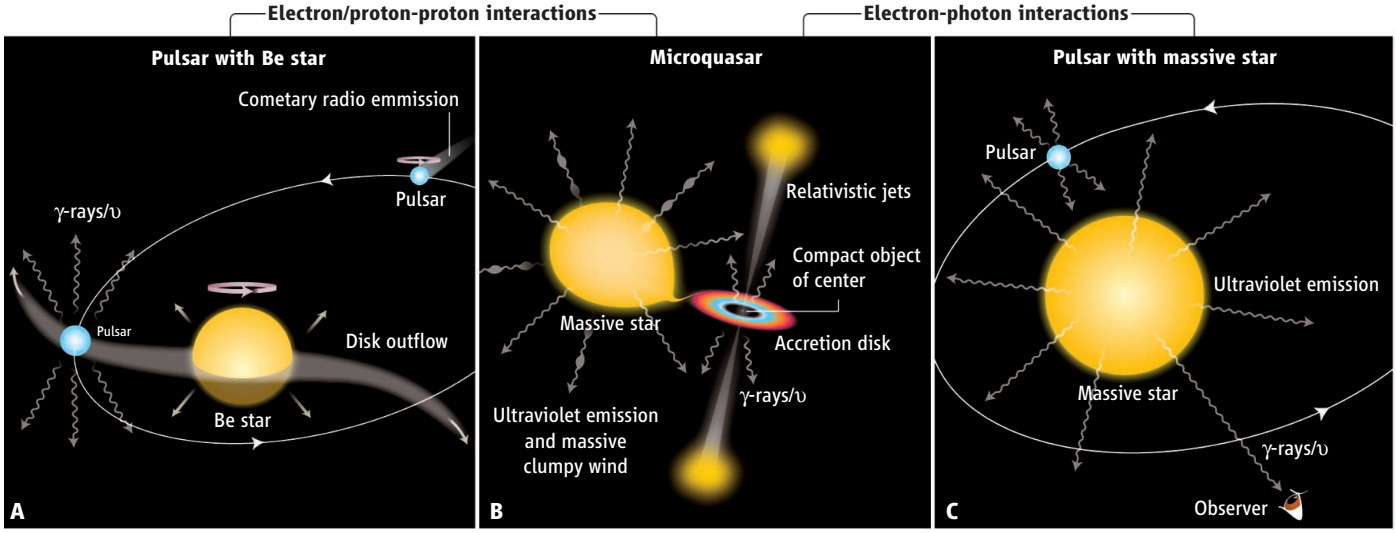

Gamma-ray binaries. Pulsar winds are powered by the rapid rotation of magnetized neutron stars. Gamma rays can be produced either by the interaction of the relativistic particles of the pulsar wind with the outflowing protons in the disk or envelope of a Be star (**A**) (e.g., PSR B1259–63 and LSI +61° 303), or by their interaction with UV photons from a very massive main-sequence star (**C**) (e.g., LS 5039 and 1FGL J1018.6–5856). (**B**) Microquasars are powered by compact objects (neutron stars or stellar-mass black holes) via mass accretion from a companion star. When the donor star is a massive star with a high-density UV flux and wind, gamma rays can be produced by electron-proton and/or electron-photon interactions. ν, neutrinos.

time variation of flux at different wavelengths was used to identify Cygnus X-3 as a gamma-ray binary (*3*), a microquasar (*4*) source of collimated relativistic jets, which was also observed at gamma rays with the Agile satellite (*5*).

1FGL J1018.6–5856 is a compact object orbiting with a period of 16.6 days around a star of more than 20 solar masses. On the basis of phenomenological similarities with other gamma-ray binaries, it is most likely a pulsar that produces strong bipolar winds of particles accelerated to highly relativistic speeds by the rapidly rotating, strong magnetic field of the spinning neutron star. The dominant physical mechanisms to produce the gamma-ray emission and its orbital modulation depend on the specific type of massive star in the compact binary (see the figure). When the star is very massive and produces a high-density field of ultraviolet (UV) photons, the main mechanism would be the up-scattering of UV photons from charged particles up to gamma-ray energies (*6*, *7*). In this scenario, maximum gamma-ray emission takes place when, relative to the observer, the compact object is on the opposite side of the star and close to the line of sight (superior conjunction). This may occur in both types of gamma-ray binaries: in high-mass microquasars such as Cygnus X-3, or in pulsars orbiting around very massive stars that produce high-density fields of UV photons, as with the stars in LS 5039 and 1FGL J1018.6–5856.

An alternative dominant mechanism to produce gamma rays that results in a somewhat different orbital modulation may operate when the star in the compact binary is of Be type. These stars are characterized by a massive outflow with disk and/or flattened envelope geometry, in fast rotation. Here, the gamma rays may be produced by the interaction of the pulsar wind particles with the ions in the massive outflow. This could be the case in the Be compact binaries PSR B1259–63 and LSI +61° 303, where the phasing of gamma-ray maximum at GeV energies is delayed relative to periastron (*2*). Detailed hadronic mechanisms that produce gamma rays have also been proposed in a diversity of astrophysical contexts (*8*, *9*).

High-energy neutrino flux could also be produced in gamma-ray binaries of the type shown in the figure, emerging from the decays of secondary charged mesons produced at proton-proton and/or proton–gamma photon interactions (*10*). In microquasars, relativistic protons from the jets interact with cold protons in clumps of the massive stellar wind, at large distances from the compact object (*11*). In the case of a pulsar-Be binary, neutrino bursts could be produced by the interaction of relativistic protons from the pulsar wind with high-density clumps of cold protons in the massive outflowing disk or envelope of the Be star. Depending on the specific parameters of these gamma-ray binaries, it remains an open question whether neutrino signals may be detected from this type of astrophysical object.

Emission at higher energy (TeV) has been detected by Cherenkov telescopes (PSR B1259–63; LSI +61° 303; and LS 5039), but it is not clear whether 1FGL J1018.6–5856 is also a TeV source. Its position is consistent with the TeV source HESS J1018–589 (*12*), but due to possible confusion with other objects in this complex star-forming region, it is unclear whether the Fermi source and a component of the HESS source are the same object. Resolving this question by using time modulation and/or more accurate positions of TeV sources will require improving the sensitivity and angular resolution of ground-based Cherenkov telescopes. The large collecting area and separation of the telescope elements in the future Cherenkov Telescope Array (*13*) will provide the sensitivity and angular resolution to consolidate this emerging research area in high-energy astrophysics.

References

1. I. F. Mirabel, *Science* **312**, 1759 (2006).
2. The Fermi LAT Collaboration, *Science* **335**, 189 (2012).
3. A. A. Abdo *et al*. Fermi LAT Collaboration, *Science* **326**, 1512 (2009).
4. I. F. Mirabel, L. F. Rodríguez, *Nature* **392**, 673 (1998).
5. M. Tavani *et al*., *Nature* **462**, 620 (2009).
6. M. M. Kaufman-Bernadó, G. E. Romero, I. F. Mirabel, *Astron. Astrophys.* **385**, L10 (2002).
7. G. Dubus, B. Cerutti, G. Henri, *Mon. Not. R. Astron. Soc.* **404**, L55 (2010).
8. F. A. Aharonian, A. M. Atoyan, *Space Sci. Rev.* **75**, 357 (1996).
9. G. E. Romero, D. F. Torres, M. M. Kaufman Bernadó, I. F. Mirabel, *Astron. Astrophys.* **410**, L1 (2003).
10. F. A. Aharonian, L. Anchordoqui, D. Khangulyan, T. Montaruli, *J. Phys. Conf. Ser.* **39**, 408 (2006).
11. M. M. Reynoso, G. E. Romero, *Astron. Astrophys.* **493**, 1 (2009).
12. E. de Ona Wilhelmi ***et al***., 38th COSPAR Scientific Assembly, 38, 2803 (2010).
13. www.cta-observatory.org

10.1126/science.1215895

CREDIT: P. HUEY/*SCIENCE*

MATERIALS SCIENCE

A Composite Matter of Alignment

Magnetic fields are used to orient reinforcing particles in polymer composites and strengthen high-stress regions that can be prone to failure.

Peter Fratzl

If you have had an eyeglass frame break, it likely did so at the point where the temple is screwed to a hinge. The holes in the frame create local stress concentrations that can initiate cracks that limit the durability of the material. Local reinforcements can be a cost-effective solution against fracture at sites such as bolt holes, where the performance of the material is challenged by additional stresses. This approach can be simple to implement in isotropic materials such as metals, but simple ways to reinforce such materials as fiber-polymer composites have been lacking. On page 199 of this issue, Erb *et al*. (*1*) propose a new method to align fibers or platelets in a polymer for the near-surface reinforcement of polymeric composites. In their approach, these inclusions are decorated with magnetic nanoparticles and oriented by a magnetic field in the production process in which the solution polymerizes to form a solid composite.

There are alternatives to reinforcement of materials. Replacing the material by a stronger one can be expensive. Alternatively, one can try to avoid the stress concentrations by better frame design, which redistributes the stresses in a more equal way (*2*). Where this is not possible because the detailed shape is fixed by other constraints, local reinforcement of the material in the area of the hole where stresses concentrate (*3*, *4*) is often the best option.

Nature is constantly dealing with challenges of this kind (*5*). The bones of our skeleton, for example, have to be stiff and fracture-resistant to support our weight, but they are still organs with a dense cell network that needs to be connected to the vasculature for nutrient supply (see the figure, panel A). Bones are pervaded by channels of various diameters that would normally be stress concentrators, much like the bolt hole in the eyeglass frame. Bone is a fiber composite (*5*) based on collagen fibrils filled with plate-like nanoparticles. In osteons, the basic building blocks of bone, these particles and fibers are arranged in concentric layers within the bone material around the blood vessel (see the figure, panel B). This assembly creates a local reinforcement and effectively protects the channel. This intricate arrangement of fibers and mineral platelets likely reduces the tendency of osteonal bone to fracture (*6*, *7*). More generally, graded properties and local reinforcements have been described as a widespread strategy to strengthen biological composites (*8*).

It seems highly desirable to find ways of controlling the orientation of fibers and platelike inclusions within engineering composites in order to create local reinforcements similar to those in bone. However, processing technologies for the cost-effective manufacturing of such complex structures have remained remarkably elusive. The highly aligned material structure that prevents crack initiation and propagation in bone is generated by a network of living cells, and such a process can hardly be mimicked to make an engineering material.

In general, new processing technologies to create structures of this kind, and in particular to align small fibers and inclusions, are required because the mechanical properties of composites are known to depend on the orientation of anisotropic inclusions. Materials with simple composite geometries have been created, such as hard-soft multilayers (*9*), which to some extent are inspired by nacre (*10*) or glass sponge (*11*). Methodologies used to synthesize these multilayered materials can be based on dip-coating (*12*), layer-by-layer assembly (*13*), or ice-templating (*14*).

Erb *et al*. tackled the alignment problem by using magnetic fields to orient inclusions decorated with magnetic nanoparticles. The inclusions were typically in the micrometer size range (either aluminum oxide platelets or calcium sulfate hemihydrate rods) and were coated with minimal concentrations of superparamagnetic iron oxide nanoparticles. Within the precursor solution of the polymeric matrix, the orientation of these inclusions could be controlled by ultralow

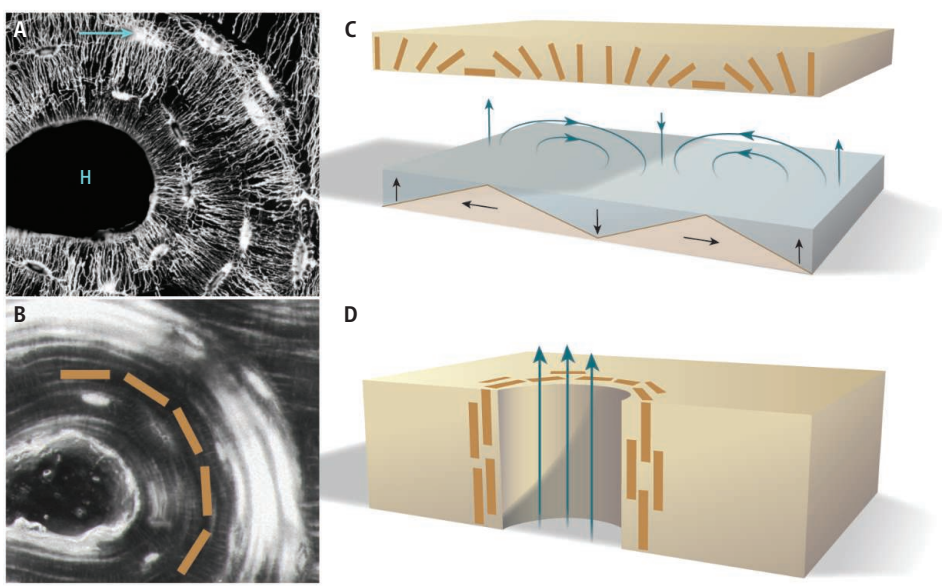

Tougher surfaces inspired by bones. (**A** and **B**) Cross-sectional view of an osteon in equine bone, based on data from (*15*). (A) Osteocyte cells (blue arrow) form a dense network visualized by a fluorescent stain (white) around the Haversian canal (labeled H), which houses the blood vessel supplying nutrients to the cells. (B) A polarized-light image of the same bone section reveals that cells have deposited the bone matrix, consisting of collagen fibrils and plate-like mineral particles, with a concentric fiber arrangement around the Haversian canal (the orientation of inclusions is schematically shown by brown rectangles). (**C** and **D**) Erb *et al*. fabricated unusual three-dimensional reinforcement architectures through orientational and spatial magnetic control, shown here schematically. (C) A gradually varying particle alignment generated by a standard refrigerator magnet's domain structure. (D) A cross section of a spatial gradient in magnetized particles that were aligned preferentially around a channel in the material.

CREDIT (PANELS C AND D): P. HUEY/*SCIENCE*

Max Planck Institute of Colloids and Interfaces, 14424 Potsdam, Germany. E-mail: peter.fratzl@mpikg.mpg.de

Published by AAAS

magnetic fields (in the millitesla range). After solidification of the polymer matrix by evaporation or by cross-linking, the local alignment of the inclusions was preserved, leaving reinforced surface regions.

The authors used this material to create laminates based on polymers with a specific orientation of inclusions within each of the layers. Like a sheet of plywood, lamination improves the mechanical properties and, in particular, the strength as compared to the plain polymer. The most impressive aspect is the level of control over the microstructures that was achieved during the synthesis process of the composite material. In near-surface regions, magnetic fields were tuned so that the orientation of inclusions ended up rotating parallel to the surface (see the figure, panel C). Local reinforcements oriented around a cylindrical hole, which the authors obtained in a similar process, are reminiscent of the concentric onion-like arrangement of collagen and mineral platelets in an osteon (see the figure, panel D). The new technology is flexible enough to generate all kinds of local reinforcements near surfaces and larger holes that could otherwise be starting points for cracks.

The materials generated by Erb *et al*. are just demonstration objects, but the research clearly shows a previously unexplored direction for developing new types of local reinforcements in polymer-based composites. If the new synthesis route can be developed for large-scale production, such materials could become useful in aeronautics, civil construction, and a variety of other fields.

References

1. R. M. Erb, R. Libanori, N. Rothfuchs, A. R. Studart, *Science* **335**, 199 (2012).
2. G. I. N. Rozvany, *Struct. Multidiscip. Optim.* **37**, 217 (2009).
3. B. Kieback, A. Neubrand, H. Riedel, *Mater. Sci. Eng. A* **362**, 81 (2003).
4. A. Mortensen, S. Suresh, *Int. Mater. Rev.* **40**, 239 (1995).
5. P. Fratzl, R. Weinkamer, *Prog. Mater. Sci.* **52**, 1263 (2007).
6. H. Peterlik, P. Roschger, K. Klaushofer, P. Fratzl, *Nat. Mater.* **5**, 52 (2006).
7. R. O. Ritchie, M. J. Buehler, P. Hansma, *Phys. Today* **62**, 41 (2009).
8. J. W. C. Dunlop, P. Fratzl, *Annu. Rev. Mater. Res.* **40**, 1 (2010).
9. O. Kolednik, J. Predan, F. D. Fischer, P. Fratzl, *Adv. Funct. Mater.* **21**, 3634 (2011).
10. S. Kamat, X. Su, R. Ballarini, A. H. Heuer, *Nature* **405**, 1036 (2000).
11. J. Aizenberg *et al*., *Science* **309**, 275 (2005).
12. A. Sellinger *et al*., *Nature* **394**, 256 (1998).
13. L. J. Bonderer, A. R. Studart, L. J. Gauckler, *Science* **319**, 1069 (2008).
14. E. Munch *et al*., *Science* **322**, 1516 (2008).
15. M. Kerschnitzki *et al*., *J. Struct. Biol.* **173**, 303 (2011).

10.1126/science.1215841

CHEMISTRY

An Elusive Intermediate Gets Caught

Direct kinetic measurements elucidate the reactivity of an unstable atmospheric species that is central to atmospheric chemistry.

George Marston

The Criegee intermediates (CIs) are central to understanding the reactions of ozone with unsaturated compounds (see the figure) (*1*). These reactions contribute directly to the oxidation of hydrocarbons in the lower atmosphere, are important sources of hydroxyl radicals, atmospheric organic acids, and carbonyl compounds, and can lead to the generation of secondary aerosols. On the local scale, these secondary aerosols contribute to the low visibility and health problems associated with photochemical smog, while on the global scale, their formation has crucial implications for climate change (*2*). Yet despite their central importance in these processes, little is known about the reactivity of CIs. On page 204 of this issue, Welz *et al*. report direct kinetic measurements of several reactions involving the simplest CI (*3*).

A clear understanding of the impacts of ozonolysis on atmospheric chemistry requires a detailed knowledge of the mechanisms of the reactions. It has been generally accepted for more than half a century (*4*) that ozone reacts with alkenes to generate CIs, species that can be described as carbonyl oxides with some biradical and zwitterionic character (see the figure) (*5*). There is plenty of qualitative evidence for this mechanism. A wealth of information about the products of ozonolysis comes from organic syntheses in the condensed phase; products from the reactions of CIs with CI scavengers such as water, organic acids, and carbonyl compounds are also consistent with the mechanism (*6*). The real problem in coming to grips with the details of the reactions and the behavior of the CIs is that these species have proved to be very difficult to detect. No direct measurements of its kinetics have been reported in the literature. The kinetics of the reactions of various CIs have been measured indirectly, but estimates of rate constants vary by orders of magnitude (*6*).

The importance of establishing rate parameters for the CI species can be illus-

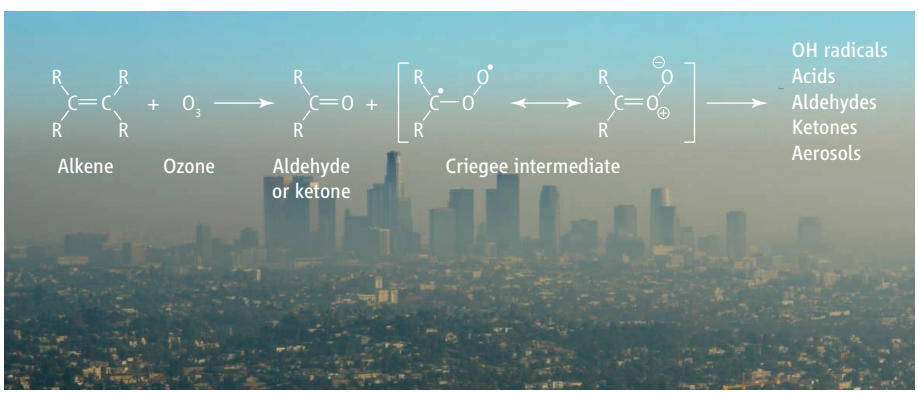

Formation and reactions of CIs in the atmosphere. The Criegee intermediates (CIs), which form during ozonolysis (left), play a central role in the formation of numerous atmospheric compounds (right). The species have been difficult to isolate, limiting the insights that could be gained into their reactions. Welz *et al*. have now succeeded in isolating the simplest CI and report direct kinetic measurements of its reactions with water, NO, NO_2, and SO_2.

Department of Chemistry, University of Reading, Whiteknights, Reading RG6 6AD, UK. E-mail: g.marston@reading.ac.uk

trated by considering the mechanism of hydroxyl radical formation in ozonolysis reactions. Hydroxyl radicals, which play a pivotal role in the chemistry of the lower atmosphere, are believed to form from the decomposition of CIs in the gas phase, with the yield varying according to structure [the simplest CI, H_2COO, has a yield of ~0.14, whereas $(CH_3)_2COO$ has a yield closer to 1.0] (*6*). It was assumed for many years that OH was formed from the decomposition of vibrationally excited CIs (known as prompt formation). However, direct, time-resolved measurements of OH radicals in the ozonolysis of a range of alkenes indicated that although the prompt mechanism is active at low pressures, decomposition of CIs stabilized by molecular collisions also generates OH radicals (*7*). Thus, to be confident that OH yields measured in the laboratory can be applied to atmospheric models, it is necessary to know rate parameters for the reactions of CIs with molecular partners in the atmosphere.

Some of this information is now available thanks to the study by Welz *et al*. The authors first photolyzed diodomethane to generate CH_2I, which they then reacted with O_2 to generate H_2COO. Using tunable radiation from a synchrotron source, they were able to record a photoionization mass spectrum of the CI, which they identified from previous experimental and theoretical work by their team (*8*). By examining the time dependence of the signal arising from the CI in the presence of varying concentrations of reactant partners, they were able to determine rate constants (or their upper limits) for the reactions of the CI with water, NO, NO_2, and SO_2.

For the reaction with water, the upper limit determined by Welz *et al*. seems broadly consistent with previous estimates (*6*). However, for the other species, the observed rate constants are very different from those proposed elsewhere (*6*). On the face of it, reaction between the CI and NO to give formaldehyde and NO_2 might be expected to be rapid given the thermodynamic drivers, but Welz *et al*. observed no reaction. In contrast, they found the reaction between the CI and NO_2 to be rather fast, with a rate constant almost as fast as that of a barrierless radical-radical reaction, despite one of the likely products being the nitrate radical. From an atmospheric chemistry perspective, this process may be a rather surprising but substantial source of nitrate radicals, which are important initiators of oxidation at night.

Although these results are unexpected, it is important to bear in mind that there have been no previous measurements of the kinetics of this species. Because it is unusual in its structure, it is hard to make comparisons with the reactivity of other species.

Perhaps the most interesting observation is that the reaction of the CI with SO_2 is very fast indeed. The likely products are formaldehyde and SO_3 (the anhydride of sulfuric acid, an important nucleating agent), and the reaction thus has potential implications for the generation of acid rain and inorganic aerosol in the atmosphere. There is also an interesting mechanistic point to consider: A previous study (*9*) showed that for alkyl-substituted CIs, OH yields were unaffected by the presence of SO_2; the estimated upper limit for the rate constant (*9*) was four orders of magnitude smaller than that proposed by Welz *et al*. It is hard to believe that substitution of hydrogen with a methyl group could have this sort of impact on the rate constant. The present results point strongly to a gap in our understanding of the mechanism for OH formation in alkene ozonolysis.

The results reported by Welz *et al*. are important to physical chemists because they are the first direct kinetic measurements of a very unusual chemical species. They are important to atmospheric chemists because they provide rates of some very important atmospheric processes. However, it remains unclear why the reactivity of the CI varies from reactant to reactant as it does, and the results are difficult to reconcile with the current understanding of OH formation in ozonolysis. Extension of the technique to examine the kinetics of H_2COO with other molecules would help to elucidate its physical chemistry and the role it plays in atmospheric chemistry. Given that the more complex CIs are central to hydroxyl radical and aerosol formation, extending the experiments to study the kinetics of substituted CIs is also of key importance for atmospheric chemists.

References and Notes

1. D. Johnson, G. Marston, *Chem. Soc. Rev.* **37**, 699 (2008).
2. S. Solomon *et al*., Eds., *Contribution of Working Group I to the Fourth Assessment Report of the Intergovernmental Panel on Climate Change* (Cambridge Univ. Press, Cambridge, UK, 2007).
3. O. Welz *et al*., *Science* **335**, 204 (2012).
4. R. Criegee, *Angew. Chem. Int. Ed. Engl.* **14**, 745 (1975).
5. D. Cremer, J. Gauss, E. Kraka, J. F. Stanton, R. J. Bartlett, *Chem. Phys. Lett.* **209**, 547 (1993).
6. J. G. Calvert *et al*., *The Mechanisms of Atmospheric Oxidation of the Alkenes* (Oxford Univ. Press, Oxford, UK, 2000).
7. N. M. Donahue, J. H. Kroll, J. G. Anderson, K. L. Demerjian, *Geophys. Res. Lett.* **25**, 59 (1998).
8. C. A. Taatjes *et al*., *J. Am. Chem. Soc.* **130**, 11883 (2008).
9. D. Johnson, A. G. Lewin, G. Marston, *J. Phys. Chem. A* **105**, 2933 (2001).

10. The author acknowledges support from the Natural Environment Research Council (NE/D013569/1, NE/G019231/1).

10.1126/science.1217165

CELL BIOLOGY

Sheddase Gets Guidance

Stefan F. Lichtenthaler

The release of a cytokine from immune cells requires a protein to guide a protease to the cell surface.

Proteases that cleave at the surface of cells release the ectodomain of membrane proteins and control the communication between cells. One example is the cytokine tumor necrosis factor–α (TNFα), which is essential for innate immunity. It is cleaved by the metalloprotease TNFα-converting enzyme (TACE or ADAM17) (*1*, *2*). Too much TNFα shedding, however, contributes to inflammatory diseases, which makes TACE an obvious drug target for conditions such as rheumatoid arthritis and sepsis. The generation of specific small-molecule TACE inhibitors has remained challenging, which has led to the search for alternative approaches to control its activity. Adrain *et al*. (*3*) and McIlwain *et al*. (*4*) report on pages 225 and 229 of this issue, respectively, that a protein called iRhom2 is essential for TACE to release TNFα from the cell surface. Mice lacking the *iRhom2* gene secrete less TNFα and succumb to bacterial infection. The findings provide exciting links between intracellular protein trafficking, cell surface proteolysis, and inflammation.

Different proteases act on membrane proteins, including rhomboid proteases and "a disintegrin and metalloprotease" (ADAM family) (*5*–*7*). These "sheddases" are themselves integral membrane proteins that cleave at or close to the transmembrane

DZNE—German Center for Neurodegenerative Diseases Munich, 80336 Munich, and Butenandt-Institute, University of Munich, 80336 Munich, Germany. E-mail: stefan.lichtenthaler@dzne.lmu.de

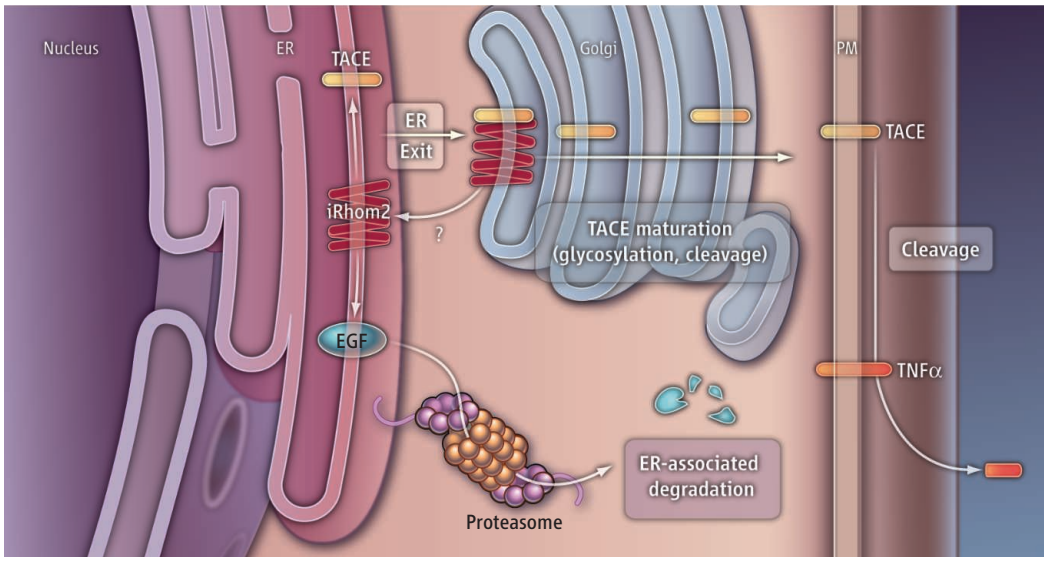

Directing cargo. iRhom2 binds immature TACE in the endoplasmic reticulum (ER) and mediates its exit to the Golgi. On the way to the plasma membrane (PM), TACE is glycosylated and its propeptide is removed. The latter activates TACE, leads to TNFα shedding from the cell surface, and weakens or terminates interaction with iRhom2. iRhom2 also promotes the ER-associated degradation of EGF receptor ligands.

domain of their substrates. Rhomboids also cleave within the membrane. Shedding is essential in various physiological processes, such as cell differentiation, cell adhesion, cytokine signaling, and axon outgrowth. Dysregulation of shedding is linked to pathophysiological conditions such as cancer, inflammatory diseases, and Alzheimer's disease, but the regulation of shedding and its connection to pathogenesis remain little understood (*8*).

The shedding process depends on the correct spatial and temporal localization of the sheddases and their substrates. Indeed, regulated transport of either substrate or protease is a mechanism to control shedding. This has been demonstrated for the proteolysis of the sterol regulatory element–binding protein, which controls cellular cholesterol homeostasis in mammals, and for the cleavage of Spitz [an epidermal growth factor (EGF)–like ligand expressed in *Drosophila melanogaster*] by a rhomboid protease to regulate EGF signaling. In both cases, different transmembrane proteins control access of the substrate to the Golgi-resident sheddase (*9*, *10*).

Adrain *et al*. and McIlwain *et al*. demonstrate that the trafficking and, as a consequence, the activity of a sheddase, can also be regulated. Both studies suggest that the polytopic membrane protein iRhom2 acts as a cargo receptor that binds TACE in the endoplasmic reticulum (ER) and promotes its journey through the Golgi, where TACE undergoes propeptide removal and complex glycosylation (*11*) (see the figure). Propeptide removal is required for full TACE activation and appears to coincide with weakened interaction between iRhom2 and TACE, allowing TACE to reach its substrates at the cell surface. This model is supported by several findings. iRhom2, which is a proteolytically inactive homolog of rhomboid proteases and localizes to the ER and Golgi, predominantly bound to immature TACE and less well to mature TACE (although it is unclear whether the interaction is direct or involves additional proteins). *iRhom2* overexpression in cell lines promoted TACE maturation and activity. In iRhom2-deficient cells, TACE remained immature and inactive and did not reach the cell surface. However, immature TACE regained its normal activity when purified and its prodomain proteolytically removed in vitro. iRhom2 appears to specifically affect TACE, as it did not affect activity or maturation of the close homolog ADAM10. Whether iRhom2 has other cargo proteins is not yet known.

Both groups also generated iRhom2-deficient mice, which were viable, fertile, and had no obvious morphological defects. Because iRhom2 is specifically expressed in hematopoietic cells, phenotypic changes appeared restricted to this tissue. Macrophages deficient in iRhom2 did not shed TNFα or other TACE substrates in response to exposure to lipopolysaccharide (LPS), whereas the secretion of other cytokines, which are not cleaved by TACE, occurred normally. The reduced TNFα secretion was also observed in vivo and allowed iRhom2-deficient mice to survive an otherwise lethal LPS dose, which is a model for septic shock. However, reduced TNFα secretion did not allow mice to efficiently fight a *Listeria* infection, which led to enhanced mortality. Protection from septic shock is also seen in mice with a myeloid cell–specific knockout of TACE (*12*), which suggests that iRhom2 specifically acts on TACE.

iRhom2 also functions in ER-associated degradation of growth factors of the EGF family (*13*), so it is unclear how it also acts as a traffic modulator for the single-span membrane protein TACE. Derlins, which comprise another class of proteolytically inactive polytopic membrane proteins, are distantly related to rhomboid proteases and are also involved in ER-associated degradation (*14*). Whether they also have a second function in protein or protease trafficking remains unknown.

As a drug target for TACE-related inflammatory diseases, iRhom2 may be a good candidate given its restricted expression pattern and the specific phenotype of iRhom2 knockout mice. However, because iRhom2 is not an enzyme, it may not be an easy drug target for small molecules. In addition, it will be important to adjust TACE activity to the optimal level, because neither too much nor too little TNFα shedding is desirable. Despite these challenges, the identification of iRhom2 as an essential regulator of TACE activity is a major step toward therapeutically targeting TACE.

References

1. R. A. Black *et al*., *Nature* **385**, 729 (1997).
2. M. L. Moss *et al*., *Nature* **385**, 733 (1997).
3. C. Adrain *et al*., *Science* **335**, 225 (2012).
4. D. R. McIlwain *et al*., *Science* **335**, 229 (2012).
5. S. F. Lichtenthaler, C. Haass, H. Steiner, *J. Neurochem.* **117**, 779 (2011).
6. M. Freeman, *Semin. Cell Dev. Biol.* **20**, 231 (2009).
7. K. Reiss, P. Saftig, *Semin. Cell Dev. Biol.* **20**, 126 (2009).
8. K. Hayashida, A. H. Bartlett, Y. Chen, P. W. Park, *Anat. Rec.* **293**, 925 (2010).
9. T. Yang *et al*., *Cell* **110**, 489 (2002).
10. J. R. Lee, S. Urban, C. F. Garvey, M. Freeman, *Cell* **107**, 161 (2001).
11. J. Schlöndorff, J. D. Becherer, C. P. Blobel, *Biochem. J.* **347**, 131 (2000).
12. K. Horiuchi *et al*., *J. Immunol.* **179**, 2686 (2007).
13. M. Zettl, C. Adrain, K. Strisovsky, V. Lastun, M. Freeman, *Cell* **145**, 79 (2011).
14. E. J. Greenblatt, J. A. Olzmann, R. R. Kopito, *Nat. Struct. Mol. Biol.* **18**, 1147 (2011).

10.1126/science.1216815

CREDIT: B. STRAUCH/*SCIENCE*

RETROSPECTIVE

Paul Mead Doty (1920–2011)

A chemist, whose DNA work underlies powerful biochemical and genetic tools, sought to control nuclear arms and foster science communication to policy-makers.

Matthew Meselson

Paul Mead Doty, early leader in applying physical chemistry to the study of synthetic polymers, proteins, and nucleic acids and in the efforts of senior U.S. scientists to bring arms control thinking to governments on both sides of the Cold War, mentor and constant friend to many in both fields, died on 5 December at age 91 at his home in Cambridge, Massachusetts.

Born 1 June 1920 in Charleston, West Virginia, the only child in a family of modest means, Doty grew up in the small town of Chicora, Pennsylvania. He majored in chemistry at Pennsylvania State University and received his doctorate in chemistry in 1944 at Columbia University. There, he and his fellow graduate student Bruno Zimm began to adapt Peter Debye's theory of light scattering to the study of large molecules in solution, a field that occupied much of Doty's early research. During 1943 to 1946, he was instructor and then assistant professor and codirector of wartime Army Quartermaster projects at Brooklyn Polytech in the Institute of Polymer Research, the foremost center of polymer science at the time. As a Rockefeller Fellow at Cambridge University in 1947, he was influenced by Max Perutz to turn his research to the study of macromolecules of biological importance. After a year as assistant professor at the University of Notre Dame, Doty was appointed assistant professor at Harvard, becoming full professor in 1956. One of the major interests in the laboratory was the physical chemistry and then the gene structure of collagen, resulting in a long series of publications coauthored by Paul and his wife, Helga Boedtker Doty, and, later, by her alone.

Doty's seminal contribution to science was the discovery that the separated chains of the DNA double helix can be specifically reunited. It was known that the two chains of the double helix could be separated by heating. But Doty's laboratory showed that the separated chains could be rejoined by incubation in solution a few degrees below the melting point, a result that came as a surprise to many. Concern that the initial observations might be due to internal folding or aggregation were decisively put to rest in a series of papers by Doty, his postdoctoral associate Julius Marmur, and others in the Doty laboratory in 1960 and 1961. The discovery opened the way to the development of many of the most powerful and widely employed methods of biological investigation and genetic engineering in current use, including primer-initiated DNA sequencing, polymerase chain reaction, and chip-based analysis of transcription.

CREDIT: SHARON WILKE/BELFER CENTER FOR SCIENCE AND INTERNATIONAL AFFAIRS

At Harvard, in part because he had become a trusted adviser to Dean McGeorge Bundy, Doty became highly effective in building molecular biology as a field distinct from traditional biology and chemistry, first in recruiting James Watson as assistant professor and later in creating a separate department, Biochemistry and Molecular Biology (BMB). Nearly all of the 16 eventual members of the new department were or became members of the U.S. National Academy of Sciences, and three received Nobel prizes. BMB existed for 27 years, from 1967 to 1994, until merging with Harvard's more traditional biology department. By the time Doty became emeritus professor in the Faculty of Arts and Sciences in 1988, he had supervised the work of some 150 undergraduate, graduate, and postdoctoral researchers, many going on to make important contributions to chemistry and molecular biology.

Doty's other professional life, equally creative, was at the intersection of science and public affairs. As chairman of the Federation of American Scientists, he was invited to the initial meeting of the Pugwash Conferences on Science and World Affairs in 1957. There he began a dialogue with senior Soviet scientists that continued throughout his life. His diary for a 1960 trip to Russia records his impression that "Surely the accessibility of at least a part of the Russian scientific community to normal contact with Western scientists and the relatively large extent to which their thinking is not subject to ideological criteria should be recognized as a bridgehead through which understanding may be expanded." There followed some 40 more trips to Russia and many meetings in the West with Russian scientists sufficiently respected by Soviet leaders to gain a serious hearing.

Doty was an initial member of President Kennedy's Science Advisory Committee, the Committee on International Security and Arms Control of the National Academy, and the Aspen summer workshop on arms control, which he founded. In 1974, with support from the Ford Foundation, Doty founded Harvard's Center for Science and International Affairs, later renamed the Belfer Center, and its journal, *International Security*. A leading center for scholarship and training in diverse aspects of science and international affairs, many of its alumnae went on to occupy top academic posts and/or high government positions in defense and foreign policy in the United States and abroad. Doty's style as director there was the same as in the laboratory—questioning, encouraging, and oblivious to seniority. In both, he consistently cut to the heart of a problem, caring more about finding answers than about promoting his own prestige or power.

The premise of Doty's approach to international security matters was that nuclear weapons are not for war-fighting or preemption but solely for deterring nuclear attack, the only role that might avoid their use entirely. Especially in the early years of the Cold War, this was by no means the settled view among senior officials on either side. Doty's influence on many who went on to occupy key positions in government and his leading role in the effort of U.S. and Soviet scientists to promote arms control must surely have helped to avoid catastrophe.

Molecular and Cellular Biology, Harvard University, Cambridge, MA 02138, USA. E-mail: msm@wjh.harvard.edu

10.1126/science.1218031

Bubblegrams Reveal the Inner Body of Bacteriophage ϕKZ

Weimin Wu,[1] Julie A. Thomas,[2] Naiqian Cheng,[1] Lindsay W. Black,[2] Alasdair C. Steven[1]*

ϕKZ is a large and complex virus that infects the Gram-negative bacterium *Pseudomonas aeruginosa* and has long-term potential for phage therapy against this pathogen. The virion has a long contractile tail and a large icosahedral capsid containing densely packed DNA (280 kb) (*1*). Observations of disrupted virions (*2*) have shown that it also contains a cylindrical structure called the inner body. However, the inner body is invisible in conventional cryogenic electron micrographs of intact virions because it cannot be distinguished from the surrounding DNA (Fig. 1A).

It has been found, serendipitously, that the inner body is exceptionally sensitive to radiation damage and explodes into bubbles of gaseous radiation products at electron doses that leave most protein complexes, including the surrounding capsid, only slightly blurred (Fig. 1B). We were able to determine its structure by using these "bubblegrams" to locate the inner body in individual nucleocapsids; then, knowing these locations and orientations, we calculated a three-dimensional reconstruction of the inner body from previously recorded, low-dose micrographs depicting the same virions in a relatively undamaged state.

The inner body is ~24 nm wide and ~105 nm long and tilted at ~22° relative to the portal axis (Fig. 1, C and D). It consists of multiple stacked tiers (Fig. 1E), and some regions have evident sixfold symmetry, as confirmed by their angular power spectra [supporting online material (SOM)]. The two ends, which are structurally distinct, are anchored on opposing hexons on either side of the capsid. The inner body has several major proteins and a number of minor proteins (*3*). The volume of the inner body as calculated here suggests a total mass of about 15 MD. The shape and position of the inner body suggest that it plays a role of organizer in the DNA packaging process. Consistent with this assignment, its tilt relative to the portal axis matches that of the ϕKZ DNA spool (*4*). The inner body is dismantled when the DNA is ejected from the capsid during infection (*2*). Inner body proteins are also likely injected into the host cell, based on the precedent of phage T7 (*5*), which also has a multitiered internal protein structure (*6*).

Bubbling is the end point to damage induced by electron irradiation of ice-embedded proteins (*7*). Although a detailed understanding of the radiation chemistry is lacking, this phenomenon appears to represent the formation of gaseous hydrogen-containing bubbles at high pressure (*8*). Why do inner body proteins bubble at relatively low electron doses (~50 electrons per Å^2 in a 0.5-s exposure)? Because there is no evidence to suggest that inner body proteins are chemically distinct from other proteins, we posit that they have a propensity to bubble because they are embedded in DNA. This impedes the diffusion of radiation products from their site of origin and promotes their build-up to concentrations at which bubbles nucleate. Support for this interpretation comes from the absence of bubbling in DNA-free particles containing the same inner body proteins. We suggest that bubblegram imaging may be productively applied to map proteins in other DNA-rich contexts such as cryosections of the cell nucleus.

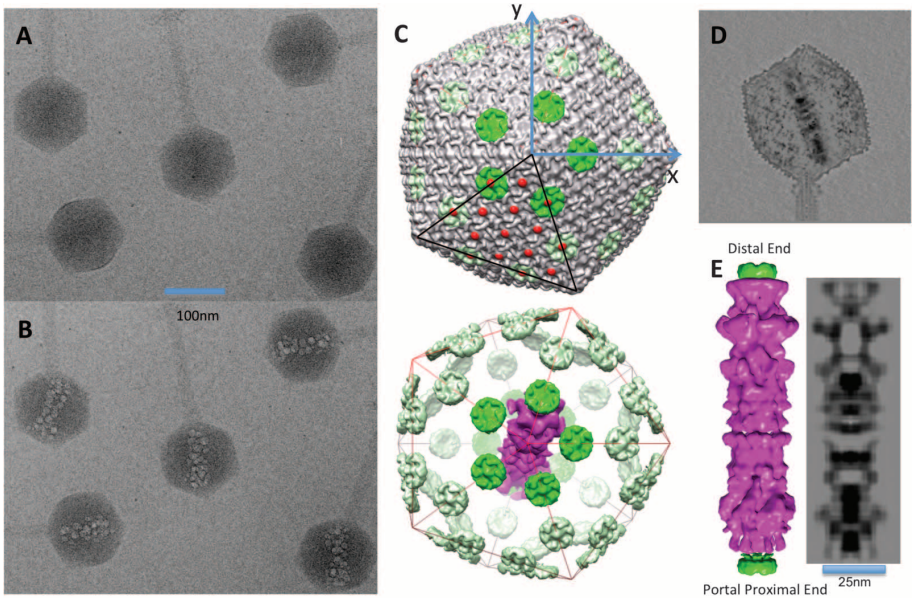

Fig. 1. Cryoelectron micrographs of purified ϕKZ virions: (**A**) initial low-dose exposure; (**B**) subsequent exposure of the same field, with bubbling in radiation-damaged virions. (**C**) Three-dimensional reconstruction of the ϕKZ capsid viewed along the axis of fivefold symmetry that passes through the portal. The capsid has T = 27 icosahedral symmetry (*4*). The centers of all hexons on one icosahedral facet are marked with red dots. Hexons in the ring of five, on one of which the inner body (in magenta) is anchored, are colored green. The symmetry-related hexons on the other side of the capsid are in pale green in the bottom image. Each of these hexons lies on a facet edge, connecting two vertices. The central axis of the inner body passes through the center of the capsid. (**D**) Central section of the ϕKZ head sampled in the plane in which the inner body axis lies. This view illustrates the tilt of the inner body relative to the portal axis and the offsetting of its point of contact with the capsid from the portal vertex. (**E**) Multitiered structure of the inner body shown in surface rendering (left, magenta) and central gray-scale section (right). The structures in (C) and (E) were sixfold rotationally averaged (justified by the angular power spectra analysis in fig. S3); the structure in (D) was not.

References and Notes

1. V. V. Mesyanzhinov *et al.*, *J. Mol. Biol.* **317**, 1 (2002).
2. V. N. Krylov *et al.*, *Can. J. Microbiol.* **30**, 758 (1984).
3. L. W. Black, J. A. Thomas, in *Viral Molecular Machines*, M. G. Rossmann, V. Rao, Eds. (Springer, New York, 2011), pp. 469–488.
4. A. Fokine *et al.*, *Structure* **15**, 1099 (2007).
5. C. Y. Chang, P. Kemp, I. J. Molineux, *Virology* **398**, 176 (2010).
6. X. Agirrezabala *et al.*, *EMBO J.* **24**, 3820 (2005).
7. J. F. Conway *et al.*, *J. Struct. Biol.* **111**, 222 (1993).
8. R. D. Leapman, S. Sun, *Ultramicroscopy* **59**, 71 (1995).

Acknowledgments: This work was supported by the Intramural Research program of NIAMS and by NIH grant AI11676 to L.W.B. The structure has been deposited at the Electron Microscopy Data Bank, reference number 10395, accession code EMD-1996.

Supporting Online Material

www.sciencemag.org/cgi/content/full/335/6065/182/DC1
Materials and Methods
Figs. S1 to S4
References (*9*–*14*)

19 September 2011; accepted 2 December 2011
10.1126/science.1214120

[1]Laboratory of Structural Biology, National Institute of Arthritis and Musculoskeletal and Skin Diseases (NIAMS), National Institutes of Health, Bethesda, MD 20892, USA. [2]Department of Biochemistry and Molecular Biology, University of Maryland School of Medicine, 108 North Greene Street, Baltimore, MD 21201, USA.

*To whom correspondence should be addressed. E-mail: stevena@mail.nih.gov

Simultaneously Mitigating Near-Term Climate Change and Improving Human Health and Food Security

Drew Shindell,[1]* Johan C. I. Kuylenstierna,[2] Elisabetta Vignati,[3] Rita van Dingenen,[3] Markus Amann,[4] Zbigniew Klimont,[4] Susan C. Anenberg,[5] Nicholas Muller,[6] Greet Janssens-Maenhout,[3] Frank Raes,[3] Joel Schwartz,[7] Greg Faluvegi,[1] Luca Pozzoli,[3]† Kaarle Kupiainen,[4] Lena Höglund-Isaksson,[4] Lisa Emberson,[2] David Streets,[8] V. Ramanathan,[9] Kevin Hicks,[2] N. T. Kim Oanh,[10] George Milly,[1] Martin Williams,[11] Volodymyr Demkine,[12] David Fowler[13]

Tropospheric ozone and black carbon (BC) contribute to both degraded air quality and global warming. We considered ~400 emission control measures to reduce these pollutants by using current technology and experience. We identified 14 measures targeting methane and BC emissions that reduce projected global mean warming ~0.5°C by 2050. This strategy avoids 0.7 to 4.7 million annual premature deaths from outdoor air pollution and increases annual crop yields by 30 to 135 million metric tons due to ozone reductions in 2030 and beyond. Benefits of methane emissions reductions are valued at $700 to $5000 per metric ton, which is well above typical marginal abatement costs (less than $250). The selected controls target different sources and influence climate on shorter time scales than those of carbon dioxide–reduction measures. Implementing both substantially reduces the risks of crossing the 2°C threshold.

Tropospheric ozone and black carbon (BC) are the only two agents known to cause both warming and degraded air quality. Although all emissions of BC or ozone precursors [including methane (CH_4)] degrade air quality, and studies document the climate effects of total anthropogenic BC and tropospheric ozone (*1*–*4*), published literature is inadequate to address many policy-relevant climate questions regarding these pollutants because emissions of ozone precursors have multiple cooling and warming effects, whereas BC is emitted along with other particles that cause cooling, making the net effects of real-world emissions changes obscure. Such information is needed, however, because multiple stakeholders are interested in mitigating climate change via control of non–carbon dioxide (CO_2)–forcing agents such as BC, including the G8 nations (L'Aquila Summit, 2009) and the Arctic Council (Nuuk Declaration, 2011). Here, we show that implementing specific practical emissions reductions chosen to maximize climate benefits would have important "win-win" benefits for near-term climate, human health, agriculture, and the cryosphere, with magnitudes that vary strongly across regions. We also quantify the monetized benefits due to health, agriculture, and global mean climate change per metric ton of CH_4 and for the BC measures as a whole and compare these with implementation costs.

Our analysis proceeded in steps. Initially, ~400 existing pollution control measures were screened with the International Institute for Applied Systems Analysis Greenhouse Gas and Air Pollution Interactions and Synergies (IIASA GAINS) model (*5*, *6*). The model estimated potential worldwide emissions reductions of particulate and gaseous species on the basis of available real-world data on reduction efficiencies of these measures where they have been applied already and examined the impact of full implementation everywhere by 2030. Their potential climate impact was assessed by using published global warming potential (GWP) values for each pollutant affected. All emissions control measures are assumed to improve air quality. We then selected measures that both mitigate warming and improve air quality, ranked by climate impact. If enhanced air quality had been paramount, the selected measures would be quite different [for example, measures primarily reducing sulfur dioxide (SO_2) emissions improve air quality but may increase warming]. The screening revealed that the top 14 measures realized nearly 90% of the maximum reduction in net GWP (table S1 and fig. S2). Seven measures target CH_4 emissions, covering coal mining, oil and gas production, long-distance gas transmission, municipal waste and landfills, wastewater, livestock manure, and rice paddies. The others target emissions from incomplete combustion and include technical measures (set "Tech"), covering diesel vehicles, clean-burning biomass stoves, brick kilns, and coke ovens, as well as primarily regulatory measures (set "Reg"), including banning agricultural waste burning, eliminating high-emitting vehicles, and providing modern cooking and heating. We refer to these seven as "BC measures," although in practice, we consider all co-emitted species (*7*).

We then developed future emissions scenarios to investigate the effects of the emissions control measures in comparison with both a reference and a potential low-carbon future: (i) a reference scenario based on energy and fuel projections of the International Energy Agency (IEA) (*8*) regional and global livestock projections (*9*) and incorporating all presently agreed policies affecting emissions (*10*); (ii) a CH_4 measures scenario that follows the reference but also adds the CH_4 measures; (iii) CH_4+BC measures scenarios that follow the reference but add the CH_4 and one or both sets of BC measures; (iv) a CO_2 measures scenario under which CO_2 emissions follow the IEA's "450 CO_2-equivalent" scenario (*8*) as implemented in the GAINS model (affecting CO_2 and co-emissions of SO_2 but not other long-lived gases); and (v) a combined CO_2 plus CH_4 and BC measures scenario. Measures are phased in linearly from 2010 through 2030, after which only trends in CO_2 emissions are included, with other emissions kept constant.

Emissions from these scenarios were then used with the ECHAM5-HAMMOZ (*11*) and GISS-PUCCINI (*12*) three-dimensional composition-climate models to calculate the impacts on atmospheric concentrations and radiative forcing (*7*). Changes in surface $PM_{2.5}$ (particles of less than 2.5 micrometers) and tropospheric ozone were used with published concentration-response relationships (*13*–*15*) to calculate health and agricultural impacts. CH_4 forcing was calculated from the modeled CH_4 concentrations. Direct ozone and aerosol radiative forcings were produced by using the fraction of total anthropogenic direct radiative forcing removed by the emission control measures, as calculated in the two models, multiplied by the best estimate and uncertainty range for direct forcing, which was determined from a literature assessment. Albedo forcing was similarly estimated on the basis of the fractional decrease of BC deposition to snow and ice surfaces. Indirect and semidirect forcings were estimated by simply assuming that these had the same fractional changes as the direct forcings (*16*). Initially, analytic equations representing rapid and slow components of the climate system

[1]NASA Goddard Institute for Space Studies and Columbia Earth Institute, Columbia University, New York, NY 10025, USA. [2]Stockholm Environment Institute, Environment Department, University of York, York YO10 5DD, UK. [3]Joint Research Centre of the European Commission, Ispra 21027, Italy. [4]International Institute for Applied Systems Analysis, Laxenburg A-2361, Austria. [5]U.S. Environmental Protection Agency, Washington, DC 20460, USA. [6]Department of Economics, Middlebury College, Middlebury, VT 05753, USA. [7]Department of Environmental Health, Harvard School of Public Health, Boston, MA 02215, USA. [8]Argonne National Laboratory, Argonne, IL 60439, USA. [9]Scripps Institute of Oceanography, University of California, San Diego, San Diego, CA 92093, USA. [10]Asian Institute of Technology, Bangkok 10400, Thailand. [11]Environmental Research Group, King's College London, London SE1 9NH, UK. [12]United Nations Environment Programme (UNEP), Nairobi 00100, Kenya. [13]Center for Ecology and Hydrology, Midlothian EH26 0QB, UK.

*To whom correspondence should be addressed. E-mail: drew.t.shindell@nasa.gov

†Present address: Eurasia Institute of Earth Sciences, Istanbul Technical University, Istanbul 34469, Turkey.

(*17*) were used to estimate global and regional (*18*) mean temperature response to the forcings.

This analytic analysis shows that the measures substantially reduce the global mean temperature increase over the next few decades by reducing tropospheric ozone, CH_4, and BC (Fig. 1). The short atmospheric lifetime of these species allows a rapid climate response to emissions reductions. In contrast, CO_2 has a very long atmospheric lifetime (hence, growing CO_2 emissions will affect climate for centuries), so that the CO_2 emissions reductions analyzed here hardly affect temperatures before 2040. The combination of CH_4 and BC measures along with substantial CO_2 emissions reductions [a 450 parts per million (ppm) scenario] has a high probability of limiting global mean warming to <2°C during the next 60 years, something that neither set of emissions reductions achieves on its own [which is consistent with (*19*)].

Work to this stage was largely in support of the Integrated Assessment of Black Carbon and Tropospheric Ozone (*20*). Here, we present detailed climate modeling and extend impact analyses to the national level, where regulations are generally applied and which provides detailed spatial information that facilitates regional impact analyses. We also provide cost/benefit analyses.

Climate modeling. We performed climate simulations driven by the 2030 CH_4 plus BC measures, by greenhouse gas changes only, and by reference emissions using the GISS-E2-S model; the same GISS atmosphere and composition models were coupled to a mixed-layer ocean (allowing ocean temperatures, but not circulation, to adjust to forcing). Direct, semidirect (aerosol effects on clouds via atmospheric heating), indirect (aerosol effects on clouds via microphysics), and snow/ice albedo (by BC deposition) forcings were calculated internally (*7*). We analyzed the equilibrium response 30 to 50 years after imposition of the measures, which is comparable with the latter decades in the analytic analysis.

The global mean response to the CH_4 plus BC measures was −0.54 ± 0.05°C in the climate model. The analytic equations yielded −0.52°C (−0.21 to −0.80°C) for 2070, which is consistent with these results. Climate model uncertainty only includes internal variations, whereas the analytic estimate includes uncertainties in forcing and climate sensitivity (but has no internal variability).

We also examined individual forcing components. Direct global mean aerosol forcings in the ECHAM and GISS models are almost identical (Table 1), despite large uncertainties generally present in aerosol forcing and the two aerosol models being fundamentally different [for example, internal versus external mixtures (*7*)]. CH_4 and ozone responses to CH_4 emissions changes are also quite similar. Ozone responses to changes in CO, volatile organic compounds, and NO_x associated with the BC measures are quite different, however. This is consistent with the nonlinear response of ozone to these precursors (*21*).

The combined indirect and semidirect radiative forcing by all aerosols in the GISS model is negative for the BC Tech and Reg measures. Although sulfate increases slightly—largely because of increases in the oxidant H_2O_2—in all emissions control scenarios, the BC measures primarily decrease BC and organic carbon (OC). The negative forcing suggests that a decreased positive semidirect effect may outweigh decreased negative indirect effects of BC and OC in this model [studies differ on the magnitude of these effects (*22*–*24*)]. Indirect effects are much larger than net direct effects for the Tech measures.

Global mean BC albedo forcing in the model is very small (Table 1), but we assume its

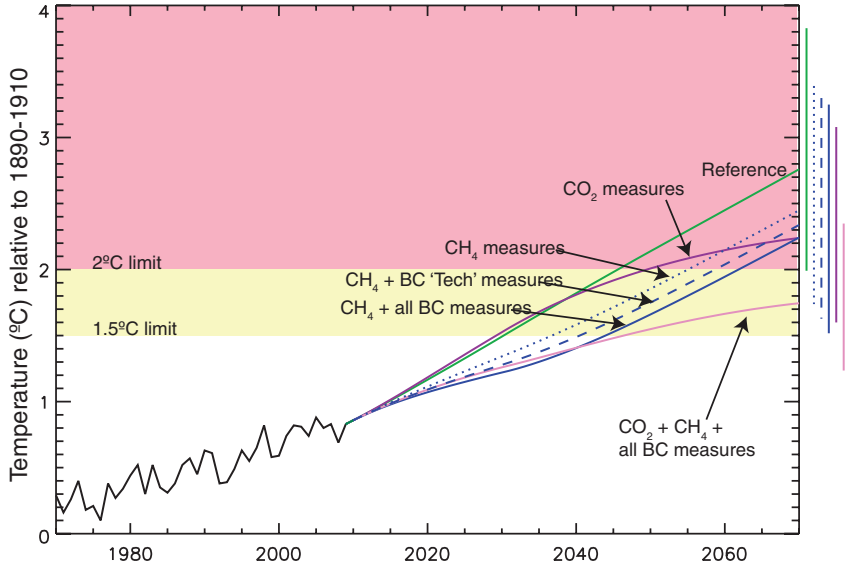

Fig. 1. Observed temperatures (*42*) through 2009 and projected temperatures thereafter under various scenarios, all relative to the 1890–1910 mean. Results for future scenarios are the central values from analytic equations estimating the response to forcings calculated from composition-climate modeling and literature assessments (*7*). The rightmost bars give 2070 ranges, including uncertainty in radiative forcing and climate sensitivity. A portion of the uncertainty is systematic, so that overlapping ranges do not mean there is no significant difference (for example, if climate sensitivity is large, it is large regardless of the scenario, so all temperatures would be toward the high end of their ranges; see www.giss.nasa.gov/staff/dshindell/Sci2012).

Table 1. ECHAM and GISS forcing (W/m^2) at 2030 due to the measures relative to the reference. Dashes indicate forcing not calculated.

	CH_4 measures	CH_4+BC Tech measures	All measures
ECHAM ozone	−0.09	−0.10	−0.10
GISS ozone	−0.10	−0.17	−0.19
ECHAM direct aerosols*	−0.01	−0.06	−0.15
GISS direct aerosols*	−0.01	−0.06	−0.17
(BC, OC, sulfate, nitrate)	(0.00, 0.00, −0.02, 0.00)	(-0.10, 0.06, −0.02, 0.01)	(−0.22, 0.07, −0.02, 0.01)
ECHAM CH_4†	−0.22	−0.22	−0.20
GISS CH_4†	−0.20	−0.20	−0.18
GISS indirect and semidirect aerosols	—	−0.14 ± 0.03	−0.16 ± 0.04
GISS BC albedo (effective forcing ×5)	—	−0.010 (−0.05)	−0.017 (−0.09)
GISS net‡	−0.32	−0.60	−0.77

*For aerosols, the value for ECHAM is the sum of the direct BC+OC+sulfate forcing. For GISS, the same sum is presented first, and individual components are listed afterward (the ECHAM model has more realistic internally mixed aerosols, so components are not separable). †CH_4 forcing at 2030 is roughly 75% of the forcing that is eventually realized from CH_4 emission changes through 2030. ‡The net forcing given here includes the effective value for BC albedo forcing. Uncertainties due to internal variability in the models are 0.01 W/m^2 or less for direct forcings and 0.001 W/m^2 for BC albedo forcing.

"effective" forcing is five times the instantaneous value (*25*, *26*). Albedo forcing can be important regionally (Fig. 2), especially in the Arctic and the Himalayas, where the measures decrease forcing up to 4 W/m^2 (not including the factor of 5). Such large regional impacts are consistent with other recent studies (*27*, *28*) and would reduce snow and ice melting.

Roughly half the forcing is relatively evenly distributed (from the CH_4 measures). The other half is highly inhomogeneous, especially the strong BC forcing, which is greatest over bright desert and snow or ice surfaces. Those areas often exhibit the largest warming mitigation, making the regional temperature response to aerosols and ozone quite distinct from the more homogeneous response to well-mixed greenhouse gases (Fig. 2) [although the impact of localized forcing extends well beyond the forcing location (*29*)]. BC albedo and direct forcings are large in the Himalayas, where there is an especially pronounced response in the Karakoram, and in the Arctic, where the measures reduce projected warming over the next three decades by approximately two thirds and where regional temperature response patterns correspond fairly closely to albedo forcing (for example, they are larger over the Canadian archipelago than the interior and larger over Russia than Scandinavia or the North Atlantic).

The largest precipitation responses to the CH_4 plus BC measures are seen in South Asia, West Africa, and Europe (Fig. 2). The BC measures greatly reduce atmospheric forcing—defined as top-of-the-atmosphere minus surface forcing—in those parts of Asia and Africa (fig. S4), which can strongly influence regional precipitation patterns (*30*–*32*). In comparison with a semiempirical estimate (*33*), the two composition-climate models represent present-day atmospheric forcing reasonably well (fig. S4). The response to greenhouse gases alone shows different spatial structure over South Asia and Europe and is much weaker everywhere (per unit of global mean forcing). The BC measures moderate a shift in the monsoon westward away from Southeast Asia into India seen during 20th- and 21st-century GISS-E2 simulations, with especially strong impacts at the Indian west coast and from Bengal to the northwest along the Himalayan foothills. Climate models' simulations of monsoon responses to absorbing aerosols vary considerably (*30*–*32*). The results suggest that the BC measures could reduce drought risk in Southern Europe and the

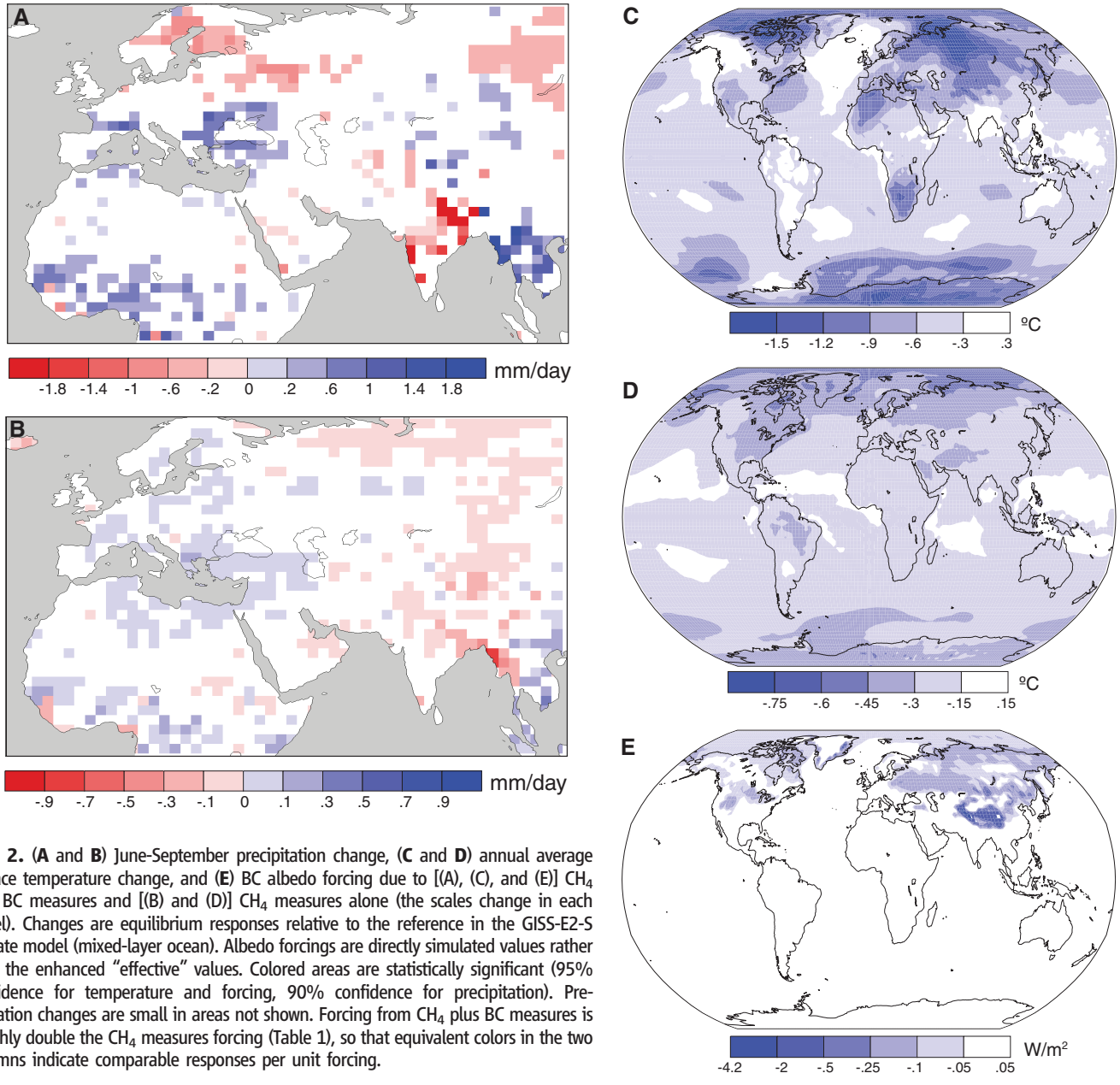

Fig. 2. (**A** and **B**) June-September precipitation change, (**C** and **D**) annual average surface temperature change, and (**E**) BC albedo forcing due to [(A), (C), and (E)] CH_4 plus BC measures and [(B) and (D)] CH_4 measures alone (the scales change in each panel). Changes are equilibrium responses relative to the reference in the GISS-E2-S climate model (mixed-layer ocean). Albedo forcings are directly simulated values rather than the enhanced "effective" values. Colored areas are statistically significant (95% confidence for temperature and forcing, 90% confidence for precipitation). Precipitation changes are small in areas not shown. Forcing from CH_4 plus BC measures is roughly double the CH_4 measures forcing (Table 1), so that equivalent colors in the two columns indicate comparable responses per unit forcing.

Sahel while reversing shifting monsoon patterns in South Asia.

Global mean impacts of packages of measures. Having established the credibility of the analytic climate calculations at the global scale [air quality simulations were shown to be realistic in (*20*)], we now briefly compare the global effects of the separate packages of measures (Table 2). The CH_4 measures contribute more than half the estimated warming mitigation and have the smallest relative uncertainty. BC Tech measures have a larger climate impact and a substantially smaller fractional uncertainty than that of the Reg measures because aerosols contribute a larger portion of the total forcing in the Reg case (and uncertainty in radiative forcing by BC or OC is much larger than for CH_4 or ozone). In the Reg case, the temperature range even includes the possibility of weak global warming, although the distribution shows a much larger probability of cooling.

For yield losses of four staple crops due to ozone, the mean values for CH_4 and BC Tech measures are comparable, whereas BC Reg measures have minimal impact. The health benefits from BC measures are far larger that those from the CH_4 measures because health is more sensitive to reduced exposure to $PM_{2.5}$ than to ground-level ozone. The large ranges for health impacts stem primarily from uncertainty in concentration-response relationships. The estimated 0.7 to 4.7 million annually avoided premature deaths are substantial in comparison with other causes of premature death projected for 2030, including tuberculosis (0.6 million), traffic accidents (2.1 million), or tobacco use (8.3 million) (*34*). There would also be large health benefits from improved indoor air quality. Because of limited data, we only estimated these for India and China, where implementation of all BC measures leads to an additional 373,000 annually avoided premature deaths (*7*).

Cost and benefit valuation. Economic analyses use the value of a statistical life (VSL) for health, world market prices for crops, and the social cost of carbon (SCC) along with global mean impacts relative to CO_2 for climate (*7*). Valuation is dominated by health effects and hence by the BC measures (Table 2). Climate valuation is large for the CH_4 measures, although it depends strongly on the metrics used. If instead of the 100-year GWP, the 100-year global temperature potential (GTP) of CH_4 is used (*35*), the value becomes $159 billion. Similarly, benefits scale with differing choices for the SCC. Climate benefits for the BC measures are based on the CH_4 measures' climate benefits times the relative global mean climate impact of the BC measures because published GWP or GTP values do not cover all species and ignore some factors affecting climate (such as aerosol indirect effects), and the ratio of the temperature responses is similar to the ratio of the integrated forcing due to a single year's emissions (GWP). This method still neglects regional effects of these pollutants on temperatures, precipitation, and sunlight available for photosynthesis.

Because the CH_4 measures largely influence CH_4 emissions alone, and CH_4 emissions anywhere have equal impact, it is straightforward to value CH_4 reductions by the metric ton. Climate benefits dominate, at $2381 per metric ton, with health second and crops third. The climate benefit per metric ton is again highly dependent on metrics. For example, instead of a $265 SCC (*36*)—a typical value assuming a near-zero discount rate—a value of $21 consistent with a ~3% discount rate could be used. Because discounting emphasizes near-term impacts, we believe a 20-year GWP or GTP should be used with the $21 SCC, in which case the valuation is $599 or $430 per metric ton, respectively. Health and agricultural benefits could also be discounted to account for the time dependence of the ozone response. Using a 5% discount rate, the mean health and agricultural benefits decrease relative to the undiscounted Table 2 values to $659 and $18 per metric ton, respectively. Climate benefits always exceed the agricultural benefits per metric ton, but climate values can be less or more than health benefits depending on the metric choices (the health benefits are similarly dependent on the assumed VSL).

A very conservative summation of benefits, using $430 for climate and discounted health and agricultural values, gives a total benefit of ~$1100 per metric ton of CH_4 (~$700 to $5000 per metric ton, using the above analyses). IEA estimates (*37*) indicate roughly 100 Tg/year of CH_4 emissions can be abated at marginal costs below $1100, with more than 50 Tg/year costing less than 1/10 this valuation (including the value of CH_4 captured for resale). Analysis using more recent cost information in the GAINS model (*38*, *39*) finds that the measures analyzed here could reduce 2030 CH_4 emissions by ~110 Tg at marginal costs below $1500 per metric ton, with 90 Tg below $250. The full set of measures reduce emissions by ~140 Tg, indicating that most would produce benefits greater than—and for approximately two-thirds of reductions far greater than—the abatement costs. Of course, the benefits would not necessarily accrue to those incurring costs.

Prior work valued CH_4 reductions at $81 ($48 to $116) per metric ton, including agriculture (grains), forestry, and nonmortality health benefits using 5% discounting (*40*). Their agricultural valuation was ~$30 ($1 to $42) per metric ton. Hence, our agriculture values are smaller but well within their large range. Those results suggest that forestry and nonmortality health effects contribute another ~$50 per metric ton of CH_4. Nonlinearities imply all valuations may shift somewhat as the background atmospheric composition changes.

GAINS estimates show that improved efficiencies lead to a net cost savings for the brick kiln and clean-burning stove BC measures. These account for ~50% of the BC measures' impact. The regulatory measures on high-emitting vehicles and banning of agricultural waste burning, which require primarily political rather than economic investment, account for another 25%. Hence, the bulk of the BC measures could probably be implemented with costs substantially less than the benefits given the large valuation of the health impacts (Table 2).

CH_4 measures by sector and region. It is also straightforward to separate the impact of CH_4 reductions in each region and sector on forcing. Because CH_4 is relatively well mixed globally, other impacts (such as crop yields) have the same proportionality as forcing. Emissions reductions in the coal mining and oil/gas production sectors

Table 2. Global impacts of measures on climate, agriculture, and health and their economic valuation. Valuations are annual values in 2030 and beyond, due to sustained application of the measures, which are nearly equal to the integrated future valuation of a single year's emissions reductions (without discounting). Climate valuations for CH_4 use GWP100 and an SCC of $265 per metric ton (*36*). Crop and health valuations use 95% confidence intervals, whereas climate valuations use ~67% uncertainty range. All values are in 2006 dollars.

	CH_4 measures	BC Tech measures	BC Reg measures
Physical Impacts			
Avoided warming in 2050 (°C)	0.28 ± 0.10	0.12 (+0.06/–0.09)	.07 (+.04/–0.09)
Annually avoided crop yield losses (millions metric tons; sum of wheat, rice, maize, and soy)	27 (+42/–20)	24 (+72/–21)	2 (+13/–3)
Annually avoided premature deaths (thousands)	47 (+40/–34)	1720 (+1529/–1188)	619 (+639/–440)
Valuation			
Climate, billions $US	331 ± 118	142 (+71/–106)	83 (+47/–106)
($US per metric ton CH_4)	(2381 ± 850)		
Crops, billions $US	4.2 ± 1.2	3.6 ± 2.6	0.4 ± 0.6
($US per metric ton CH_4)	(29 ± 8)		
Health, billions $US	148 ± 99	3717 (+3236/–2563)	1425 (+1475/–1015)
($US per metric ton CH_4)	(1080 ± 721)		

have the largest impacts, with municipal waste third (Fig. 3). Globally, sectors encompassing fossil fuel extraction and distribution account for nearly two thirds of the benefits because technology to control emissions from these sectors is readily available.

Examining benefits by sector and region, the largest by a considerable amount are from coal mining in China (Fig. 3). Oil and gas production in Central Africa, the Middle East, and Russia are next, followed by coal mining in South Asia, gas transmission in Russia (in high-pressure mains), and municipal waste in the United States and China. Ranking is obviously quite sensitive to regional groupings and country size, and there is substantial uncertainty in emissions from certain sectors in some regions. In particular, using national emission factors (instead of the Intergovernmental Panel on Climate Change default methodology) would lower the coal-mining potential from India and Southern Africa substantially. Nonetheless, those eight regional/sectoral combinations alone represent 51% of the total impact from all CH_4 measures.

Regional and national impacts. Upon examination of impacts of the CH_4 plus BC measures, avoided warming is greatest in central and northern Asia, southern Africa, and around the Mediterranean (Fig. 4, fig. S5, and table S5). Three of the top four national-level responses are in countries with strong BC albedo forcing (Tajikistan, Kyrgyzstan, and Russia). In contrast, the atmospheric forcing linked to regional hydrologic cycle disruption is reduced most strongly in south Asia and west Africa, where the measures greatly decrease BC emissions. Total numbers of avoided premature deaths are greatest in developing nations in Asia and Africa with large populations and high PM concentrations (and large emissions changes). Turning to per capita impacts, premature deaths are reduced most strongly in countries of south Asia, followed by central Africa, then east and southeast Asia, in a pattern quite similar to the atmospheric forcing impacts.

For crop production, China, India, and the United States, followed by Pakistan and Brazil, realize the greatest total metric tonnage gains. Looking instead at percentage yield changes, impacts are largest in the Middle East, with large changes also in central and south Asia. There is a large impact on percentage crop yields in Mexico that is quite distinct from neighboring countries, reflecting the influence of local emission changes. Impacts vary greatly between crops for changes in total production (fig. S6), with largest impacts occurring where the distribution and seasonal timing of crop production coincide with high ozone concentrations (*7*). Percentage yield changes are more consistent, however. Additional crop yield benefits would result from the avoided climate change, but they are not considered here.

Avoided warming is spread much more evenly over the Earth than other impacts. Both climate benefits in terms of reductions in regional atmospheric forcing and air quality–related human health benefits are typically largest in the countries of south Asia and central Africa, whereas agricultural benefits are greatest in the Middle East, where ozone reductions are large. Because many nations in these areas face great development challenges, realization of these benefits would be especially valuable in those areas.

Discussion. The results clearly demonstrate that only a small fraction of air quality measures provide substantial warming mitigation. Nonetheless, the CH_4 and BC emissions reduction measures examined here would have large benefits to global and regional climate, as well as to human health and agriculture. The CH_4 measures lead to large global climate and agriculture benefits and relatively small human health benefits, all with high confidence and worldwide distribution. The BC measures are likely to provide substantial global climate benefits, but uncertainties are much larger. However, the BC measures cause large regional human health benefits, as well as reduce regional hydrology cycle disruptions and cryosphere melting in both the Arctic and the Himalayas and improve regional agricultural yields. These benefits are more certain and are typically greatest in and near areas where emissions are reduced. Results are robust across the two composition-climate models. Protecting public health and food supplies may take precedence over avoiding climate change in most countries, but knowing that these measures also mitigate climate change may help motivate policies to put them into practice.

We emphasize that the CH_4 and BC measures are both distinct from and complementary to CO_2 measures. Analysis of delayed implemen-

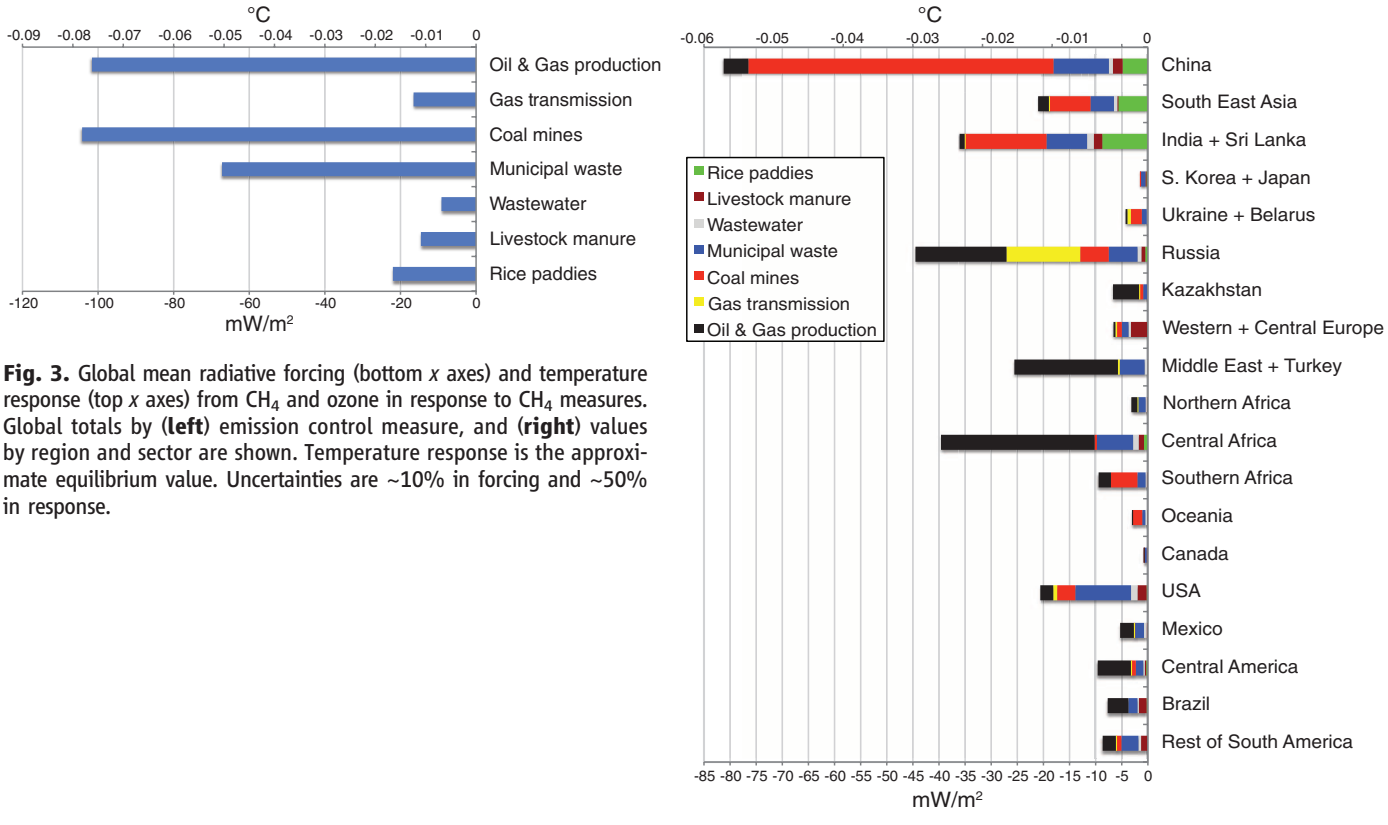

Fig. 3. Global mean radiative forcing (bottom *x* axes) and temperature response (top *x* axes) from CH_4 and ozone in response to CH_4 measures. Global totals by (**left**) emission control measure, and (**right**) values by region and sector are shown. Temperature response is the approximate equilibrium value. Uncertainties are ~10% in forcing and ~50% in response.

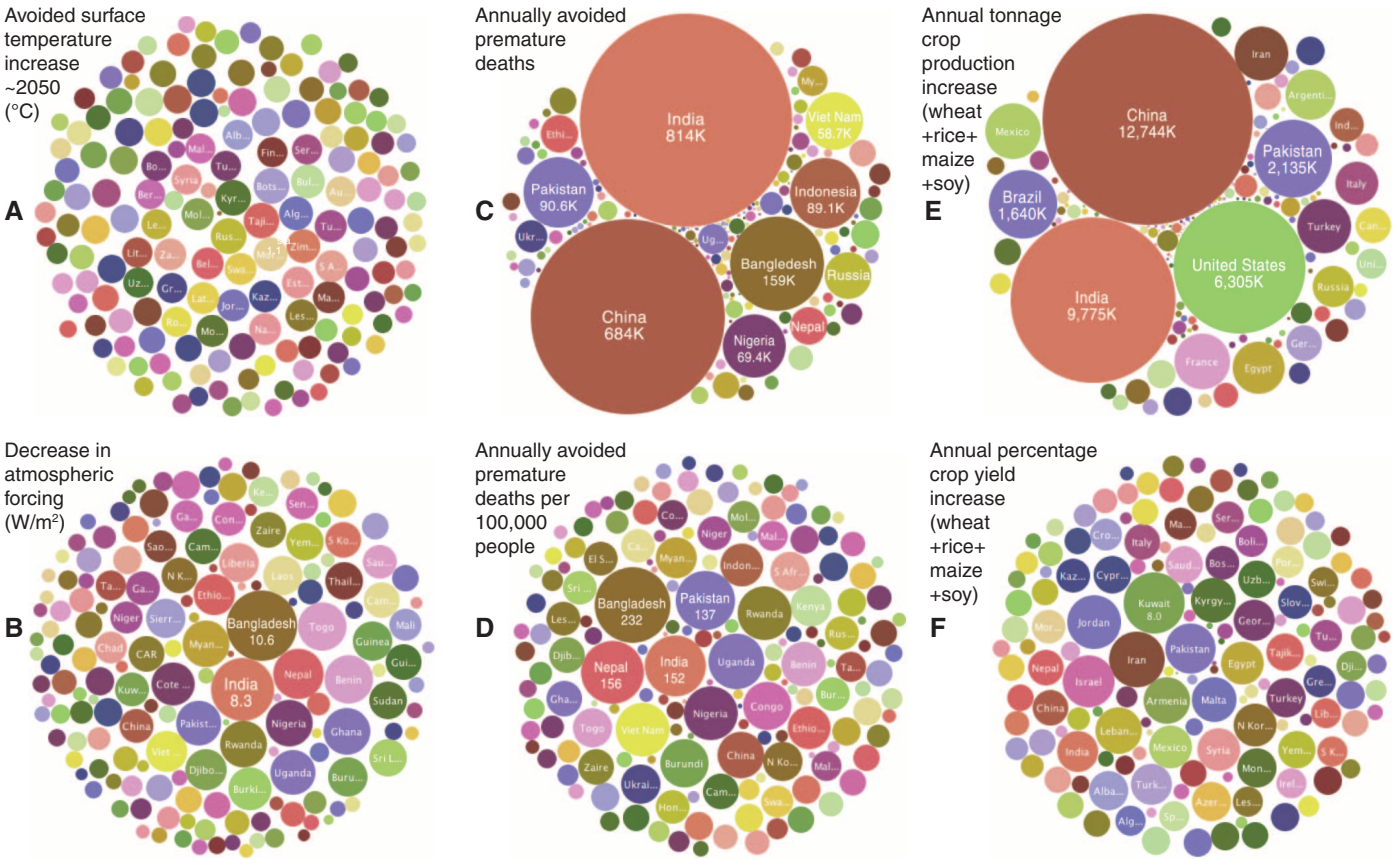

Fig. 4. National benefits of the CH_4 plus BC measures versus the reference scenario. Circle areas are proportional to values for (**A** and **B**) climate change, (**C** and **D**) human health (values for population over age 30), and (**E** and **F**) agriculture. Surface temperature changes are from the GISS-E2-S simulation. Health, agriculture, and atmospheric forcing impacts are based on the average of GISS and ECHAM concentration changes and are for 2030 and beyond. Uncertainties are ~60% for global mean temperatures, with national scale uncertainties likely greater, ~60% for atmospheric forcing, ~70% for health, and roughly −70%/+100% for crops [see (*7*) for factors included in uncertainties, most of which are systematic for atmospheric forcing, health, and agriculture so that much smaller differences between regions are still significant]. Interactive versions providing values for each country are at www.giss.nasa.gov/staff/dshindell/Sci2012, whereas alternate presentations of these data are in fig. S5 and table S5.

tation of the CH_4 and BC measures (fig. S3) shows that early adoption provides much larger near-term benefits but has little impact on long-term temperatures (*20*). Hence, eventual peak warming depends primarily on CO_2 emissions, assuming air quality–related pollutants are removed at some point before peak warming.

Valuation of worldwide health and ecosystem impacts of CH_4 abatement is independent of where the CH_4 is emitted and usually outweighs abatement costs. These benefits are therefore potentially suitable for inclusion in international mechanisms to reduce CH_4 emissions, such as the Clean Development Mechanism under the United Nations Framework Convention on Climate Change or the Prototype Methane Financing Facility (*41*). Many other policy alternatives exist to implement the CH_4 and BC measures, including enhancement of current air quality regulations. The realization that these measures can slow the rate of climate change and help keep global warming below 2°C relative to preindustrial in the near term, provide enhanced warming mitigation in the Arctic and the Himalayas, and reduce regional disruptions to traditional rainfall patterns—in addition to their local health and local-to-global agricultural benefits—may help prompt widespread and early implementation so as to realize these manifold benefits.

References and Notes

1. M. Z. Jacobson, *J. Geophys. Res.* **115** (D14), D14209 (2010).
2. D. T. Shindell *et al.*, *J. Geophys. Res.* **111**, D08302 (2006).
3. P. Forster *et al.*, in *Climate Change 2007: The Physical Science Basis*, S. Solomon, Ed. (Cambridge Univ. Press, New York, 2007).
4. P. Stier, J. Feichter, E. Roeckner, S. Kloster, M. Esch, *Atmos. Chem. Phys.* **6**, 3059 (2006).
5. Z. Klimont *et al.*, *Tellus B Chem. Phys. Meterol.* **61**, 602 (2009).
6. K. Kupiainen, Z. Klimont, *Atmos. Environ.* **41**, 2156 (2007).
7. Materials and methods are available as supporting material on *Science* Online.
8. International Energy Agency, *World Energy Outlook* (OECD/IEA, Paris, 2009).
9. N. Alexandratos *et al.*, "World agriculture: Towards 2030/2050. Interim report. Prospects for food, nutrition, agriculture and major commodity groups" (Food and Agriculture Organization, Rome, 2006).
10. J. Cofala, M. Amann, Z. Klimont, K. Kupiainen, L. Hoglund-Isaksson, *Atmos. Environ.* **41**, 8486 (2007).
11. L. Pozzoli *et al.*, *J. Geophys. Res.* **113** (D7), D07308 (2008).
12. D. T. Shindell *et al.*, *Atmos. Chem. Phys.* **6**, 4427 (2006).
13. D. Krewski *et al.*, "Extended follow-up and spatial analysis of the American Cancer Society study linking particulate air pollution and mortality" (Health Effects Institute, Boston, 2009).
14. M. Jerrett *et al.*, *N. Engl. J. Med.* **360**, 1085 (2009).
15. R. Van Dingenen *et al.*, *Atmos. Environ.* **43**, 604 (2009).
16. V. Ramaswamy *et al.*, in *Climate Change 2001*, J. T. Houghton, Ed. (Cambridge Univ. Press, Cambridge, 2001), pp. 349–416.
17. O. Boucher, P. Friedlingstein, B. Collins, K. P. Shine, *Environ. Res. Lett.* **4**, 044007 (2009).
18. D. Shindell, G. Faluvegi, *Atmos. Chem. Phys.* **10**, 3247 (2010).
19. V. Ramanathan, Y. Xu, *Proc. Natl. Acad. Sci. U.S.A.* **107**, 8055 (2010).
20. United Nations Environment Programme and World Meteorological Organization, "Integrated Assessment of Black Carbon and Tropospheric Ozone" (Nairobi, 2011).
21. S. Sillman, *Atmos. Environ.* **33**, 1821 (1999).
22. D. Koch, A. Del Genio, *Atmos. Chem. Phys.* **10**, 7685 (2010).
23. S. E. Bauer, S. Menon, D. Koch, T. C. Bond, K. Tsigaridis, *Atmos. Chem. Phys.* **10**, 7439 (2010).
24. W. T. Chen, Y. H. Lee, P. J. Adams, A. Nenes, J. H. Seinfeld, *Geophys. Res. Lett.* **37**, L09801 (2010).
25. M. G. Flanner, C. S. Zender, J. T. Randerson, P. J. Rasch, *J. Geophys. Res.* **112** (D11), D11202 (2007).
26. D. Koch *et al.*, *J. Clim.* **22**, 2659 (2009).

27. Y. Qian, M. G. Flanner, L. R. Leung, W. Wang, *Atmos. Chem. Phys.* **11**, 1929 (2011).
28. M. Kopacz *et al.*, *Atmos. Chem. Phys.* **11**, 2837 (2011).
29. D. Shindell *et al.*, *J. Geophys. Res.* **115**, D19110 (2010).
30. G. A. Meehl, J. M. Arblaster, W. D. Collins, *J. Clim.* **21**, 2869 (2008).
31. C. Wang, D. Kim, A. M. L. Ekman, M. C. Barth, P. J. Rasch, *Geophys. Res. Lett.* **36**, L21704 (2009).
32. V. Ramanathan *et al.*, *Proc. Natl. Acad. Sci. U.S.A.* **102**, 5326 (2005).
33. V. Ramanathan, G. Carmichael, *Nat. Geosci.* **1**, 221 (2008).
34. C. D. Mathers, D. Loncar, *PLoS Med.* **3**, e442 (2006).
35. J. S. Fuglestvedt *et al.*, *Atmos. Environ.* **44**, 4648 (2010).
36. R. S. J. Tol, *Economics: The Open-Access, Open-Assessment E-Journal* **2**, 1 (2008).
37. International Energy Agency, "Building the Cost Curves for the Industrial Sources of Non-CO2 Greenhouse Gases" (IEA Greenhouse Gas R&D Programme Cheltenham, UK, 2003).
38. L. Höglund-Isaksson, W. Winiwarter, A. Tohka, "Potentials and costs for mitigation of non-CO2 greenhouse gases in the European Union until 2030—Methodology" (IIASA Report, Laxenburg, Austria, 2010).
39. M. Amann *et al.*, *Environ. Model. Softw.* **26**, 1489 (2011).
40. J. J. West, A. M. Fiore, *Environ. Sci. Technol.* **39**, 4685 (2005).
41. www.globalmethanefund.org; accessed 23 May 2011.
42. J. Hansen *et al.*, *Proc. Natl. Acad. Sci. U.S.A.* **103**, 14288 (2006).

Acknowledgments: Funding was provided by UNEP and the World Meteorological Organization (WMO), NASA's Applied Sciences and Atmospheric Chemistry Modeling and Analysis Programs, and the Clean Air Task Force to IIASA. We thank all the authors and reviewers who contributed to the UNEP/WMO Integrated Assessment of Black Carbon and Tropospheric Ozone.

Supporting Online Material

www.sciencemag.org/cgi/content/full/335/6065/183/DC1
Materials and Methods
Figs. S1 to S6
Tables S1 to S5
References

20 June 2011; accepted 28 November 2011
10.1126/science.1210026

Periodic Emission from the Gamma-Ray Binary 1FGL J1018.6–5856

The Fermi LAT Collaboration*

Gamma-ray binaries are stellar systems containing a neutron star or black hole, with gamma-ray emission produced by an interaction between the components. These systems are rare, even though binary evolution models predict dozens in our Galaxy. A search for gamma-ray binaries with the Fermi Large Area Telescope (LAT) shows that 1FGL J1018.6–5856 exhibits intensity and spectral modulation with a 16.6-day period. We identified a variable x-ray counterpart, which shows a sharp maximum coinciding with maximum gamma-ray emission, as well as an O6V((f)) star optical counterpart and a radio counterpart that is also apparently modulated on the orbital period. 1FGL J1018.6–5856 is thus a gamma-ray binary, and its detection suggests the presence of other fainter binaries in the Galaxy.

Two types of interacting binaries containing compact objects are expected to emit gamma rays (*1*): microquasars—accreting black holes or neutron stars with relativistic jets (*2*)—and rotation-powered pulsars interacting with the wind of a binary companion (*3*). Microquasars should typically be powerful x-ray sources when active, and hence such gamma ray–emitting systems may already be known x-ray binaries. Indeed, the bright x-ray source Cygnus X-3 is now known to be such a source (*4*, *5*). The existence of pulsars interacting with stellar companions of early spectral types is predicted as an initial stage in the formation of high-mass x-ray binaries (HMXBs) containing neutron stars (*6*). These interacting pulsars are predicted to be much weaker x-ray emitters and may not yet be known or classified x-ray sources. Gamma-ray binaries may thus not be as rare as they appear to be, and many systems may await detection.

A gamma-ray binary is expected to show orbitally modulated gamma-ray emission due to a combination of effects, including changes in viewing angle and, in eccentric orbits, the degree of the binary interaction, both of which depend on binary phase. Periodic gamma-ray modulation has indeed been seen in LS 5039 (period 3.9 days), LS I +61° 303 (26.5 days), and Cygnus X-3 (4.8 hours) (*4*, *7*, *8*), and gamma-ray emission is at least orbital phase–dependent for the PSR B1259–63 system (3.4 years) (*9*). However, the putative gamma-ray binary HESS J0632+057, for which a 321-day x-ray period is seen, has not yet been shown to exhibit periodic gamma-ray emission (*10*). PSR B1259–63 contains a pulsar, and LS 5039 and LS I +61° 303 are suspected, but not proved, to contain pulsars, whereas Cygnus X-3 is a black hole candidate. A search for periodic modulation of gamma-ray flux from LAT sources may thus lead to the detection of further gamma-ray binaries, potentially revealing the predicted HMXB precursor population. The first Fermi LAT (*11*) catalog of gamma-ray sources ("1FGL") contains 1451 sources (*12*), a large fraction of which do not have confirmed counterparts at other wavelengths and thus are potentially gamma-ray binaries.

To search for modulation, we used a weighted photon method to generate light curves for all 1FGL sources in the energy range 0.1 to 200 GeV (*13*). We then calculated power spectra for all sources. From an examination of these, in addition to modulation from the known binaries LS I +61° 303 and LS 5039, we noted the presence of a strong signal near a period of 16.6 days from 1FGL J1018.6–5856 (Fig. 1). 1FGL J1018.6–5856 has a cataloged 1- to 100-GeV flux of 2.9×10^{-8} photons cm^{-2} s^{-1}, making it one of the brighter LAT sources. The source's location at right ascension (R.A.) = 10^h 18.7^m, declination (decl.) = –58° 56.30′ (J2000; ±1.8′, 95% uncertainty) means that it lies close to the galactic plane (b = –1.7°), marking it as a good candidate for a binary system. 1FGL J1018.6–5856 has been noted to be positionally coincident with the supernova remnant G284.3–1.8 (*12*) and the TeV source HESS J1018–589 (*14*), although it has not been shown that these sources are actually related.

The modulation at a period of 16.6 days has a power more than 25 times the mean value of the power spectrum and has a false-alarm probability of 3×10^{-8}, taking into account the number of statistically independent frequency bins. From both the power spectrum itself (*15*) and from fitting the light curve, we derived a period of 16.58 ± 0.02 days. The folded light curve (Fig. 1) has a sharp peak together with additional broader modulation. We modeled this to determine the epoch of maximum flux T_{max} by fitting a function consisting of the sum of a sine wave and a Gaussian function, and obtained T_{max} = modified Julian date (MJD) 55403.3 ± 0.4.

The gamma-ray spectrum of 1FGL J1018.6–5856 shows substantial curvature through the LAT passband. To facilitate discussion of the lower-energy (<1 GeV) and higher-energy (>1 GeV) gamma rays, we adopted as our primary model a broken power law with photon indices $\Gamma_{0.1-1}$ and Γ_{1-10} for energies below and above 1 GeV, respectively. The best-fit values (*13*) are $\Gamma_{0.1-1} = 2.00 \pm 0.04_{stat} \pm 0.08_{syst}$ and $\Gamma_{1-10} = 3.09 \pm 0.06_{stat} \pm 0.12_{syst}$, along with an integral energy flux above 100 MeV of $(2.8 \pm 0.1_{stat} \pm 0.3_{syst}) \times 10^{-10}$ erg cm^{-2} s^{-1}. A power law with exponential cutoff (*7*, *8*), $dN/dE = N_0(E/\mathrm{GeV})^{-\Gamma} \exp(-E/E_c)$, gives an acceptable fit with $\Gamma = 1.9 \pm 0.1$ and $E_c = 2.5 \pm 0.3$ GeV (statistical errors only). Although this spectral shape is qualitatively similar to that of pulsars and of LS I +61° 303 and LS 5039, so far no detection of pulsed gamma-ray emission has been reported (*16*).

To investigate variability on the 16.6-day period, we folded the data into 10 uniform bins in orbital phase and then refit the broken power-law parameters within each phase bin. The resulting

*All authors with their affiliations appear at the end of this paper.

folded light curve (Fig. 2) indicates substantial variability in both the source brightness and spectral shape. In agreement with the detection of multiple harmonics of the orbital period in the power spectrum, there appear to be two primary features. For phases 0.2 to 0.6, the spectral curvature decreases and the peak of the spectral energy distribution lies below the LAT passband (indicated by $\Gamma_{0.1-1} > 2$). The onset of this soft spectrum is approximately coincident with a rise in x-ray emission and a peak in radio emission (see below). A weaker peak appears in the low-energy (< 1 GeV) γ-ray flux at phase 0.5 (Fig. 2). For the remaining phases, the LAT spectrum hardens with a comparatively sharp rise to, and fall from, a peak around 1 GeV ($\Gamma_{0.1-1} < 2$, $\Gamma_{1-10} > 2$). The variable spectral shape implies that only a modest fraction of the flux could represent steady magnetospheric emission from a pulsar.

We undertook observations of the location of 1FGL J1018.6–5856 covering the energy range 0.3 to 10 keV by means of the X-ray Telescope (XRT) onboard the Swift satellite. The first observation was obtained on 29 September 2009 with an exposure of 5 ks. A single source was detected in the XRT image (Fig. 3) within the LAT error circle. We then obtained additional observations from January to April 2011 to search for x-ray variability (*13*) and found large amplitude variability. Folded on the gamma-ray ephemeris (Fig. 4), there is a sharp peak in x-ray flux, coincident with the gamma-ray peak. However, in addition to this, a sine wave–like periodic modulation is also seen that peaks near phase 0.3 to 0.4.

Swift Ultraviolet/Optical Telescope (UVOT) (*17*) observations were obtained simultaneously with the x-ray observations. The x-ray source is positionally coincident with a bright source seen in the UVOT images (Fig. 3) (*13*), which in turn is coincident with a source in the U.S. Naval Observatory B1.0 catalog at (J2000.0) R.A. = $10^h\ 18^m\ 55^s.60 \pm 0.1''$, decl. = –58° 56′ 46.2″ ± 0.1″. Spectroscopic observations of the optical counterpart were performed using the South African Astronomical Observatory 1.9-m telescope and the 2.5-m telescope at the Las Campanas Observatory. Absorption lines due to H, He I, and He II identify it as an early-type star. We used a spectral atlas (*18*) to estimate the spectral type. He II λ4686 is present in absorption, which indicates a main-sequence star. The ratio of He II λ4541 to He I λ4471 implies an O6 spectral type. Weak emission is seen from N III but not He II, which indicates an ((f)) classification. We therefore estimate the spectral type as O6V((f)). This is very similar to the spectral type of LS 5039 (*19*). Interstellar absorption bands provide an estimate of the reddening, $E(B-V)$, defined as the relative absorption in the B and V optical bands; from the features at 4430 and 5780 Å, we derive $E(B-V) = 0.9$ and 1.6, respectively. Taking $V \sim 12.6$ from measurements with the All Sky Automated Survey (ASAS) (*20*), we derive a distance, d, to 1FGL J1018.6–5856 from Earth of 5 ± 2 kpc, allowing for uncertainties in the reddening and spectral classification.

Radio observations of the 1FGL J1018.6–5856 region were obtained with the Australia Telescope Compact Array (ATCA) at frequencies of 5.5 and 9 GHz. A faint radio source at R.A. = $10^h\ 18^m\ 55^s.580$, decl. = –58° 56′ 45.5″ (±0.1″ and 0.3″, respectively) is coincident with the stellar position. The radio source was clearly seen to be variable (Fig. 4). Unlike the gamma-ray and x-ray modulation, there is no obvious brightening in the radio at phase zero. Instead, it appears that the radio may be following the smoother sine wave–like component of the x-ray modulation.

1FGL J1018.6–5856 shares many properties with LS 5039. They are both fairly steady gamma-ray sources on long time scales, their periodic modulations have not shown large changes, and their optical counterparts are of a very similar spectral type. The x-ray light curve of LS 5039 appears to be highly repeatable (*21*, *22*), and the x-ray light curve of 1FGL J1018.6–5856 also shows repeatable behavior with a flux increase around phase 0 repeated over four orbital periods. The lack of variability in UV/optical brightness is also reminiscent of LS 5039 (*23*, *24*). This suggests that there is little ellipsoidal modulation of the primary star and hence that it substantially underfills its Roche lobe. On the other hand, the relative phasing of the gamma-ray spectral modulation and flux modulation differ from those of LS 5039 where the spectrum is softest when the flux is highest (*8*). Also, for LS 5039 the phases of maximum x-ray and gamma-ray do not coincide (*8*, *22*). The brightest peak in the folded gamma-ray light curve of 1FGL J1018.6–5856 at phase 0 is associated with the hardest gamma-ray spectrum and is coincident with x-ray flaring and minimum radio emission. Finally, 1FGL J1018.6–5856 has a much longer orbital period.

The gamma-ray modulation observed in 1FGL J1018.6–5856 could be due to anisotropic inverse Compton (IC) scattering between stellar photons and high-energy electrons that varies with orbital phase, as proposed for LS 5039 and LS I +61° 303 (*7*, *8*). However, the modulation amplitude is considerably lower in 1FGL J1018.6–5856 [$(f_{max} - f_{min})/(f_{max} + f_{min}) \approx 25\%$] relative to that of LS 5039 (≈ 60%). Modulation amplitude should increase with eccentricity and is highest for systems viewed edge-on (*25*); however, in the case of LS I +61° 303, the modulation fraction has been observed to undergo large changes (*26*). If the IC scattering interpretation is correct, then this implies that 1FGL J1018.6–5856 has both low inclination and low eccentricity. For comparison, the eccentricity of LS 5039 has been reported to be in the range of 0.3 to 0.5 (*19*, *27*, *28*). Although a low inclination angle implies that it would be difficult to measure the radial velocity of the companion from optical studies, the small Doppler shifts predicted would facilitate a pulsation search at GeV energies.

The gamma-ray spectral variability of 1FGL J1018.6–5856 over the orbit is also reminiscent of

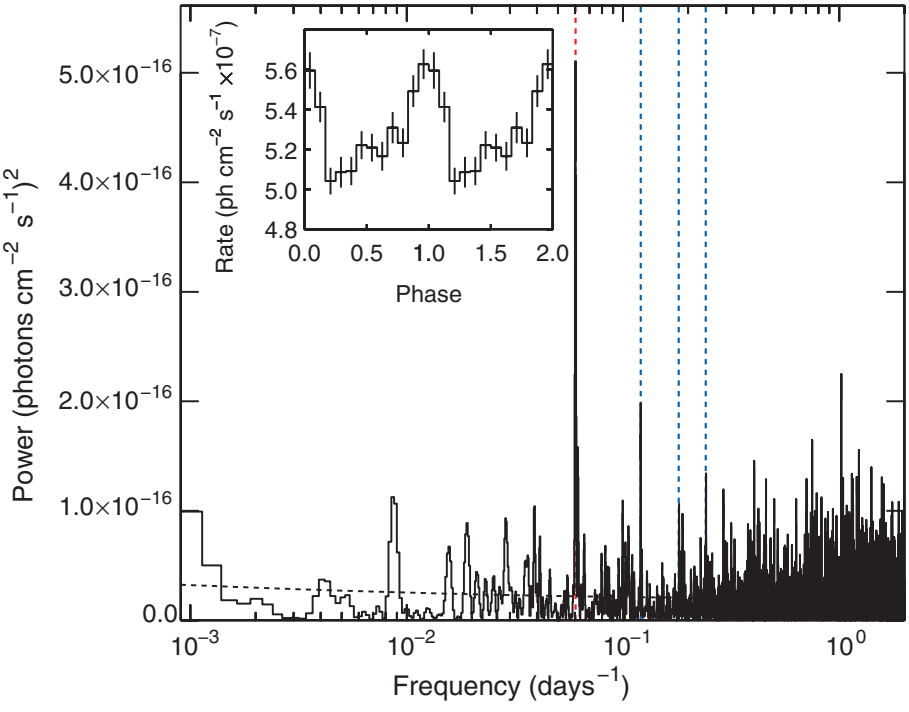

Fig. 1. Power spectrum of the LAT weighted photon light curve (E > 100 MeV) of 1FGL J1018.6–5856. The power spectrum is oversampled by a factor of 4 relative to its nominal resolution. The red dashed line indicates the 16.6-day period; the blue dashed lines are the second, third, and fourth harmonics of this. The dashed black line is a fit to the continuum power. The inset shows the weighted photon light curve folded on the 16.6-day period.

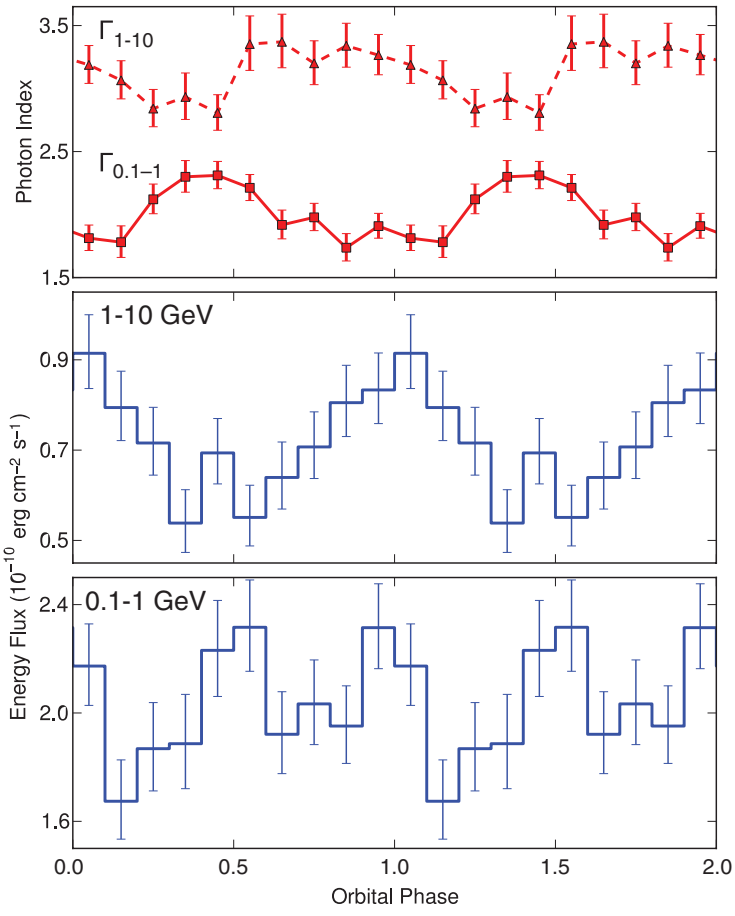

Fig. 2. The orbital modulation of the flux and spectral indices of 1FGL J1018.6–5856 in the 0.1 to 10 GeV band as measured with the Fermi LAT. $\Gamma_{0.1\text{–}1}$ and $\Gamma_{1\text{–}10}$ are photon spectral indices for energies below and above 1 GeV, respectively, using a broken power-law model.

LS 5039 but is unlike the behavior of LS I +61° 303. If the high-energy electron distribution remains constant along the orbit, spectral changes due to the anisotropic IC cross section are expected only if the inclination is substantial. In this case, harder spectra are expected to occur when the stellar photons are forward-scattered by the electrons (i.e., at inferior conjunction), which is also typically when the scattering rate is at its orbital minimum. However, for 1FGL J1018.6–5856 the hardness ratio and flux are correlated, unlike for LS 5039 (*8*). If periastron passage coincides with inferior conjunction, then a high photon density might compensate for the unfavorable interaction angle, but this requires fine-tuning of the orbital parameters. The spectral variability is more likely to reflect intrinsic variations—for instance, in the cooling of emitting particles. Moreover, both PSR B1259–63 and LS I +61° 303 (*7*, *9*) show that a simple model may not be correct. The phasing of gamma-ray maximum at GeV energies is not consistent with IC scattering on stellar photons, as it is delayed in both PSR B1259–63 and LS I +61° 303, implying that other mechanisms may be at work. For example, there could be other seed photon sources, Doppler boosting, or other radiative mechanisms at work.

The gamma-ray energy flux of 1FGL J1018.6–5856 implies a luminosity of $\sim 8 \times 10^{35}$ $(d/5\ \mathrm{kpc})^2$ ergs s^{-1} ($E > 100$ MeV), whereas the implied x-ray luminosity is highly variable with fluxes up to $\sim 10^{34}$ $(d/5\ \mathrm{kpc})^2$ ergs s^{-1}. For comparison, the gamma-ray luminosity of LS 5039 is $\sim 2 \times 10^{35}$ $(d/2.5\ \mathrm{kpc})^2$ ergs s^{-1} (*26*). This is somewhat surprising; relative to LS 5039, the orbital period of 1FGL J1018.6–5856 (longer by a factor of 4)

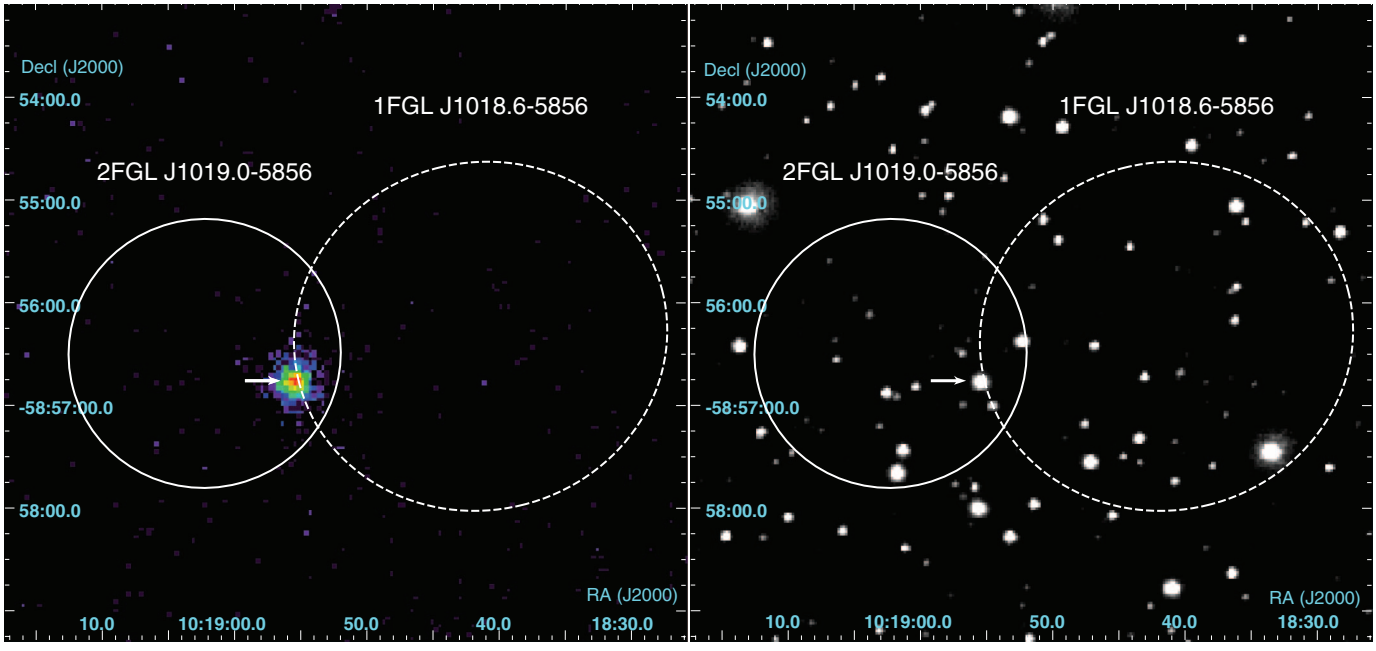

Fig. 3. Swift XRT x-ray (left) and UVOT-W1 (right) images of the region around 1FGL J1018.6–5856. The x-ray–optical counterpart is marked by an arrow near the center of both images. The LAT 95% confidence ellipses from the 1FGL (*12*) and 2FGL (*29*) catalogs are marked.

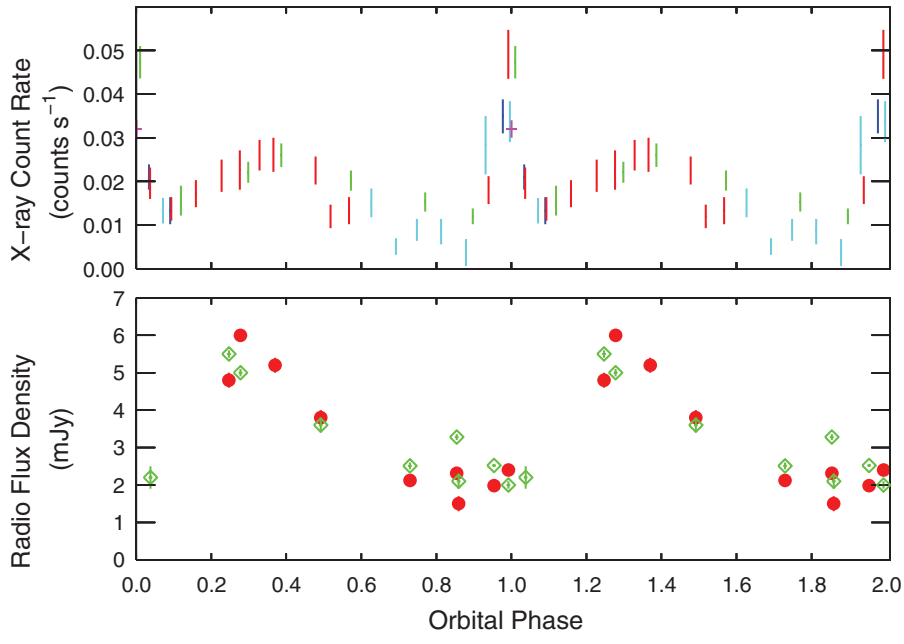

Fig. 4. X-ray (upper panel) and radio (lower panel) observations of 1FGL J1018.6–5856 folded on the orbital period. The x-ray data are from the Swift XRT and cover the energy range 0.3 to 10 keV. For the x-ray observations, the different colors indicate data taken from different 16.58-day orbital cycles. For the radio data, green diamonds indicate 9-GHz data and red circles 5.5-GHz data. The radio data are from the ATCA.

implies a major axis that is larger by a factor of 2.5, so that the mean stellar radiation density seen by the compact object is smaller by a factor of 6. The higher gamma-ray luminosity of 1FGL J1018.6–5856 indicates that the power injected in nonthermal particles must therefore be substantially higher in 1FGL J1018.6–5856 than in LS 5039. The similarity to LS 5039 suggests that we may be observing a rapidly rotating neutron star interacting with its companion. This raises the possibility that the neutron star rotation period might be detectable, as is the case with PSR B1259–63. However, our observations cannot definitely exclude an accreting neutron star or black hole.

References and Notes

1. I. F. Mirabel, *Science* **312**, 1759 (2006).
2. J. M. Paredes, J. Martí, M. Ribó, M. Massi, *Science* **288**, 2340 (2000).
3. G. Dubus, *Astron. Astrophys.* **456**, 801 (2006).
4. A. A. Abdo *et al.*; Fermi LAT Collaboration, *Science* **326**, 1512 (2009).
5. M. Tavani *et al.*, *Nature* **462**, 620 (2009).
6. E. J. A. Meurs, E. P. J. van den Heuvel, *Astron. Astrophys.* **226**, 88 (1989).
7. A. A. Abdo *et al.*, *Astrophys. J.* **701**, L123 (2009).
8. A. A. Abdo *et al.*, *Astrophys. J.* **706**, L56 (2009).
9. A. A. Abdo *et al.*, *Astrophys. J.* **736**, L11 (2011).
10. S. D. Bongiorno *et al.*, *Astrophys. J.* **737**, L11 (2011).
11. W. B. Atwood *et al.*, *Astrophys. J.* **697**, 1071 (2009).
12. A. A. Abdo *et al.*, *Astrophys. J. Suppl. Ser.* **188**, 405 (2010).
13. See supporting material on *Science* Online.
14. E. de Ona Wilhelmi *et al.*, paper presented at the 38th COSPAR Scientific Assembly, 23 July 2010, Bremen, Germany (paper E19-0082-10, poster Thu-286).
15. J. H. Horne, S. L. Baliunas, *Astrophys. J.* **302**, 757 (1986).
16. P. M. Saz Parkinson *et al.*, *Astrophys. J.* **725**, 571 (2010).
17. P. W. A. Roming *et al.*, *Space Sci. Rev.* **120**, 95 (2005).
18. N. R. Walborn, E. L. Fitzpatrick, *Publ. Astron. Soc. Pac.* **102**, 379 (1990).
19. M. V. McSwain *et al.*, *Astrophys. J.* **600**, 927 (2004).
20. G. Pojmański, *Acta Astronomica* **52**, 397 (2002).
21. T. Kishishita, T. Tanaka, Y. Uchiyama, T. Takahashi, *Astrophys. J.* **697**, L1 (2009).
22. T. Takahashi *et al.*, *Astrophys. J.* **697**, 592 (2009).
23. J. S. Clark *et al.*, *Astron. Astrophys.* **376**, 476 (2001).
24. J. Martí, P. Luque-Escamilla, J. L. Garrido, J. M. Paredes, R. Zamanov, *Astron. Astrophys.* **418**, 271 (2004).
25. G. Dubus, B. Cerutti, G. Henri, *Astron. Astrophys.* **477**, 691 (2008).
26. D. Hadasch, http://arxiv.org/abs/1111.0350 (2011).
27. J. Casares *et al.*, *Mon. Not. R. Astron. Soc.* **364**, 899 (2005).
28. G. E. Sarty *et al.*, *Mon. Not. R. Astron. Soc.* **411**, 1293 (2011).
29. The Fermi-LAT Collaboration, http://arxiv.org/abs/1108.1435 (2011).

Acknowledgments: The Fermi LAT Collaboration acknowledges support from a number of agencies and institutes for both development and the operation of the LAT as well as scientific data analysis. These include NASA and the U.S. Department of Energy (United States); CEA/Irfu and IN2P3/CNRS (France); ASI and INFN (Italy); MEXT, KEK, and JAXA (Japan); and the K. A. Wallenberg Foundation, the Swedish Research Council, and the National Space Board (Sweden). Additional support from INAF in Italy and CNES in France for science analysis during the operations phase is also gratefully acknowledged. Fermi LAT data are available from the Fermi Science Support Center (http://fermi.gsfc.nasa.gov/ssc). This work made use of data supplied by the UK Swift Science Data Centre at the University of Leicester. G.D. was supported by European Community contract ERC-StG-200911.

The Fermi LAT Collaboration

M. Ackermann,[1] M. Ajello,[1] J. Ballet,[2] G. Barbiellini,[3,4] D. Bastieri,[5,6] A. Belfiore,[7,8,9] R. Bellazzini,[10] B. Berenji,[1] R. D. Blandford,[1] E. D. Bloom,[1] E. Bonamente,[11,12] A. W. Borgland,[1] J. Bregeon,[10] M. Brigida,[13,14] P. Bruel,[15] R. Buehler,[1] S. Buson,[5,6] G. A. Caliandro,[16] R. A. Cameron,[1] P. A. Caraveo,[9] E. Cavazzuti,[17] C. Cecchi,[11,12] Ö. Çelik,[18,19,20] E. Charles,[1] S. Chaty,[2] A. Chekhtman,[21]† C. C. Cheung,[22]†‡ J. Chiang,[1] S. Ciprini,[12,23] R. Claus,[1] J. Cohen-Tanugi,[24] S. Corbel,[2,25] R. H. D. Corbet,[18,20]‡ S. Cutini,[17] A. de Luca,[26] P. R. den Hartog,[1] F. de Palma,[13,14] C. D. Dermer,[27] S. W. Digel,[1] E. do Couto e Silva,[1] D. Donato,[19,28] P. S. Drell,[1] A. Drlica-Wagner,[1] R. Dubois,[1] G. Dubus,[29] C. Favuzzi,[13,14] S. J. Fegan,[15] E. C. Ferrara,[18] W. B. Focke,[1] P. Fortin,[15] Y. Fukazawa,[30] S. Funk,[1] P. Fusco,[13,14] F. Gargano,[14] D. Gasparrini,[17] N. Gehrels,[18] S. Germani,[11,12] N. Giglietto,[13,14] F. Giordano,[13,14] M. Giroletti,[31] T. Glanzman,[1] G. Godfrey,[1] I. A. Grenier,[2] J. E. Grove,[27] S. Guiriec,[32] D. Hadasch,[16] Y. Hanabata,[30] A. K. Harding,[18] M. Hayashida,[1,33] E. Hays,[18] A. B. Hill,[34] R. E. Hughes,[35] G. Jóhannesson,[36] A. S. Johnson,[1] T. J. Johnson,[22]† T. Kamae,[1] H. Katagiri,[37] J. Kataoka,[38] M. Kerr,[1]‡§ J. Knödlseder,[39,40] M. Kuss,[10] J. Lande,[1] F. Longo,[3,4] F. Loparco,[13,14] M. N. Lovellette,[27] P. Lubrano,[11,12] M. N. Mazziotta,[14] J. E. McEnery,[18,28] P. F. Michelson,[1] W. Mitthumsiri,[1] T. Mizuno,[30] C. Monte,[13,14] M. E. Monzani,[1] A. Morselli,[41] I. V. Moskalenko,[1] S. Murgia,[1] T. Nakamori,[38] M. Naumann-Godo,[2] J. P. Norris,[42] E. Nuss,[24] M. Ohno,[43] T. Ohsugi,[44] A. Okumura,[1,43] N. Omodei,[1] E. Orlando,[1,45] M. Ozaki,[43] D. Paneque,[1,46] D. Parent,[47]† M. Pesce-Rollins,[10] M. Pierbattista,[2] F. Piron,[24] G. Pivato,[6] T. A. Porter,[1] S. Rainò,[13,14] R. Rando,[5,6] M. Razzano,[7,10] A. Reimer,[1,48] O. Reimer,[1,48] S. Ritz,[7] R. W. Romani,[1] M. Roth,[49] P. M. Saz Parkinson,[7] C. Sgrò,[10] E. J. Siskind,[50] G. Spandre,[10] P. Spinelli,[13,14] D. J. Suson,[51] H. Takahashi,[44] T. Tanaka,[1] J. G. Thayer,[1] J. B. Thayer,[1] D. J. Thompson,[18] L. Tibaldo,[5,6] M. Tinivella,[10] D. F. Torres,[16,52] G. Tosti,[11,12] E. Troja,[18]|| Y. Uchiyama,[1] T. L. Usher,[1] J. Vandenbroucke,[1] G. Vianello,[1,53] V. Vitale,[42,54] A. P. Waite,[1] B. L. Winer,[35] K. S. Wood,[27] M. Wood,[1] Z. Yang,[55,56] S. Zimmer,[55,56] M. J. Coe,[34] F. Di Mille,[57] P. G. Edwards,[58] M. D. Filipović,[59] J. L. Payne,[59] J. Stevens,[60] M. A. P. Torres[61]

[1]W. W. Hansen Experimental Physics Laboratory, Kavli Institute for Particle Astrophysics and Cosmology, Department of Physics and SLAC National Accelerator Laboratory, Stanford University, Stanford, CA 94305, USA. [2]Laboratoire AIM, CEA-IRFU/CNRS/Université Paris Diderot, Service d'Astrophysique, CEA Saclay, 91191 Gif-sur-Yvette, France. [3]Istituto Nazionale di Fisica Nucleare, Sezione di Trieste, I-34127 Trieste, Italy. [4]Dipartimento di Fisica, Università di Trieste, I-34127 Trieste, Italy. [5]Istituto Nazionale di Fisica Nucleare, Sezione di Padova, I-35131 Padova, Italy. [6]Dipartimento di Fisica "G. Galilei," Università di Padova, I-35131 Padova, Italy. [7]Santa Cruz Institute for Particle Physics, Department of Physics and Department of Astronomy and Astrophysics, University of California, Santa Cruz, CA 95064, USA. [8]Università degli Studi di Pavia, 27100 Pavia, Italy. [9]INAF–Istituto di Astrofisica Spaziale e Fisica Cosmica, I-20133 Milano, Italy. [10]Istituto Nazionale di Fisica Nucleare, Sezione di Pisa, I-56127 Pisa, Italy. [11]Istituto Nazionale di Fisica Nucleare, Sezione di Perugia, I-06123 Perugia, Italy. [12]Dipartimento di Fisica, Università degli Studi di Perugia, I-06123 Perugia, Italy. [13]Dipartimento di Fisica "M. Merlin" dell'Università e del Politecnico di Bari, I-70126 Bari, Italy. [14]Istituto Nazionale di Fisica Nucleare, Sezione di Bari, 70126 Bari, Italy. [15]Laboratoire Leprince-Ringuet, École Polytechnique, CNRS/IN2P3, Palaiseau, France. [16]Institut de Ciències de l'Espai (IEEE-CSIC), Campus UAB, 08193 Barcelona, Spain. [17]Agenzia Spaziale Italiana (ASI) Science Data Center, I-00044 Frascati (Roma), Italy. [18]NASA Goddard Space Flight Center, Greenbelt, MD 20771, USA. [19]Center for Research and Exploration in Space Science and Technology and NASA Goddard Space Flight Center, Greenbelt, MD 20771, USA. [20]Center for Space Sciences and Technology, University of Maryland Baltimore County, Baltimore, MD 21250, USA. [21]Artep Inc., 2922 Excelsior Springs Court, Ellicott City, MD 21042, USA. [22]National Research Council Research Associate, National Academy of Sciences, Washington, DC 20001, USA. [23]ASI Science Data Center, I-00044 Frascati (Roma), Italy. [24]Laboratoire Univers et Particules de Montpellier, Université Montpellier 2, CNRS/IN2P3, Montpellier, France. [25]Institut Universitaire de France, 75005 Paris, France. [26]Istituto Universitario di Studi Superiori, I-27100 Pavia, Italy. [27]Space Science Division, Naval Research Laboratory, Washington, DC 20375, USA. [28]Department of Physics and Department of Astronomy, University of Maryland, College Park, MD 20742, USA. [29]Institut de Planétologie et d'Astrophysique de Grenoble, Université Joseph Fourier-Grenoble 1/CNRS-INSU, UMR 5274, Grenoble F-38041, France. [30]Department of Physical Sciences, Hiroshima University, Higashi-Hiroshima, Hiroshima 739-8526, Japan. [31]INAF Istituto di Radioastronomia, 40129 Bologna, Italy. [32]Center for Space Plasma and Aeronomic Research, University of Alabama, Huntsville, AL 35899, USA. [33]Department of Astronomy, Graduate School of Science, Kyoto University,

Sakyo-ku, Kyoto 606-8502, Japan. [34]School of Physics and Astronomy, University of Southampton, Highfield, Southampton SO17 1BJ, UK. [35]Department of Physics, Center for Cosmology and Astro-Particle Physics, Ohio State University, Columbus, OH 43210, USA. [36]Science Institute, University of Iceland, IS-107 Reykjavik, Iceland. [37]College of Science, Ibaraki University, 2-1-1, Bunkyo, Mito 310-8512, Japan. [38]Research Institute for Science and Engineering, Waseda University, 3-4-1, Okubo, Shinjuku, Tokyo 169-8555, Japan. [39]CNRS, IRAP, F-31028 Toulouse Cedex 4, France. [40]GAHEC, Université de Toulouse, UPS-OMP, IRAP, Toulouse, France. [41]Istituto Nazionale di Fisica Nucleare, Sezione di Roma "Tor Vergata," I-00133 Roma, Italy. [42]Department of Physics, Boise State University, Boise, ID 83725, USA. [43]Institute of Space and Astronautical Science, JAXA, 3-1-1 Yoshinodai, Chuo-ku, Sagamihara, Kanagawa 252-5210, Japan. [44]Hiroshima Astrophysical Science Center, Hiroshima University, Higashi-Hiroshima, Hiroshima 739-8526, Japan. [45]Max-Planck-Institut für extraterrestrische Physik, 85748 Garching, Germany. [46]Max-Planck-Institut für Physik, D-80805 München, Germany. [47]Center for Earth Observing and Space Research, College of Science, George Mason University, Fairfax, VA 22030. [48]Institut für Astro- und Teilchenphysik and Institut für Theoretische Physik, Leopold-Franzens-Universität Innsbruck, A-6020 Innsbruck, Austria. [49]Department of Physics, University of Washington, Seattle, WA 98195, USA. [50]NYCB Real-Time Computing Inc., Lattingtown, NY 11560, USA. [51]Department of Chemistry and Physics, Purdue University Calumet, Hammond, IN 46323, USA. [52]Institució Catalana de Recerca i Estudis Avançats (ICREA), Barcelona, Spain. [53]Consorzio Interuniversitario per la Fisica Spaziale (CIFS), I-10133 Torino, Italy. [54]Dipartimento di Fisica, Università di Roma "Tor Vergata," I-00133 Roma, Italy. [55]Department of Physics, Stockholm University, AlbaNova, SE-106 91 Stockholm, Sweden. [56]Oskar Klein Centre for Cosmoparticle Physics, AlbaNova, SE-106 91 Stockholm, Sweden. [57]Australian Astronomical Observatory–Las Campanas Observatory, Colina, El Pino Casilla 601, La Serena, Chile. [58]Australia Telescope National Facility, CSIRO Astronomy and Space Science, Narrabri, NSW 2390, Australia. [59]University of Western Sydney, Locked Bag 1797, Penrith, NSW 2751, Australia. [60]CSIRO Astronomy and Space Science, Epping, NSW 1710, Australia. [61]Harvard-Smithsonian Center for Astrophysics, Cambridge, MA 02138, USA.

†Resident at Naval Research Laboratory, Washington, DC 20375, USA.
‡To whom correspondence should be addressed. E-mail: robin.corbet@nasa.gov (R.H.D.C.); kerrm@stanford.edu (M.K.); teddy.cheung.ctr@nrl.navy.mil (C.C.C.)
§Einstein Fellow.
‖NASA Postdoctoral Program Fellow.

Supporting Online Material
www.sciencemag.org/cgi/content/full/335/6065/189/DC1
Materials and Methods
Figs. S1 to S4
References (*30*–*46*)

14 September 2011; accepted 16 November 2011
10.1126/science.1213974

Universal Signatures of Fractionalized Quantum Critical Points

Sergei V. Isakov,[1] Roger G. Melko,[2] Matthew B. Hastings[3,4]*

Ground states of certain materials can support exotic excitations with a charge equal to a fraction of the fundamental electron charge. The condensation of these fractionalized particles has been predicted to drive unusual quantum phase transitions. Through numerical and theoretical analysis of a physical model of interacting lattice bosons, we establish the existence of such an exotic critical point, called XY*. We measure a highly nonclassical critical exponent $\eta = 1.493$ and construct a universal scaling function of winding number distributions that directly demonstrates the distinct topological sectors of an emergent Z_2 gauge field. The universal quantities used to establish this exotic transition can be used to detect other fractionalized quantum critical points in future model and material systems.

It is noteworthy that, in this age of high-energy accelerator experiments, certain types of fundamental quantum particles can only be studied in tabletop condensed-matter physics experiments. Consider, for example, the electron, carrying fundamental charge e. Unlike the proton, whose charge originates from quarks with fractional charge, no energy is sufficiently high to break up the charge of an electron. However, as demonstrated by the measurement of fractional Hall conductance, if one places an electron in certain clean two-dimensional (2D) materials in a strong magnetic field, its charge can break into fractions—$e/3$, $e/5$, and so on (*1*)—with each fractional charge arising from a quasiparticle emerging as an excitation of the ground state.

Such quasiparticles share all the important characteristics of real particles. In deconfined phases of matter with a gap to excitations, the quasiparticles can be separated a large distance from each other, making them well-defined localized objects with a sharp energy-momentum dispersion relation. For more than a decade, condensed-matter physicists have searched for fractionalized particles in systems other than Hall effect materials. Theoretical predictions have identified a class of low-temperature paramagnets, the quantum spin liquids, as holding particular promise for supporting them (*2*–*4*). However, experimental searches for these fractional charges and their parent spin-liquid vacuum remain unconvincing. This is partly a result of the difficulty in constructing measurements that are able to identify their experimental signatures in the variety of materials—ranging from fabricated solid-state devices to organic magnets—thought to harbor spin-liquid states (*5*). An interesting recent experimental candidate is a set of materials that may display fractional particles with a gapless Fermi surface (*6*–*11*), where interaction between quasiparticles makes it problematic to even define a fractionalized excitation (*12*). In bosonic systems, such interacting gapless fractional quasiparticles have been proposed to mediate quantum critical points that exist in certain order-to-order transitions (*13*). For these Landau-violating critical points (which rely on long-wavelength fluctuations of fractional particles), signatures of the fractionalization are manifest in universal quantities, such as critical exponents, instead of specific material-dependent quantities.

A major goal of the theoretical community has been to demonstrate the existence of these "deconfined" quantum critical points in realistic microscopic models, with the use of large-scale numerical simulation (*14*). In this work, we used quantum Monte Carlo (QMC) to study deconfined quantum criticality in the context of an order-to-disorder transition between a superfluid and a gapped spin-liquid state, in a physical model of lattice bosons. The model we examine is a variant of the Bose-Hubbard Hamiltonian, introduced in (*15*), which is a simple model of hard-core bosons hopping (with strength t) on a 2D kagome lattice with an energetic constraint (V) favoring three bosons per hexagonal lattice plaquette: $H = -t\sum_{\langle ij\rangle}[b_i^\dagger b_j + b_i b_j^\dagger] + V\sum_{\hexagon}(n_{\hexagon})^2$ (i and j are nearest-neighbor lattice sites; $b_i^\dagger$ and b_i are boson creation and annihilation operators,

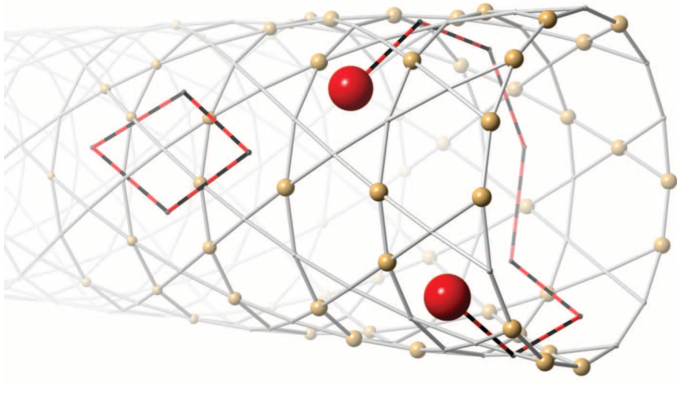

Fig. 1. A section of the toroidal kagome lattice simulation cell. Gold spheres label sites occupied by bosons in a representative configuration. Red spheres are fractional charges, marking "defect hexagons" (those that do not have three bosons per site). Defect hexagons are shown joined by an open string. We also show a representative closed string not associated with fractionalized particles.

[1]Theoretische Physik, ETH Zurich, 8093 Zurich, Switzerland. [2]Department of Physics and Astronomy, University of Waterloo, Waterloo, Ontario N2L 3G1, Canada. [3]Department of Physics, Duke University, Durham, NC 27708, USA. [4]Microsoft Research, Station Q, California NanoSystems Institute Building, University of California, Santa Barbara, CA 93106, USA.

*To whom correspondence should be addressed. E-mail: xhastings@gmail.com

respectively; and $n_{\hexagon}$ is the density of bosons around a hexagonal lattice plaquette). This model has been shown to contain a superfluid–to–spin-liquid quantum phase transition at $V/t \approx 7$ through the measurement of the topological entanglement entropy (*15*). In that work, two universal exponents were measured at the critical point, related to the divergence of the correlation length (ν) and the isotropy of the space and time dimensions (z); both fall in the conventional 3D XY universality class. A section of the toroidal kagome lattice geometry used in our QMC simulations, along with a representative boson configuration, is shown in Fig. 1.

This system conserves total charge (the boson particle number). Deep in the spin-liquid phase ($V >> t$), it is known (*16*) that exotic quasiparticles carrying a half-odd integer charge exist as fundamental excitations out of the ground-state vacuum. At infinite V and half filling, the system is restricted to a space of states with three particles in each hexagon. In this limit, the model can be mapped to a dimer model on a triangular lattice formed by the centers of the hexagons, with three dimers per site (*16*). Turning on a nonvanishing t/V produces virtual excitations out of this space of states, leading to effective exchange terms, which give a quantum spin-liquid phase. Imagine removing a single particle from this state, creating a pair of defect sites in the dimer model with only two dimers. In a phase with mobile, deconfined defects, these defects can become separated by large distances, and because the state has a total charge of –1 relative to the vacuum, each defect carries a charge of –1/2. Similarly, defects with four dimers carry a charge of +1/2. The model is thus in a Z_2 spin-liquid phase, but electric defects carry a half-odd charge (*17*). Overlaying this configuration with a fixed reference configuration gives a transition graph, which is a gas of strings, with open strings connecting defects (*2*). There are three dimers per site, so strings may intersect (in Fig. 1 we only show two strings for clarity). Because links in the string arise alternately from the given configuration and the reference configuration, links need not have a particle on them in the image shown.

Colloquially, one can view the fractionalized particles as a square root of the boson field, with the Z_2 gauge field present due to the sign ambiguity in the square root. Let $b^\dagger$,b denote creation and annihilation operators for the real physical bosons, and let $\phi^\dagger$,ϕ denote the same operators for the fractionalized particles. At an XY* critical point, the fractionalized field ϕ undergoes an ordinary XY transition (*18*–*20*). This dramatically affects the observed critical exponents (*21*, *22*), because the order parameter b usually associated with the transition is actually a composite operator, made up of two ϕ fields. This leads to the same exponent ν as in the ordinary XY critical point. However, the exponent η controlling the equal-time ground-state correlation function $\langle b^\dagger(0)\, b(x)\rangle$ is substantially modified, leading to $\eta \approx 1.47(3)$, as estimated by field theoretic and Monte Carlo simulations of the correlation of a composite operator in the 3D XY model (*23*, *24*). This is in marked contrast to the value $\eta \approx 0.038$ in the ordinary 3D XY transition (*25*).

The measurement of η in the kagome model is challenging because QMC does not directly access the superfluid order parameter operators necessary to measure the relevant correlation function. To overcome this fact, we have measured the equal time Green's function in real space: $G(x) \equiv G(\tau = 0, r) = \langle b^\dagger(0) b(r)\rangle$ (τ is the imaginary time and r is the radial coordinate) (*26*, *27*). This measurement involves keeping track of the defects created in the nonlocal loop algorithm (*28*) as it traverses the QMC's d+1 space-time simulation cell (d is the spatial dimension). At the critical point, $G(r)$ should decay at sufficiently long distances as $1/r^{1+\eta}$. Finite size effects can be minimized by looking at $G(L/m)$, which decays as $1/L^{1+\eta}$, where L is the linear system size and m is some (fixed) number. In Fig. 2, we show $G(L/6)$ as a function of L. The Green's function decays algebraically with $\eta = 1.493$ (*10*), a value that is consistent with η for a composite operator in the 3D XY model. This strongly nonclassical η shows that the boson operator b is indeed a composite operator of fractionalized excitations.

More direct evidence can be obtained from topological properties, as we now show by constructing new scaling functions that exploit universality, and as such can be used as a test for the existence of fractionalized excitations in other models and experiments. Consider a path in imaginary time in which a total of n_x of the ϕ particles wind around the x direction of the torus geometry. In this case, the total charge W_x that winds around the torus is equal to only $n_x/2$. However, the only closed paths in imaginary time that are allowed are those in which n_x is even, as the physical charge W_x winding around the torus must be an integer. This is a manifestation of topological

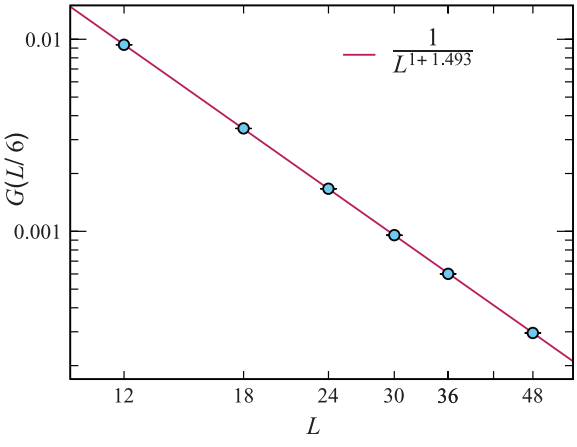

Fig. 2. Equal time Green's function $G(L/6) = \langle b^\dagger(0,0)\, b(L/6,0)\rangle$ as a function of system size L.

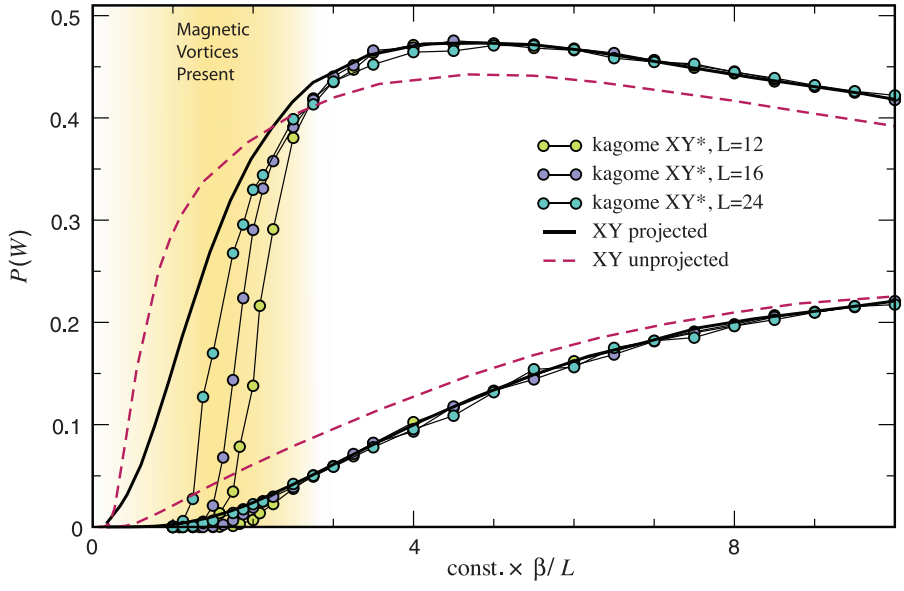

Fig. 3. Comparison of winding number distribution $P(W_x)$ for the kagome lattice XY* transition at $L = 12$, 16, 24 to $P_{even}(2W_x)$ for a conventional 24-by-24 square-lattice XY transition (*30*). Dashed lines show the unprojected distribution of XY winding numbers $P(W)$ for comparison. Upper curves are $W = 1$ and lower are $W = 2$. The x axis is β/L for the kagome lattice model and β/L multiplied by a nonuniversal velocity ratio for the XY model.

properties of the Z_2 gauge field. The gauge field is gapped, so it does not affect the dynamics of the ϕ field, but there are a total of eight different topological sectors (two sectors in each space direction and one in the time direction), and summing over sectors restricts to even winding and an even number of the fractionalized particles (see Fig. 1, where winding a particle drags a string, changing the topological sector). It is known that the winding-number variance $\langle W_x^2 \rangle$ in the ordinary XY model is a universal function of $L/v\beta$, where L is the length scale of the torus, v is a nonuniversal velocity, and β is the inverse temperature. It is natural that the full winding-number distribution, as quantified by the probabilities $P(W_x)$ of observing a given winding, is also a universal function (*29*). Thus, the universal critical properties of the winding number distribution W_x in our model can be computed from a model undergoing an ordinary XY transition in 2+1 dimensions, by restricting to sectors with even winding numbers n_x,n_y and an even total particle number. Then, one can determine the probability of observing a given n_x with

$$P(W_x) = P_{\text{even}}(2W_x) \quad (1)$$

where $P_{\text{even}}(2W_x)$ is the probability, after projecting onto these even sectors, of observing $n_x = 2W_x$. Whereas one does not know the scaling functions controlling P_{even} analytically, we have sampled them using quantum Monte Carlo on a different model that contains a conventional XY transition (*30*). The prediction of the theory shows excellent agreement for two distinct scaling functions (Fig. 3) over the majority of the observed curve. The disagreement at higher temperatures is a result of low-energy magnetic excitations (*30*); as system size is increased, the range of agreement improves.

This provides a direct test of the fractionalized charge. The fit of all the scaling functions uses only a single adjustable parameter, the nonuniversal velocity ratio $v_{\text{XY}}/v_{\text{kagome}}$. In the limit of $v\beta/L \to \infty$, the winding numbers become large, and both the projected and unprojected winding-number distributions converge to approximate Gaussians, so the projection onto even numbers has little effect on the variance. Then, one will observe $\langle W_x^2 \rangle_{\text{XY}^*} = (1/4)\langle W_x^2 \rangle_{\text{XY}}$, where the subscripts denote the two different universality classes and we assume both models are at the same ratio $v\beta/L$. However, testing this agreement is difficult as it requires an accurate measurement of the nonuniversal velocity. In fact, the best way we have found to measure the nonuniversal velocity (as the high-temperature measurements are complicated by the magnetic excitations) is to study the full distribution of scaling functions, which provides a much more stringent test. Note also that the scaling functions of the unprojected XY model are very different from the projected functions at moderate $v/L\beta$, where both functions are strongly non-Gaussian and non-Poissonian.

As mentioned above, Fig. 3 shows slow convergence to universal scaling in the high-temperature critical regime (small $v\beta/L$). To understand this, we have considered the phase diagram of the model as a function of V/t and temperature T. At small V/t, the model is superfluid at zero temperature, with a continuous transition at nonzero temperature, which is likely Kosterlitz-Thouless. There is some evidence that at larger V/t, but still below the critical point, the phase transition becomes first-order, similar to behavior seen in (*31*). This is probably due to vortices where the phase of ϕ winds by π, which are more relevant at long length scales than the usual 2π vortices. Close to the critical point, the transition might return to being continuous at nonzero temperature (*32*). However, the presence of low-energy Z_2 magnetic vortices has a strong effect on the nonzero temperature properties.

The scenarios that are consistent with the numerical data are those for $V >> t$; the electric defects have an energy of order V and so are of much higher energy than the magnetic defects. Increasing t reduces the energy of the electric defects due to gain in kinetic energy, until this energy vanishes at the transition. However, even a few magnetic defects can strongly influence the winding-number distribution; the number of magnetic defects is roughly $L^2\exp(-\text{const.}/T)$, where "const." is a constant, and so for $T \sim 1/L$, the number of magnetic defects is exponentially suppressed, but for moderate L, the prefactor leads to a substantial effect manifest as slow convergence of the scaling function at small β/L, as shaded in orange in Fig. 3.

We have conclusively established the existence of a phase transition with deconfined fractionalized excitations in QMC simulations of a physical model of lattice bosons. The topological properties of this transition are demonstrated by universal scaling functions of the winding number. This test of the fractionalized charge uses the full winding distribution and may be regarded as a strongly interacting analog of current fluctuation measurements used experimentally to test fractionalized charge, as in (*33*). The full winding distribution can be determined from the dependence of the free energy on flux through the torus and, hence, may be experimentally accessible using methods as in (*34*). It would be interesting to develop these experimental ideas further, perhaps in the context of herbertsmithite (*35*), which may contain a quantum critical point in the XY* universality class (*36*).

One can imagine more general deconfined quantum critical points with other gapped gauge fields, such as a Z_k gauge field. Lattice models for such theories are lacking, but if found, the winding number distribution that we have introduced will present a clear test of the universality class. The fact that topological properties remain important even at the critical point suggests that such systems, despite being gapless, might be useful for quantum computing applications in the future.

References and Notes

1. R. B. Laughlin, *Phys. Rev. Lett.* **50**, 1395 (1983).
2. D. S. Rokhsar, S. A. Kivelson, *Phys. Rev. Lett.* **61**, 2376 (1988).
3. M. Hermele *et al.*, *Phys. Rev. B* **70**, 214437 (2004).
4. Y. Tang, A. W. Sandvik, *Phys. Rev. Lett.* **107**, 157201 (2011).
5. L. Balents, *Nature* **464**, 199 (2010).
6. M. Yamashita *et al.*, *Science* **328**, 1246 (2010).
7. M. S. Block, D. N. Sheng, O. I. Motrunich, M. P. A. Fisher, *Phys. Rev. Lett.* **106**, 157202 (2011).
8. Y. Shimizu, K. Miyagawa, K. Kanoda, M. Maesato, G. Saito, *Phys. Rev. Lett.* **91**, 107001 (2003).
9. Y. Kurosaki, Y. Shimizu, K. Miyagawa, K. Kanoda, G. Saito, *Phys. Rev. Lett.* **95**, 177001 (2005).
10. O. I. Motrunich, *Phys. Rev. B* **72**, 045105 (2005).
11. S.-S. Lee, P. A. Lee, *Phys. Rev. Lett.* **95**, 036403 (2005).
12. In the case of (*6*–*11*), interactions of spinons with a $U(1)$ gauge field probably lead to a non-Fermi liquid.
13. T. Senthil, A. Vishwanath, L. Balents, S. Sachdev, M. P. A. Fisher, *Science* **303**, 1490 (2004).
14. A. W. Sandvik, *Phys. Rev. Lett.* **98**, 227202 (2007).
15. S. V. Isakov, M. B. Hastings, R. G. Melko, *Nat. Phys.* **7**, 772 (2011).
16. L. Balents, M. P. A. Fisher, S. M. Girvin, *Phys. Rev. B* **65**, 224412 (2002).
17. This can be viewed as a topological quantum field theory, with particles 1, $e^{+1/2}$, $e^{-1/2}$, m, ... , where $e^{\pm 1/2}$ denotes the charge on the electric particle, m denotes a magnetic particle, and the ... denote an infinite sequence of additional particles with charge shifted by any integer.
18. A. V. Chubukov, T. Senthil, S. Sachdev, *Phys. Rev. Lett.* **72**, 2089 (1994).
19. A. V. Chubukov, S. Sachdev, T. Senthil, *Nucl. Phys. B* **426**, 601 (1994).
20. T. Senthil, O. Motrunich, *Phys. Rev. B* **66**, 205104 (2002).
21. S. V. Isakov, T. Senthil, Y. B. Kim, *Phys. Rev. B* **72**, 174417 (2005).
22. T. Grover, T. Senthil, *Phys. Rev. B* **81**, 205102 (2010).
23. P. Calabrese, A. Pelissetto, E. Vicari, *Phys. Rev. E* **65**, 046115 (2002).
24. H. G. Ballesteros, L. A. Fernández, V. Martin-Mayor, A. Muñoz Sudupe, *Phys. Lett. B* **387**, 125 (1996).
25. M. Campostrini, M. Hasenbusch, A. Pelissetto, P. Rossi, E. Vicari, *Phys. Rev. B* **63**, 214503 (2001).
26. N. V. Prokof'ev, B. V. Svistunov, I. S. Tupitsyn, *Phys. Lett. A* **238**, 253 (1998).
27. A. Dorneich, M. Troyer, *Phys. Rev. E* **64**, 066701 (2001).
28. O. F. Syljuåsen, A. W. Sandvik, *Phys. Rev. E* **66**, 046701 (2002).
29. A. Del Maestro, I. Affleck, *Phys. Rev. B* **82**, 060515 (2010).
30. Supporting material is available on *Science* Online.
31. S. V. Isakov, A. Paramekanti, Y. B. Kim, *Phys. Rev. B* **76**, 224431 (2007).
32. There is a possibility to have a first-order transition for any finite temperature (for large enough V/t) but a continuous transition at zero temperature without any fine tuning if one has a term in the free energy that makes the transition weakly first-order, and this term is only relevant in two dimensions and irrelevant in 2+1 dimensions. We thank L. Balents for pointing this out.
33. A. Bid, N. Ofek, M. Heiblum, V. Umansky, D. Mahalu, *Phys. Rev. Lett.* **103**, 236802 (2009).
34. N. C. Koshnick, H. Bluhm, M. E. Huber, K. A. Moler, *Science* **318**, 1440 (2007).
35. J. S. Helton *et al.*, *Phys. Rev. Lett.* **98**, 107204 (2007).
36. Y. Huh, L. Fritz, S. Sachdev, *Phys. Rev. B* **81**, 144432 (2010).

Acknowledgments: We thank L. Balents, S. Sachdev, and T. Senthil for enlightening discussions. M.B.H. thanks the Aspen Center for Physics for hospitality. This work has been supported by the Natural Sciences and Engineering Research Council of Canada and the Swiss HP^{2}C initiative. Simulations were performed on the Brutus cluster at ETH Zurich and the computing facilities of SHARCNET.

Supporting Online Material

www.sciencemag.org/cgi/content/full/335/6065/193/DC1
SOM Text
Figs. S1 to S6
References (*37*–*39*)

4 August 2011; accepted 18 November 2011
10.1126/science.1212207

Bistability in Atomic-Scale Antiferromagnets

Sebastian Loth,[1,2]* Susanne Baumann,[1,3] Christopher P. Lutz,[1] D. M. Eigler,[1] Andreas J. Heinrich[1]*

Control of magnetism on the atomic scale is becoming essential as data storage devices are miniaturized. We show that antiferromagnetic nanostructures, composed of just a few Fe atoms on a surface, exhibit two magnetic states, the Néel states, that are stable for hours at low temperature. For the smallest structures, we observed transitions between Néel states due to quantum tunneling of magnetization. We sensed the magnetic states of the designed structures using spin-polarized tunneling and switched between them electrically with nanosecond speed. Tailoring the properties of neighboring antiferromagnetic nanostructures enables a low-temperature demonstration of dense nonvolatile storage of information.

Nanometer-scale ferromagnets are used as magnetic bits to hold information in mass storage devices. Antiferromagnets have been difficult to switch and sense because of their lack of net magnetic moment, but they offer advantages such as insensitivity to magnetic fields.

In ferromagnetic materials, the magnetic moments of the constituent atoms align, yielding a net magnetic moment. The direction of this magnetization can be changed by the application of a magnetic field or by spin-polarized currents (*1*). As magnetic devices shrink toward atomic dimensions, new tools to fabricate and probe them with atomic resolution are emerging (*2*–*4*). These have revealed magnetic bistability in ferromagnetic islands (*5*, *6*) and chains (*7*), having as few as 30 atoms, as well as in metal-organic molecules (*8*–*10*).

[1]IBM Research Division, Almaden Research Center, 650 Harry Road, San Jose, CA 95120, USA. [2]Max Planck Research Group–Dynamics of Nanoelectronic Systems, Centre for Free-Electron Laser Science, Hamburg, and Max Planck Institute for Solid State Research, Stuttgart, Germany. [3]Department of Physics, University of Basel, Klingelbergstrasse 82, 4056 Basel, Switzerland.

*To whom correspondence should be addressed. E-mail: heinrich@almaden.ibm.com (A.J.H.); sebastian.loth@mpsd.cfel.de (S.L.).

Antiferromagnets have neighboring atoms with counteraligned magnetic moments. The absence of a net magnetic moment makes imaging the magnetic structure of antiferromagnets more difficult. Antiferromagnetic (AFM) domains in thin films have been imaged using x-ray scattering (*11*). On the atomic scale, the spin structure of antiferromagnets has been observed by scanning tunneling microscopy (*12*, *13*) and atomic force microscopy (*14*). So far, controlled switching of antiferromagnets has required the help of nearby ferromagnetic domains (*15*), magnetoelectricity (*16*), or optical pulses (*17*). We investigated the role that AFM nanostructures can play as candidates for magnetic storage and spintronic devices.

We assembled AFM nanostructures with a low-temperature scanning tunneling microscope (STM) by placing Fe atoms in a regular pattern on a surface (Fig. 1A). The spins of neighboring Fe atoms couple antiferromagnetically by an exchange interaction with strength J = 1.2 meV (*18*) (fig. S1). The Fe atoms were placed at a binding site on a Cu_2N surface, for which Fe has a large magnetic anisotropy field that aligns its spin to the resulting easy axis (*19*). A magnetic field of up to 6 T was applied in order to make the microscope's tip spin-sensitive by polarizing its magnetic apex (*18*) and in order to test the effect of magnetic field on the nanostructures.

In assemblies of just a few magnetic atoms, the atomic spins often couple to form quantum superposition states (*20*). For AFM coupling, this results in a singlet ground state, characterized by a wave function in which all spins populate opposing spin states equally (*21*). In contrast, we find that isolated AFM structures with as few as six Fe atoms exhibit stable Néel states, in which the spin orientation alternates between neighboring atoms. These states can be well described by the classical Ising model (*22*), in which the spins always point along one axis. Spin-polarized STM images of a linear eight-atom chain (Fig. 1, B to E) can clearly distinguish the two Néel states. The spin-polarized STM tip forms a magnetic tunnel junction in which the conductance alternates between high (parallel alignment of tip and sample spins) and low (antiparallel alignment) as the tip passes from atom to atom along the chain (*12*, *13*, *23*). Identical chains built from Mn atoms do not show the magnetic bistability and do not exhibit a spin-polarized contrast along the chain (fig. S2). A key difference between Fe and Mn chains is the strength of the magnetic anisotropy, which is ~50 times stronger in Fe than in Mn on this surface (*19*). The strong easy-axis anisotropy of Fe evidently stabilizes the two Néel states as observable magnetic states.

The stability of the magnetic states was not affected by imaging them using an applied voltage of <2 mV, but voltages in excess of ~7 mV caused switching. To intentionally switch the magnetic state of the entire antiferromagnet, the tip was held stationary over any Fe atom of the structure, and tunnel current was passed through it at >7 mV until a step, indicating a change in magnetic state, was observed in the current (Fig. 2A). Subsequently, the voltage was lowered to prevent further switching. Near the 7-mV switching threshold, the Néel state in which the spin of the atom

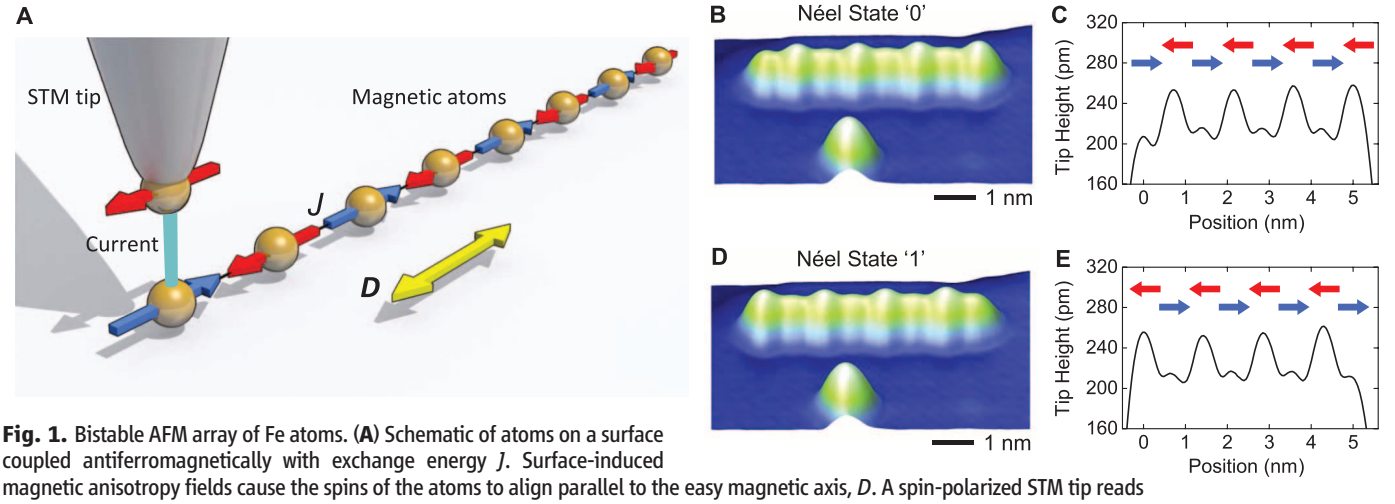

Fig. 1. Bistable AFM array of Fe atoms. (**A**) Schematic of atoms on a surface coupled antiferromagnetically with exchange energy J. Surface-induced magnetic anisotropy fields cause the spins of the atoms to align parallel to the easy magnetic axis, D. A spin-polarized STM tip reads the magnetic state of the structure by magnetoresistive tunneling. A magnetic field applied parallel to D polarizes the tip. (**B**) Spin-polarized STM image of a linear chain of eight Fe atoms assembled on a Cu_2N overlayer on Cu(100). This is a constant-current image using 2 mV and 1 pA. Spins are in Néel state 0. (**C**) Section through center of chain in (B) with the spin orientation of each Fe atom indicated by colored arrows. (**D** and **E**) Same as (B) and (C) but in Néel state 1.

under the tip is aligned with the magnetic field was occupied ~90% of the time (Fig. 2A). This directionality offers a path toward controlled directional switching. An alternative process to switch AFM structures, the use of spin transfer torque (*1*, *5*), has previously been proposed (*24*, *25*).

We found that the state switched most readily when the tip was placed over an end atom of a chain. The switching between magnetic states was found to occur stochastically, with a uniform probability per unit of time, which we characterized by means of a switching rate (*18*) (fig. S3). This rate increased rapidly when the tunneling current was increased.

With increasing voltage, the switching rate exceeded the bandwidth of the STM's current amplifier, so a pulsed-voltage scheme was used to determine the fast switching rates (Fig. 2B). Submicrosecond pulses were applied to the junction (*26*), and each pulse was followed by a low-voltage window in which the resulting magnetic state was detected (*18*). The switching rate increased faster than in proportion to the voltage up the highest voltage tested, with switching times of ~20 ns at 0.5 V (Fig. 2C). This demonstrates electrical switching of the AFM nanostructures at high speeds and femtojoule energies.

To investigate the stability of the Néel states, we examined the thermal switching rates of linear chains of Fe atoms with varying length, (1×*n*), and arrays of two coupled chains, (2×*n*) (Fig. 3). All structures containing eight or more atoms were found to be stable at the lowest temperature, 0.5 K. Spontaneous flipping between the two Néel states sets in with increasing temperature. Structures with more atoms remain stable to higher temperatures (Fig. 3, A to C) (*6*, *27*).

Above ~5 K, the switching rates of the (1×6), (1×8), and (2×6) arrays follow the Arrhenius law with comparable spin reversal barriers, $E_B \sim 7$ to 12 meV, and exponential prefactors, $\rho_0 \sim 10^8$ s^{-1} (Fig. 3E and table S1). This prefactor falls in the typical range, 10^7 to 10^{14}, found for ferromagnetic nanoparticles (*5*, *28*) and magnetic molecules (*29*). The values for E_B are comparable to the threshold for voltage-induced switching (Fig. 2C) and to the energy $2S^2J = 9.6$ meV ($S = 2$ for Fe) needed to create a single Ising domain wall within one of the chains by flipping one or more consecutive spins at the end of a chain (*22*). This indicates that current- and temperature-induced switching between the two Néel states is accomplished by propagating domain walls along each chain.

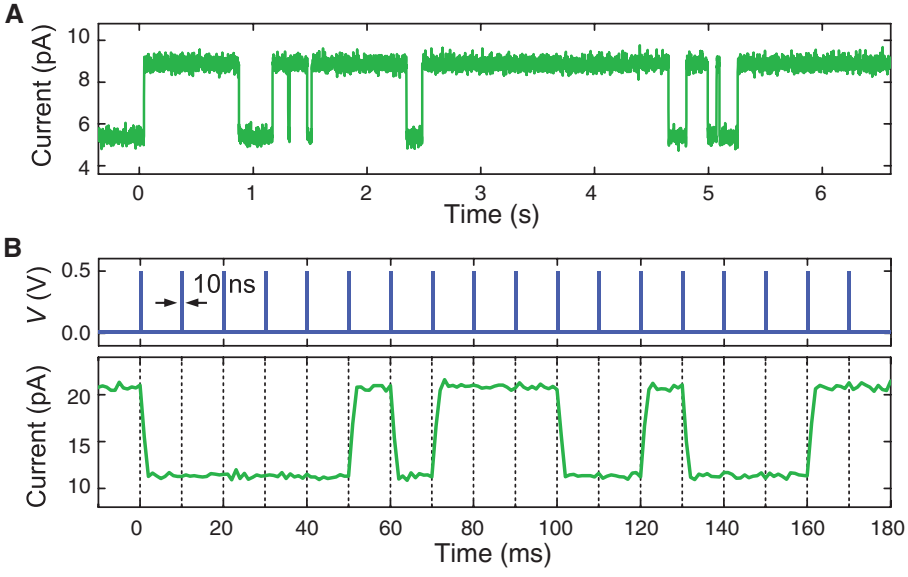

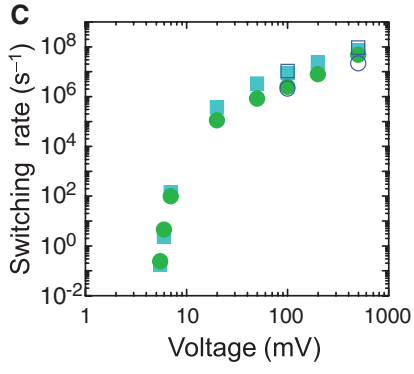

Fig. 2. Switching between Néel states induced by tunneling electrons. (**A**) Tunnel current as a function of time at 7 mV. The tip is placed over an end atom of a (1×8) Fe chain. The chain switches its magnetic state about twice per second. (**B**) Same as (A) but with pulsed voltage *V* to demonstrate fast switching. Pulses of 0.5 V and 10-ns duration were applied every 10 ms (at dashed vertical lines). Between pulses, only 2 mV was applied (below the threshold for switching) to sense the magnetic state. (**C**) Switching rate versus sample voltage *V*. Voltage was applied continuously for $|V| < 10$ mV and as 5- to 1000-ns pulses for $|V| > 10$ mV. Green circles indicate transitions from low to high current; blue squares indicate high to low. Open symbols were recorded at negative sample voltage. Magnetic field 1 T and temperature 0.5 K for all panels. Tip-sample distance was set at 20 pA and 2 mV for (B) and (C).

Below ~5 K, the switching rates of the (1×6) and (1×8) chains become independent of temperature. Such behavior is consistent with quantum tunneling of magnetization (*30*), which is typically observed in few-atom molecular magnets (*8*, *9*) and also occurs in magnetic nanoparticles (*28*). Here, it causes the AFM nanostructures to evolve between the two Néel states, thus limiting their stability even though thermal switching is frozen out. Comparison of the structures of Fig. 3E highlights two avenues to reduce quantum tunneling: First, through increasing the chain length. The addition of two atoms, from (1×6) to (1×8), reduced the tunneling rate 1000-fold. Second, through the coupling of two chains, from (1×6) to (2×6) as shown in Fig. 3D. Even though the spin coupling between chains of $J' = 0.03$ meV per atom (*18*) is much weaker than the exchange coupling within a chain, *J*, it suppresses tunneling markedly. The large difference in the strength of *J* and *J′* is linked to the Cu_2N surface's crystal structure and is evidence of a superexchange-mediated interaction in the Cu_2N molecular network (*18*–*20*) (fig. S1).

A different manifestation of quantum tunneling of magnetization can be found in the (2×4) array, which has a much reduced exponential prefactor and energy barrier, 1.5 meV. This energy is comparable to $4 \times 2S^2J' = 1.1$ meV, the energy required to frustrate the weak coupling between the two short chains. This low barrier and the much-reduced exponential prefactor of only $\rho_0 = 5 \times 10^3$ s^{-1}, indicate a reversal process in which one entire chain switches in a thermally assisted tunneling process (*29*).

The thermal switching rates were found to be independent of magnetic field (fig. S4), and both Néel states were occupied for equal amounts of time (fig. S3), showing that these AFM arrays are fully spin-compensated. The AFM nanostructures are magnetically stable even in the absence of an external magnetic field (fig. S6).

The (2×6) array is highly stable at low temperatures, where switching was observed so rarely that no tunneling rate could be derived. We experimentally determined a lower limit for the stability of these arrays of less than one switching event per 17 hours at 0.5 K.

A challenge to miniaturizing the bits in ferromagnetic storage media is the interaction of neighboring bits because of their dipolar magnetic fields (*31*). This would not be present in AFM storage media. At atomic dimensions, however, exchange interactions can still cause undesired coupling between neighboring bits (*27*). Figure 4A shows an AFM byte, a dense packing of eight (2×6) Fe arrays, with each array representing one bit of information. The structure was engineered to have reduced bit-to-bit exchange interactions. Neighboring bits were staggered in a way that places the atoms of any given bit symmetrically between the atoms of the neighboring bits, resulting in a near-perfect cancellation of bit-to-bit exchange couplings through geometric frustration (Fig. 4B) (*23*).

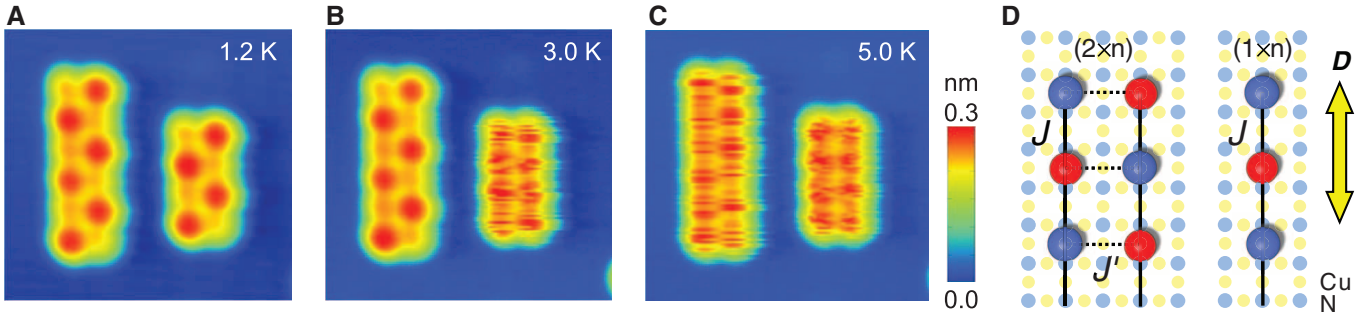

Fig. 3. Thermal stability of AFM arrays. (**A** to **C**) STM images of (2×6) and (2×4) arrays of Fe atoms. (A) 1.2 K. Both arrays have stable Néel states. (B) 3.0 K. The smaller array switched rapidly during the image. (C) 5.0 K. Both arrays switched rapidly. Image size, 7.7 × 7.7 nm. Image was taken at 2 mV and 3 pA, and image acquisition time was 52 s. (**D**) Schematic of the atomic positions of Fe and Cu_2N substrate atoms in (2×*n*) and (1×*n*) arrays. Cu atoms, yellow; N atoms, light blue. Ball colors depict the spin alignment of one Néel state, with red being parallel and blue antiparallel with the tip's spin. (**E**) Arrhenius plot of the switching rates for the arrays of (A) and a (1×8) and (1×6) chain (fig. S5). The determination of switching rates is explained in fig. S3. Magnetic field was 3 T. Fig. S4 shows comparison to a 1-T field. Fit parameters are given in table S1.

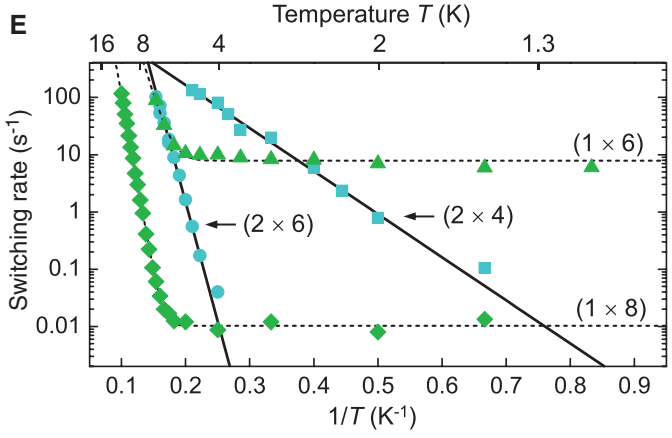

Fig. 4. Ultradense AFM data storage. (**A**) Non–spin-polarized STM image, 24 × 8 nm, of eight (2×6) arrays assembled from Fe atoms. (**B**) Schematic of the bits in (A), with colors as in Fig. 3D. J_b and J_b': pairwise canceling exchange couplings between atoms in neighboring bits. (**C**) Information storage in a magnetic byte. A color-coded difference between spin-polarized and spin-averaged images is shown, with red corresponding to higher tip height and blue to lower tip height in the spin-polarized image. (Top) All eight bits in logic 1 state (as defined by the spin orientation of the top two Fe atoms in each bit). (Middle) Alternating pattern of 1 and 0. (Bottom) All 0. More bit patterns are shown in fig. S7.

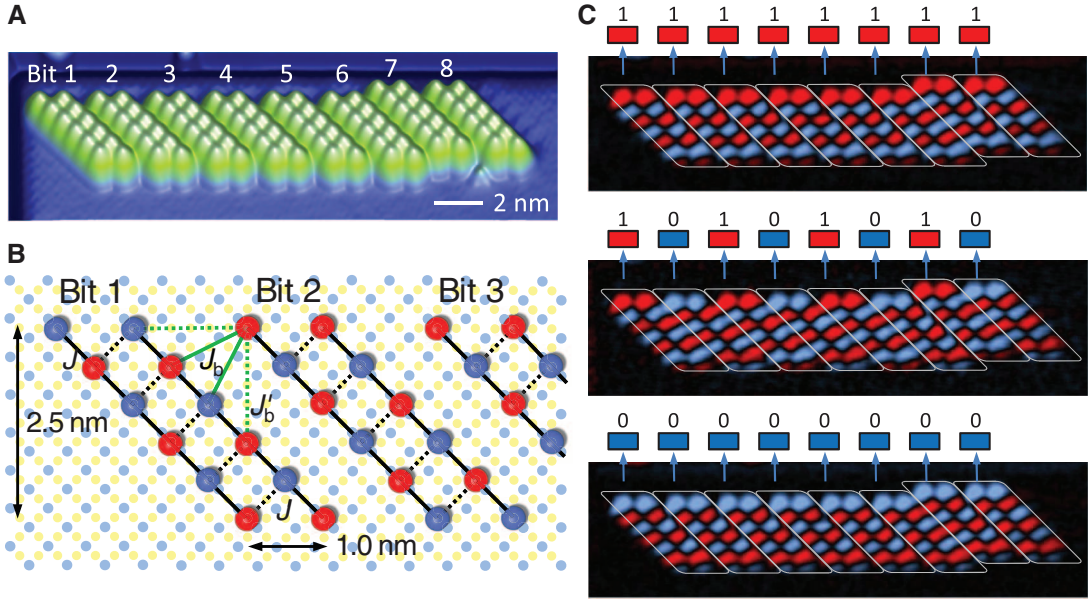

Each of the eight bits shown in Fig. 4A can be switched without perturbing the state of the other bits. Figure 4C and fig. S7 show short sequences of test arrangements written into the byte. These configurations are stable over a time scale of hours, and readout was achieved by topographic imaging. Each bit occupies an area of only 9 nm^2.

The arrangement of Fe atoms that form each bit in the byte is a variant on the (2×6) array (compare Fig. 3D and Fig. 4B), in which the ends of each bit are beveled to give the endmost atoms of each bit the same spin orientation. This provides clarity in viewing the state and shows that the exact arrangement of atoms is not critical for magnetic stability.

Our results demonstrate that switchable nanoscale antiferromagnets are candidates for future memory, storage, and spintronic applications.

References and Notes

1. C. Chappert, A. Fert, F. N. Van Dau, *Nat. Mater.* **6**, 813 (2007).
2. R. Wiesendanger, H.-J. Güntherodt, G. Güntherodt, R. J. Gambino, R. Ruf, *Phys. Rev. Lett.* **65**, 247 (1990).
3. J. W. Lau, J. M. Shaw, *J. Phys. D Appl. Phys.* **44**, 303001 (2011).
4. J. V. Barth, G. Costantini, K. Kern, *Nature* **437**, 671 (2005).
5. G. Herzog, S. Krause, R. Wiesendanger, *Appl. Phys. Lett.* **96**, 102505 (2010).
6. S. Krause *et al.*, *Phys. Rev. Lett.* **103**, 127202 (2009).
7. P. Gambardella *et al.*, *Nature* **416**, 301 (2002).
8. J. D. Rinehart, M. Fang, W. J. Evans, J. R. Long, *Nat. Chem.* **3**, 538 (2011).
9. L. Thomas *et al.*, *Nature* **383**, 145 (1996).
10. J. R. Friedman, M. P. Sarachik, J. Tejada, R. Ziolo, *Phys. Rev. Lett.* **76**, 3830 (1996).
11. F. Nolting *et al.*, *Nature* **405**, 767 (2000).
12. S. Heinze *et al.*, *Science* **288**, 1805 (2000).
13. C. L. Gao, W. Wulfhekel, J. Kirschner, *Phys. Rev. Lett.* **101**, 267205 (2008).
14. U. Kaiser, A. Schwarz, R. Wiesendanger, *Nature* **446**, 522 (2007).

15. I. E. T. Iben, in *31st EOS/ESD Symposium* (ESD Association, Rome, NY, 2009), p. 1.
16. X. Chen, A. Hochstrat, P. Borisov, W. Kleemann, *Appl. Phys. Lett.* **89**, 202508 (2006).
17. A. V. Kimel *et al.*, *Nat. Phys.* **5**, 727 (2009).
18. Supporting material is available on *Science* Online.
19. C. F. Hirjibehedin *et al.*, *Science* **317**, 1199 (2007).
20. C. F. Hirjibehedin, C. P. Lutz, A. J. Heinrich, *Science* **312**, 1021 (2006).
21. O. Waldmann, T. Guidi, S. Carretta, C. Mondelli, A. L. Dearden, *Phys. Rev. Lett.* **91**, 237202 (2003).
22. I. Bose, A. K. Pal, *Eur. Phys. J. B* **77**, 139 (2010).
23. A. A. Khajetoorians, J. Wiebe, B. Chilian, R. Wiesendanger, *Science* **332**, 1062 (2011).
24. P. M. Haney, R. A. Duine, A. S. Núñez, A. H. MacDonald, *J. Magn. Magn. Mater.* **320**, 1300 (2008).
25. S. Urazhdin, N. Anthony, *Phys. Rev. Lett.* **99**, 046602 (2007).
26. S. Loth, M. Etzkorn, C. P. Lutz, D. M. Eigler, A. J. Heinrich, *Science* **329**, 1628 (2010).
27. S. Mørup, D. E. Madsen, C. Frandsen, C. R. H. Bahl, M. F. Hansen, *J. Phys. Condens. Matter* **19**, 213202 (2007).
28. W. Wernsdorfer *et al.*, *Phys. Rev. Lett.* **79**, 4014 (1997).
29. D. Gatteschi, R. Sessoli, J. Villain, *Molecular Nanomagnets* (Oxford Univ. Press, New York, 2006).
30. B. Barbara, E. M. Chudnovsky, *Phys. Lett. A* **145**, 205 (1990).
31. E. E. Fullerton *et al.*, *Appl. Phys. Lett.* **77**, 3806 (2000).

Acknowledgments: We acknowledge B. Melior for expert technical assistance. S.L., C.P.L., and A.J.H. thank the Office of Naval Research for financial support. A patent application regarding information storage in antiferromagnetic nanostructures was filed with the U.S. Patent and Trademark Office.

Supporting Online Material

www.sciencemag.org/cgi/content/full/335/6065/196/DC1
Materials and Methods
Figs. S1 to S7
Table S1
References (*32*–*38*)

19 September 2011; accepted 28 November 2011
10.1126/science.1214131

Composites Reinforced in Three Dimensions by Using Low Magnetic Fields

Randall M. Erb, Rafael Libanori, Nuria Rothfuchs, André R. Studart*

The orientation and distribution of reinforcing particles in artificial composites are key to enable effective reinforcement of the material in mechanically loaded directions, but remain poor if compared to the distinctive architectures present in natural structural composites such as teeth, bone, and seashells. We show that micrometer-sized reinforcing particles coated with minimal concentrations of superparamagnetic nanoparticles (0.01 to 1 volume percent) can be controlled by using ultralow magnetic fields (1 to 10 milliteslas) to produce synthetic composites with tuned three-dimensional orientation and distribution of reinforcements. A variety of structures can be achieved with this simple method, leading to composites with tailored local reinforcement, wear resistance, and shape memory effects.

The widespread use and increasing relevance of composite materials are primarily due to their higher strength-to-weight ratio (specific strength) compared to metals, and higher toughness (flaw tolerance) compared to ceramics. Polymer-matrix composites are predominantly assembled with ceramic, metal, or polymeric one-dimensional (1D) reinforcement such as glass, steel, aramide (Kevlar), or carbon long fibers. These fibers are typically tens of micrometers in diameter and increase the strength and stiffness along the long axis of the reinforcement because of the transfer of stress across the reinforcement-polymer interfaces parallel with the load. (*1*) However, 1D reinforcement makes manufactured materials weak in the other two dimensions, which can be partially overcome through laminating 1D layers at varied angles, weaving fibers into 2D arrays, by using 2D reinforcement particles such as platelets or synthesizing lamellar structures (*1*–*9*).

Few 3D reinforcement solutions have been proposed to reinforce artificial composites, including the insertion of out-of-plane fibers by mechanical punching (*10*); the formation of special fiber arrays by using textile processes like weaving, braiding, stitching, and knitting (*11*); and the growth of aligned carbon nanotubes on the surface of the reinforcing woven fibers (*12*, *13*). Three-dimensional reinforcement is also present in composites containing randomly oriented short fibers or platelets. However, these approaches either lead to a decrease in in-plane mechanical properties or do not allow for deliberate control over the distribution and 3D orientation of high concentrations of reinforcing nano- and microparticles. The lack of controlled reinforcement in the third dimension makes manufactured composites susceptible to impact damage (*2*, *14*), wear (*15*), longitudinal microbuckling of fibers (*16*), delamination (*2*), and long-term fatigue (*13*, *17*).

Structural biological composites tackle this problem by accurately controlling the orientation of anisotropic nano- and micro-sized building blocks so as to reinforce the material in specific directions to multidirectional external loads (*18*–*20*). Examples include the spiral twisting of mineralized collagen fibrils in bone (*21*); the out-of-plane oriented calcite prisms and in-plane oriented aragonite platelets in the outer and inner layers of seashells, respectively (*22*); and the out-of-plane oriented hydroxyapatite prisms and in-plane oriented mineralized collagen fibrils in tooth enamel and dentin, respectively (*23*). Capturing some of the design principles underlying the exquisite architecture of such biological materials would allow us to overcome many of the mechanical limitations of current artificial composites.

We propose a strategy to obtain microstructured artificial composites exhibiting 3D architectures and enhanced mechanical behavior. The approach relies on the application of external magnetic fields and field gradients to align and position anisotropic reinforcing microparticles within the composite matrix. As typical reinforcing particles are often diamagnetic, requiring extremely high magnetic fields for alignment (~1 T) (*24*), we first coat them with superparamagnetic nanoparticles to make them more responsive to magnetic fields. Though a similar method has been previously used (*25*) to align carbon nanotubes with fields in the range 0.2 to 1 T, we have discovered through experiments and theoretical energy models that using the right geometry of reinforcement particles leads to an ultrahigh magnetic response (UHMR). Indeed, the magnetic field required to align the reinforcement particles can be reduced to the value of 0.8 mT. This alignment field is only an order of magnitude above Earth's natural magnetic field (~0.05 mT) and is orders of magnitude below the magnetic field of rare-earth magnets (~200 mT), common solenoids (~20 mT), and even standard refrigerator magnets (~10 mT).

To determine the optimum particle size that will show an UHMR effect, we theoretically predict the minimum magnetic field required for alignment, H_{min}, for different sizes, aspect ratios, and geometries of reinforcing elements. The dependence of H_{min} on the size of nonmagnetic platelets and rods coated with magnetic material can be estimated by computing the difference in magnetic (U_m) and gravitational (U_g) energies of the system as compared to the internal thermal energy (k_BT, where k_B is the Boltzmann factor and T is temperature) that serves to randomize alignment. The magnetic energy U_m is calculated with an ellipsoidal shell model that reflects that the slight amount of magnetic material lies only in an outer layer coating the reinforcing element (SOM text). The magnetic energy is dependent upon the particle's orientation with respect to the magnetic field, ψ, and is smallest when the long axis of the particle is parallel with the applied magnetic field ($\psi = 0°$). Further, the gravitational energy of a particle resting on a horizontal surface is also dependent upon the orientation with

Complex Materials, Department of Materials, ETH Zurich, 8093 Zurich, Switzerland.

*To whom correspondence should be addressed. E-mail: andre.studart@mat.ethz.ch

respect to the surface, θ, and is smallest when the particle's long axis is parallel with the surface (θ = 0°).

To estimate the minimum magnetic field required for alignment, we describe the system in terms of a canonical partition function Z, with the out-of-plane alignment as one of the possible energy states. We consider the case of out-of-plane magnetic fields, for which ψ = 90° –θ. The effect of the particle characteristics on H_{min} is investigated by computing the magnetic field strength that ensures that most UHMR particles in suspension exhibit a reasonably good alignment—i.e., angles within the range 75° to 90°. The probability $P_{75–90}$ that 90% of the UHMR particles are within this range can be determined by dividing the Boltzmann factor of this out-of-plane state by the partition function as follows:

$$P_{75°–90°} = \int_{75°}^{90°} e^{[U_m(H_{min},\psi) - U_g(\theta)]/k_B T} d\theta \Big/ Z = 0.9$$
$$\text{where } Z = \int_{0°}^{90°} e^{[U_m(H_{min},\psi) - U_g(\theta)]/k_B T} d\theta \quad (1)$$

Here, Z is the sum of the Boltzmann factors of all possible states of orientation of the particles. The equations used to calculate the potential energies U_m and U_g are available online (SOM text). To simplify the analysis and obtain a first approximation for H_{min}, we neglect the contributions of orientational and packing entropy to the free energy of the system (*26*). This simplification is partly justified in that packing entropy is only relevant for particle concentrations higher than those used in most of our experiments (14.2 vol % platelets, SOM text).

Our model predictions indicate that the alignment of nonmagnetic platelets and rods of 5 and 10 μm in length, respectively, with modest surface coatings of iron oxide nanoparticles (~0.5 vol %) requires fields that are orders of magnitude lower than for particles with different geometries (Fig. 1, A and C). Thermal and gravitational energies dominate for particles smaller and larger than a few micrometers, respectively, which substantially increases the field required for alignment.

To verify the theoretical analysis, we apply magnetic fields to surface-magnetized platelets and rods with average size within the optimum range required for alignment. The magnetized surface coating is formed upon addition of the reinforcing particles to an aqueous suspension of 12-nm iron oxide nanoparticles with oppositely charged surface at a specific pH. Under these conditions, adsorption is driven through electrostatic interactions and is further enhanced by short-range van der Waals attraction, eventually becoming irreversible. We investigate both 7.5-μm-long, 200-nm-thick alumina platelets (Alusion, Antaria, Bentley, Australia) and 10-μm-long, 1-μm-thick calcium sulfate hemihydrate rods that exhibit, respectively, positive and negative surface charge in water at pH = 7 (*27*). To coat such reinforcing elements, we add 1 vol % particles (platelets or rods) in aqueous suspensions of 0.0052 vol % oppositely charged iron oxide nanoparticle suspensions (anionic EMG-705 or cationic EMG-605, Ferrotec, Germany) until complete adsorption occurs (Fig. 1E).

The magnetic field required to align the surface-magnetized platelets and rods agrees very well with the theoretical estimates (Fig. 1, B and D, and movie S1), confirming that it is possible to orient reinforcing elements of a few micrometers in length by using very low magnetic fields. Changing the initial concentration of iron oxide nanoparticles in the suspension controls the magnetization of the reinforcing particles. We have found that the selection of anisotropic particles within the optimum size range enables minimum use of the iron oxide nanoparticles, down to even a few hundred parts per million (0.01 vol %) of magnetic particles with respect to the reinforcing element. Such a concentration of magnetic particles requires a field of 30 mT (Fig. 1F).

This UHMR effect is favored by the 2D confinement of magnetic nanoparticles on the surface of the reinforcing particles. The field required for alignment of the hypothetical case in which magnetic particles are homogeneously distributed throughout the entire volume of the reinforcing element is 69% larger than if the magnetic nanoparticles are only on the surface (SOM text). The confinement of magnetic nanoparticles to increase the magnetic response of anisotropic objects is in fact also used by magnetotactic bacteria to align themselves along Earth's magnetic field to find regions in the ocean with low oxygen concentrations (*28*).

The ultrahigh magnetic response of the coated anisotropic particles is of general interest in applications that require combined spatial and orientational control of suspended particles (*29*). We exploit this effect to orient reinforcing particles in a polymer matrix and thus obtain artificial composites exhibiting distinctive mechanical reinforcing and shape memory effects.

Reinforced composites with controlled orientation of reinforcements are prepared by dispersing

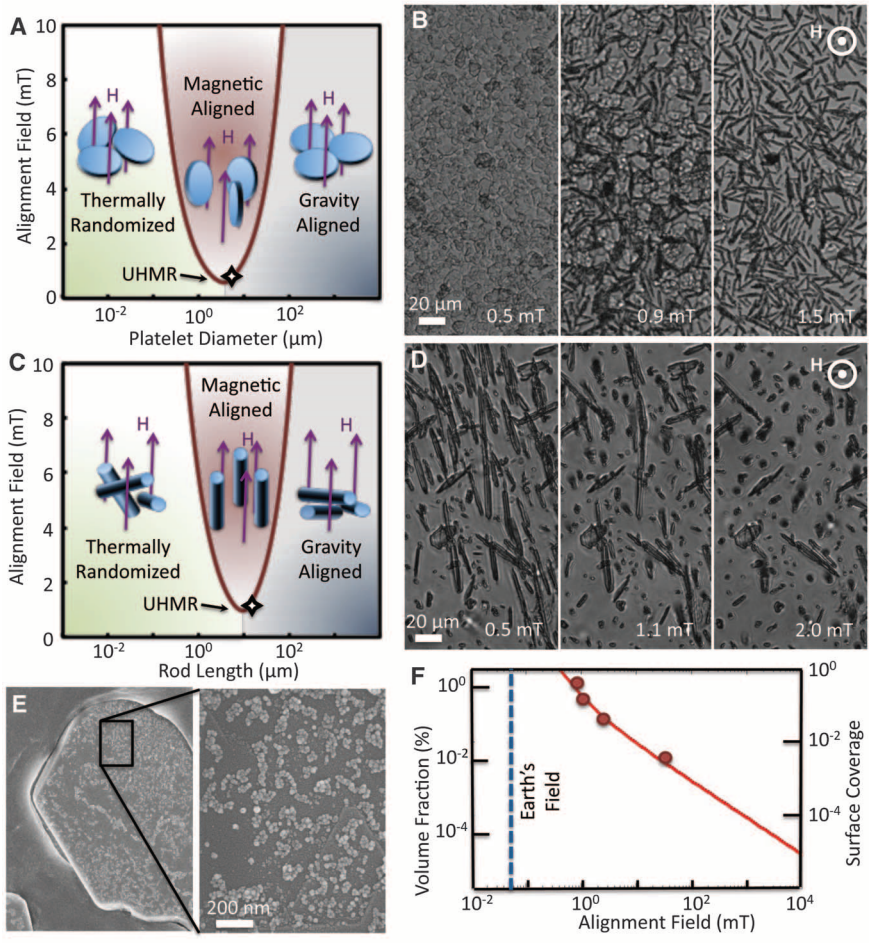

Fig. 1. Ultrahigh magnetic response (UHMR) of surface-magnetized rods and platelets. The theoretical minimum alignment field, H_{min}, is plotted for (**A**) platelets (aspect ratio, s = 37) and (**C**) rods (s = 30) with a surface coating of magnetic nanoparticles of 0.5 vol %. Specific gravity values of 3.98 and 2.5 g/cm^3 were used in the calculations, consistent with the experimentally studied alumina platelets and calcium sulfate rods, respectively. Iron oxide–coated (**B**) alumina platelets and (**D**) calcium sulfate hemihydrate rods with optimum sizes exhibit an ultrahigh magnetic response, aligning with the extremely low magnetic fields predicted by the theory. (**E**) Example of 0.5 vol % (13% surface coverage) of iron oxide nanoparticles on an alumina platelet that leads to alignment at 1 mT consistent with theory in (**F**).

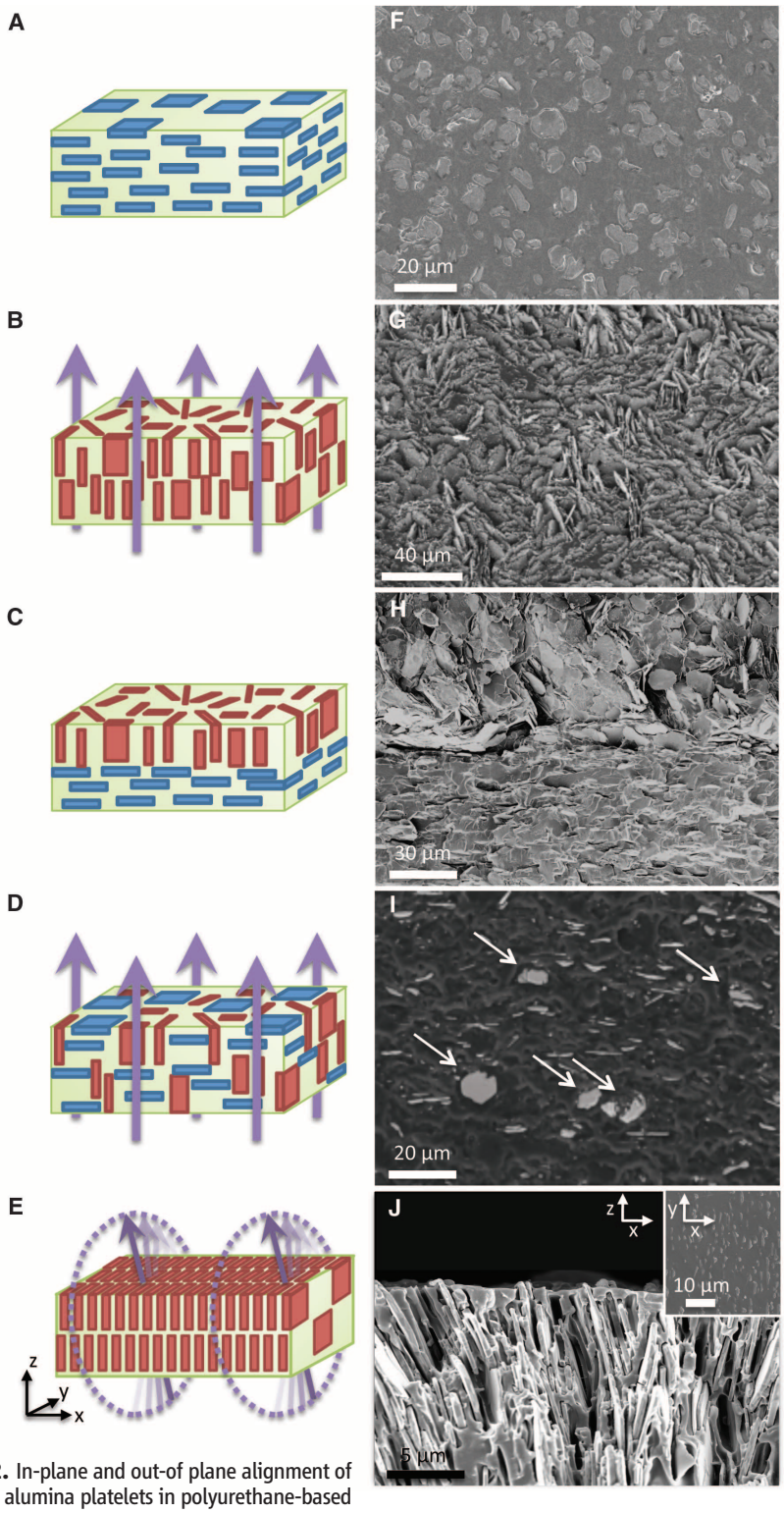

Fig. 2. In-plane and out-of plane alignment of UHMR alumina platelets in polyurethane-based composites. (**A** and **B**) Schematic and (**F** and **G**) top-view scanning electron micrographs (SEMs) of in-plane and out-of-plane reinforced composites (20 vol % Al_2O_3 in polyurethane), made without and with an out-of-plane magnetic field, respectively. (**C**) Schematic and (**H**) SEM of cross section of laminated layers of in- and out-of-plane reinforced composites (20 vol% Al_2O_3 in polyurethane). (**D**) Schematic and (**I**) SEM of cross section of mixed alignment with 5 vol % highly magnetized (1 wt % Fe_3O_4/Al_2O_3) and 5 vol % weakly magnetized (0.1 wt % Fe_3O_4/Al_2O_3) alumina platelets in polyurethane produced with sequential magnetic field applications. Arrows indicate platelets in the second orientation direction. (**E**) Schematic and (**J**) SEM of cross section of an alumina-polyurethane composite formed under rotating magnetic field that allows for ultrahigh packing fractions. Inset shows top view of composite.

UHMR anisotropic particles in a fluid, aligning and positioning them with a magnetic field, and finally consolidating the fluid to fix the oriented structure. Consolidation may occur through solvent evaporation if the fluid is a polymer solution, through temperature- or light-induced reactions if the fluid is a monomeric solution, or by simply cooling a molten polymeric matrix. We find that the higher viscosity of some of the polymer solutions and resins used for composite fabrication slows the orientation process but does not change the minimum magnetic field required for alignment.

Examples of composites obtained by applying linear, uniform magnetic fields to fluid suspensions containing magnetite-coated alumina platelets, thermoplastic polyurethane elastomer (PU, Elastollan C 64 D 53, BASF), and polyvinylpyrrolidone (PVP, Sigma-Aldrich, molecular mass 360,000 g/mol) are shown in Fig. 2, A, B, F, and G. In these examples, 2.4 g of platelets, 2.2 g of polyurethane, and 0.75 g of polyvinylpirrolidone were suspended or dissolved in 150 ml of dimethylformamide (DMF, Sigma-Aldrich), and the end composites contained 60 vol % PU, 20 vol% PVP, and 20 vol % alumina. The orientation of the UHMR particles in the consolidated matrices directly reflects the direction of the magnetic field applied. Magnetic alignment and fixation of the UHMR platelets were also possible by using epoxy and acrylate-based resins as polymeric matrix.

In addition to homogeneously reinforced polymers, multilayer composites are easily obtained by laminating together layers of reinforced polymer with specific orientations (Fig. 2, C and H). The resulting composites exhibit an external layer with out-of-plane oriented platelets and an internal layer with in-plane oriented platelets. This should lead to a highly structured artificial composite displaying the unusual and often-desired combination of hardness and wear resistance in the outer layer and strength and toughness in the inner layer by using the same basic building blocks. Single-batch synthesis composites with this architecture can also be prepared simply by mixing reinforcing particles with different magnetic nanoparticle coverage during processing and then applying a combination of magnetic fields. To demonstrate this, we added 4.025 g each of platelets with 13% and 1% surface coverage of iron oxide to 20 g polyurethane (RoPlasthan 2020R, resin-to-hardener weight ratio 3:1) and poured the mixture into a polyethylene mold. The sample was then subjected to an 80-mT horizontal field for 5 min followed by a 10-mT vertical field for 10 min. The resulting structure shows platelets in both configurations, depending upon their surface coverage (Fig. 2, D and I). Further, because of the low concentration of iron oxide nanoparticles within the composite and the slight permeability of water through the polyurethane matrix, in this system it is even possible to completely remove magnetic iron oxide nanoparticles for applications that forbid even this slight mag-

netic content. This can be accomplished by submerging the consolidated material in a permeating phosphoric acid aqueous solution to completely dissolve the iron oxide nanoparticles without affecting the orientation of reinforcing particles (fig. S3) (*27*).

Although the alignment of platelets by using linear, static magnetic fields allows for the preparation of composites with unusual structures and properties, the concentration of platelets aligned in the out-of-plane direction is limited to about 20 vol % due to steric hindrance effects resulting from the lack of orientational control over the second axis of platelets. This issue can be circumvented by using rotating, linear magnetic fields. A rotating field in the *Y-Z* plane will align the reinforcement platelets along this plane due to energy considerations, pinning two degrees of orientational freedom (Fig. 2, E and J). This alignment is contingent upon the frequency of the rotating field being high enough to prevent synchronous rolling of misaligned platelets. Through such biaxial alignment of the reinforcement platelets, it is possible to reach very high concentrations of out-of-plane aligned platelets, even 50 vol %.

Control of the orientation of reinforcing particles enables tailoring of properties in specific directions. We investigated the effect of the orientation of reinforcing particles on the mechanical behavior of homogeneously reinforced polymers by measuring the tensile mechanical properties of specimens containing reinforcement aligned parallel or perpendicular to the applied load (Fig. 3A). The reinforced sample containing 20 vol % parallel-aligned platelets exhibits on average 63% and 86% higher yield strength as compared to the pure matrix and the perpendicular-aligned platelets, respectively. Likewise, the average elastic modulus of the composites with parallel-oriented platelets was 2.8-fold higher as compared to the pure polyurethane matrix, whereas a moderate increase is observed if compared with composites having perpendicular-aligned platelets (table S1 and SOM text).

We use simple rules of mixtures (*5*) to obtain a quantitative relation between the aligned architecture and the resulting mechanical properties of the composites. Assuming pull-out mode of fracture, the yield strength, σ_c, of the composite is given by

$$\sigma_c = \phi_p \frac{\tau_y s}{2} + (1 - \phi_p)\sigma_m \qquad (2)$$

where τ_y is the shear strength of the lesser of either the polymer matrix or the platelet/polymer interface, s is the platelet aspect ratio, σ_m is the yield tensile strength of the matrix, and ϕ_p is the volume fraction of platelets. Taking σ_m = 28.6 MPa (Fig. 3A), we find that the yield strength of the composite with in-line reinforcement (σ_c = 46.8 MPa) can be accurately described by Eq. 2 if the value of τ_y is equal to 6.5 MPa. Such τ_y is lower than the value of 14.3 MPa expected for the shear strength of the polymer matrix (σ_m /2), suggesting that fracture in this case is controlled by the weaker platelet/polymer interface. This indicates that further reinforcement with parallel-aligned platelets is possible by optimizing the platelet/polymer interfacial bonding in this system.

In addition to the tensile properties, hardness values were measured for homogeneous composites

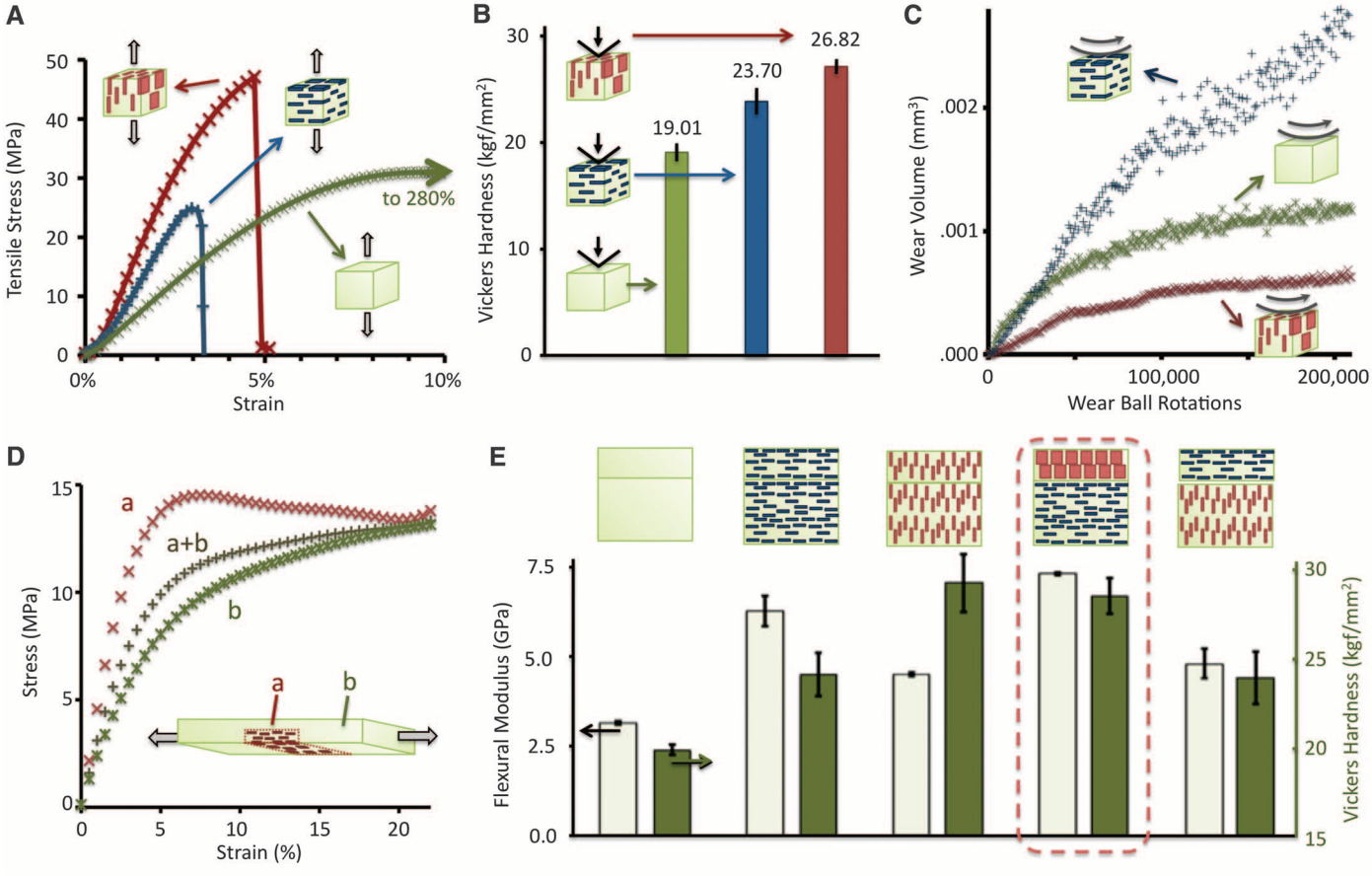

Fig. 3. Enhanced mechanical properties of composites containing aligned UHMR platelets. (**A**) Representative increased tensile strength for polyurethane-based polymers with 20 vol % Al_2O_3 platelets parallel with applied force (red) versus perpendicular (blue) and nonreinforced (green) samples. (**B**) Increased hardness for reinforced methacrylate resins with 10 vol % Al_2O_3 platelets parallel to the applied load versus perpendicular and nonreinforced samples. (**C**) Increased wear resistance for acrylate-based composite films of dental resins with 1 vol % added out-of-plane aligned Al_2O_3 reinforcement. (**D**) Localized stiffening in a polyurethane film by using magnetically induced spatial gradients in the 3 vol % Al_2O_3 particle reinforcement. (**E**) Flexural modulus and out-of-plane hardness of bilayer rectangular bars (30 mm by 5 mm by 3 mm) with different combinations of reinforcement orientation. The schematic drawings show the cross sections of the tested structures, with the bottom layer corresponding to the region subjected to tension in three-point bending and the top layer corresponding to the region subjected to out-of-plane hardness measurements.

with 10 vol % UHMR platelets in methacrylate-based composites. Samples with reinforcement particles oriented parallel to the applied load showed increased hardness compared to perpendicular reinforcement and nonreinforced samples (Fig. 3B). Composite films containing alumina platelets aligned out-of-plane also exhibit outstanding wear resistance. Wear was measured by sliding a zirconia ball subjected to a normal load of 1.98 N over acrylate-based composite films with double deionized water as lubricating medium (*27*). A commercial acrylate-based composite dental resin (Clearfil AP-X, Kuraray, Japan) with 85 wt % isotropic glass microparticles was subjected to wear testing (Fig. 3C) and demonstrated a total wear volume of 0.001 mm^3. Instead, a nominal 1 vol% of UHMR platelets were added to the resin in both the in-plane and out-of-plane orientations. Orientation of only 1 vol % platelets normal to the wear ball (out-of-plane) decreases the maximum wear volume by 77% as compared to the samples with in-plane oriented reinforcement. Such wear volume is also 45% lower than that observed in the pure commercial resin. Observation of the worn area of tested films suggests that the out-of-plane oriented hard platelets remain strongly locked within the surrounding polymer matrix, effectively impeding the penetration of the zirconia ball into the material during sliding. In contrast, isotropic particles and in-plane aligned platelets can be more easily removed from the matrix by the shear stresses developed under the sliding ball, leading to more pronounced wear. In contrast to the tensile mechanical properties, a quantitative analysis of the effect of reinforcement orientation on the hardness and wear of such anisotropic structures is less straightforward due to the complicated stress states in these cases.

To illustrate the benefit of building composites with controlled 3D reinforcement, we produced bilayer structures with tailored reinforcement architectures by laminating together layers of 10 vol % alumina platelets in an epoxy resin (similar to those in Fig. 2C) (*27*). The platelets in each individual layer were aligned both in-plane or out-of-plane by using rotating linear magnetic fields, leading to the structures schematically shown in Fig. 3E. Rectangular bars of the various created structures were evaluated with regards to out-of-plane hardness and flexure modulus under three-point bending. Typically, structures containing platelets aligned in-plane exhibit high flexural modulus but low out-of-plane hardness. Conversely, composites containing only out-of-plane oriented platelets exhibit higher out-of-plane hardness but lower flexural modulus. Instead, by creating a laminate structure exhibiting out-of-plane alignment in the upper layer and in-plane orientation in the bottom layer, one can produce a composite with both increased flexural modulus and increased out-of-plane hardness. Despite the much lower concentration of inorganic phase present in the synthetic composites, a similar architecture is found in seashells (*22*).

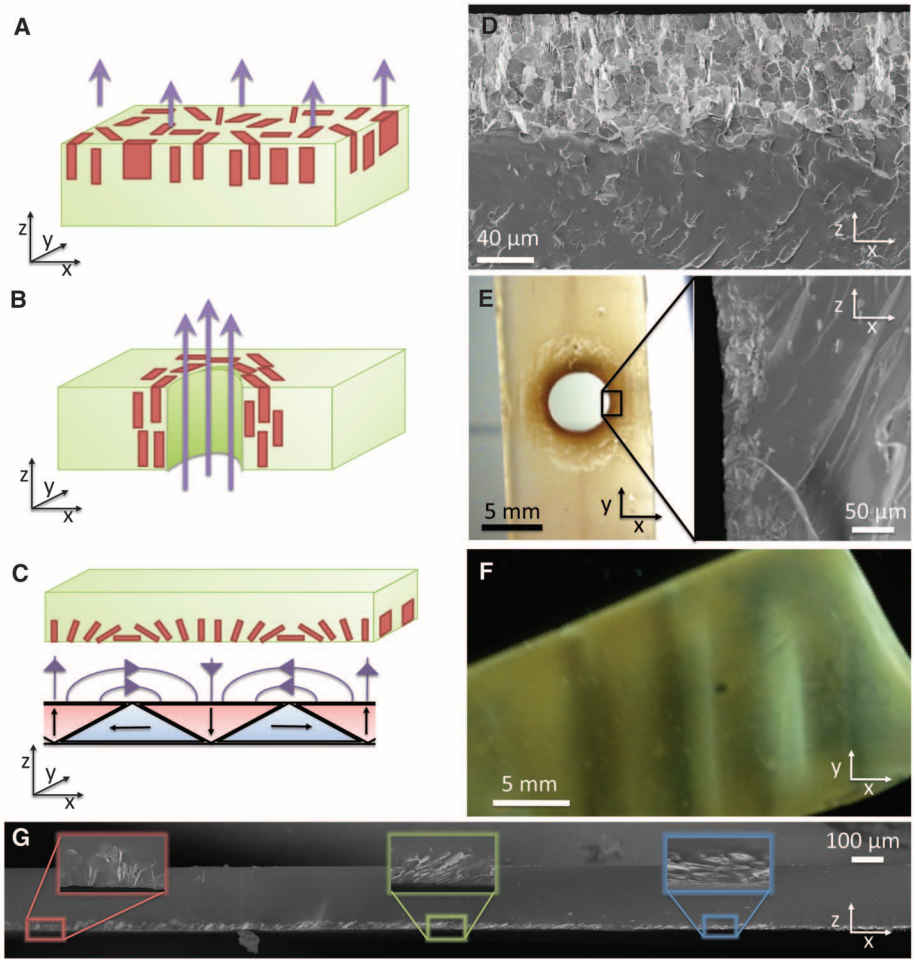

Fig. 4. Unusual 3D reinforcement architectures through advanced orientational and spatial magnetic control. (**A** and **B**) Schematic and (**D** and **E**) SEMs of cross-section of a spatial gradient in UHMR particles attracted preferentially to the composite edge or around a material weak point, respectively, due to a magnetic field gradient. Composites are 5 vol % Al_2O_3 in (D) polyurethane and (E) PVA. (**C**) Schematic of a standard refrigerator magnet's domain structure leading to gradually varying UHMR particle alignment as seen in (**G**) for a 5 vol % Al_2O_3 in PVA swellable composite. Such structures can locally swell to different extents depending on the platelet orientation, leading to the reversible formation of topographical ripples in the polymer (**F**).

Exploiting various conventional magnetophoretic techniques with these UHMR reinforcement particles allows for the facile synthesis of even more elaborate composite architectures. For example, this technique can be used to concentrate UHMR particles to specific regions of the film before consolidation of the matrix. In this case, a magnetic field gradient has to be established to drive the UHMR particles to the region of interest. This is exemplified in Fig. 4, A and D, by a polyurethane/alumina composite exhibiting out-of-plane aligned UHMR platelets that were concentrated on the surface of the film. To demonstrate that concentrated UMHR particles can locally reinforce the polymer matrix, we conducted tensile tests on 2 mm by 12 mm by 0.1 mm polyurethane samples with a 5-mm stripe of reinforced area produced with a hand-held rare-earth magnet (Fig. 3D). The highly heterogeneous composite obtained exhibit distinct local elastic moduli that can be estimated by using simple rules of mixtures (SOM text). Local stiffening of 180% was estimated by evaluating the elastic modulus of the reinforced and nonreinforced areas in independent tensile tests (Fig. 3D, SOM text). A straightforward extension of this method is to use spatial magnetic gradients to locally reinforce around weak points of a composite part, as exemplified in Fig. 4, B and E, for a composite with 5 vol % UHMR particles in poly(vinyl alcohol) containing a central hole (PVA, molecular mass = 13,000 to 23,000 g/mol, Sigma Aldrich).

The possible reinforcement orientations that can be achieved are in principle only limited by the magnetic field patterns that can be created. Indeed, ordinary refrigerator magnets that exhibit multiple magnetic domain patterns can be used to produce composites with reinforcing particles that gradually change orientation across the film (Fig. 4, C and G). Such tailored local orientation of reinforcing elements is a key design principle to control organ movements in wood cells and wheat awns (*30*). The physical constraints im-

posed by the cellulose microfibrils specially arranged on the plant cell wall lead to complex actuation behavior. Likewise, we demonstrate that PVA hydrogel films containing reinforcing platelets with gradually changing local orientation can reversibly change their shape from straight to well-defined wavy patterns upon drying or swelling of the hydrogel matrix (Fig. 4F).

Given the possibility to precisely control the position and orientation of reinforcing particles within the matrix, the method outlined here offers a way to locally tailor the properties of composite materials by using the same set of initial building blocks. The myriad of unusual properties including out-of-plane global or local increases in composite stiffness, strength, hardness, wear resistance, and the shape memory effect achieved by simply controlling the orientation and position of reinforcing elements suggest the enormous potential of this approach.

References and Notes

1. D. Hull, T. W. Clyne, *An Introduction to Composite Materials*, D. R. Clarke, S. Suresh, I. M. Ward, Eds., Cambridge Solid State Science Series (Cambridge Univ. Press, Cambridge, 1996).
2. T. W. Chou, *Microstructural Design of Fiber Composites* (Cambridge Univ. Press, Cambridge, 1992).
3. E. Munch *et al.*, *Science* **322**, 1516 (2008).
4. S. Deville, E. Saiz, R. K. Nalla, A. P. Tomsia, *Science* **311**, 515 (2006).
5. L. J. Bonderer, A. R. Studart, L. J. Gauckler, *Science* **319**, 1069 (2008).
6. Z. Y. Tang, N. A. Kotov, S. Magonov, B. Ozturk, *Nat. Mater.* **2**, 413 (2003).
7. A. Walther *et al.*, *Nano Lett.* **10**, 2742 (2010).
8. P. Podsiadlo *et al.*, *Science* **318**, 80 (2007).
9. Z. Burghard *et al.*, *Nano Lett.* **9**, 4103 (2009).
10. G. Freitas, C. Magee, P. Dardzinski, T. Fusco, *J. Adv. Mater.* **25**, 36 (1994).
11. A. P. Mouritz, M. K. Bannister, P. J. Falzon, K. H. Leong, *Compos. Part A Appl. Sci. Manuf.* **30**, 1445 (1999).
12. V. P. Veedu *et al.*, *Nat. Mater.* **5**, 457 (2006).
13. H. Qian, E. S. Greenhalgh, M. S. P. Shaffer, A. Bismarck, *J. Mater. Chem.* **20**, 4751 (2010).
14. W. J. Cantwell, J. Morton, *Composites* **22**, 347 (1991).
15. S. Ozcan, P. Filip, *Wear* **259**, 642 (2005).
16. P. M. Jelf, N. A. Fleck, *J. Compos. Mater.* **26**, 2706 (1992).
17. L. Tong, A. P. Mouritz, M. Bannister, *3D Fibre Reinforced Polymer Composites* (Elsevier, Amsterdam, 2002).
18. C. Ortiz, M. C. Boyce, *Science* **319**, 1053 (2008).
19. P. Fratzl, R. Weinkamer, *Prog. Mater. Sci.* **52**, 1263 (2007).
20. F. Barthelat, C. M. Li, C. Comi, H. D. Espinosa, *J. Mater. Res.* **21**, 1977 (2006).
21. W. Wagermaier *et al.*, *Biointerphases* **1**, 1 (2006).
22. H. J. Qi, B. J. F. Bruet, J. S. Palmer, C. Ortiz, M. C. Boyce, in *Mechanics of Biological Tissues*, G. A. Holzapfel, R. W. Ogden, Eds. (Springer-Verlag, Graz, Austria, 2005).
23. V. Imbeni, J. J. Kruzic, G. W. Marshall, S. J. Marshall, R. O. Ritchie, *Nat. Mater.* **4**, 229 (2005).
24. D. van der Beek *et al.*, *Phys. Rev. E* **73**, 011409 (2006).
25. M. A. Correa-Duarte *et al.*, *J. Phys. Chem. B* **109**, 19060 (2005).
26. L. Onsager, *Ann. N.Y. Acad. Sci.* **51**, 627 (1949).
27. Materials and methods are available as supporting material on *Science* Online.
28. D. Faivre, D. Schüler, *Chem. Rev.* **108**, 4875 (2008).
29. S. B. Bubenhofer *et al.*, *Nanotechnology* **20**, 485302 (2009).
30. P. Fratzl, R. Elbaum, I. Burgert, *Faraday Discuss.* **139**, 275, discussion 309, 419 (2008).

Acknowledgments: We thank T. Tervoort, L. van Breemen, K. Feldman, M. Imhof, J. Hofstetter, R. Stahel, R. Ehrbar, P. Zweifel, B. Wegmann, and M. Schinhammer for experimental assistance, and Antaria, Huntsman Advanced Materials, Rosen and BASF for supplying the alumina platelets, polymers, and resins. We acknowledge internal funding from ETH Zurich and the Swiss National Science Foundation (grant 200021_135306/1), as well as support by the Electron Microscopy Center of ETH Zurich (EMEZ). ETH Zurich has applied for the following patent: A. R. Studart, R. M. Erb, R. Libanori, Method for the production of reinforced materials and reinforced materials obtained using the method, European patent application 10003358.8, priority date 29 March 2010.

Supporting Online Material

www.sciencemag.org/cgi/content/full/335/6065/199/DC1
Materials and Methods
SOM Text
Figs. S1 to S11
References (*31*–*40*)
Movie S1

7 July 2011; accepted 25 October 2011
10.1126/science.1210822

Direct Kinetic Measurements of Criegee Intermediate (CH_2OO) Formed by Reaction of CH_2I with O_2

Oliver Welz,[1] John D. Savee,[1] David L. Osborn,[1] Subith S. Vasu,[1] Carl J. Percival,[2] Dudley E. Shallcross,[3] Craig A. Taatjes[1]*

Ozonolysis is a major tropospheric removal mechanism for unsaturated hydrocarbons and proceeds via "Criegee intermediates"—carbonyl oxides—that play a key role in tropospheric oxidation models. However, until recently no gas-phase Criegee intermediate had been observed, and indirect determinations of their reaction kinetics gave derived rate coefficients spanning orders of magnitude. Here, we report direct photoionization mass spectrometric detection of formaldehyde oxide (CH_2OO) as a product of the reaction of CH_2I with O_2. This reaction enabled direct laboratory determinations of CH_2OO kinetics. Upper limits were extracted for reaction rate coefficients with NO and H_2O. The CH_2OO reactions with SO_2 and NO_2 proved unexpectedly rapid and imply a substantially greater role of carbonyl oxides in models of tropospheric sulfate and nitrate chemistry than previously assumed.

In 1949, Rudolf Criegee proposed that ozonolysis of alkenes proceeds via carbonyl oxide biradicals, in an ozonolysis mechanism that is now generally accepted (*1*). Because a large fraction of the tropospheric oxidation of unsaturated hydrocarbons is initiated by reaction with ozone (*2*), these biradical "Criegee intermediates" play a substantial role in the tropospheric budgets of secondary organic aerosols (SOAs), ozone, NO_x, NO_y, and HO_x. For example, the OH radical, key to the oxidizing capacity of the troposphere, is formed by a sequence of photochemical reactions involving ozone:

$$O_3 + h\nu \rightarrow O(^1D) + O_2 \quad (1)$$

$$O(^1D) + H_2O \rightarrow OH + OH \quad (2)$$

These reactions depend on the presence of sunlight and water vapor. However, field measurements (*3*) have shown that OH levels in winter and summer are very similar in UK urban environments (*4*), despite the fact that in winter the efficiency of the reaction in Eq. 1 drops by at least 50%. Harrison *et al.* (*4*) showed that winter production of OH via ozonolysis of alkenes, dominated by Criegee radical chemistry, makes up this difference. SOAs can also be initiated by Criegee intermediate reactions (*5*, *6*).

Although decades of theoretical studies and indirect experimental evidence support the importance of Criegee radicals in the troposphere [e.g., (*7*)], the quantitative effects of their chemistry remain uncertain (*8*) because it has been impossible to make direct measurements of Criegee reactions with key atmospheric species. Until now, determination of rate constants for Criegee reactions has been carried out by investigating changes in the products of ozonolysis upon addition of different reagents or scavengers (*9*, *10*). Interpretation of such experiments requires modeling the full complexity of ozonolysis, in which the production, stabilization, and removal of Criegee intermediates are all imperfectly understood. Although an internally consistent picture of Criegee chemistry has been slowly emerging (*11*), absolute rate coefficient estimates with key atmospheric species continue to range over 4 to 5 orders of magnitude (*12*).

Recently the photoionization spectrum of the simplest gas-phase Criegee intermediate, formaldehyde oxide (which we denote as CH_2OO), was measured in the chlorine atom–initiated oxidation of dimethyl sulfoxide (DMSO) (*13*). In

[1]Combustion Research Facility, Mail Stop 9055, Sandia National Laboratories, Livermore, CA 94551–0969, USA. [2]School of Earth, Atmospheric and Environmental Sciences, University of Manchester, Williamson Building, Oxford Road, Manchester M13 9PL, UK. [3]School of Chemistry, University of Bristol, Bristol BS8 1TS, UK.

*To whom correspondence should be addressed. E-mail: cataatj@sandia.gov

the present work, another pathway to stabilized CH_2OO is demonstrated: the reaction of CH_2I with O_2. The iodomethyl radical, CH_2I, is an important intermediate in the breakdown of organic iodides, and its dominant fate is reaction with O_2 (*14*). The CH_2I and O_2 reaction has several possible product channels:

$$CH_2I + O_2 \rightarrow CH_2IOO \quad (3a)$$

$$CH_2I + O_2 \rightarrow CH_2O + IO \quad (3b)$$

$$CH_2I + O_2 \rightarrow I + CH_2O_2 \text{ (various isomers)} \quad (3c)$$

Eskola *et al*. (*15*) used laser photolytic initiation and photoionization mass spectrometric detection to study this reaction and found that atomic iodine (channel 3c) is the principal direct product of the reaction at low pressures. We find that the coproduct isomer is CH_2OO and that it can be formed in sufficient quantities to carry out direct chemical kinetics studies.

In the present experiments, CH_2I was produced by 248-nm photolysis of diiodomethane, CH_2I_2, at 298 K and 4 torr, in a large excess of O_2. The reacting mixture was interrogated by tunable synchrotron photoionization mass spectrometry. A time-resolved mass spectrum from the CH_2I_2/O_2 system is shown in Fig. 1. The resolution of the mass spectrometer is sufficient to establish that the nominal mass/charge (m/z) = 46 peak arises from CH_2O_2 and not, for example, C_2H_6O (fig. S1). The formation rate of the m/z = 46 species is correlated with the disappearance rate of CH_2I (m/z = 141) (figs. S2 to S4), establishing that CH_2OO is a direct product from the reaction of CH_2I with O_2. Tuning the synchrotron photon energy allows a photoionization spectrum of the m/z = 46 species to be measured (Fig. 2). The photoionization spectrum agrees with that measured for CH_2OO in chlorine-initiated DMSO oxidation (*13*) and with CCSD(T)/CBS (coupled-cluster with single and double excitations and perturbative treatment of triple excitations/complete basis set extrapolation) calculations for the CH_2OO ionization energy (expected to be accurate to 0.05 eV) (*16*). Dioxirane and formic acid have much higher ionization energies, 10.82 eV and 11.33 eV (*16*, *17*). The mass and the photoionization spectrum support unambiguous assignment of the product as formaldehyde oxide, CH_2OO. A small formic acid signal is observed at longer times (fig. S5), which could be produced by reaction of the Criegee intermediate.

The longest CH_2OO lifetime observed, $\tau \sim 2$ ms (Fig. 3), is well below estimates for thermal isomerization or dissociation of CH_2OO (*18*, *19*). Changes in decay rates with different wall coatings [supporting online material (SOM) text] suggest that heterogeneous loss contributes to CH_2OO removal in these experiments. Formaldehyde (CH_2O) formation is correlated with the disappearance of CH_2OO, implying that most of the formaldehyde is produced by reactions of the Criegee intermediate rather than from the direct reaction of CH_2I with O_2. This observation is consistent with the conclusions of other researchers (*20*, *21*) that channel 3b is minor. The experimental lifetime is long enough to allow direct pseudo–first-order measurements of relatively rapid reactions of CH_2OO. We have carried out such measurements of Criegee intermediate reactions with SO_2, NO_2, NO, and H_2O.

Addition of SO_2 and NO_2 produced a more rapid decay of CH_2OO, as shown in Fig. 3 for the SO_2 reaction and in fig. S9 for the NO_2 reaction. For measurements of the reaction with NO and NO_2, $^{13}CH_2OO$ was used because $^{14}NO_2$ appears at nearly the same mass as $^{12}CH_2OO$. The ^{13}C kinetic isotope effect is expected to be far smaller than the experimental uncertainties in the rate coefficient measurements. The reciprocal of the lifetime of CH_2OO is linearly related to the excess reactant concentration, with the second-order rate coefficient as the slope (Fig. 4 and fig. S10).

The final analysis (SOM text) yields rate coefficients at 298 K (and 4 torr) of $3.9 \times 10^{-11} \pm 0.7 \times 10^{-11}$ cm^3 s^{-1} (95% uncertainty) for CH_2OO with SO_2 and 7×10^{-12} cm^3 s^{-1} for $^{13}CH_2OO$ with NO_2, with asymmetric 95% uncertainty bounds of $+3 \times 10^{-12}$ and -2×10^{-12} cm^3 s^{-1}. These rate coefficients are from 50 to 10,000 times larger than estimates typically used in tropospheric models (*7*, *8*). The reaction of CH_2OO with SO_2 (*22*) has additional laboratory relevance because it has been used to scavenge Criegee intermediates and as a reference for measurements of other Criegee reactions. Recent theoretical work (*23*) has estimated a nearly collision-limited rate coefficient ($\sim 4 \times 10^{-10}$ cm^3 s^{-1}) for the reaction of CH_2OO with SO_2, much higher than previous experiments but within a factor of 10 of the present direct measurements. The ratio of initial CH_2OO to final CH_2O amplitudes changes little upon addition of SO_2 (fig. S14), suggesting that SO_3 plus CH_2O is a product channel.

Addition of NO up to [NO] = 5×10^{15} cm^{-3} or H_2O up to [H_2O] = 3×10^{16} cm^{-3} produced no measurable increase in the decay rate of CH_2OO (figs. S11 to S13). Reaction of NO with CH_2OO is postulated to form CH_2O and NO_2 (*8*); however, no product formation could be observed in these experiments. The reaction of CH_2OO with water is thought to produce hydroxymethylhydroperoxide ($HOCH_2OOH$, HMHP) by association (*24*) or to catalyze isomerization (*25*). The photon energy of the measurements, 10.5 eV, is well below the ionization energy of formic acid (*17*) and dioxirane (*16*) (Fig. 2), so the isomerization channel would still lead to a loss of photoionization signal at m/z = 46. The photoionization behavior of HMHP is unknown, but at the highest water concentrations a very faint product signal, much too small for kinetic analysis, can be observed at m/z = 64.

Assuming that a change of 25% in the decay rate constant of CH_2OO would be readily detectable, the maximum concentrations of H_2O and NO used in conjunction with the observed

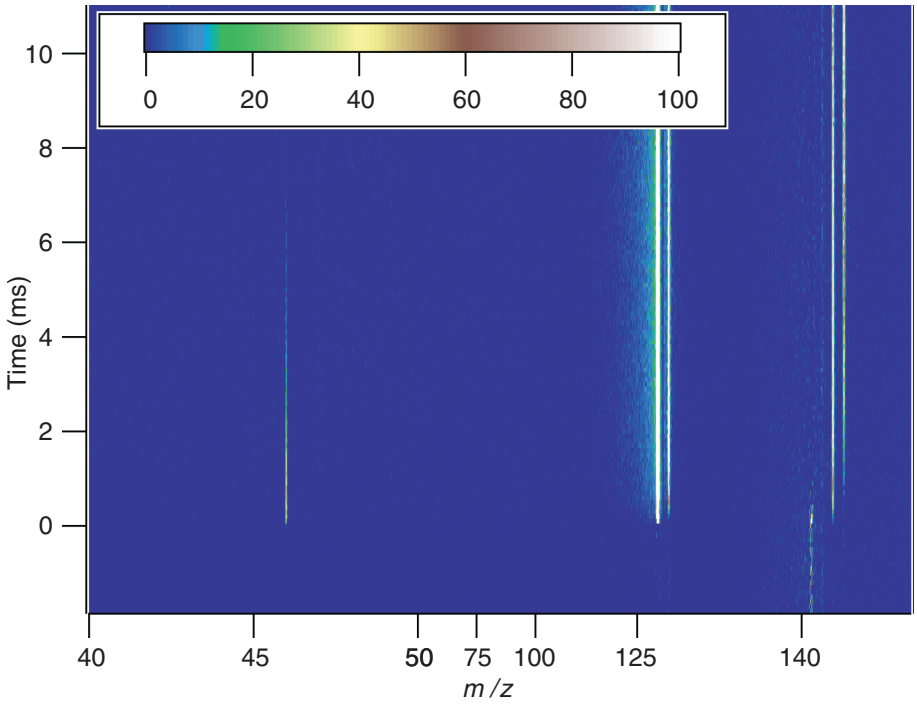

Fig. 1. Time-resolved mass spectrum at 10.5 eV, acquired during photolysis of CH_2I_2 in the presence of O_2. (Note the changing *x*-axis scale.) Signal levels before the arrival of the photolysis laser pulse have been subtracted, and only positive signals are shown. The formation of CH_2OO is observed at m/z = 46, and CH_2I (m/z = 141) appears above a background from dissociative ionization of CH_2I_2. Other primary and secondary products (I, IO, HI, and HOI) are also evident.

zero-reagent decay constants (~500 s^{-1} for the water experiments, ~1100 s^{-1} for the NO experiments) give upper limits of $k(H_2O) < 4 \times 10^{-15}$ cm^3 s^{-1} and $k(NO) < 6 \times 10^{-14}$ cm^3 s^{-1}. The upper limit for reaction with water is above literature estimates of the rate constant (*12*) and tends to confirm the established models. On the other hand, the reaction with NO is two orders of magnitude slower than literature estimates (*2*).

The direct determinations of the rate constants for CH_2OO with SO_2 and NO_2, however, are considerably higher than previous estimates. Placing the present results into a tropospheric chemistry model (*26*) implies a substantial role of Criegee intermediates in sulfate and nitrate chemistry. Steady-state analysis (SOM text) shows that, if the rate coefficient for other Criegee intermediates is similar to that for CH_2OO, Criegee intermediates could be at least as important an oxidizer of SO_2 as OH across much of the terrestrial boundary layer. Reaction of Criegee intermediates with NO_2 may be an important daytime and nighttime source of nitrate radical. The present rate coefficient for the Criegee plus NO_2 reaction would increase the modeled NO_3 concentration by up to 20%, the enhancement scaling linearly with alkene concentration.

Low-volatility products, such as organic acids or hydroperoxides, of unimolecular and bimolecular Criegee reactions contribute to organic aerosol formation (*7*, *27*). The production of a Criegee biradical from the CH_2I plus O_2 reaction might affect modeling of oxidation and aerosol chemistry in the marine boundary layer (*28*). The exothermic (*16*) formation of CH_2OO plus I will compete with stabilization to CH_2IO_2, so full assessment of that impact will require measurements of branching fractions at atmospheric pressure. The demonstration that CH_2I and O_2 forms a Criegee intermediate as the dominant, if not sole, CH_2O_2 isomer indicates broad utility for Criegee chemistry investigations. For example, it may be possible to determine optical spectra for gas-phase CH_2OO by using this reaction; reported measurements of product ultraviolet spectra from CH_2I and O_2 (*20*, *29*) may already include contributions from the Criegee intermediate. Direct optical monitoring of Criegee intermediates could probe Criegee formation and reaction at atmospheric pressure. Additionally, reactions of other α-iodoalkyl radicals with O_2 may be used to form substituted Criegee intermediates and investigate their kinetics.

Reaction rate coefficients under tropospheric conditions are pressure- and temperature-dependent, and reactions are commonly affected by the presence of water and the participation of weakly bound complexes (*30*, *31*). Measurement of rate coefficients at one set of conditions, as in this work, does not completely characterize a reaction; for example, if the reactions have a substantial stabilization component, the rate constants could be substantially larger at atmospheric pressure. Decades of ozonolysis studies have mapped a web of dependences on conditions and scavenger species (*11*). The combination of a method for stabilized Criegee production and unambiguous photoionization detection of Criegee intermediates now enables direct study of these complicated relationships.

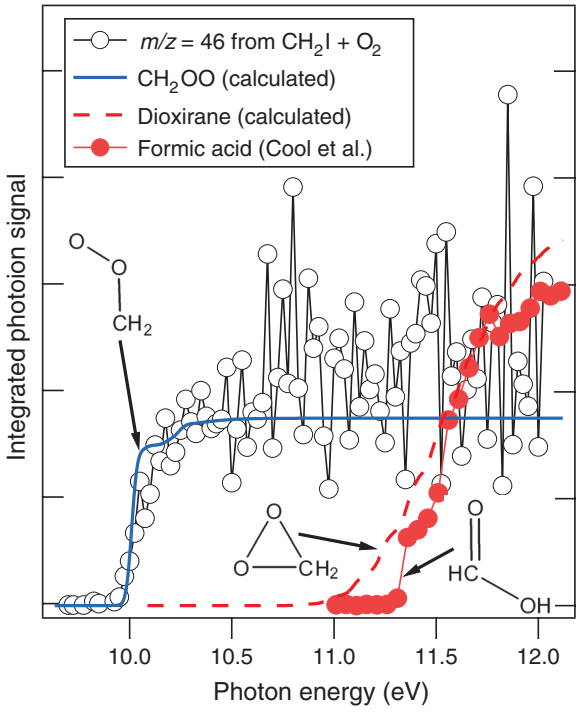

Fig. 2. Photoionization spectrum of the mass = 46 product of the CH_2I plus O_2 reaction, integrated over the first 2 ms after photolysis. The calculated photoionization spectra of the Criegee intermediate CH_2OO and dioxirane (*13*), the experimental photoionization spectrum for formic acid (*17*), as well as schematic chemical structures, are shown for reference.

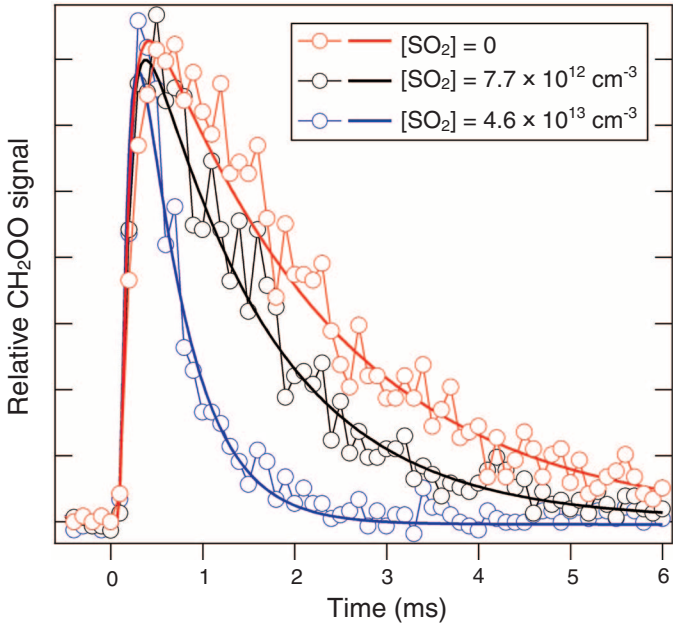

Fig. 3. Time-dependent CH_2OO signal for various concentrations of SO_2. Solid lines represent fits to the data traces, including convolution with a measured instrument response function (SOM text), from which pseudo–first-order decay constants are derived.

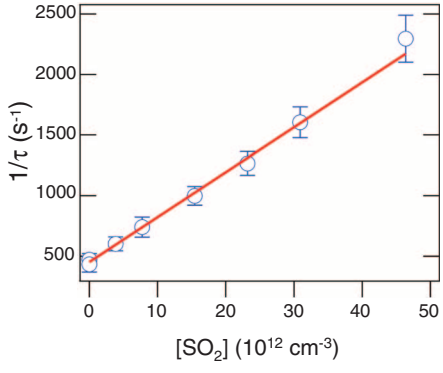

Fig. 4. Dependence of the pseudo–first-order Criegee intermediate decay constant (reciprocal of the lifetime τ) on the concentration of SO_2. Error bounds are 95% uncertainty estimates based on least-squares analysis of the unweighted fits as depicted in Fig. 3, which include >20 points across the relevant decay. The second-order rate coefficient is given by the slope of the linear fit.

References and Notes

1. R. Criegee, *Angew. Chem. Int. Ed. Engl.* **14**, 745 (1975).
2. J. G. Calvert *et al*., *The Mechanisms of Atmospheric Oxidation of the Alkenes* (Oxford Univ. Press, New York, 2000).
3. D. E. Heard *et al*., *Geophys. Res. Lett.* **31**, L18112 (2004).
4. R. M. Harrison *et al*., *Sci. Total Environ.* **360**, 5 (2006).
5. K. J. Heaton, R. L. Sleighter, P. G. Hatcher, W. A. Hall 4th, M. V. Johnston, *Environ. Sci. Technol.* **43**, 7797 (2009).
6. J. H. Kroll, J. H. Seinfeld, *Atmos. Environ.* **42**, 3593 (2008).
7. D. Johnson, G. Marston, *Chem. Soc. Rev.* **37**, 699 (2008).
8. S. Hatakeyama, H. Akimoto, *Res. Chem. Intermed.* **20**, 503 (1994).
9. M. S. Alam *et al*., *Phys. Chem. Chem. Phys.* **13**, 11002 (2011).
10. A. A. Presto, N. M. Donahue, *J. Phys. Chem. A* **108**, 9096 (2004).
11. N. M. Donahue, G. T. Drozd, S. A. Epstein, A. A. Presto, J. H. Kroll, *Phys. Chem. Chem. Phys.* **13**, 10848 (2011).
12. J. D. Fenske, A. S. Hasson, A. W. Ho, S. E. Paulson, *J. Phys. Chem. A* **104**, 9921 (2000).
13. C. A. Taatjes *et al*., *J. Am. Chem. Soc.* **130**, 11883 (2008).
14. L. J. Carpenter, *Chem. Rev.* **103**, 4953 (2003).
15. A. J. Eskola, D. Wojcik-Pastuszka, E. Ratajczak, R. S. Timonen, *Phys. Chem. Chem. Phys.* **8**, 1416 (2006).
16. M. T. Nguyen, T. L. Nguyen, V. T. Ngan, H. M. T. Nguyen, *Chem. Phys. Lett.* **448**, 183 (2007).
17. T. A. Cool, J. Wang, K. Nakajima, C. A. Taatjes, A. McIlroy, *Int. J. Mass Spectrom.* **247**, 18 (2005).
18. M. Olzmann, E. Kraka, D. Cremer, R. Gutbrod, S. Andersson, *J. Phys. Chem. A* **101**, 9421 (1997).
19. J. H. Kroll, J. S. Clarke, N. M. Donahue, J. G. Anderson, K. L. Demerjian, *J. Phys. Chem. A* **105**, 1554 (2001).
20. T. J. Gravestock, M. A. Blitz, W. J. Bloss, D. E. Heard, *ChemPhysChem* **11**, 3928 (2010).
21. T. J. Dillon, M. E. Tucceri, R. Sander, J. N. Crowley, *Phys. Chem. Chem. Phys.* **10**, 1540 (2008).
22. R. A. Cox, S. A. Penkett, *Nature* **230**, 321 (1971).
23. T. Kurtén, J. R. Lane, S. Jørgensen, H. G. Kjaergaard, *J. Phys. Chem. A* **115**, 8669 (2011).
24. S. Gäb, E. Hellpointner, W. V. Turner, F. Korte, *Nature* **316**, 535 (1985).
25. A. S. Hasson *et al*., *J. Phys. Chem. A* **107**, 6176 (2003).
26. A. T. Archibald *et al*., *Atmos. Chem. Phys.* **10**, 8097 (2010).
27. F. Paulot *et al*., *Atmos. Chem. Phys.* **11**, 1989 (2011).
28. C. D. O'Dowd *et al*., *Nature* **417**, 632 (2002).
29. J. Sehested, T. Ellermann, O. J. Nielsen, *Int. J. Chem. Kinet.* **26**, 259 (1994).
30. W. Klemperer, V. Vaida, *Proc. Natl. Acad. Sci. U.S.A.* **103**, 10584 (2006).
31. S. Aloisio, J. S. Francisco, *Acc. Chem. Res.* **33**, 825 (2000).

Acknowledgments: Additional pseudo–first-order rate constants and spectroscopic data underpinning this work are presented in the SOM. This work is supported by the Division of Chemical Sciences, Geosciences, and Biosciences, the Office of Basic Energy Sciences, the U.S. Department of Energy. D.E.S. and C.J.P. thank Natural Environment Research Council for funding. The Advanced Light Source is supported by the Director, Office of Science, Office of Basic Energy Sciences, Materials Sciences Division, of the U.S. Department of Energy under contract DE-AC02-05CH11231 at Lawrence Berkeley National Laboratory. Sandia is a multiprogram laboratory operated by Sandia Corporation, a Lockheed Martin company, for the National Nuclear Security Administration under contract DE-AC04-94-AL85000. We thank A. Eskola (Helsinki) for drawing our attention to the reaction of CH_2I with O_2, H. Johnsen (Sandia) for technical support of this experiment, and H. Huang, J. Zádor, and L. Sheps (Sandia) for discussions on data analysis. The experiments were conceived by C.A.T., C.J.P., and D.E.S. and designed and carried out by O.W., J.D.S., C.A.T., and D.L.O., with assistance from S.S.V. All authors participated in the data analysis and interpretation and contributed to the manuscript.

Supporting Online Material

www.sciencemag.org/cgi/content/full/335/6065/204/DC1
Materials and Methods
Figs. S1 to S14
Tables S1 and S2
References (*32*–*51*)

26 August 2011; accepted 18 November 2011
10.1126/science.1213229

Sucrose Efflux Mediated by SWEET Proteins as a Key Step for Phloem Transport

Li-Qing Chen,[1]* Xiao-Qing Qu,[1,2]* Bi-Huei Hou,[1] Davide Sosso,[1] Sonia Osorio,[3] Alisdair R. Fernie,[3] Wolf B. Frommer[1]†

Plants transport fixed carbon predominantly as sucrose, which is produced in mesophyll cells and imported into phloem cells for translocation throughout the plant. It is not known how sucrose migrates from sites of synthesis in the mesophyll to the phloem, or which cells mediate efflux into the apoplasm as a prerequisite for phloem loading by the SUT sucrose–H^+ (proton) cotransporters. Using optical sucrose sensors, we identified a subfamily of SWEET sucrose efflux transporters. AtSWEET11 and 12 localize to the plasma membrane of the phloem. Mutant plants carrying insertions in *AtSWEET11* and *12* are defective in phloem loading, thus revealing a two-step mechanism of SWEET-mediated export from parenchyma cells feeding H^+-coupled import into the sieve element–companion cell complex. We discuss how restriction of intercellular transport to the interface of adjacent phloem cells may be an effective mechanism to limit the availability of photosynthetic carbon in the leaf apoplasm in order to prevent pathogen infections.

Breeding has led to marked increases in crop yield. Increased yield potential has mainly been attributed to improvements in allocation efficiency, defined as the amount of total biomass allocated into harvestable organs (*1*, *2*). Despite the critical importance of sucrose translocation in this process, we do not understand mechanistically how changes in translocation efficiency may have contributed to an increase in harvestable products. Allocation of photoassimilates in plants is conducted by transport of sucrose from the photosynthetic "sources" (predominantly leaves) to the heterotrophic "sinks" (meristems, roots, flowers, and seeds) (*3*–*5*). Sucrose, the predominant transport form of sugars in many plant species [see (*6*) for an overview of the different sugars and translocation mechanisms], is produced in leaf mesophyll cells, particularly in the palisade parenchyma of dicots and the bundle sheath of monocots.

In apoplasmic loaders, sucrose is loaded into the sieve element–companion cell complex (SE/CC) in the phloem by the sucrose-H^+ cotransporter SUT1 (named SUC2 in *Arabidopsis*) from the apoplasm (cell wall space) (*7*–*11*). However, sucrose must effuse from inside the cell into the cell wall, either directly from mesophyll cells (after which it travels to the phloem in the apoplasm) or from cells closer to the site of loading (having traveled cell-to-cell through plasmodesmata). Both the site and the mechanism of sucrose efflux remain to be elucidated, although it has been argued that a site in the vicinity of the site of phloem loading is most probable (*4*, *5*).

We identified proteins that can transport sucrose across the plasma membrane: AtSWEET10 to 15 in *Arabidopsis* and OsSWEET11 and 14 in rice (*Oryza sativa*). We found that *AtSWEET11* and *12* are expressed in phloem cells, and that inhibition by mutation reduces leaf assimilate exudation and leads to increased sugar accumulation in leaves. Thus, apoplasmic phloem loading occurs in a two-step model: Sucrose exported by SWEETs from phloem parenchyma cells feeds the secondary active proton-coupled sucrose transporter SUT1 in the SE/CC.

The sucrose efflux transporters were identified by means of a Förster resonance energy transfer (FRET) sensor-based screen. Because humans do not seem to possess sucrose transporters, we reasoned that human cell lines should lack endogenous sucrose transport activity and should thus represent a suitable functional expression system for heterologous sucrose transporters. A preliminary set of ~50 candidate genes encoding membrane proteins with unknown function as well as members of the recently identified SWEET glucose effluxer family (*12*) were coexpressed with the FRET sucrose sensor FLIPsuc90μΔ1V (*13*) in human embryonic kidney (HEK) 293T cells. AtSWEET10 to 15, which all belong to clade III of the AtSWEET family

[1]Carnegie Institution for Science, 260 Panama Street, Stanford, CA 94305, USA. [2]Key Laboratory of Plant and Soil Interactions, College of Resources and Environmental Sciences, China Agricultural University, 100193 Beijing, China. [3]Max-Planck-Institut für Molekulare Pflanzenphysiologie, Am Mühlenberg 1, 14476 Potsdam, Germany.

*These authors contributed equally to this work.
†To whom correspondence should be addressed. E-mail: wfrommer@stanford.edu

(*12*), enabled HEK293T cells to accumulate sucrose, as detected by a negative ratio change in sensor output (Fig. 1A). To corroborate these findings, we tested the clade III orthologs OsSWEET11 and 14 from rice (Fig. 1B) and found that they also transport sucrose. By contrast, proteins from the other SWEET clades did not show detectable sucrose uptake into HEK293T cells (Fig. 1A). Clade III SWEETs showed preferential transport activity for sucrose over glucose and did not appear to transport maltose (Fig. 1C and fig. S2). The ability of clade III SWEETs to export sucrose was shown by time-dependent efflux of [^{14}C]sucrose injected into *Xenopus* oocytes (Fig. 1D and fig. S2D) and was further supported by the reversibility of sucrose accumulation as measured by optical sensors in mammalian cells (Fig. 1E and fig. S3). SWEETs function as low-affinity sucrose transporters (affinity constant K_m for sucrose uptake by AtSWEET12 was ~70 mM, K_m for efflux was >10 mM; Fig. 1F and fig. S4, A to C). The largely pH-independent transport activity supports a uniport mechanism (fig. S4D). The observed transport characteristics are compatible with those of the low-affinity components for sucrose transport detected in vivo (*14*, *15*).

AtSWEET11 and *12* are highly expressed in leaves [microarray data and translatome data (*16*, *17*) (figs. S5A and S6)] and were found to be coexpressed with genes involved in sucrose biosynthesis and phloem loading (e.g., sucrose phosphate synthase, *SUC2*, and *AHA3*; fig. S5, B and C). The tissue-specific expression and cellular localization of AtSWEET11 and 12 and the phenotypes of *sweet* mutants were analyzed to determine the physiological role of the sucrose transporters.

AtSWEET11 and 12 are close paralogs, with 88% similarity at the amino acid level. Lines carrying single T-DNA (transfer DNA; *Agrobacterium tumefaciens*) insertions (fig. S7) in the *AtSWEET11* and *12* loci did not show any obvious altered morphological phenotype when compared to the wild-type Col-0 or wild-type siblings segregated from the same mutant populations. However, at higher light levels, the double mutant line was smaller relative to wild-type controls (20 to 35% reduction in rosette diameter depending on light conditions; Fig. 2A and fig. S8) and contained elevated starch levels at the end of the diurnal dark period (Fig. 2, B and C). Moreover, mature leaves of the double mutant contained higher sucrose levels both at the end of the light period and the end of the dark period (Fig. 2D). Leaves also accumulated higher levels of hexoses, as also observed in plants exposed to sucrose (*18*) or plants in which phloem loading has been blocked (*9*, *19*). Accumulation of free sugars is expected to lead to down-regulation of photosynthesis through sugar signaling networks (*20*). The starch accumulation phenotype was partially complemented by expression of either *AtSWEET11* or *12* under their respective promoters in the double mutant (fig. S9). Together, these data indicate an impaired ability of the mutants to export sucrose from the leaves. Direct [$^{14}CO_2$]-labeling experiments indicated that under low light conditions (in which the double mutant did not accumulate high starch levels; fig. S10), the double mutant exported ~50% of fixed ^{14}C relative to controls (Fig. 2E). It is noteworthy that the mutant was affected with respect to leaf size, photosynthetic capacity, and steady-state sugar levels; thus, the apparent efflux rates may be compounded by these parameters.

Reduced efflux of sugars from leaves is expected to lead to reduced translocation of photoassimilates to the roots, thus negatively affecting

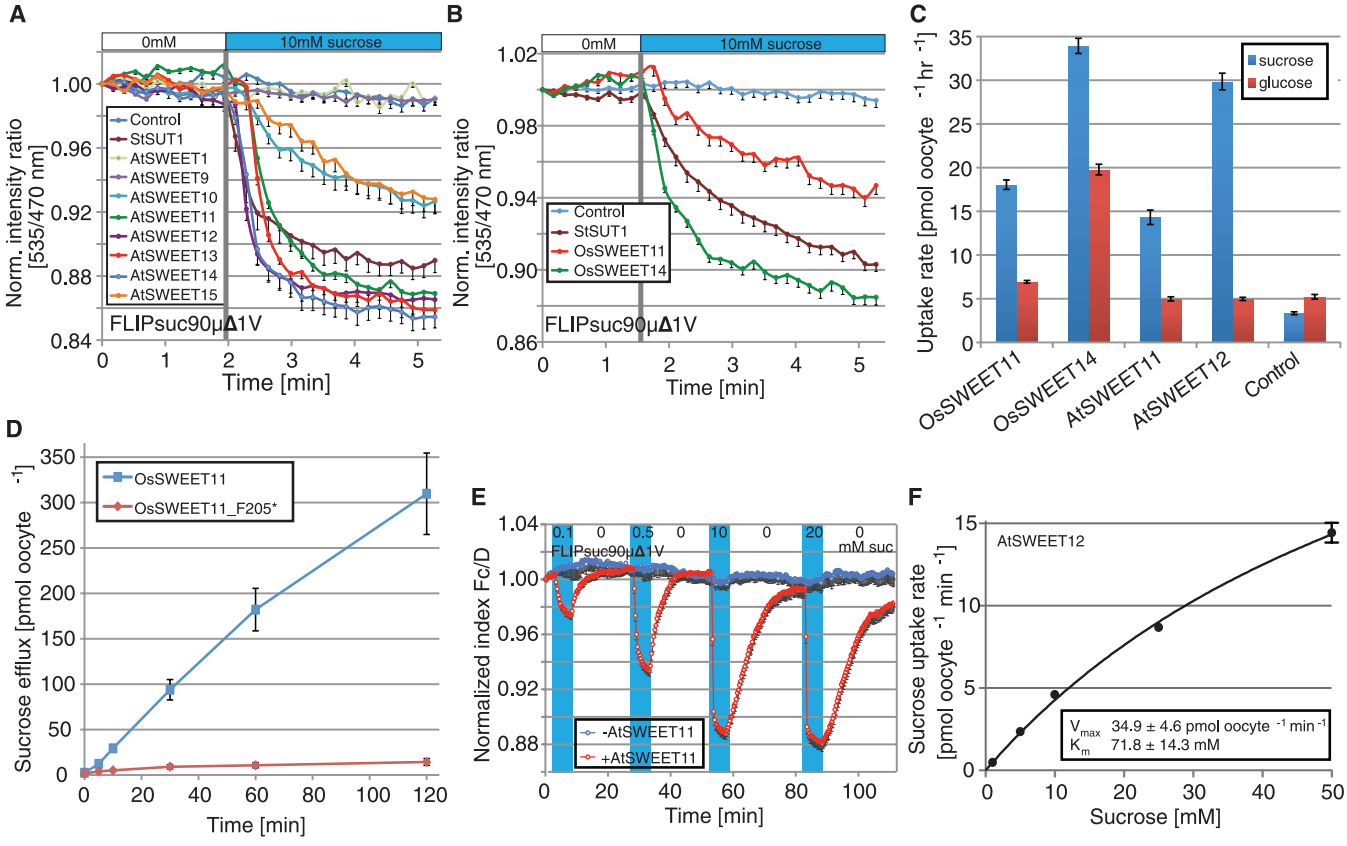

Fig. 1. Identification of sucrose transporters. (**A** and **B**) HEK293T cell–FRET sensor uptake assay. (A) Of ~50 membrane protein genes tested, AtSWEET10 to 15 showed sucrose influx as measured with the sucrose sensor FLIPsuc90μΔ1V; HEK293T cells transfected with sensor only ("control") or the sensor and the H^+/sucrose cotransporter StSUT1 served as controls (fig. S1) (*7*) (±SEM, $n \geq 11$). (B) The rice transporters OsSWEET11 and 14 mediate sucrose transport in HEK293T cells (±SEM, $n \geq 11$). (**C**) Oocyte uptake assay: OsSWEET11 and 14 and AtSWEET11 and 12 mediate [^{14}C]sucrose uptake (1 mM sucrose; ±SEM, $n \geq 7$). (**D**) Oocyte efflux assay: [^{14}C]sucrose efflux by OsSWEET11 in *Xenopus* oocytes injected with 50 nl of a solution containing 50 mM [^{14}C]sucrose; the truncated version OsSWEET11_F205* served as control (±SEM, $n \geq 7$). (**E**) HEK293T cell–FRET sensor transport assay: Reversible accumulation of sucrose in HEK293T cells by AtSWEET11 (±SEM, $n \geq 10$; Fc/D, FRET index). (**F**) Oocyte uptake assay: Kinetics of AtSWEET12 for sucrose uptake in *Xenopus* oocytes (±SEM, $n \geq 14$).

root growth and the ability to acquire mineral nutrients (*9*, *10*). When germinated in the light on sugar-free media, *atsweet11;12* mutants exhibited reduced root length (Fig. 2, F and G). Addition of sucrose to the media rescued the root growth deficiency of *atsweet11;12* mutants (Fig. 2, F and G). A similar sucrose-dependent root growth deficiency has also been observed for the *Arabidopsis* sucrose/H^+ cotransporter *suc2* mutant (*11*). Both the *suc2* and the *atsweet11;12* mutants are apparently able to acquire sucrose or sucrose-derived hexoses from the medium to restore root growth that had been restricted by a carbohydrate deficiency.

The growth phenotype for *atsweet11;12* is not as severely affected as described previously for the *suc2* mutant (*9*–*11*). The *Arabidopsis* genome encodes several SWEET paralogs, including the closely related transporters AtSWEET10, 13, 14, and 15, which we show here to function as sucrose transporters. Quantitative polymerase chain reaction analyses showed that *AtSWEET13*, which is typically expressed at low levels in leaves, is induced by a factor of ~16 in the *atsweet11;12* double mutant (fig. S11). Thus, in contrast to the secondary active SE/CC loaders SUT1/SUC2, SWEETs function as redundant elements of phloem loading. It is noteworthy that *ossweet14* rice mutants display stunted growth, possibly as a result of reduced sugar efflux from leaves as well (*21*).

Taken together, the data indicate that clade III SWEETs are involved in export of sucrose and are responsible for the previously undescribed first step in phloem loading. The efflux of sucrose to the apoplasm could theoretically occur directly at the site of production in mesophyll cells, from bundle sheath cells, or from phloem parenchyma cells. Localization of *AtSWEET11* and *12* driven by their native promoters, as translational enhanced green fluorescent protein (eGFP) or GUS fusions, revealed that both proteins are present in the vascular tissue including minor and major veins, which in *Arabidopsis* are considered "to participate in phloem loading" (*22*) (Fig. 3, A to D, and fig. S12). The subcellular localization of eGFP-tagged AtSWEET11 and 12 was consistent with localization to the plasma membrane [Fig. 3, E and F; further supported by data from cauliflower mosaic virus (CaMV) 35S-SWEET-YFP plants, fig. S13]. AtSWEET11 and 12 were both expressed in select cells in the phloem, which form cell files along the veins (Fig. 3, C, D, and F, and fig. S12). Most likely, these cells correspond to phloem parenchyma. However, there are no known markers that would allow us to unambiguously identify these cells. Data from cell-specific translatome studies show that *AtSWEET11/12*-expressing cells have a clearly distinct translatome when compared to *SUC2*-expressing companion cells (fig. S6) (*17*). These data exclude the possibility that *SWEET11* and *12* are expressed to high levels in companion cells, supporting a localization in phloem parenchyma cells as the only remaining cell type in the phloem besides the enucleate sieve elements.

Further, *OsSWEET11/Xa13*, encoding a sucrose uniporter and functioning as a rice susceptibility (S) gene (*Xa13*) for specific pathovars of

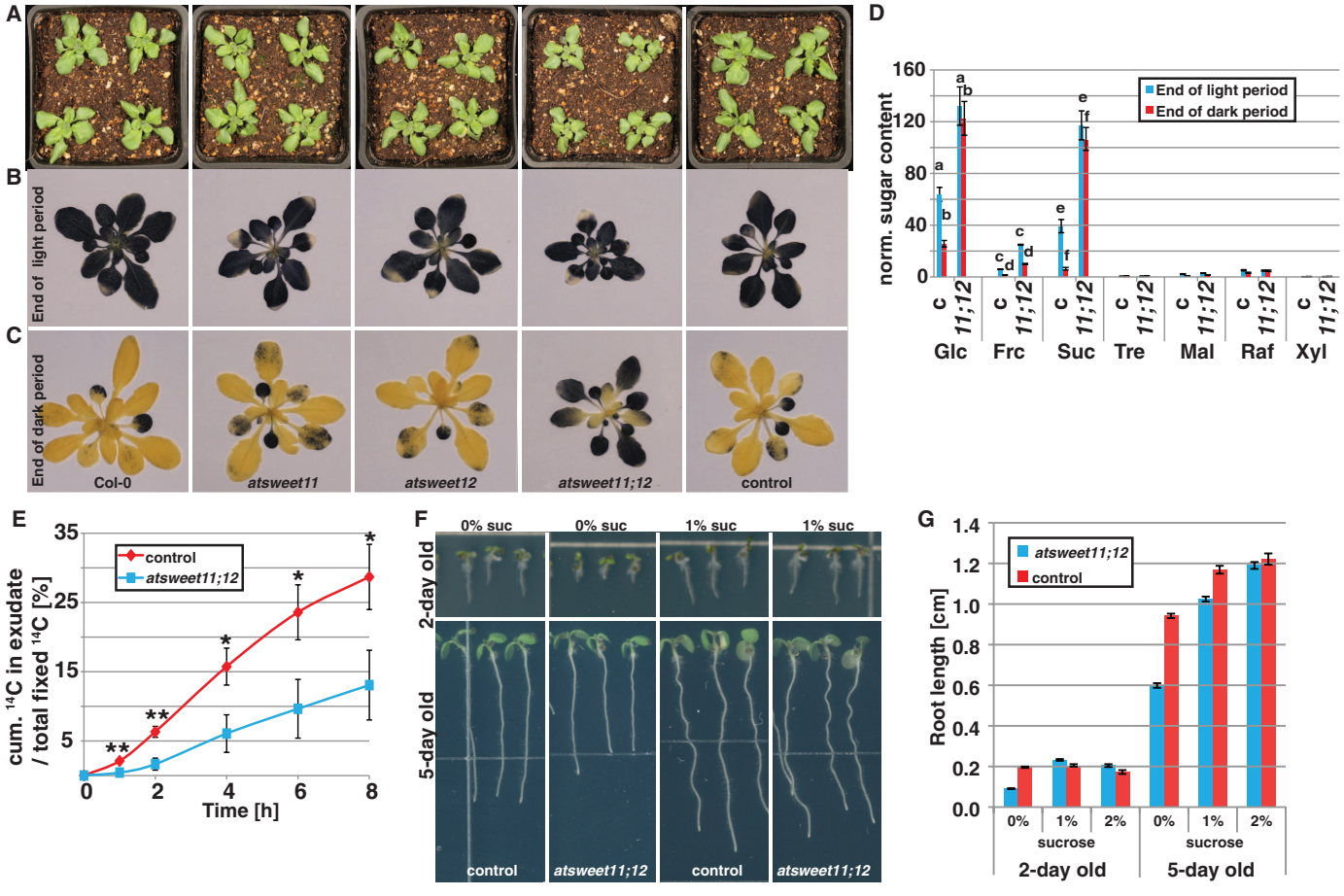

Fig. 2. Phenotypic characterization of AtSWEET11 and 12 mutants. (**A**) Reduced growth of the *atsweeet11;12* double mutant relative to Col-0 wild type and isogenic wild type (control). (**B** and **C**) Elevated starch accumulation in *atsweeet11;12* single and double mutants at the end of the light and dark periods (high light conditions). (**D**) Sugar levels in mature leaves at the end of the light and dark periods (±SEM, $n \geq 6$; identical letters indicate significance between pairs (daytime) according to *t* test ($P \leq 0.001$; high light conditions). Glc, glucose; Frc, fructose; Suc, sucrose; Tre, trehalose; Mal, maltose; Raf, raffinose; Xyl, xylose; c, control; *11;12*, *atsweet11;12*. (**E**) Cumulative exudation of [^{14}C]-derived assimilates from cut petioles of leaves fed with $^{14}CO_2$ (^{14}C in exudate shown as percentage in exudate plus exudate from the previous exudation period for each time point; ±SEM, $n = 5$; **t* significant at $P < 0.05$, ***t* significant at $P < 0.01$) (low light conditions). (**F** and **G**) Impaired root growth of *atsweet11;12* seedlings grown on sugar-free media and media supplemented with sucrose [±SEM, $n \geq 60$; two-way analysis of variance indicates a significant interaction ($P < 0.0001$) between genotype and sucrose treatment].

Xanthomonas oryzae pv. *oryzae*, was found to be expressed in the phloem of uninfected rice leaves (*23*), indicating that OsSWEET11 may play a similar role in phloem loading. Coimmunolocalization of SUT1/SUC2 and SWEET11/12 to an extent detectable by transmission electron microscopy will be required to unambiguously define the cell type in which the SWEETs are functioning.

Our findings are compatible with a model suggested by Geiger (*24*), in which sucrose moves symplasmically via plasmodesmata toward the phloem and then effluxes close to the site of apoplasmic loading (fig. S15). We predict that communication is needed to coordinate the efflux from phloem parenchyma with the uptake into the SE/CC to prevent spillover and limit the availability of nutrient resources for pathogens in the apoplasm of the leaf. Invertases and glucose/H^+ cotransporters that are induced during pathogen infection may serve in retrieval of sugars spilled at the infection site (*25*). It is tempting to speculate that sugar- and turgor-controlled regulatory mechanisms involved in post-phloem unloading may also apply to sucrose efflux in the phloem loading process (*26*, *27*). The availability of SWEET sucrose transporters, together with FRET sensors (*28*), provides valuable tools for studying the regulatory networks coordinating local and long-distance transport and metabolism.

Clade III SWEETs had previously been implicated as key targets of biotrophic pathogens. OsSWEET11 and 14 are co-opted during infection of rice by *Xanthomonas oryzae* pv. *oryzae* (Xoo) (*12*, *21*, *29*, *30*). Pathovar-specific effectors secreted by Xoo activate the transcription of clade III SWEET genes, and mutations in the effector binding sites in SWEET promoters lead to resistance to Xoo in a wide spectrum of rice lines (*21*, *29*–*31*). Our finding that these SWEETs are key elements of the phloem translocation machinery indicates that the pathogen retools a critical physiological function (i.e., a cellular sucrose efflux mechanism in the phloem) to gain access to the plant's energy resources at the site of infection.

However, this function is redundant in the plant. Such redundancy in both pathogen and host functions has been attributed to increased system robustness and may have evolved to allow the plant to survive mutations in essential functions that create pathogen resistance (*32*). It is possible that the highly localized transfer of sucrose between phloem parenchyma and SE/CC has evolved to limit sucrose release into the apoplasm to a limited interface of adjacent cells inside the phloem, and thus to reduce the availability of sucrose in the apoplasm to pathogens. Pathogens can overcome this first line of defense by targeting exactly this efflux mechanism in order to gain access to sugars in cells surrounding the infection site—for example, in the epidermis or mesophyll. Invertase and monosaccharide transporters, which are also typically induced during infection, may then serve as a secondary line of defense to reduce apoplasmic sugar levels at the infection site (*25*). The work presented here adds a crucial item to the list of machinery essential for carbon allocation: the transport proteins responsible for the efflux of sucrose to apoplasm in preparation for phloem loading.

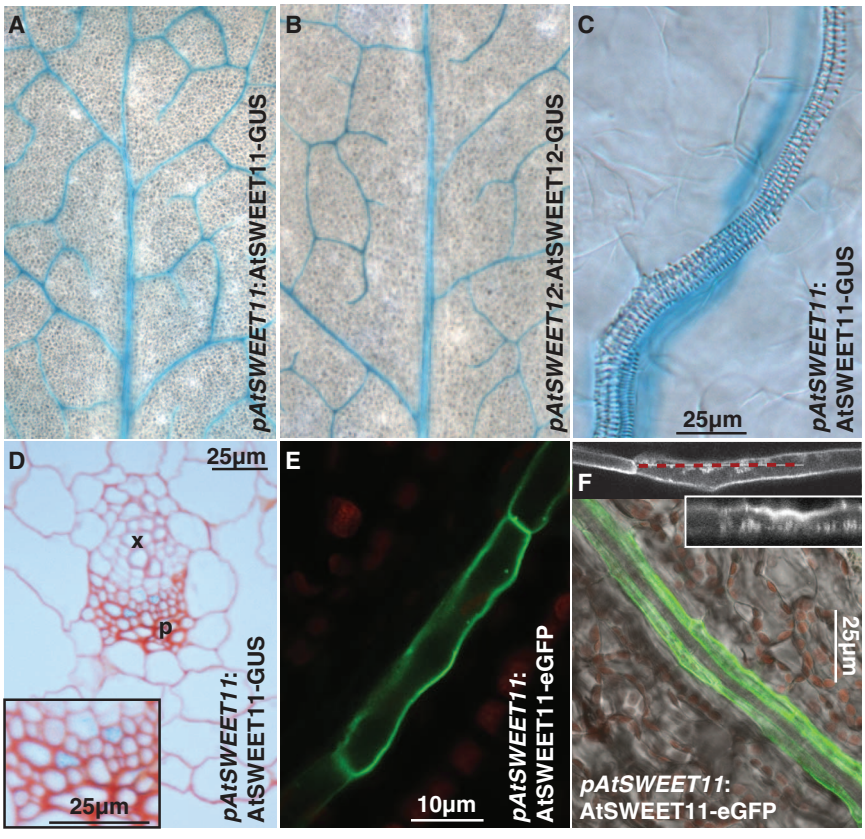

Fig. 3. GUS and eGFP localization of *AtSWEET11* and *12* promoter-reporter fusions. (**A** to **D**) GUS histochemistry analysis in rosette leaves of transgenic *Arabidopsis* plants expressing translational GUS fusions of *AtSWEET11* [(A), (C), and (D)] or 12 (B) from their native promoters. (A) and (B), GUS staining detected in leaf vein network; (C), high-resolution images of expression in one cell file of an individual vein; (D), cross section of *Arabidopsis* leaf showing cell-specific localization of AtSWEET11. (**E** and **F**) Confocal images of eGFP fluorescence in sepal vein cell files of transgenic *Arabidopsis* plants expressing translational AtSWEET11-eGFP fusions under control of its native promoter. Insets in (F) show eGFP channel in black and white; red dashed line in upper inset indicates position of *z*-scan shown in lower inset. eGFP accumulation is observed in static puncta, which may be caused by accumulation of AtSWEET11 in membranes in cell wall ingrowths, a characteristic feature of phloem parenchyma cells (*33*). The presence of cell wall ingrowth was confirmed by electron microscopy (fig. S14).

References and Notes

1. X. G. Zhu, S. P. Long, D. R. Ort, *Annu. Rev. Plant Biol.* **61**, 235 (2010).
2. A. H. Paterson, Z. K. Li, *Proc. Natl. Acad. Sci. U.S.A.* **108**, 10931 (2011).
3. S. Lalonde, D. Wipf, W. B. Frommer, *Annu. Rev. Plant Biol.* **55**, 341 (2004).
4. R. T. Giaquinta, *Annu. Rev. Plant Physiol.* **34**, 347 (1983).
5. B. G. Ayre, *Mol. Plant* **4**, 377 (2011).
6. Q. Fu, L. Cheng, Y. Guo, R. Turgeon, *Plant Physiol.* **157**, 1518 (2011).
7. J. W. Riesmeier, B. Hirner, W. B. Frommer, *Plant Cell* **5**, 1591 (1993).
8. J. W. Riesmeier, L. Willmitzer, W. B. Frommer, *EMBO J.* **11**, 4705 (1992).
9. J. W. Riesmeier, L. Willmitzer, W. B. Frommer, *EMBO J.* **13**, 1 (1994).
10. L. Bürkle *et al.*, *Plant Physiol.* **118**, 59 (1998).
11. J. R. Gottwald, P. J. Krysan, J. C. Young, R. F. Evert, M. R. Sussman, *Proc. Natl. Acad. Sci. U.S.A.* **97**, 13979 (2000).
12. L. Q. Chen *et al.*, *Nature* **468**, 527 (2010).
13. I. Lager, L. L. Looger, M. Hilpert, S. Lalonde, W. B. Frommer, *J. Biol. Chem.* **281**, 30875 (2006).
14. R. Lemoine, S. Delrot, *FEBS Lett.* **249**, 129 (1989).
15. J. W. Maynard, W. J. Lucas, *Plant Physiol.* **70**, 1436 (1982).
16. J. W. Yu *et al.*, *Mol. Cell* **13**, 677 (2004).
17. S. Santagata *et al.*, *Science* **292**, 2041 (2001).
18. D. Osuna *et al.*, *Plant J.* **49**, 463 (2007).
19. A. C. Srivastava, S. Ganesan, I. O. Ismail, B. G. Ayre, *Plant Physiol.* **148**, 200 (2008).
20. F. Rolland, E. Baena-Gonzalez, J. Sheen, *Annu. Rev. Plant Biol.* **57**, 675 (2006).
21. G. Antony *et al.*, *Plant Cell* **22**, 3864 (2010).
22. E. Haritatos, R. Medville, R. Turgeon, *Planta* **211**, 105 (2000).
23. Z. Chu *et al.*, *Theor. Appl. Genet.* **112**, 455 (2006).
24. D. R. Geiger, S. A. Sovonick, T. L. Shock, R. J. Fellows, *Plant Physiol.* **54**, 892 (1974).
25. P. N. Sutton, M. J. Gilbert, L. E. Williams, J. L. Hall, *Physiol. Plant.* **129**, 787 (2007).
26. J. W. Patrick, C. E. Offler, *J. Exp. Bot.* **52**, 551 (2001).
27. Y. Zhou *et al.*, *J. Exp. Bot.* **60**, 71 (2009).
28. S. Okumoto, H. Takanaga, W. B. Frommer, *New Phytol.* **180**, 271 (2008).

29. B. Yang, A. Sugio, F. F. White, *Proc. Natl. Acad. Sci. U.S.A.* **103**, 10503 (2006).
30. M. Yuan, Z. Chu, X. Li, C. Xu, S. Wang, *Plant Cell Physiol.* **50**, 947 (2009).
31. Z. Chu *et al.*, *Genes Dev.* **20**, 1250 (2006).
32. A. Lundby, H. Mutoh, D. Dimitrov, W. Akemann, T. Knöpfel, *PLoS ONE* **3**, e2514 (2008).
33. K. Ataka, V. A. Pieribone, *Biophys. J.* **82**, 509 (2002).

Acknowledgments: We thank G. Grossmann and D. Ehrhardt for advice and help with confocal imaging; J. Bailey-Serres for help with the translatome analyses; K. Barton and T. Liu for plastic embedding and sectioning help and advice; and V. Lanquar and A. Jones for critical reading of the manuscript. Supported by U.S. Department of Energy grant DE-FG02-04ER15542 and National Institute of Diabetes and Digestive and Kidney Diseases grant 1RO1DK079109 (W.B.F.); the Carnegie Institution and the Scholarship Program of the Chinese Scholarship Council (grant 2009635108) (X.-Q.Q.); and the Max-Planck-Gesellschaft (S.O. and A.R.F.). Author contributions: W.B.F. and L.-Q.C. conceived and designed the experiments. L.-Q.C., X.-Q.Q., D.S., B.-H.H., and S.O. performed the experiments. W.B.F., L.-Q.C., X.-Q.Q., D.S., B.-H.H., S.O., and A.R.F. analyzed the data. L.-Q.C. and W.B.F. wrote the manuscript.

Supporting Online Material
www.sciencemag.org/cgi/content/full/science.1213351/DC1
Materials and Methods
Figs. S1 to S15
References (*34*–*60*)

30 August 2011; accepted 8 November 2011
Published online 8 December 2011;
10.1126/science.1213351

Changes in Wind Pattern Alter Albatross Distribution and Life-History Traits

Henri Weimerskirch,[1]* Maite Louzao,[1,2]† Sophie de Grissac,[1] Karine Delord[1]

Westerly winds in the Southern Ocean have increased in intensity and moved poleward. Using long-term demographic and foraging records, we show that foraging range in wandering albatrosses has shifted poleward in conjunction with these changes in wind pattern, while their rates of travel and flight speeds have increased. Consequently, the duration of foraging trips has decreased, breeding success has improved, and birds have increased in mass by more than 1 kilogram. These positive consequences of climate change may be temporary if patterns of wind in the southern westerlies follow predicted climate change scenarios. This study stresses the importance of foraging performance as the key link between environmental changes and population processes.

The vast majority of studies of the effects of changing environments on species biology have been conducted in terrestrial ecosystems and temperature and rainfall have been the main environmental factors considered (*1*, *2*), potentially ignoring other key climatic variables. In marine systems, wind is a major component of the environment, and climate change–induced alterations in oceanic wind regimes and strength have already occurred (*3*) and are predicted to increase (*4*). For example, over the past 50 years, Southern Hemisphere westerlies have shifted poleward and increased in intensity following movement of the Southern Annular Mode (SAM, characterized as increased pressure between 40° and 65°S) into a positive phase (*5*, *6*). Such changes in wind regime may affect the movement or distribution of wind-dependent species, such as migratory land birds (*7*) or pelagic seabirds (*8*–*10*). Pelagic seabirds, in particular, are wide-ranging predators that rely extensively on wind to move at low costs between breeding and foraging sites (*8*, *11*), suggesting that they may be highly affected by wind pattern changes.

Here, we investigate whether changes in wind conditions over the Southern Ocean have influenced the foraging ecology and life-history traits of the wandering albatross (*Diomedea exulans*), one of the most wide-ranging pelagic seabirds. We aimed to assess whether the foraging performance of albatrosses has changed over the past few decades in relation to wind conditions and to understand the possible consequences of such change on life history (i.e., breeding performance and condition). We combine data on the duration of foraging trips and breeding success collected over nearly 40 years, from 1966 to 2010, as well as foraging performance and body mass (1989 to 2010) of breeders from Crozet Islands, located in the windiest area of the Southern Ocean.

In the western Indian Ocean sector of the Southern Ocean, wind speeds have increased in the center of the westerly flow (Fig. 1), as well as locally at Crozet (Fig. 2B), as a result of the shift of the global SAM index into a positive phase (Fig. 2A). No changes occurred in subtropical waters, whereas wind speed increased in sub-Antarctic waters, especially south of Crozet (table S1 and Fig. 1). When decomposing wind into its two components—zonal wind from west to east, and meridional wind from north to south (Fig. 1)—the most pronounced changes have occurred for the latter. The meridional component has strongly increased and shifted poleward, whereas these trends were not as strong for the zonal component (Figs. 1 and 2, C and D).

Crozet wandering albatrosses foraged from subtropical to Antarctic waters at a maximum range of more than 3500 km (Fig. 1, upper panels). Although both sexes overlap in the latitudinal band of 40° to 50°S, males prefer colder waters at the latitude of Crozet or to the south (down to 60°S), whereas females favor warmer waters to the north as far as 30°S (Fig. 1, lower panels). Foraging parameters estimated from tracking data have changed over the past 20 years in parallel to changes in wind conditions. The northern range (the most northerly latitude attained during a foraging trip) of wandering albatrosses was strongly influenced by meridional winds and shifted extensively poleward in females and to a smaller extent in males (Table 1 and Fig. 3), whereas there was no significant trend over time for the southern range (Table 1). Concurrently, there was a significant decrease in the maximum distance from the colony (Table 1, foraging range).

As shown by earlier studies (*8*, *11*), wind strongly influenced albatross flight speed. We found that the meridional component best explained the increase in flight speed during a foraging trip (Table 1). Flight speeds increased until 2008, whereas the last value of the time series (2010) was characterized by very low wind speeds, comparable to those in the early 1990s (Figs. 2 and 3). Travel speed (daily distance covered) increased in both sexes, in relation to wind speed, whereas total distance covered did not change (Table 1 and Fig. 3). Females spent a higher proportion of the overall foraging time in flight than males (Fig. 3). Thus, the increase in the daily distance covered was due, for females, to an increase in flight speed with a concomitant shift in distribution poleward into more windy conditions, whereas for males it was due to shorter time periods spent sitting on the water.

Even though the total distance covered did not increase over years, the duration of foraging trips decreased due to increasing meridional winds (Table 1). This decrease in the duration of trips was confirmed over a longer period (during the past 4 decades; in 1970, 1989, 1999, and 2008) from an independent large data set: The mean duration of foraging trips was highly variable (2 to 35 days), similar between sexes, and decreased by 22% between 1970 and 2008 (from 12.4 ± 6.8 to 9.7 ± 5.5 days; fig. S1, mixed effect analysis of variance, year effect $F_{3,724} = 11.3$, $P < 0.001$). Finally, the angle between flight direction and wind direction shifted by 10° from 1989 to 2010, with birds tending to use tail winds to a larger extent in the 1990s than in the 2000s (fig. S2).

[1]Centre d'Etudes Biologiques de Chizé, CNRS, 79360 Villiers en Bois, France. [2]Helmholtz Centre for Environmental Research, Permoserstrasse 15, 04318 Leipzig, Germany.

*To whom correspondence should be addressed. E-mail: henriw@cebc.cnrs.fr

†Present address: Instituto Español de Oceanografía, CO Xixón, Camín de l'Arbeyal s/n, 33212 Xixón, Spain.

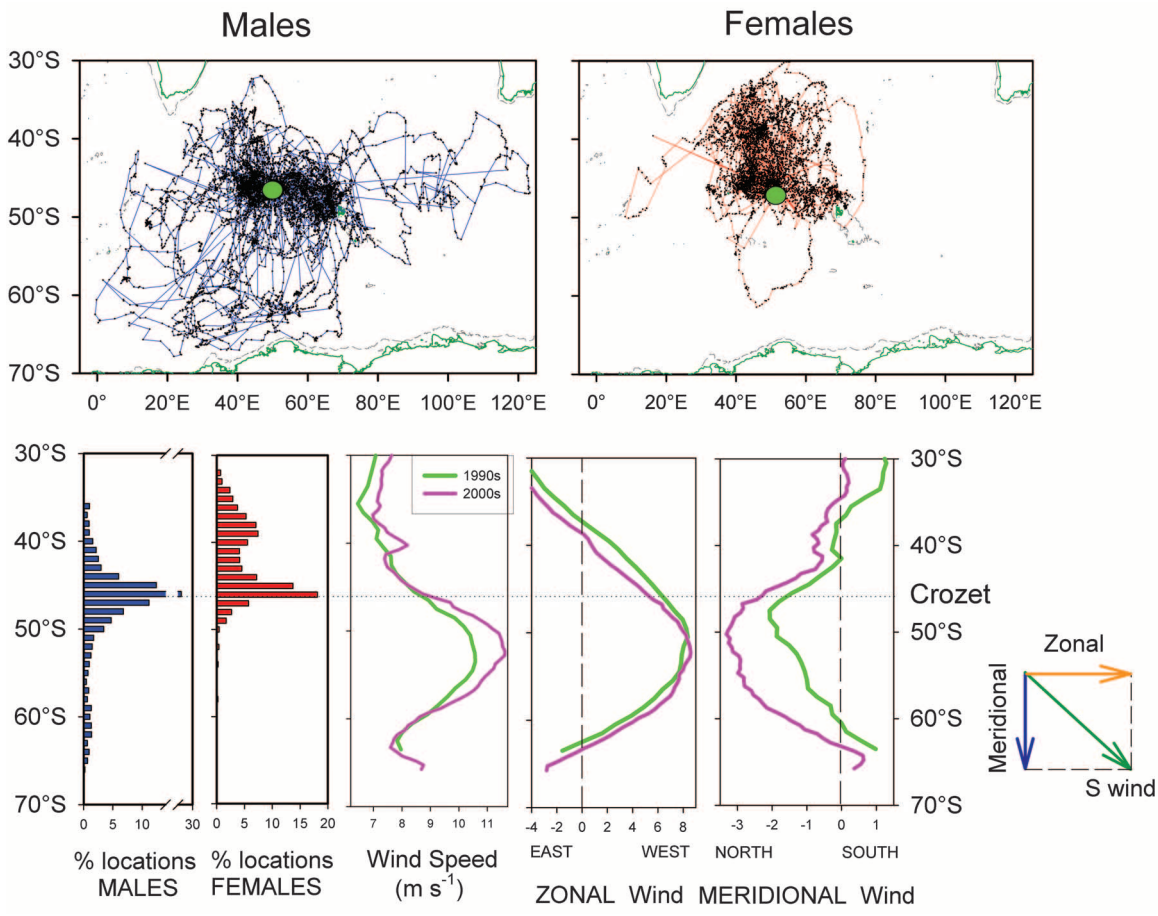

Fig. 1. Foraging trips (**Upper panels**), and frequency distribution according to latitude of locations (**Lower two left panels**) of breeding male and female wandering albatrosses during incubation period (January to February 1989 to 2010). (**Lower three right panels**) Changes in wind speed (S wind), and zonal and meridional winds according to latitudes during two periods (1990 to 1995 and 2000 to 2005). Green dots (upper panels) and dotted line (lower panels) indicate position of Crozet Islands

The breeding success of wandering albatrosses was on average 76.0 ± 6.5% and increased over the past 40 years (Fig. 4A). Breeding success is the result of failures that mainly occur during incubation (81.7 ± 9.1% of total failures, n = 18 years). We found that failures during incubation were explained by the foraging trip duration (generalized linear models, $F_{1,310}$ = 5.7, P = 0.018). Specifically, the probability of breeding failure increased with the duration of foraging trips. In parallel, the body mass of incubating males and females increased significantly over the past 20 years by 1 kg, i.e., by 10 to 12% of the body mass ($F_{8,519}$ = 12.3, P < 0.0001 and $F_{8,498}$ = 17.2, P < 0.0001, respectively; Fig. 4B). This increase in body mass was not related to changes in body size (no change in the length of the beak length was recorded over the same period; males: $F_{9,424}$ = 1.5, P = 0.143; females: $F_{9,402}$ = 1.46, P = 0.158).

Wandering albatrosses appear so far to have benefited from wind changes occurring in the Southern Ocean, with higher speeds allowing for more rapid travel. In wandering albatrosses, the probability of prey encounter and capture is related to the daily distances individuals are able to cover (*12*). In the 2000s, birds moved quicker than in the 1990s and thus were able to cover similar distances during shorter bouts at sea. Simultaneously, tracked birds shifted their range southward (Fig. 3), a trend also documented from line transects in the southwestern Indian Ocean over the past 30 years (*13*). Females have shifted poleward their northern range to a larger extent than males. This southward shift of the northern range allows females to fly at higher speeds in windier areas, as well as in waters less distant from the colonies, and thus to further reduce foraging time. Because males and females share incubation duties (*14*), the reduction of foraging time resulted in shorter incubation shifts and thus a lower probability

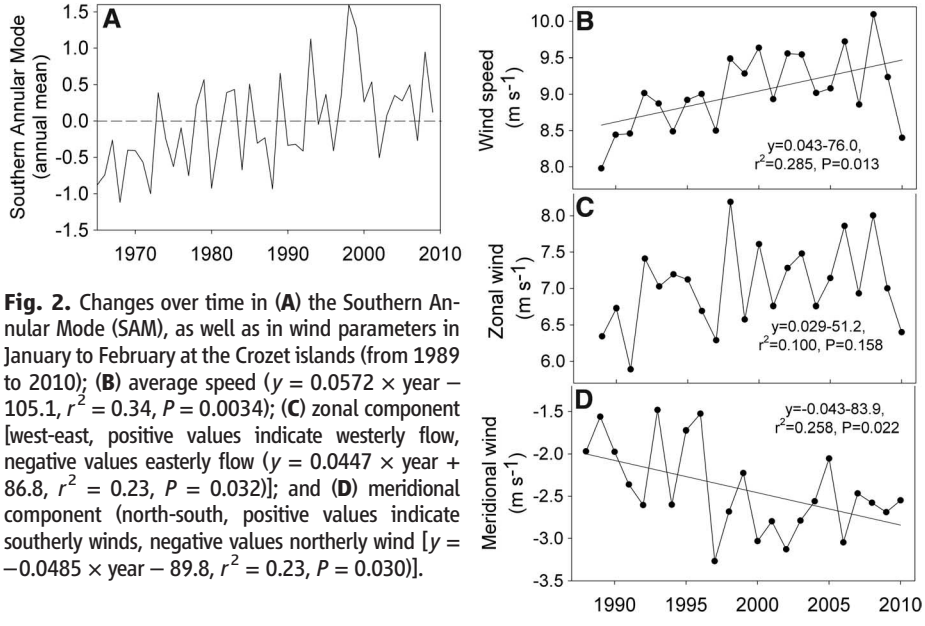

Fig. 2. Changes over time in (**A**) the Southern Annular Mode (SAM), as well as in wind parameters in January to February at the Crozet islands (from 1989 to 2010); (**B**) average speed (y = 0.0572 × year − 105.1, r^2 = 0.34, P = 0.0034); (**C**) zonal component [west-east, positive values indicate westerly flow, negative values easterly flow (y = 0.0447 × year + 86.8, r^2 = 0.23, P = 0.032)]; and (**D**) meridional component (north-south, positive values indicate southerly winds, negative values northerly wind [y = −0.0485 × year − 89.8, r^2 = 0.23, P = 0.030)].

Table 1. Estimated parameters (±SE) of retained models of the stepwise procedure using the Akaike Information Criteria (AIC) scores to explain foraging parameters of wandering albatrosses.

Parameter	Final model	Sex		Year		Wind speed (WS)		Meridional wind (MW)		AIC
			P-value	Estimate (±SE)	*P*-value	Estimate (±SE)	*P*-value	Estimate (±SE)	*P*-value	
Trip duration	~Year + MW + sex:year			−0.029 ± 0.087	0.017			+0.615 ± 0.195	0.002	512.4
Total distance covered	~WS					−465 ± 169	0.007			2674.9
Maximum range	~Year + WS			−19.7 ± 8.0	0.025	−136.2 ± 40	0.001			2297.7
Travel speed	~Sex + year + WS	F > M	0.004	0.128 ± 0.029	<0.001	0.271 ± 0.138	0.052			296.3
Flight speed	~MW							-0.207 ± 0.09	0.023	196.1
Percent time on water	~Sex + year + MW + sex:MW	M > F	<0.001	−0.741 ± 0.219	<0.001			2.10 ± 0.751	0.007	492.5
Northern range	~Sex + MW	F > M	<0.001					0.221 ± 0.162	0.013	451.6
Southern range	~Sex + WS	F > M	<0.001			0.623 ± 0.249	0.013			504.1

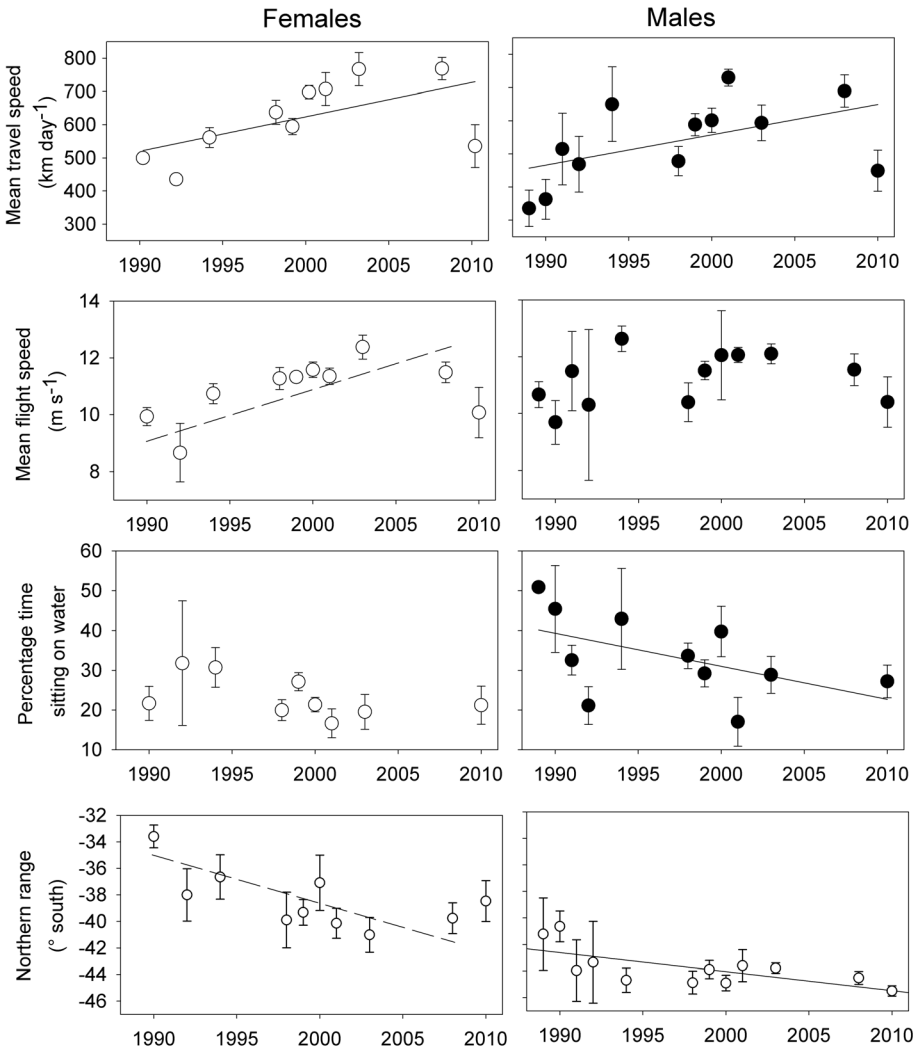

Fig. 3. Changes between 1989 and 2010 in four foraging parameters of male and female Crozet wandering albatrosses (mean ± 1 SD). Continuous lines indicate significant trends over time. (Dotted lines indicate significant trends over years when the atypical 2010 year is excluded from analysis.)

of breeding failure. Our results indicate that shorter foraging trips and fasts of incubating birds on the nest likely account for the increase in breeding success. The observed southward shift of the northern range of females may also have positive consequences in terms of conservation. The wandering albatross Crozet population has decreased as a result of adult mortality, especially in females, due to longline fishing targeting tuna in subtropical waters (*15*, *16*). If the range of breeding females moves southward due to environmental changes, they will be less likely to overlap with tuna longliners, whose effort has not shifted southward during the past 50 years (*17*).

One of the most unexpected changes we observed over the past 20 years was a considerable increase of both males and females by more than 1 kg in body mass. Such an increase in mass for a similar structural size has important implications for flight performance because it results in an increase in wing loading (*18*). Higher wing loading allows albatrosses using dynamic soaring flight to exploit windier zones, because stronger winds increase airspeeds and lift required by high wing loading (*19*). Thus, increased mass may not only be the result of increased body stores due to shorter fasts of birds on the nest but may also constitute an adaptive response to windier conditions.

So far, past climate changes have affected positively the foraging efficiency and foraging range of wandering albatrosses, ultimately improving breeding success and reducing mortality risks, respectively. However, these positive effects may not last in the future. Indeed, the shift to positive values of the SAM during the past half century is projected to carry on, with westerlies continuing to move poleward and increase in intensity (fig. S3). By 2080, wind speed, as well as meridional and zonal winds, should be higher south of Crozet, but lower to the north, with a reversing of zonal and meridional wind at the extremes of the range of wandering albatrosses (fig. S3) with several potential consequences for the Crozet population. Travel and flight speeds will not respond linearly to the increase in wind speed, and too strong gales winds become unfavorable for dynamic soaring flights (*20*). In addition, the poleward shift of westerlies to an increasing distance to the south of the colonies will likely make the location of Crozet less optimal for central-place foraging birds. In addition, if the present trend in the use of tail to side winds continues, costs of foraging should increase with increasing head winds and more distant favorable winds (*8*). Similarly to

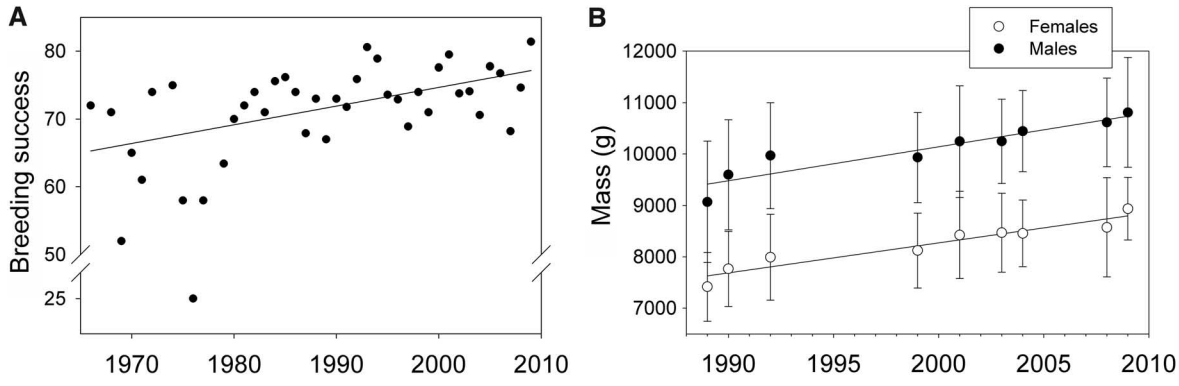

Fig. 4. (**A**) Changes in breeding success over the past 40 years ($r^2 = 0.30$, $P = 0.0003$). From 1988 to 2009 only, $r^2 = 0.19$, $P = 0.048$. (**B**) Changes over the past 20 years in the mass of breeding wandering albatrosses in January to February.

wandering albatrosses, the movements of many other species of albatrosses and petrels are strongly constrained by wind conditions (*8*, *21*), and species richness of Procellariiformes is positively associated to wind speed (*22*). Thus, future research should consider wind fields as an important driver of the distribution and migration of these oceanic species.

References and Notes

1. C. Parmesan, *Annu. Rev. Ecol. Syst.* **37**, 637 (2006).
2. G.-R. Walther *et al.*, *Nature* **416**, 389 (2002).
3. I. R. Young, S. Zieger, A. V. Babanin, *Science* **332**, 451 (2011).
4. S. Solomon, *Climate Change 2007: The Physical Science Basis. Contribution of Working Group I to the Fourth Assessment Report of the Intergovernmental Panel on Climate Change* (Cambridge Univ. Press, Cambridge, 2007).
5. N. P. Gillett, D. W. Thompson, *Science* **302**, 273 (2003).
6. D. W. Thompson, S. Solomon, *Science* **296**, 895 (2002).
7. T. Alerstam, D. Christie, A. Ulfstrand, *Bird Migration* (Cambridge Univ. Press, Cambridge, 1993).
8. H. Weimerskirch, T. Guionnet, J. Martin, S. A. Shaffer, D. P. Costa, *Proc. Biol. Sci.* **267**, 1869 (2000).
9. A. M. Felicísimo, J. Muñoz, J. González-Solis, *PLoS ONE* **3**, e2928 (2008).
10. R. M. Suryan *et al.*, *PLoS ONE* **3**, e4016 (2008).
11. E. Wakefield *et al.*, *Ecol. Monogr.* **79**, 663 (2009).
12. H. Weimerskirch, A. Gault, Y. Cherel, *Ecology* **86**, 2611 (2005).
13. C. Péron *et al.*, *Glob. Change Biol.* **16**, 1895 (2010).
14. H. Weimerskirch, *Oecologia* **102**, 37 (1995).
15. H. Weimerskirch, N. Brothers, P. Jouventin, *Biol. Conserv.* **79**, 257 (1997).
16. G. N. Tuck, T. Polacheck, J. P. Croxall, H. Weimerskirch, *J. Appl. Ecol.* **38**, 1182 (2001).
17. G. N. Tuck, T. Polacheck, C. M. Bulman, *Biol. Conserv.* **114**, 1 (2003).
18. C. Pennycuick, *Bird Flight Performance: A Practical Calculation Manual* (Oxford Univ. Press, Oxford, 1989).
19. S. A. Shaffer, H. Weimerskirch, D. Costa, *Funct. Ecol.* **15**, 203 (2001).
20. T. Alerstam, G. A. Gudmundsson, B. Larsson, *Philos. Trans. R. Soc. Lond. B Biol. Sci.* **340**, 55 (1993).
21. J. González-Solís *et al.*, *Mar. Ecol. Prog. Ser.* **391**, 221 (2009).
22. R. Davies, U. Irlich, S. Chown, K. Gaston, *Glob. Ecol. Biogeogr.* **19**, 98 (2009).

Acknowledgments: The long-term data on the demography and foraging ecology of wandering albatrosses at Possession Island, Crozet Islands, were supported by the French Polar Institute IPEV (program no. 109 to H.W.), with additional funding from the Prince Albert II de Monaco Foundation. The study is a contribution to the Program ANR Biodiversité 2005-11 REMIGE. We acknowledge the modeling groups, the Program for Climate Model Diagnosis and Intercomparison (PCMDI), and the World Climate Research Programme's (WCRP's) Working Group on Coupled Modeling (WGCM) for their roles in making available the WCRP CMIP-3 multimodel data set. Support for data and model selection was provided by S. Jenouvrier. We thank the many field workers involved in the Crozet long-term monitoring since 1966 and in tracking programs since 1989, and D. Besson for help with the management of the demographic database. M.L. was funded by a postdoctoral contract of the Spanish Ministry of Education and Science (Ref. EX2007-1148) and Marie Curie Individual Fellowship (PIEF-GA-2008-220063). We are grateful to L. Riotte-Lambert for help with data analysis and C. Barbraud, C. A. Bost, Y. Cherel, and S. Jenouvrier for comments on the manuscript.

Supporting Online Material

www.sciencemag.org/cgi/content/full/335/6065/211/DC1
Materials and Methods
SOM Text
Figs. S1 to S3
References (*23*–*25*)

24 June 2011; accepted 11 October 2011
10.1126/science.1210270

Plant Species Richness and Ecosystem Multifunctionality in Global Drylands

Fernando T. Maestre,[1]* José L. Quero,[1] Nicholas J. Gotelli,[2] Adrián Escudero,[1] Victoria Ochoa,[1] Manuel Delgado-Baquerizo,[3] Miguel García-Gómez,[1,4] Matthew A. Bowker,[5] Santiago Soliveres,[1] Cristina Escolar,[1] Pablo García-Palacios,[1] Miguel Berdugo,[1] Enrique Valencia,[1] Beatriz Gozalo,[1] Antonio Gallardo,[3] Lorgio Aguilera,[6] Tulio Arredondo,[7] Julio Blones,[8] Bertrand Boeken,[9] Donaldo Bran,[10] Abel A. Conceição,[11] Omar Cabrera,[12] Mohamed Chaieb,[13] Mchich Derak,[14] David J. Eldridge,[15] Carlos I. Espinosa,[12] Adriana Florentino,[16] Juan Gaitán,[10] M. Gabriel Gatica,[17] Wahida Ghiloufi,[13] Susana Gómez-González,[18] Julio R. Gutiérrez,[6] Rosa M. Hernández,[19] Xuewen Huang,[20] Elisabeth Huber-Sannwald,[7] Mohammad Jankju,[21] Maria Miriti,[22] Jorge Monerris,[23] Rebecca L. Mau,[24] Ernesto Morici,[25] Kamal Naseri,[21] Abelardo Ospina,[16] Vicente Polo,[1] Aníbal Prina,[25] Eduardo Pucheta,[17] David A. Ramírez-Collantes,[23] Roberto Romão,[11] Matthew Tighe,[26] Cristian Torres-Díaz,[18] James Val,[27] José P. Veiga,[28] Deli Wang,[29] Eli Zaady[30]

Experiments suggest that biodiversity enhances the ability of ecosystems to maintain multiple functions, such as carbon storage, productivity, and the buildup of nutrient pools (multifunctionality). However, the relationship between biodiversity and multifunctionality has never been assessed globally in natural ecosystems. We report here on a global empirical study relating plant species richness and abiotic factors to multifunctionality in drylands, which collectively cover 41% of Earth's land surface and support over 38% of the human population. Multifunctionality was positively and significantly related to species richness. The best-fitting models accounted for over 55% of the variation in multifunctionality and always included species richness as a predictor variable. Our results suggest that the preservation of plant biodiversity is crucial to buffer negative effects of climate change and desertification in drylands.

Two decades of research have revealed causal linkages between biodiversity and univariate measures of ecosystem functioning, such as primary productivity or nitrogen accumulation, in many terrestrial and aquatic habitats (*1*–*4*). These relationships suggest that the loss of biodiversity may impair the functioning of natural ecosystems and thus diminish

the number and quality of services they provide (*5*–*7*). Ecosystems are valued for their ability to maintain multiple functions and services simultaneously [multifunctionality (*8*)]. If the maintenance of biodiversity is to be justified as a strategy for enhancing ecosystem services (*5, 9*), it is essential to understand how biodiversity affects multifunctionality (*8*–*10*). Existing knowledge comes from controlled small-scale experiments from a limited number of ecosystems, mainly in North America and Europe (*8*–*12*). Furthermore, biodiversity is by no means the only, or even the primary, driver of ecosystem functioning, which is also influenced by other biotic and abiotic factors (*13, 14*). Given this complexity, a rigorous examination is needed of the role of biodiversity in maintaining multifunctionality at a large number of sites that represent a wide range of spatial variability in resource availability, abiotic factors, and species richness and composition (*15*).

Arid, semi-arid, and dry-subhumid ecosystems (called hereafter "drylands") constitute some of the largest terrestrial biomes, collectively covering 41% of Earth's land surface and supporting over 38% of the global human population (*16*). Drylands host many endemic plant and animal species (*5*) and include about 20% of the major centers of global plant diversity and over 30% of the designated endemic bird areas (*17*). These ecosystems are also highly vulnerable to global environmental change and desertification (*16, 18*). Nevertheless, the relationship between biodiversity and ecosystem functioning has seldom been studied in drylands (*19*). We evaluated how the richness of perennial vascular plants (hereafter "species richness") and a range of key abiotic factors (climate, slope, elevation, and soil texture) relate to multifunctionality in 224 dryland ecosystems sampled from all continents except Antarctica (map S1). We surveyed plots measuring 30 m × 30 m, which were large enough to represent the main ecosystem features at each site, and assessed 14 ecosystem functions related to the cycling and storage of carbon (C: organic C, β-glucosidase, pentoses, hexoses, aromatic compounds, and phenols), nitrogen (N: total N, NO_3^--N, NH_4^+-N, aminoacids, proteins, and potential N transformation rate), and phosphorus (P: available inorganic P and phosphatase). These functions were chosen because they deliver some of the fundamental supporting and regulating ecosystem services (*9, 18, 20*) and because they are used to identify the onset of desertification processes (*21*). Our survey captured a substantial range of the climatic conditions, ecosystem types, and soil classes found in drylands worldwide (fig. S1 and map S1).

We first evaluated the direct relationship between species richness and multifunctionality at the global scale using both nonspatial [ordinary least-squares (OLS)] and spatial [simultaneous autoregression (SAR)] regression models (*20*). Because we did not experimentally control for other abiotic and biotic factors that are known to affect ecosystem functioning, significant relationships would indicate potentially strong effects of richness on multifunctionality. To quantify multifunctionality, we calculated *Z*-scores (standardized deviates) of the 14 functions evaluated (*20*). The multifunctionality index *M* for each plot was the average *Z*-score for all functions measured within the plot. This index measures all functions on a common scale of standard deviation units, has good statistical properties, and is well correlated with previously proposed indices for quantifying multifunctionality (*20*) (fig. S4). Multifunctionality was positively and significantly ($P < 0.05$) related to species richness, according to both OLS and SAR models (Fig. 1A). Separate analyses of functions related to the C, N, and P cycles (*20*) also yielded positive and significant relationships with species richness in all cases when using OLS regression (Fig. 1, B to D). When SAR regressions were used, significant relationships were found only for functions related to C cycling (Fig. 1, B to D).

We then evaluated whether the observed effects of species richness were important as compared to those of abiotic factors, with a multimodel inference approach based on information theory and OLS regression (*22*). We built separate models using the multifunctionality index *M* and functions from the N, C, and P cycles as dependent variables, and seven abiotic variables [sand content, slope, elevation, and four components derived from a principal-components analysis of 21 available climatic variables (*20*)] plus species richness as potential independent variables. Among the 255 possible models resulting from all possible combinations of these independent variables, we selected the set of best-fitting models that minimized the second-order Akaike information criterion (AIC_c). Collinearity among independent variables in these models was negligible (*20*) (table S15). Whenever a model included species richness as an important predictor, we compared its AIC_c to that of the corresponding model without species richness; differences < 2.0 in AIC_c between alternative models indicate that they are approximately equivalent in explanatory power (*22*). To account for potential effects of spatial autocorrelation between sites, latitude and longitude were included in all the models (*23*).

The best and most parsimonious models (smallest AIC_c and fewest variables with comparable AIC_c, respectively) describing global multifunctionality contained 9 and 7 predictor variables (Table 1). Both models explained more than 55% of the variance found in multifunctionality, and included species richness. In both cases, the removal of species richness as a predictor variable substantially reduced the model fit (Table 1). These results were virtually identical to those obtained with SAR regression and OLS models that included quadratic terms, to account for potential autocorrelation and nonlinear effects, respectively (*20*) (tables S2 and S3), and for models that used other multifunctionality indices proposed in the literature (*20*) (table S13). Species richness

[1]Área de Biodiversidad y Conservación, Departamento de Biología y Geología, Escuela Superior de Ciencias Experimentales y Tecnología, Universidad Rey Juan Carlos, Calle Tulipán Sin Número, 28933 Móstoles, Spain. [2]Department of Biology, University of Vermont, Burlington, VT 05405, USA. [3]Departamento de Sistemas Físicos, Químicos y Naturales, Universidad Pablo de Olavide, Carretera de Utrera kilómetro 1, 41013 Sevilla, Spain. [4]Departamento de Ingeniería y Morfología del Terreno, Escuela Técnica Superior de Ingenieros de Caminos, Canales y Puertos, Universidad Politécnica de Madrid, Calle Profesor Aranguren Sin Número, 28040 Madrid. [5]U.S. Geological Survey, Southwest Biological Science Center, Post Office Box 5614, ARD Building, Northern Arizona University, Flagstaff, AZ 86011, USA. [6]Departamento de Biología, Universidad de La Serena, Casilla 599, La Serena, Chile. [7]División de Ciencias Ambientales, Instituto Potosino de Investigación Científica y Tecnológica, Código Postal 78210 San Luis Potosí, San Luis Potosí Mexico. [8]Laboratorio de Biología Vegetal, Centro de Agroecología Tropical, Instituto de Estudios Científicos y Tecnológicos, Universidad Simón Rodríguez, Apdo 47925, Caracas, Venezuela. [9]Jacob Blaustein Institutes for Desert Research, Ben-Gurion University of the Negev, Sde-Boqer Campus 84990, Israel. [10]Instituto Nacional de Tecnología Agropecuaria, Estación Experimental San Carlos de Bariloche, Casilla de Correo 277 (8400), Bariloche, Río Negro, Argentina. [11]Departamento de Ciências Biológicas, Universidade Estadual de Feira de Santana, Avenida Transnordestina Sin Número, Bairro Novo Horizonte, Feira de Santana, Brasil. [12]Instituto de Ecología, Universidad Técnica Particular de Loja, San Cayetano Alto, Marcelino Champagnat, Loja, Ecuador. [13]Université de Sfax, Faculté des Sciences, Unité de Recherche Plant Diversity and Ecosystems in Arid Environments, Route de Sokra, kilomètre 3.5, Boîte Postale 802, 3018, Sfax, Tunisia. [14]Direction Régionale des Eaux et Forêts et de la Lutte Contre la Désertification du Rif, Avenue Mohamed 5, Boîte Postale 722, 93000 Tétouan, Morocco. [15]School of Biological, Earth and Environmental Sciences, University of New South Wales, Sydney, New South Wales 2052, Australia. [16]Instituto de Edafología, Facultad de Agronomía, Universidad Central de Venezuela, Ciudad Universitaria, Caracas, Venezuela. [17]Departamento de Biología, Facultad de Ciencias Exactas, Físicas y Naturales, Universidad Nacional de San Juan, J5402DCS Rivadavia, San Juan, Argentina. [18]Laboratorio de Genómica y Biodiversidad, Departamento de Ciencias Básicas, Universidad del Bío-Bío, Chillán, Chile. [19]Laboratorio de Biogeoquímica, Centro de Agroecología Tropical, Universidad Experimental Simón Rodríguez, Apdo 47925, Caracas, Venezuela. [20]Department of Biology and Chemistry, Hulunbuir College, Hailar, Inner Mongolia 021008, China. [21]Department of Range and Watershed Management, Faculty of Natural Resources and Environment, Ferdowsi University of Mashhad, Azadi Square, Mashhad, 91775–1363, Iran. [22]Department of Evolution, Ecology and Organismal Biology, Ohio State University, 318 West 12th Avenue, Columbus, OH 43210, USA. [23]Departamento de Biología, Facultad de Ciencias, Universidad Nacional Agraria La Molina, Avenida La Molina Sin Número, Lima, Peru. [24]Department of Biological Sciences, Northern Arizona University, Post Office Box 5640, Flagstaff, AZ 86011–5640, USA. [25]Facultad de Agronomía, Universidad Nacional de La Pampa, Casilla de Correo 300, 6300 Santa Rosa, La Pampa, Argentina. [26]Department of Agronomy and Soil Science, School of Environmental and Rural Science, University of New England, Armidale, New South Wales 2351, Australia. [27]Office of Environment and Heritage, Post Office Box 363, Buronga, New South Wales 2739, Australia. [28]Departamento de Ecología Evolutiva, Museo Nacional de Ciencias Naturales, José Gutiérrez Abascal, 2, 28006 Madrid, Spain. [29]Institute of Grassland Science, Northeast Normal University, Key Laboratory of Vegetation Ecology, Ministry of Education, Changchun, Jilin 130024, China. [30]Department of Natural Resources and Agronomy, Agriculture Research Organization, Ministry of Agriculture, Gilat Research Center, Mobile Post Negev 85280, Israel.

*To whom correspondence should be addressed. E-mail: fernando.maestre@urjc.es

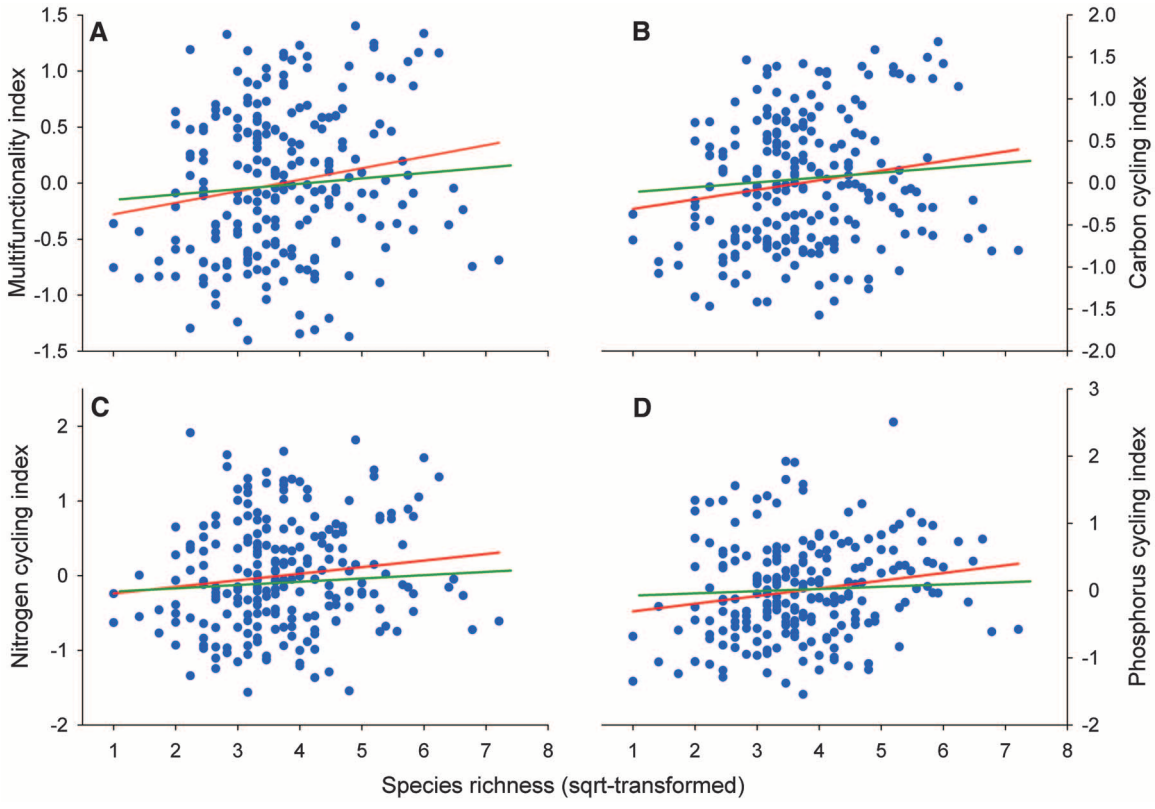

Fig. 1. Relationship between perennial plant species richness and ecosystem multifunctionality (**A**) measured in a global survey of drylands. Similar relationships for C (**B**), N (**C**), and P (**D**) cycling are shown. Red and green lines are the fitted lines from OLS and SAR regressions, respectively. Results of regressions are as follows: (A) OLS, R^2 (percent of variation in multifunctionality explained by the model) = 0.030, $P = 0.009$; SAR, $R^2 = 0.022$, $P = 0.027$; (B) OLS, $R^2 = 0.029$, $P = 0.011$; SAR, $R^2 = 0.022$, $P = 0.027$; (C) OLS, $R^2 = 0.018$, $P = 0.044$; SAR, $R^2 = 0.014$, $P = 0.082$; and (D) OLS, $R^2 = 0.032$, $P = 0.008$; SAR, $R^2 = 0.016$, $P = 0.061$.

was also an important factor in separate models of C and N cycling (tables S4, S5, S7, S8, S10, and S11) but had weaker effects on P cycling (tables S6, S9, and S12). Overall, the general result that species richness makes important contributions to multifunctionality was robust to the analytical methods used and to the choice of multifunctionality index.

To quantify the relative importance of the different predictors of multifunctionality, we summed the Akaike weights for each predictor across all the models in which it occurred (*20, 22*); the larger this sum, the more important a given variable is relative to the other variables used in the same models. By this criterion, the two most important predictors of multifunctionality were annual mean temperature [reflected in large negative loadings for the fourth principal component of the climatic variables (*20*)] and the sand content of the soil (Fig. 2A). Both variables were negatively related to multifunctionality: Higher ecosystem functionality was found at cooler temperatures and lower sand content (table S14). The importance of species richness was very similar to that of mean temperature and sand content. Indeed, species richness was more important than climatic variables such as mean annual rainfall and mean temperature and rainfall in the driest quarter [reflected in loadings on the first and third principal components of the climatic variables, respectively (*20*)]. Similar results were obtained when functions related to the C and N cycles were evaluated separately (Fig. 2, B and C). Species richness was less important to P cycling than were other abiotic factors such as sand content, elevation, and annual rainfall (Fig. 2D).

Table 1. Best-fitting regression models of ecosystem multifunctionality. Each column represents a different predictor variable (red, perennial plant species richness; green, abiotic variables; blue, climatic variables; gold, geographic variables). Of all 255 possible models, the best 8 models are presented, ranked according to AIC_c value. AIC_c measures the relative goodness of fit of a given model; the lower its value, the more likely it is that this model is correct. Unshaded cells indicate variables that were not included in a particular model. The first and third models of the table are the best and most parsimonious models, respectively; the same models without species richness had $R^2 = 0.539$, $AIC_c = 293.236$, $\Delta AIC_c = 10.486$; and $R^2 = 0.515$, $AIC_c = 300.078$, $\Delta AIC_c = 17.328$, respectively. ΔAIC_c, difference between the AIC_c of each model and that of the best model; w_i, Akaike weights; C1, C2, C3, and C4, first, second, third, and fourth components of a principal-components analysis conducted with climatic variables; SA, sand content; SL, slope angle (square root–transformed); EL, elevation (square root–transformed); LA, latitude; and LO, longitude.

Species richness	Abiotic		Climatic				Geographic			R^2	AIC_c	ΔAIC_c	w_i
	SL	SA	C1	C2	C3	C4	LA	LO	EL				
■	■	■	■		■	■	■	■	■	0.564	282.750	0	0.217
■	■	■				■	■	■	■	0.559	283.226	0.475	0.171
■	■	■	■	■		■	■	■	■	0.554	283.595	0.845	0.143
■	■	■	■	■	■		■	■	■	0.558	283.862	1.111	0.125
■	■	■	■	■	■	■	■	■	■	0.565	284.502	1.751	0.091
■	■	■	■		■		■	■	■	0.556	284.637	1.887	0.085
■	■	■		■	■	■	■	■	■	0.561	284.677	1.927	0.083
■	■	■	■	■		■	■	■	■	0.560	285.035	2.285	0.069

The positive effects of species richness on multifunctionality may be mediated through increased net primary production (NPP), which has cascading effects on multiple organisms and ecosystem processes (*1, 24*). However, the relationship between plant species richness and NPP is uncertain (*25*), and NPP could not be measured in this study. We speculate instead that complementarity in the use of resources such as water (*2, 9*), which has been demonstrated in drylands and can occur without changes in NPP (*26, 27*), accounts for correlations between species richness and multifunctionality. Our results also implicate soil water conditions, which are largely affected by temperature and soil texture (*28*), as an important driver of multifunctionality.

By itself, species richness accounted for only a small fraction of the observed variation in the

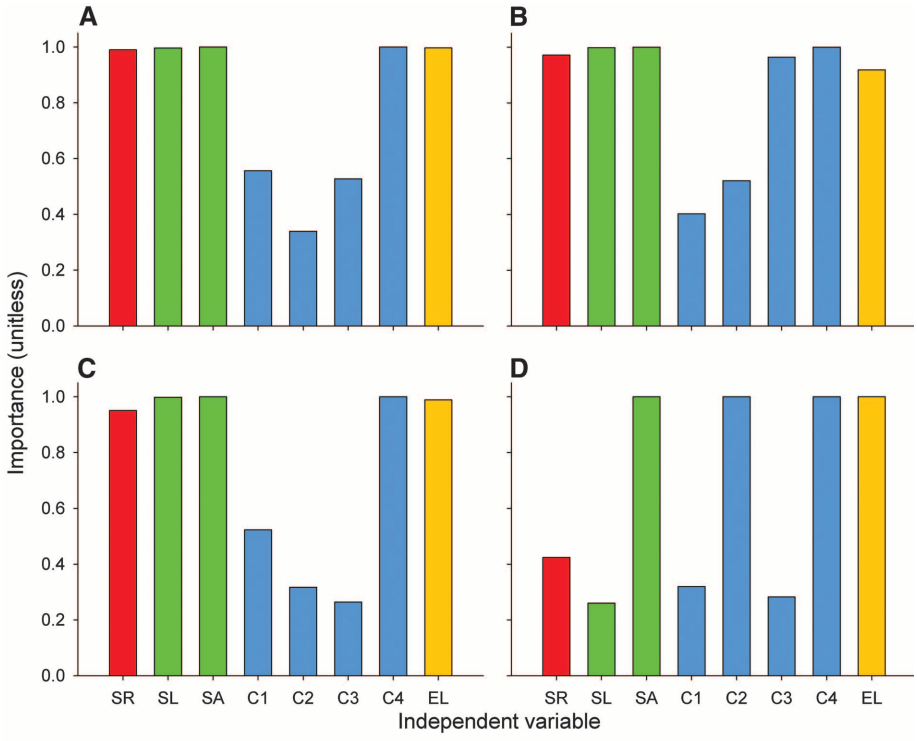

Fig. 2. Relative importance of perennial plant species richness (red column) and other predictor variables in models of ecosystem multifunctionality (**A**) and C (**B**), N (**C**), and P (**D**) cycling. The height of each bar is the sum of the Akaike weights of all models that included the predictor of interest, taking into account the number of models in which each predictor appears. Variable abbreviations are as in Table 1.

multifunctionality of drylands (Fig. 1). However, the best-fitting models accounted for over 55% of this variation and always included species richness (Table 1). The unexplained variation probably reflects factors not measured in our global survey, including the intensity of herbivory, historical patterns of land use, the presence of keystone and invasive species, and differences in components of biodiversity such as soil fauna, whose changes along environmental gradients do not necessarily track those of plant richness (*28*–*30*).

Climate change models predict increases in average annual temperature in drylands of up to 4°C by the end of the 21st century (*31*). Our results suggest that such an increase will reduce the ability of dryland ecosystems to perform multiple functions related to C, N, and P cycling. Ongoing climate change is also likely to reduce local species richness (*32*) and to increase the extent of areas affected by desertification (*16, 18*), both of which will negatively affect ecosystem functioning. However, these outcomes are uncertain because of the complex interactions and contrasting effects of increases in temperature, which we found to reduce multifunctionality, and in atmospheric carbon dioxide concentrations, which can ameliorate water stress in dryland vegetation and potentially minimize biodiversity losses (*33, 34*). Because the quality and quantity of ecosystem services depend largely on ecosystem functions such as those measured in this study (*5, 9*), increased plant species richness may enhance the services provided by dryland ecosystems. Our findings also suggest that such richness may be particularly important for maintaining ecosystem functions linked to C and N cycling, which sustain C sequestration and soil fertility (*18, 28*). Because land degradation is often accompanied by the loss of soil fertility (*16, 18*), plant species richness may also promote ecosystem resistance to desertification.

The consistent effects of species richness on multifunctionality over and above those of climate and of abiotic factors highlight the importance of plant biodiversity as a driver of multifunctionality in drylands. The positive relationship between species richness and multifunctionality found is consistent with experimental results obtained in temperate grasslands and in microbial, biological soil crust, and aquatic communities (*8*–*12*). Collectively, these results suggest that the correlation between species richness and multifunctionality may be a general pattern in nature that reflects a cause-and-effect linkage.

References and Notes

1. B. J. Cardinale *et al.*, *Am. J. Bot.* **98**, 572 (2011).
2. D. U. Hooper *et al.*, *Ecol. Monogr.* **75**, 3 (2005).
3. A. Hector *et al.*, *Science* **286**, 1123 (1999).
4. P. Flombaum, O. E. Sala, *Proc. Natl. Acad. Sci. U.S.A.* **105**, 6087 (2008).
5. Millennium Ecosystem Assessment, *Ecosystems and Human Well-Being: Biodiversity Synthesis* (World Resources Institute, Washington, DC, 2005).
6. S. Naeem, D. E. Bunker, A. Hector, M. Loreau, C. Perrings, Eds., *Biodiversity, Ecosystem Functioning and Human Wellbeing. An Ecological and Economic Perspective* (Oxford Univ. Press, Oxford, 2009).
7. Z. Guo, L. Zhang, Y. Li, *PLoS ONE* **5**, e13113 (2010).
8. E. S. Zavaleta, J. R. Pasari, K. B. Hulvey, G. D. Tilman, *Proc. Natl. Acad. Sci. U.S.A.* **107**, 1443 (2010).
9. F. Isbell *et al.*, *Nature* **477**, 199 (2011).
10. A. Hector, R. Bagchi, *Nature* **448**, 188 (2007).
11. L. Gamfeldt, H. Hillebrand, P. R. Jonsson, *Ecology* **89**, 1223 (2008).
12. F. T. Maestre, A. P. Castillo-Monroy, M. Bowker, R. Ochoa-Hueso, *J. Ecol.* 10.1111/j.1365-2745.2011.01918.x (2011).
13. F. T. Maestre *et al.*, *Philos. Trans. R. Soc. London Ser. B* **365**, 2057 (2010).
14. J. A. Godbold, M. Solan, *Mar. Ecol. Prog. Ser.* **396**, 273 (2009).
15. D. A. Wardle, M. Jonsson, *Front. Ecol. Environ* **8**, 10 (2010).
16. J. F. Reynolds *et al.*, *Science* **316**, 847 (2007).
17. R. P. White, J. Nackoney, *Drylands, People, and Ecosystem Goods and Services: A Web-Based Geospatial Analysis* (World Resources Institute, Washington, DC, 2003); www.wri.org/publication/content/8241.
18. Millennium Ecosystem Assessment, *Ecosystems and Human Well-Being: Desertification Synthesis* (World Resources Institute, Washington, DC, 2005).
19. A search on the Institute for Scientific Information's Web of Science (18 November 2011) using the keywords "species AND (diversity OR richness) AND (community OR ecosystem) AND (function OR functioning OR production OR productivity OR biomass OR predation OR decomposition OR herbivory)" yielded 14,136 documents, only 2.5% of which contained the word "arid."
20. Materials and methods are available as supporting material on *Science* Online.
21. F. T. Maestre, A. Escudero, *Ecology* **90**, 1729 (2009).
22. K. P. Burnham, D. R. Anderson, *Model Selection and Multimodel Inference: A Practical Information-Theoretic Approach* (Springer, New York, ed. 2, 2002).
23. J. A. F. Diniz-Filho, T. F. L. V. B. Rangel, L. M. Bini, *Glob. Ecol. Biogeogr.* **17**, 479 (2008).
24. R. M. Pringle, T. P. Young, D. I. Rubenstein, D. J. McCauley, *Proc. Natl. Acad. Sci. U.S.A.* **104**, 193 (2007).
25. P. B. Adler *et al.*, *Science* **333**, 1750 (2011).
26. T. G. O'Connor, L. M. Haines, H. A. Snyman, *J. Ecol.* **89**, 850 (2001).
27. D. U. Hooper, P. M. Vitousek, *Ecol. Monogr.* **68**, 121 (1998).
28. W. G. Whitford, *Ecology of Desert Systems* (Academic Press, San Diego, CA, 2002).
29. T. Wu, E. Ayres, R. D. Bardgett, D. H. Wall, J. R. Garey, *Proc. Natl. Acad. Sci. U.S.A.* **108**, 17720 (2011).
30. R. D. Evans, R. Rimer, L. Sperry, J. Belnap, *Ecol. Appl.* **11**, 1301 (2001).
31. S. Solomon *et al.*, *Climate Change 2007: The Physical Science Basis. Contribution of Working Group I to the Fourth Assessment Report of the Intergovernmental Panel on Climate Change* (Cambridge Univ. Press, Cambridge, 2007).
32. O. E. Sala *et al.*, *Science* **287**, 1770 (2000).
33. J. A. Morgan *et al.*, *Nature* **476**, 202 (2011).
34. F. I. Woodward, C. K. Kelly, *Ecol. Lett.* **11**, 1229 (2008).

Acknowledgments: We thank all the technicians that assisted with field and laboratory work; T. Navarro and Z. Noumi for their help with plant species identification; and J. Bascompte, J. F. Reynolds, K. J. van Groenigen, W. van der Putten, and two anonymous reviewers for helpful comments. This research was funded by the European Research Council under the European Community's Seventh Framework Programme (FP7/2007-2013)/ERC Grant agreement 242658 (BIOCOM). The Ciencia y Tecnología para el Desarrollo program (CYTED) funded networking activities (EPES, Acción 407AC0323). The data used in the primary analyses are available in the supporting online material. The authors declare no competing financial interests.

F.T.M. and A.E. designed the study. Field data were collected by all authors except A.E., A.G., N.J.G., B.G., E.V., and M.B. Laboratory analyses were done by V.O., A.G., M.B., M.D.B., E.V., and B.G. Data analyses were done by F.T.M., assisted by N.J.G. The paper was written by F.T.M., and all authors contributed to the subsequent drafts.

Supporting Online Material
www.sciencemag.org/cgi/content/full/335/6065/214/DC1
Materials and Methods
Figs. S1 to S10
Tables S1 to S15
References (*35*–*137*)

Database S1
Map S1

18 October 2011; accepted 24 November 2011
10.1126/science.1215442

A DOC2 Protein Identified by Mutational Profiling Is Essential for Apicomplexan Parasite Exocytosis

Andrew Farrell,[1]* Sivasakthivel Thirugnanam,[1]* Alexander Lorestani,[1]* Jeffrey D. Dvorin,[2,3]* Keith P. Eidell,[1] David J.P. Ferguson,[4] Brooke R. Anderson-White,[1] Manoj T. Duraisingh,[2]† Gabor T. Marth,[1]† Marc-Jan Gubbels[1]†

Exocytosis is essential to the lytic cycle of apicomplexan parasites and required for the pathogenesis of toxoplasmosis and malaria. DOC2 proteins recruit the membrane fusion machinery required for exocytosis in a Ca^{2+}-dependent fashion. Here, the phenotype of a *Toxoplasma gondii* conditional mutant impaired in host cell invasion and egress was pinpointed to a defect in secretion of the micronemes, an apicomplexan-specific organelle that contains adhesion proteins. Whole-genome sequencing identified the etiological point mutation in TgDOC2.1. A conditional allele of the orthologous gene engineered into *Plasmodium falciparum* was also defective in microneme secretion. However, the major effect was on invasion, suggesting that microneme secretion is dispensable for *Plasmodium* egress.

The lytic replication cycle is central to the pathology of apicomplexan diseases such as malaria caused by *Plasmodium* spp. and toxoplasmosis caused by *Toxoplasma gondii*. Motility of parasites between host cells, within which replication occurs, is powered by actinomyosin motors connecting with extracellular substrate through transmembrane adhesion proteins secreted through organelles known as micronemes (*1*). A pivotal event in triggering motility is the release of Ca^{2+} from compartments within the parasite, which activates myosin and triggers microneme secretion (*2*). Recently, calcium-dependent protein kinases required for egress were identified in *Plasmodium falciparum* (PfCDPK5) and *Toxoplasma* (TgCDPK1) (*3*, *4*).

To investigate this critical process, we used temperature-sensitive mutants in the lytic cycle of *Toxoplasma* by means of chemical mutagenesis (*5*). Upon phenotype induction, mutant F-P2 displayed a reduced invasion competency (Fig. 1A) and complete inability to egress (*6*), but intracellular growth progressed normally (*6*). Three distinct Ca^{2+}-dependent events are required for egress and invasion: extrusion of the apical conoid, motility, and microneme secretion. Conoid extrusion in F-P2 was indistinguishable from wild-type parasites (Fig. 1B and figs. S1 and S5C) (*7*–*9*). Motility was assessed via video microscopy, and the incidence of the three motility modes of *Toxoplasma* tachyzoites (circular and helical gliding and twirling) (movies S1 to S3) were scored (*9*, *10*). Under

[1]Department of Biology, Boston College, Chestnut Hill, MA 02467, USA. [2]Department of Immunology and Infectious Diseases, Harvard School of Public Health, Boston, MA 02115, USA. [3]Division of Infectious Diseases, Children's Hospital Boston, Boston, MA 02115, USA. [4]Nuffield Department of Clinical Laboratory Science, University of Oxford, John Radcliffe Hospital, Oxford OX3 9DU, UK.

*These authors contributed equally to this work.
†To whom correspondence should be addressed. E-mail: mduraisi@hsph.harvard.edu (M.T.D.); marth@bc.edu (G.T.M); gubbelsj@bc.edu (M.-J.G.)

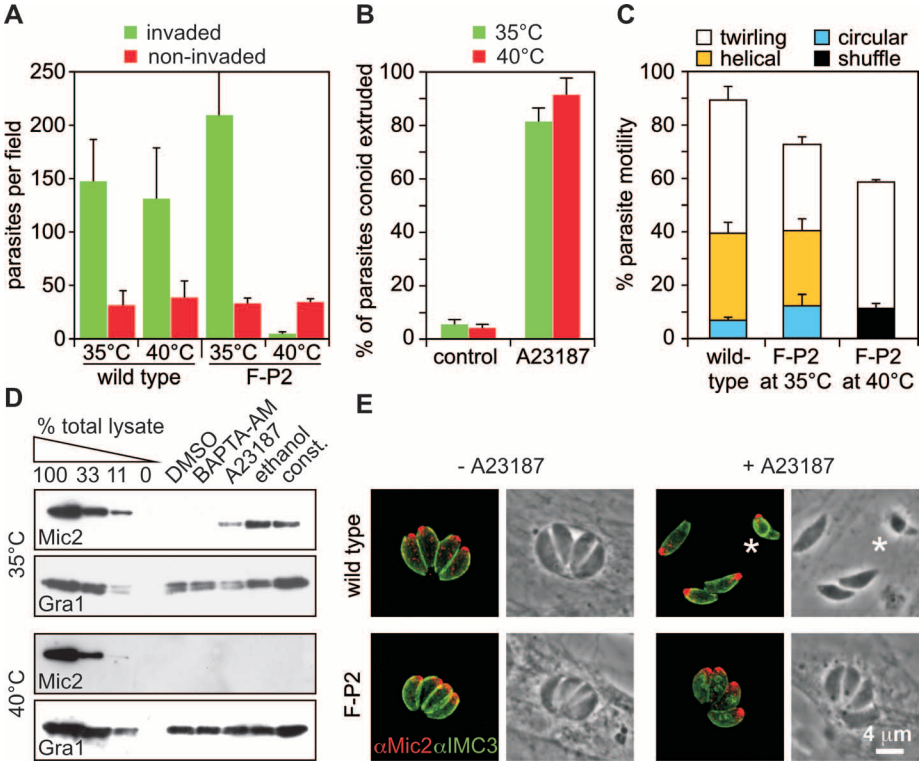

Fig. 1. Mutant F-P2 has a microneme secretion defect. (**A**) Red-green invasion assays were performed on the 2F-1-YFP2 wild-type and F-P2 mutant parasite lines. Parasites were phenotypically induced for 24 hours at the restrictive temperature (40°C). Averages of four independent experiments +SD are shown. (**B**) Conoid extrusion of Ca^{2+}-ionophore (A23187)–induced or vehicle control–treated parasites was determined for parasites grown at 35° or 40°C. Averages of three independent experiments +SD are shown. (**C**) Incidence of various motility modes determined by video microscopy over 1 min for wild-type (parent 2F-1-YFP2) and F-P2 parasites at conditions as indicated. Averages of four independent experiments +SEM are shown. (**D**) Microneme secretion of F-P2 parasites measured by means of Western blot detection of Mic2 protein released in the supernatant upon various stimuli and vehicle control (dimethyl sulfoxide). "const." represents uninduced, constitutive secretion over a 60-min period. Gra1 serves as loading control. (**E**) Immunofluorescence assay of Mic2 and IMC3 (marking the peripheral cytoskeleton) of wild-type and F-P2 at 40°C with or without ionophore stimulation shows micronemes are intact in F-P2. Phase images show vacuolar membrane is intact in F-P2 at 40°C. Asterisks mark the egressing parasite.

restrictive conditions, no circular or helical gliding was observed for F-P2 (Fig. 1C). Rather, induced F-P2 displayed twirling and shuffling, a distinct motility mode in which parasites abruptly move back and forward (Fig. 1C and movie S4), which has been previously observed with inhibitors of *Toxoplasma* invasion (*11*) and in certain *T. gondii* (*12*) and *P. falciparum* sporozoite (*13*, *14*) microneme protein knockouts. With no net change in parasite position, neither twirling nor shuffling is thought to be effective in invasion or egress. We also assessed microneme release upon increasing the intracellular Ca^{2+} concentration ($[Ca^{2+}]_i$) (*8*, *9*, *15*). No Mic2 microneme protein release was detected under restrictive conditions for F-P2, but we readily detected dense granule protein release (Gra1) and Mic2 release in the controls (Fig. 1D and fig. S2). Constitutive microneme secretion was also not detected (Fig. 1D) (*16*). Impaired microneme secretion did not appear to be caused by a defect in microneme formation, morphology, or organelle number because these features were normal (Fig. 1E and fig. S3). Thus, impaired microneme secretion in F-P2 apparently results in parasites unable to provide the traction required for productive motility.

Although other *Toxoplasma* genotypes in chemical mutants have been successfully mapped by genetic complementation (*5*), we were unable to complement F-P2. We set out to identify the etiological mutation with whole-genome mutational profiling using high-throughput sequencing (Fig. 2 and table S1) (*17*). We identified 31 validated single-nucleotide polymorphisms (SNPs) between parent and mutant lines: 8 are in coding regions, 6 are intronic, and 19 are intergenic (table S1). To identify the sole gene responsible for the microneme secretion defect, we focused on gene *TGGT1_049850*, which contains Ca^{2+}-dependent membrane-binding C2 domains (*18*, *19*) and harbors a missense mutation (T to C, encoding Phe to Ser) at position 124 (fig. S4). Complementation with cosmid PSBMG64 (*9*), which spans the entire wild-type locus, resulted in completely restored F-P2 growth (Fig. 3A and fig. S5A), secretion of micronemes (Fig. 3B and fig. S5C), and egress (fig. S5B) and largely restored the motility defect (Fig. 3C). To confirm that the point mutation in *TGGT1_049850* was solely responsible for the phenotype, we complemented with both wild-type and F-P2 mutant cDNA cloned into *T. gondii* expression plasmids. As anticipated, the wild-type allele restores F-P2 growth at 40°C, whereas the mutant allele does not (Fig. 3D).

Gene *TGGT1_049850* encodes a predicted protein of 1990 amino acids (fig. S4). Orthologs are strongly conserved across the Apicomplexa and some ciliates (such as *Paramecium tetrauarelia*) (Fig. 4A). Motif searches and sequence alignments (*9*) identified four conserved sequence blocks,

A

Sequence feature	parent	F-P2
Total bp sequenced	6,074,293,500	6,527,102,400
Total paired end reads	40,495,290	43,514,016
Total reads aligned	36,504,440	39,362,485
Total reads aligned (%)	90.1	90.5
Human reads (%)	32.2	49.4
T. gondii reads (%)	57.9	44.1
GT1 genome covered (%)	96.5	96.9
Reads in unassembled contigs (%)	0.9	0.7
Total SNPs called	982	1015

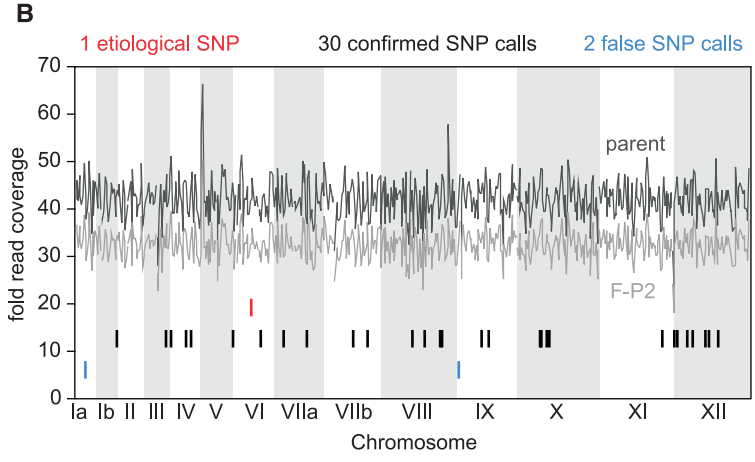

Fig. 2. Results of paired-end Illumina resequencing of parent and F-P2 genomes. (**A**) Sequencing and alignment statistics. Genomic DNA of F-P2 and its parent were sequenced to >30-fold coverage on an Illumina GA2 instrument. Sequence reads were aligned to the closely related GT1 strain reference genome by using the MOSAIK read mapper (*9*). Coverage was sufficient to call sequence differences between F-P2 and RH in >95% of the GT1 reference. Using the FreeBayes variation calling program (*28*) and appropriate filtering, 982 SNPs are shared between the two samples and 33 are specific to F-P2. (**B**) Read coverage across the chromosomes of parent and F-P2. Fold coverage is averaged over 100-kb windows. The chromosomal localization of the 33 called SNPs between parent and F-P2 are shown, differentiated by confirmed and false SNP calls. Of the latter, 31 were positively confirmed by means of Sanger sequencing; 77% were mutations of an A/T base, corroborating the proclivity of *N*-ethyl-*N*-nitrosourea toward AT:GC and AT:TA substitutions when compared with the rate of 45% of the SNPs shared between the RH and GT1 strains.

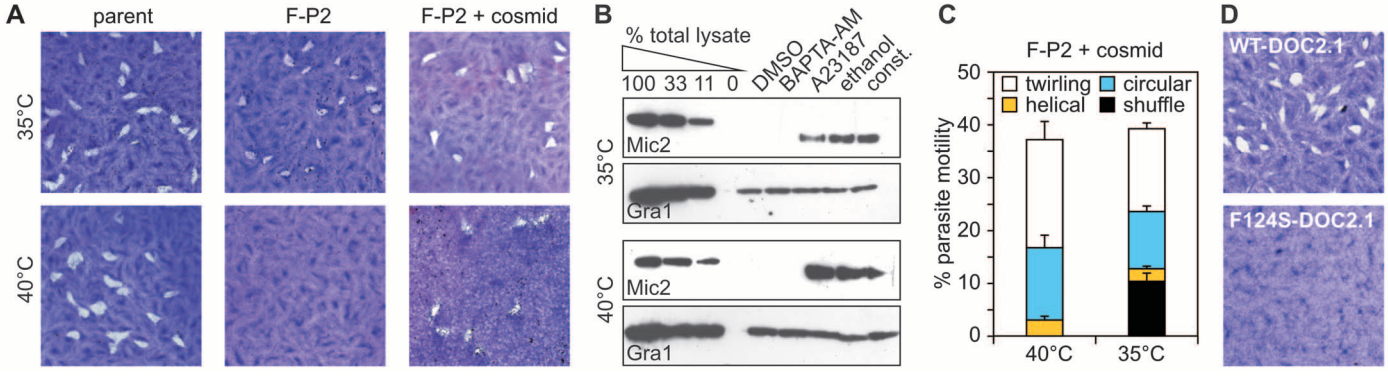

Fig. 3. Genetic complementation of F-P2 with cosmid PSBMG64 restores the wild-type phenotype. (**A**) Plaque assays of parent line (2F-1-YFP2), F-P2, and complemented mutant as indicated. (**B**) Microneme secretion of complemented F-P2 parasites (Fig. 1D, legend). (**C**) Incidence of various motility modes determined by means of video microscopy over 1 min at conditions as indicated. Averages of four independent experiments shown + SEM. (**D**) Plaque assays representing F-P2 complementation with plasmids expressing cDNA encoding the (top) wild-type TgDOC2.1 allele or (bottom) F-P2 mutant allele.

with block 2 containing a tandem C2 domain, as well as extensive coiled-coil domains in the C terminus of all orthologs (Fig. 4A). The mutated Phe^{124} lies in block 1 and is conserved across all orthologs, suggesting that this residue is critical for function (Fig. 4A and fig. S4). Block 1 appears to be a degenerate C2 domain because a C2 domain was identified just above the consensus cut-off in the *Eimeria tenella* and *Paramecium tetraurelia* orthologs.

Tandem C2 domain proteins function in Ca^{2+}-mediated exocytosis [for example, neurotransmitter release (*20*)] and encompass proteins with a transmembrane domain—such as synaptotagmin—whereas others lack such a domain—such as the double C2 (DOC2) proteins. The C2 domains in cytosolic DOC2A and DOC2B proteins bind Ca^{2+}, facilitating soluble *N*-ethylmaleimide–sensitive factor (NSF) attachment protein (SNAP) receptor (SNARE) protein–dependent membrane fusion of secretory vesicles with the plasma membrane (*20*, *21*). We named our protein TgDOC2.1 by taking into account the primary structure and the orthologous function of *TGGT1_049850* in microneme secretion. Structural prediction suggests that TgDOC2.1 can bind Ca^{2+} ions through conserved Asp residues in the C2 domains (fig. S6) (*22*). TgDOC2.1 does not contain additional recognizable domains to provide further mechanistic insights such as interactions with mammalian uncoordinated protein 18 (Munc18), Munc13, or SNARE proteins, although C2 domains could directly fulfill such role.

To determine whether the mechanism in *Toxoplasma* is conserved, we generated a *P. falciparum* line allowing inducible regulation of the orthologous DOC2.1 gene, via genetic fusion of a destabilizing domain (DD) to the PfDOC2.1 C terminus (PFL2110c) (fig. S7). The DD fusion protein is stabilized by the synthetic ligand Shld1 and targeted for degradation in absence of Shld1 (*3*, *23*). PfDOC2.1 levels were reduced by 57 ± 13% in the absence of Shld1 (Fig. 4B and fig. S8). To test the effect of PfDOC2.1 on growth, we optimized conditions for measuring parasite replication over multiple cycles by varying initial parasitemia and hematocrit (fig. S9). PfDOC2.1-deficient parasites exhibited an 87% decrease in parasitemia over three cycles (Fig. 4C). D10-PfCDPK4-DD parasites, with an inducible knockdown in PfCDPK4 and replicating equally in the presence or absence of Shld1 (*3*), were used as a control. At this level of PfDOC2.1 knockdown, parasite development within a single asexual cycle through the schizont stage and the number of merozoite nuclei per segmented schizont was unchanged, and accumulation of unruptured schizonts was not observed (fig. S10). To evaluate the contribution of PfDOC2.1 to parasite invasion, parasites were cultured in the absence of Shld1 from the ring stage to the schizont stage and divided into two populations so as to complete invasion with or without Shld1 present (fig. S11). Invasion was decreased 34 ± 9% as compared with parasites rescued by the addition of Shld1 and restoration of PfDOC2.1 levels (Fig. 4D). This decreased invasion efficiency was sufficient to explain the decreased replication rate. To directly identify a defect in microneme secretion, we examined the release of parasite proteins into the supernatants after reinvasion. In the absence of Shld1, release of PfEBA-175, a microneme protein, into the supernatant was decreased by 44 ± 14% (Fig. 4, E and F, and fig. S12A) when normalized for the amount of PfSERA5, a parasitophorous vacuole protein, but the relative use of alternative invasion pathways was unaffected by PfDOC2.1 levels (fig. S12B), suggesting a global defect in invasion secondary to incomplete microneme discharge.

Thus, TgDOC2.1 constitutes a second level of Ca^{2+}-dependent control of *Toxoplasma* microneme secretion, in addition to the recently identified calcium-dependent protein kinase, TgCDPK1 (*4*). Because DOC2.1 probably facilitates membrane fusion, it probably acts downstream of the CDPKs. Conservation of DOC2.1 and Ca^{2+}-dependent secretory organelles in ciliates indicates the shared

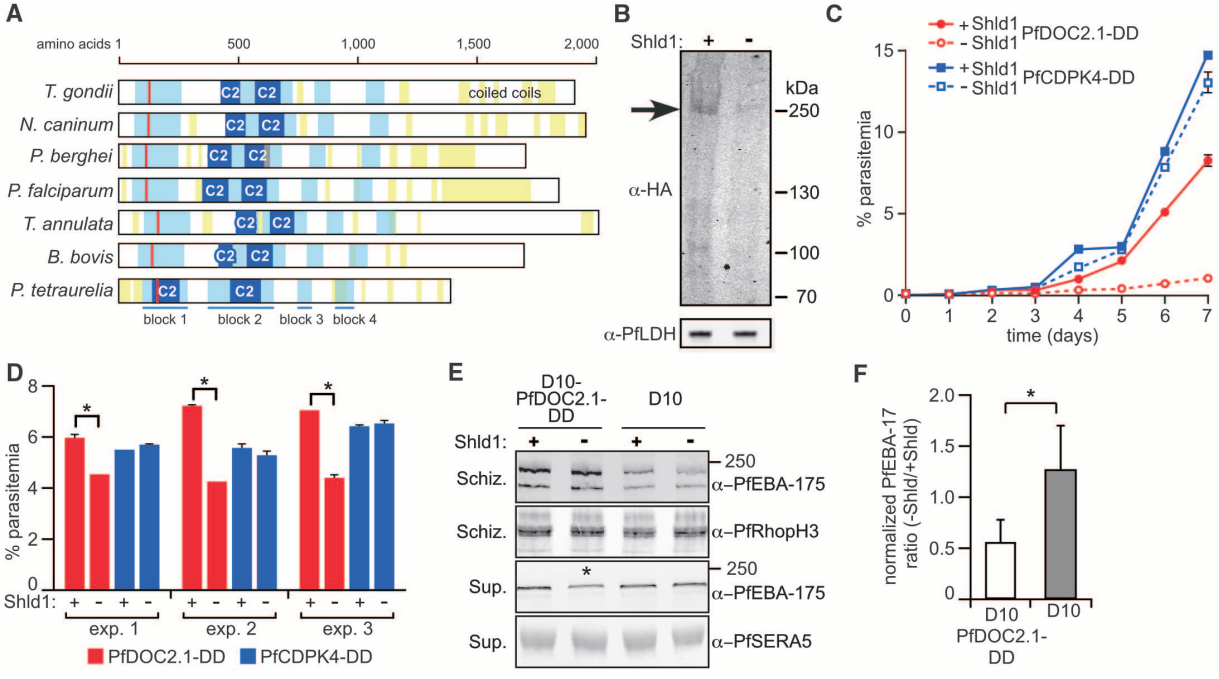

Fig. 4. DOC2.1 has a conserved role in microneme secretion. (**A**) Schematic of DOC2.1 orthologs in Apicomplexa and ciliate *Paramecium tetraurelia*. Four conserved blocks are color-coded in light blue, C2 domains are in dark blue, and coiled-coil regions are in yellow. The red line marks the conserved phenylalanine mutated to serine in F-P2. (**B**) Lysates from D10-PfDOC2.1-DD parasites cultured ± Shld1 probed with antibody to hemagglutinin (HA) (PfDOC2.1; just over 250 kD, arrow) or antibody to PfLDH (loading control). Normalized PfDOC2.1 ratio (± Shld1) is 0.43 ± 0.13. (**C**) Replication curves of D10-PfDOC2.1-DD parasites maintained ± Shld1 (mean ± range, $n = 2$ replicates). (**D**) D10-PfDOC2.1-DD parasites were maintained without Shld1 from early ring stage to segmented schizont stage then incubated an additional 8 to 12 hours ± Shld1; resulting newly invaded rings were counted via fluorescence-activated cell sorting [mean ± SD, $n = 3$ replicates (for D10-CDPK4-DD in experiment 3, $n = 1$ replicates), three separate experiments, $^*P < 0.001$, *t* test]. (**E**) Immunoblots evaluating the release of indicated parasite invasion ligands. Synchronized ring-stage cells were incubated ± Shld1. Supernatants of ruptured schizonts lysates (saponin) were collected. The asterisk indicates a 44 ± 14% decrease in PfEBA-175 release from D10-PfDOC2.1-DD parasites. (**F**) Mean ratio of PfEBA-175 released into supernatant ($n = 4$ biological replicates; +95% CI, $^*P < 0.01$, *t* test).

ancestry of micronemes (*24*, *25*). Although PfDOC2.1 knockdown in *P. falciparum* has a clear effect on invasion, at this level of knockdown it did not result in an egress defect, suggesting that *Plasmodium* merozoites may rely on microneme secretion for invasion but on qualitatively different exoneme secretion for egress from the erythrocyte (*26*). However, in *Toxoplasma* mutant F-P2 both invasion and egress were defective because microneme secretion plays a central role in both of these processes (*27*), highlighting divergent roles for secretory organelles in egress between these organisms. This multilayered Ca^{2+}-mediated control of microneme secretion may underscore tight temporal regulation, and this mechanism appears ancestral to the ciliates and the Apicomplexa.

References and Notes

1. J. Baum, T. W. Gilberger, F. Frischknecht, M. Meissner, *Trends Parasitol.* **24**, 557 (2008).
2. K. Nagamune, S. N. Moreno, E. N. Chini, L. D. Sibley, *Subcell. Biochem.* **47**, 70 (2008).
3. J. D. Dvorin *et al.*, *Science* **328**, 910 (2010).
4. S. Lourido *et al.*, *Nature* **465**, 359 (2010).
5. M. J. Gubbels *et al.*, *PLoS Pathog.* **4**, e36 (2008).
6. K. P. Eidell, T. Burke, M. J. Gubbels, *Mol. Biochem. Parasitol.* **171**, 97 (2010).
7. M. G. Del Carmen, M. Mondragón, S. González, R. Mondragón, *Cell. Microbiol.* **11**, 967 (2009).
8. V. B. Carruthers, S. N. Moreno, L. D. Sibley, *Biochem. J.* **342**, 379 (1999).
9. Materials and methods are available as supporting material on *Science* Online.
10. S. Håkansson, H. Morisaki, J. Heuser, L. D. Sibley, *Mol. Biol. Cell* **10**, 3539 (1999).
11. K. L. Carey, N. J. Westwood, T. J. Mitchison, G. E. Ward, *Proc. Natl. Acad. Sci. U.S.A.* **101**, 7433 (2004).
12. M. H. Huynh, V. B. Carruthers, *PLoS Pathog.* **2**, e84 (2006).
13. S. Hegge *et al.*, *FASEB J.* **24**, 2222 (2010).
14. S. Münter *et al.*, *Cell Host Microbe* **6**, 551 (2009).
15. J. L. Lovett, N. Marchesini, S. N. Moreno, L. D. Sibley, *J. Biol. Chem.* **277**, 25870 (2002).
16. D. M. Wetzel, L. A. Chen, F. A. Ruiz, S. N. Moreno, L. D. Sibley, *J. Cell Sci.* **117**, 5739 (2004).
17. D. R. Smith *et al.*, *Genome Res.* **18**, 1638 (2008).
18. S. Martens, *Biochem. Soc. Trans.* **38**, 213 (2010).
19. W. Cho, R. V. Stahelin, *Biochim. Biophys. Acta* **1761**, 838 (2006).
20. R. Friedrich, A. Yeheskel, U. Ashery, *Mol. Neurobiol.* **41**, 42 (2010).
21. A. J. Groffen *et al.*, *Science* **327**, 1614 (2010).
22. S. Martens, H. T. McMahon, *Natl. Rev.* **9**, 543 (2008).
23. L. A. Banaszynski, L. C. Chen, L. A. Maynard-Smith, A. G. Ooi, T. J. Wandless, *Cell* **126**, 995 (2006).
24. C. Erxleben, H. Plattner, *J. Cell Biol.* **127**, 935 (1994).
25. B. S. Leander, P. J. Keeling, *Trends Ecol. Evol.* **18**, 395 (2003).
26. K. Koussis *et al.*, *EMBO J.* **28**, 725 (2009).
27. B. F. Kafsack *et al.*, *Science* **323**, 530 (2009).
28. G. T. Marth *et al.*, *Nat. Genet.* **23**, 452 (1999).

Acknowledgments: We thank C. Nussbaum and C. Russ of the "Broad Sequencing Platform" and D. Sibley, J.-F. Dubremetz, M.-F. Cesbron-Delauw, J.-C. Doury, and M. Makler (Flow Inc.) for kindly sharing reagents. F-P2 was originally generated in the laboratory of B. Striepen. This work was supported by National Institutes of Health grants AI081220 to M.-J.G. and G.T.M., AI057919 and AI088314 to M.T.D., HG004719 to G.T.M., and AI087874 to J.D.D.; a Knights Templar Eye Foundation grant to S.T., a Wellcome Trust equipment grant to D.J.P.F., a Burroughs Wellcome Fund New Investigator in the Pathogenesis of Infectious Disease Fellowship to M.T.D., and an American Heart Association Scientist Development Grant (0635480N) to M.-J.G. *Toxoplasma gondii* GT1 sequence and annotation are from L. Caler at the J. Craig Venter Institute. Sequence reads have been deposited at the National Center for Biotechnology Information sequence read archive under accession no. SRA046023.

Supporting Online Material

www.sciencemag.org/cgi/content/full/335/6065/218/DC1
Materials and Methods
Figs. S1 to S12
Tables S1 to S2
References (*29*–*54*)
Movies S1 to S4

7 July 2011; accepted 29 November 2011
10.1126/science.1210829

Cytoplasmic Dynein Moves Through Uncoordinated Stepping of the AAA+ Ring Domains

Mark A. DeWitt, Amy Y. Chang, Peter A. Combs, Ahmet Yildiz*

Cytoplasmic dynein is a homodimeric AAA+ motor that transports a multitude of cargos toward the microtubule minus end. How the two catalytic head domains interact and move relative to each other during processive movement is unclear. Here, we tracked the relative positions of both heads with nanometer precision and directly observed the heads moving independently along the microtubule. The heads remained widely separated, and their stepping behavior varied as a function of interhead separation. One active head was sufficient for processive movement, and an active head could drag an inactive partner head forward. Thus, dynein moves processively without interhead coordination, a mechanism fundamentally distinct from the hand-over-hand stepping of kinesin and myosin.

Cytoplasmic dynein forms a 1.2-MD complex that uses adenosine triphosphate (ATP) hydrolysis to power minus-end–directed motility along microtubules. The catalytic head domain is composed of six AAA+ [adenosine triphosphatases (ATPases) associated with diverse cellular activities] modules arranged in a ring (*1*). ATPase activity at AAA1 is essential for dynein motility (*2*). The two rings are connected by the dimerization of N-terminal tail domains and bind to the microtubule through a ~15-nm coiled-coil stalk bearing a small microtubule-binding domain (MTBD). Dynein is required for many cellular processes, including organelle transport and cell division, and dynein malfunction can lead to motor neuron degeneration (*3*).

Despite recent advances in understanding dynein's structure (*4*) and mechanism (*5*, *6*), the stepping mechanism of dimeric dynein during processive motion remains unclear. Studies of kinesin and myosin motors have shown that their heads take alternating steps in a hand-over-hand (HoH) fashion (*7*–*9*). Dynein motility also requires two heads (*6*), but it is unclear whether they coordinate with each other to achieve processive motion (*10*). Dynein's structure and origin are distinct from kinesin and myosin, suggesting that it may use a different mechanism.

To investigate dynein's stepping mechanism, we tracked the movement of an artificially dimerized, tail-truncated yeast cytoplasmic dynein [glutathione *S*-transferase–Dyn_{331kD} (GST-Dyn_{331kD})], which has similar stepping properties to native dynein (*6*). First, we tracked the movement of dynein labeled with a single quantum dot (QD) at 2 msec temporal resolution in the presence of rate-limiting ATP (Fig. 1A and fig. S1). As reported previously (*5*, *6*), the distribution of step sizes was multimodal. The step-size histogram of head-labeled dynein revealed two major peaks at 9.3 ± 0.7 and 17.5 ± 1.2 nm that were nearly twice as large as the peaks observed in the tail histogram (4.8 ± 0.3 and 8.7 ± 0.9 nm) (Fig. 1B). The probability of backward stepping (p_{BW}) was 0.2. The dwell-time histogram for head-labeled dynein at 12 μM ATP (Fig. 1C) was best fit by a convolution of one slow ($k_1 = 2.1 \pm 0.2$ sec^{-1}) and one fast ($k_2 = 14.1 \pm 2.5$ sec^{-1}) exponential rate constant. The product of k_2 and the average head step size ($d_{head} = 10.2$ nm) agrees well with the average velocity of dynein at saturating [ATP] (124 nm/sec). This data excludes the symmetric HoH model, which predicts the stepping kinetics of a head to be a convolution of two equal rate constants (fig. S2). Instead, the dwell-time histogram of tail-labeled dynein was well described by a kinetic model in which the heads can step independently and the tail moves each time either head takes a step ($k'_1 = 1.2 \pm 0.1$ sec^{-1}; $k'_2 = 12.2 \pm 2.7$ sec^{-1}) (fig. S2).

To directly address how the two heads interact and move relative to each other, we labeled GST-Dyn_{331kD} with different-colored QDs (17 to 22 nm in size) (table S1) at the C termini and simultaneously tracked the positions of the heads during processive movement (*11*). The fluorescent signal was split into two channels and registered

Department of Physics, and Department of Molecular and Cellular Biology, University of California, Berkeley, CA 94720, USA.

*To whom correspondence should be addressed. E-mail: yildiz@berkeley.edu

to 3-nm precision (figs. S3 to S5). Representative traces (Fig. 2A, fig. S6, and movies S1 and S2) clearly showed that either head could take a step regardless of which head was leading, a mechanism distinct from HoH. Although most steps showed a canonical alternating pattern, one head could take multiple consecutive (nonalternating) steps before the other head moved (Fig. 2B). Nonalternating stepping occurred about half as often as alternating stepping (32% of steps, fig. S7). This may partly be due to the time needed for a head to complete its ATPase cycle before it can take another step.

The heads often walked along different protofilaments (fig. S6), with the leading head preferentially located to the right of the trailing head (Fig. 2C and fig. S8). Measurements using organic dyes showed that the heads were separated by 23.0 ± 13.2 nm (mean ± SD) (fig. S9), excluding the possibility of a stacking interaction between the AAA+ rings (*12*).

The heads frequently swapped the lead, but not strictly after every step of the motor. The stepping characteristics of a head in the leading and trailing positions differed substantially depending on interhead separation, forming the basis of the high variability in dynein's step size (*6*). The on-axis (parallel to the microtubule long axis) step size decreased by ~0.4 nm per nanometer increase in interhead separation (Fig. 3A). The trailing head took larger (d = 17.5 nm) forward and fewer (p_{BW} = 0.14) backward steps. In contrast, the leading head took significantly shorter (d = 1.5 nm) forward and more frequent (p_{BW} = 0.45) backward steps. The off-axis (perpendicular to the microtubule long axis) step size also decreased with interhead separation but without a net bias toward left or right (Fig. 3B). The stepping probabilities of the leading and trailing heads were nearly identical when they were positioned close (10 to 20 nm) to each other. At larger separations, 65% of the steps were taken by the trailing head (Fig. 3C).

The heads of native dynein also moved independently, and their stepping behavior varied as a function of interhead separation, similar to GST-Dyn$_{331kD}$ (figs. S10 and S11). The results show that the tail domain is not involved in interhead coordination.

Our results show that dynein's stepping mechanism is different from processive kinesins and myosins. The stepping motion of these motors is driven by the power stroke of the bound head, which moves the trailing head forward. For dynein, we propose a tethered excursion model (Fig. 3D), in which a conformational change that produces the minus-end bias occurs in the unbound head. Either head can bind ATP at the AAA1 site, followed by its release from the microtubule (*13*). The linker undergoes a minus-end–directed priming stroke upon ATP hydrolysis (*14*), which moves its MTBD forward. The large and flexible linker allows the released head to diffuse over a wide area, resulting in both large interhead separations and variable step sizes.

The heads experience intramolecular tension at large separations, and the power stroke of the bound head may occasionally trigger the release of the other head. In fact, we observed that the stepping probability of the trailing head increased at large separations (Fig. 3C). This result is consistent with force-induced movement of dynein, which requires less force when it is pulled toward the minus end (*15*). In addition, tension can bias the diffusional search of the tethered head toward the bound head, preventing further extension of the dimer (Fig. 3D).

The tethered excursion model predicts that a single force-generating head in a dynein dimer can both take a step and drag an inactive head forward. We tested the motility of a heterodimeric dynein with one wild-type head (WT$_h$) and one mutant head lacking the ability to hydrolyze ATP at the AAA1 domain (Mut$_h$) (*6*, *16*). Mut$_h$

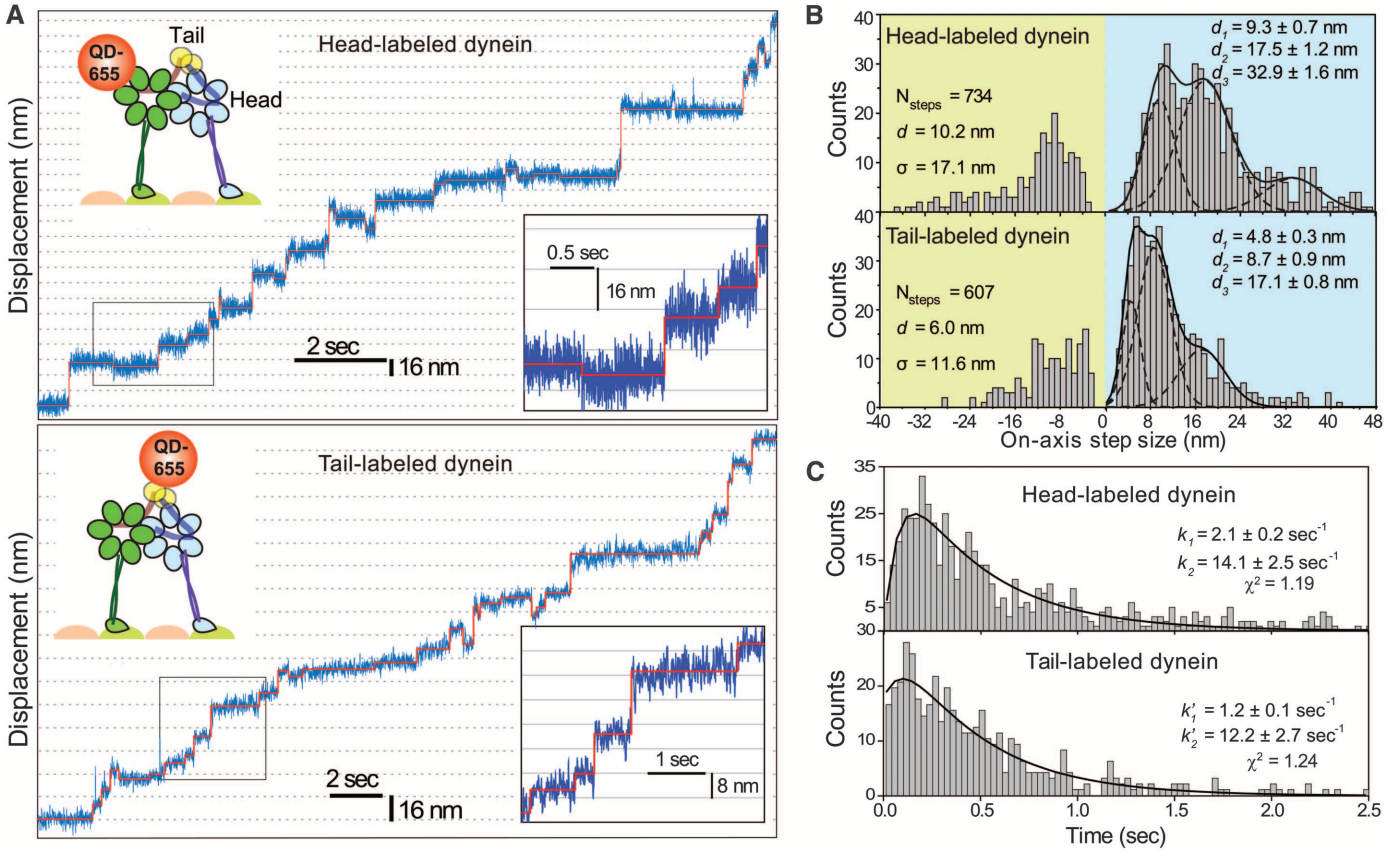

Fig. 1. (**A**) Step-size measurements of tail- and head-labeled GST-Dyn$_{331kD}$ with a single QD-655 at 2-msec temporal resolution. The QD position (blue traces) was fit by a step-finding algorithm (solid red lines). (**B**) Multiple Gaussian fits to step-size histograms reveal two major peaks at 9.3 and 17.5 nm for the head and 4.8 and 8.7 nm for the tail. (**C**) Dwell-time histogram of head-stepping fitted to a convolution of two unequal rate constants and that of tail-stepping fitted to a model assuming uncoordinated stepping between two heads, each with two unequal rate constants.

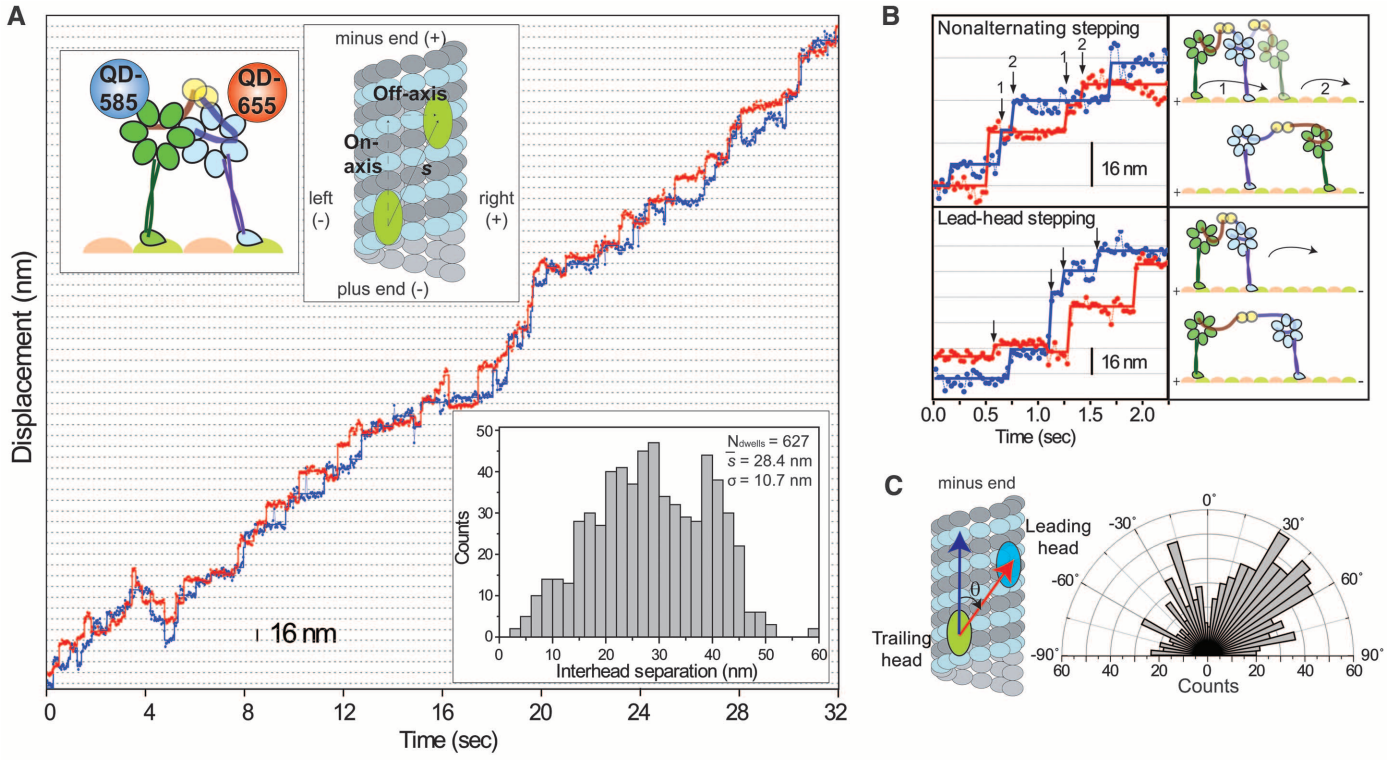

Fig. 2. (**A**) Stepping trace of GST-Dyn$_{331kD}$ labeled with QD-585 (blue) and QD-655 (red) shows that the heads move independently of each other during processive runs. The heads are separated by 28.4 ± 10.7 nm (bottom inset). (**B**) Examples of nonalternating and lead-head stepping (arrows) show that dynein stepping deviates from the HoH mechanism. (**C**) Histogram of the angles between the interhead separation vector (red arrow) and the microtubule long axis (blue arrow).

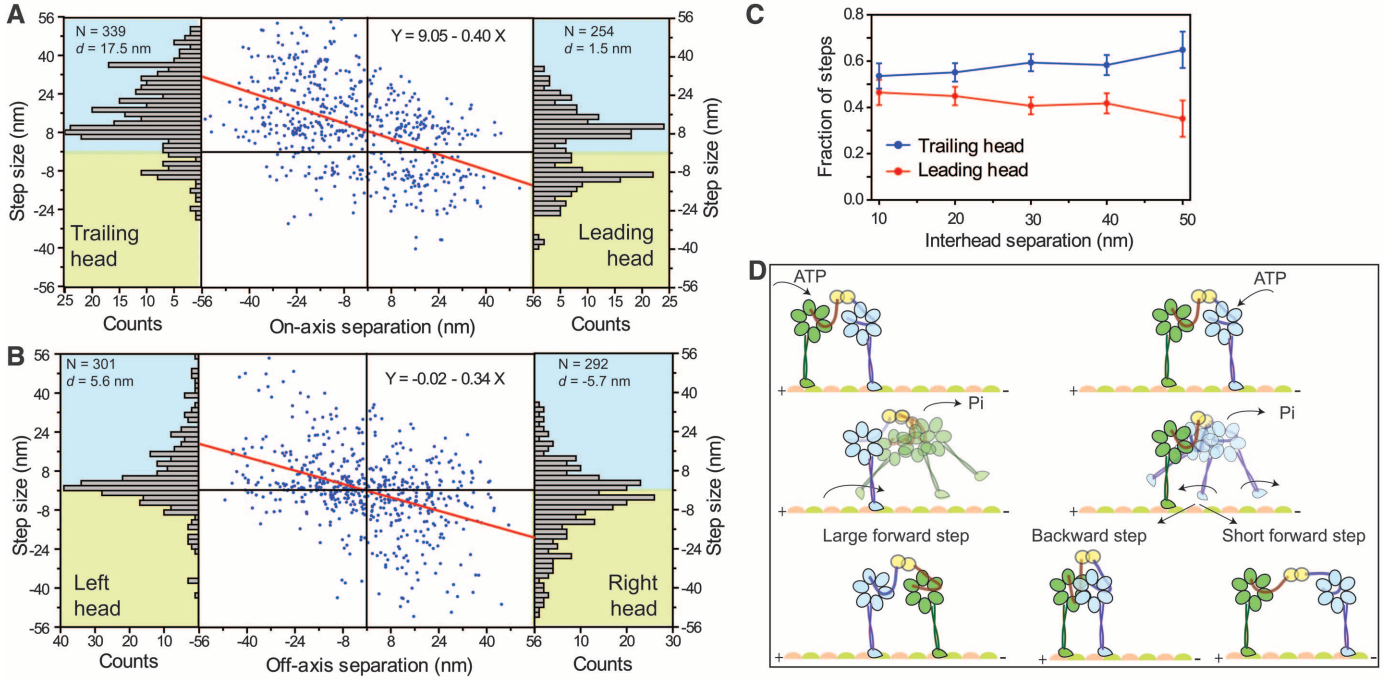

Fig. 3. (**A**) The on-axis step size (blue dots) of GST-Dyn$_{331kD}$ decreases linearly (red line) as a function of interhead separation and is biased forward by 9.1 ± 0.6 nm. The leading head takes shorter (d = 1.5 nm) steps with more frequent (p_{BW} = 0.45) backward steps, compared with the trailing head (d = 17.5 nm; p_{BW} = 0.14) (bar graphs). (**B**) Off-axis step sizes show a linear dependence on interhead separation without a bias to move toward the right (positive) or left (negative). (**C**) Fraction of the steps taken by the leading and trailing heads at different interhead separations (mean ± SEM). (**D**) Tethered excursion model for the dynein stepping mechanism. Either the leading or the trailing head can hydrolyze ATP and release from the microtubule. A diffusional search of the trailing head (green) is biased forward by interhead tension and the linker swing, resulting in a large forward step. In contrast, linker swing and tension bias the diffusion of the leading head (blue) in opposing directions, resulting in either a backward step or a short forward step.

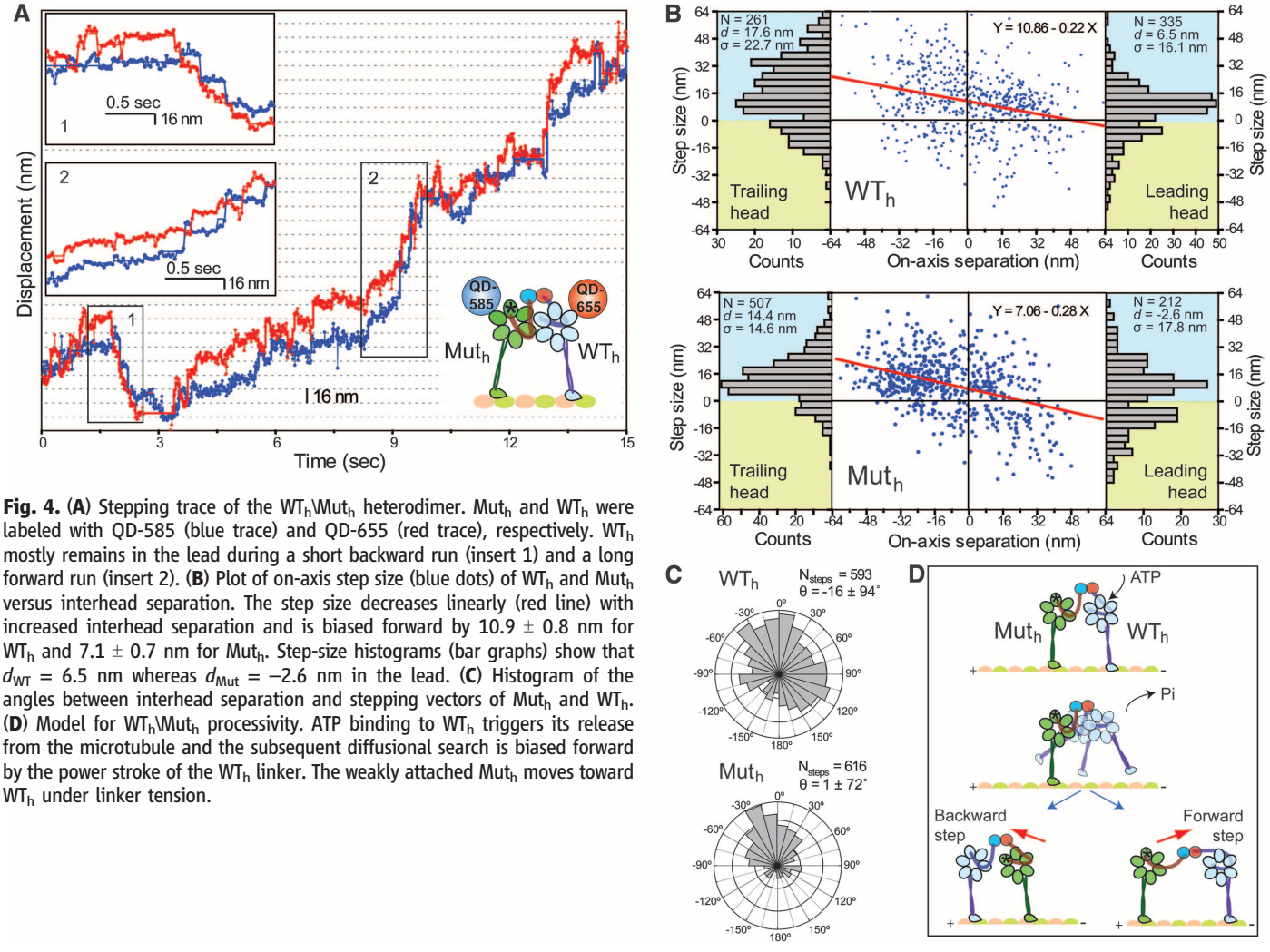

Fig. 4. (**A**) Stepping trace of the WT$_h$\Mut$_h$ heterodimer. Mut$_h$ and WT$_h$ were labeled with QD-585 (blue trace) and QD-655 (red trace), respectively. WT$_h$ mostly remains in the lead during a short backward run (insert 1) and a long forward run (insert 2). (**B**) Plot of on-axis step size (blue dots) of WT$_h$ and Mut$_h$ versus interhead separation. The step size decreases linearly (red line) with increased interhead separation and is biased forward by 10.9 ± 0.8 nm for WT$_h$ and 7.1 ± 0.7 nm for Mut$_h$. Step-size histograms (bar graphs) show that d_{WT} = 6.5 nm whereas d_{Mut} = –2.6 nm in the lead. (**C**) Histogram of the angles between interhead separation and stepping vectors of Mut$_h$ and WT$_h$. (**D**) Model for WT$_h$\Mut$_h$ processivity. ATP binding to WT$_h$ triggers its release from the microtubule and the subsequent diffusional search is biased forward by the power stroke of the WT$_h$ linker. The weakly attached Mut$_h$ moves toward WT$_h$ under linker tension.

cannot undergo a power stroke (*17*) and is weakly associated with the microtubule (*13*). The WT$_h$\Mut$_h$ heterodimer moved processively toward the microtubule minus end (movies S3 and S4, Fig. 4A, and figs. S12 and S13). WT$_h$ was found in the lead 66% of the time (fig. S14). Similarly, during occasional short (4 to 5 steps) backward runs, WT$_h$ remained in the leading position toward the plus end.

Mut$_h$ exhibited different stepping characteristics in both the leading and trailing positions (Fig. 4B) than WT$_h$. The on-axis step size of Mut$_h$ had reduced (7.1 ± 0.7 nm) minus-end–directed bias, compared with WT$_h$ (10.9 ± 0.8 nm). The probability of Mut$_h$ being in the lead decreased as interhead separation increased (<25% at 30+ nm separations) (fig. S15), and Mut$_h$ was more likely to step backward from the lead (d = –2.6 nm; p_{BW} = 0.44) (Fig. 4B). The average step size and stepping rate of Mut$_h$ were similar to those of WT$_h$ (figs. S14 and S15). Mut$_h$ stepping was mostly directed toward WT$_h$, whereas the direction of WT$_h$ stepping was largely independent of the position of Mut$_h$ (Fig. 4C).

Thus, dynein motility does not require allosteric communication between the AAA1 sites, and only one force-generating head is sufficient for processive movement. WT$_h$ usually remains in the lead and drives forward movement. The detachment of Mut$_h$ from the microtubule can be facilitated by ATP binding to its AAA1 site (*13*). Alternatively, Mut$_h$ can release under tension generated through the power stroke of WT$_h$. Because Mut$_h$ lacks the ability to generate a power stroke, its step size is mainly biased toward the WT$_h$ under tension (Fig. 4D).

Our results challenge established views of motor processivity that require coordination between the mechanochemical cycles of the heads. Kinesin (*18*, *19*) and myosin (*20*) motility rely on mechanical and chemical gating mechanisms that allow the leading head to stay bound to its track while the trailing head moves forward. Dynein clearly moves by a different mechanism. We see no evidence of strict gating that keeps the heads out of phase. Processivity requires two heads to be physically connected (*6*) to prevent detachment of the motor when one of the heads steps forward. It is possible that simultaneous detachment of both heads is stochastic. Dynein's high duty ratio (*21*) may allow the motor to take many steps before dissociation. Processivity in the absence of gating is also achieved by multiple monomeric kinesins (*22*) and engineered dimeric motors that have poor mechanochemical communication between the heads (*18*, *23*). Further understanding of the molecular basis of dynein processivity will require simultaneous monitoring of the linker conformations and stepping motion of the leading and trailing head domains.

References and Notes

1. S. A. Burgess, M. L. Walker, H. Sakakibara, P. J. Knight, K. Oiwa, *Nature* **421**, 715 (2003).
2. T. Kon, M. Nishiura, R. Ohkura, Y. Y. Toyoshima, K. Sutoh, *Biochemistry* **43**, 11266 (2004).
3. K. M. Ori-McKenney, J. Xu, S. P. Gross, R. B. Vallee, *Nat. Cell Biol.* **12**, 1228 (2010).
4. A. P. Carter, C. Cho, L. Jin, R. D. Vale, *Science* **331**, 1159 (2011).
5. R. Mallik, B. C. Carter, S. A. Lex, S. J. King, S. P. Gross, *Nature* **427**, 649 (2004).
6. S. L. Reck-Peterson *et al.*, *Cell* **126**, 335 (2006).
7. A. Yildiz *et al.*, *Science* **300**, 2061 (2003).
8. C. L. Asbury, A. N. Fehr, S. M. Block, *Science* **302**, 2130 (2003).
9. A. Yildiz, M. Tomishige, R. D. Vale, P. R. Selvin, *Science* **303**, 676 (2004).
10. D. Tsygankov, A. W. Serohijos, N. V. Dokholyan, T. C. Elston, *J. Chem. Phys.* **130**, 025101 (2009).

11. L. S. Churchman, Z. Okten, R. S. Rock, J. F. Dawson, J. A. Spudich, *Proc. Natl. Acad. Sci. U.S.A.* **102**, 1419 (2005).
12. D. Nicastro *et al.*, *Science* **313**, 944 (2006).
13. K. Imamula, T. Kon, R. Ohkura, K. Sutoh, *Proc. Natl. Acad. Sci. U.S.A.* **104**, 16134 (2007).
14. A. J. Roberts *et al.*, *Cell* **136**, 485 (2009).
15. A. Gennerich, A. P. Carter, S. L. Reck-Peterson, R. D. Vale, *Cell* **131**, 952 (2007).
16. C. Cho, S. L. Reck-Peterson, R. D. Vale, *J. Biol. Chem.* **283**, 25839 (2008).
17. T. Kon, T. Mogami, R. Ohkura, M. Nishiura, K. Sutoh, *Nat. Struct. Mol. Biol.* **12**, 513 (2005).
18. A. Yildiz, M. Tomishige, A. Gennerich, R. D. Vale, *Cell* **134**, 1030 (2008).
19. B. E. Clancy, W. M. Behnke-Parks, J. O. Andreasson, S. S. Rosenfeld, S. M. Block, *Nat. Struct. Mol. Biol.* **18**, 1020 (2011).
20. S. Nishikawa *et al.*, *Cell* **142**, 879 (2010).
21. T. Shima, K. Imamula, T. Kon, R. Ohkura, K. Sutoh, *J. Struct. Biol.* **156**, 182 (2006).
22. T. Kamei, S. Kakuta, H. Higuchi, *Biophys. J.* **88**, 2068 (2005).
23. J. C. Liao, M. W. Elting, S. L. Delp, J. A. Spudich, Z. Bryant, *J. Mol. Biol.* **392**, 862 (2009).

Acknowledgments: We thank R. D. Vale and A. P. Carter for providing yeast strains; T. Bilyard, F. B. Cleary, and S. Shih for critical evaluation of the manuscript; and K. Schimert for technical assisstance. This work is supported by NIH [GM094522 (A.Y.), GM08295 (M.A.D. and P.A.C.)], NSF [MCB-1055017 (A.Y.)], and Burroughs Wellcome Foundation (A.Y.).

Supporting Online Material

www.sciencemag.org/cgi/content/full/science.1215804/DC1
Materials and Methods
Figs. S1 to S15
Table S1
References (*24*–*29*)
Movies S1 to S4

26 October 2011; accepted 24 November 2011
Published online 8 December 2011;
10.1126/science.1215804

Tumor Necrosis Factor Signaling Requires iRhom2 to Promote Trafficking and Activation of TACE

Colin Adrain,[1]† Markus Zettl,[1]*† Yonka Christova,[1] Neil Taylor,[2] Matthew Freeman[1]‡

The cytokine tumor necrosis factor (TNF) is the primary trigger of inflammation. Like many extracellular signaling proteins, TNF is synthesized as a transmembrane protein; the active signal is its ectodomain, which is shed from cells after cleavage by an ADAM family metalloprotease, ADAM17 (TNFα-converting enzyme, TACE). We report that iRhom2 (RHBDF2), a proteolytically inactive member of the rhomboid family, is required for TNF release in mice. iRhom2 binds TACE and promotes its exit from the endoplasmic reticulum. The failure of TACE to exit the endoplasmic reticulum in the absence of iRhom2 prevents the furin-mediated maturation and trafficking of TACE to the cell surface, the site of TNF cleavage. Given the role of TNF in autoimmune and inflammatory diseases, iRhom2 may represent an attractive therapeutic target.

Proteolytic release of the extracellular domain of transmembrane proteins is an important mechanism for generating signals that regulate major aspects of animal development, physiology, immunity, and pathology (*1*, *2*). An important example of regulated ectodomain shedding is the cytokine tumor necrosis factor (TNF), the primary trigger of inflammatory responses. TNF is associated with many human diseases, including rheumatoid arthritis, Crohn's disease, atherosclerosis, psoriasis, sepsis, diabetes, and obesity. Its blockade is licensed as a therapy for a number of conditions and is being assessed for others (*3*). Soluble, active TNF is shed from the plasma membrane by the ADAM family metalloprotease TACE (TNFα-converting enzyme, also known as ADAM17) (*4*). Despite the medical importance of TNF and other transmembrane signaling proteins, the regulation of ectodomain shedding remains poorly understood. Both the transmembrane forms of the signaling proteins themselves and the shedding proteases are subject to control by posttranslational modification, interaction with specific partners, and regulated intracellular trafficking and compartmentalization (*5*–*9*). The relative physiological importance, however, of these different modes of regulation is unclear.

We have investigated the regulation of ectodomain shedding by genetic and cellular approaches, both in *Drosophila* and mammalian cells. This has led to the recent discovery of a new class of polytopic endoplasmic reticulum (ER) proteins, the iRhoms, which are noncatalytic relatives of rhomboid intramembrane proteases (Fig. 1A) (*10*). *Drosophila* iRhom regulates epidermal growth factor (EGF) receptor signaling by interacting with EGF family ligands in the ER, shunting them into the ER-associated degradation (ERAD) pathway (*11*). iRhoms are conserved in all metazoans, and in cell culture assays, their mammalian counterparts, iRhom1 and iRhom2, can also promote ERAD of EGF. In mammals, however, their physiological role is unknown. We therefore generated a null mutation in the gene that encodes iRhom2 (RHBDF2) in mice (*12*) (fig. S1A). *iRhom2*$^{-/-}$ (knockout, KO) mice appeared normal: They were viable and fertile, with no morphological defects. Unlike iRhom1, which is widely expressed, iRhom2 is predominantly expressed in immune cells, particularly macrophages (*13*, *14*), where its expression was specifically up-regulated in response to lipopolysaccharide (LPS) stimulation (Fig. 1B). We therefore challenged *iRhom2*$^{-/-}$ mice with LPS, to mimic bacterial infection, and measured the serum concentration of proinflammatory cytokines. Interleukin-1β (IL-1β), IL-6, and IL-12 were induced normally but, remarkably, TNF induction was almost completely abolished in mutant mice (Fig. 1C). Macrophages are the most abundant source of TNF; consistent with this, in vitro differentiated bone marrow–derived macrophages (BMDMs) from *iRhom2*$^{-/-}$ mice failed to secrete TNF in response to LPS (Fig. 1D).

The failure of TNF secretion in *iRhom2*$^{-/-}$ mice [confirmed in this issue; see (*15*)] is not caused by its loss of expression: RNA levels were unaffected (fig. S2A), and protein levels were actually elevated in *iRhom2*$^{-/-}$ macrophages (Fig. 2, A and B). This result was confirmed by cell surface labeling followed by affinity precipitation, which showed an increase in the accumulation of the full-length, membrane-tethered form of TNF on the plasma membrane of mutant cells (Fig. 2C). Furthermore, inhibition of the shedding protease TACE in wild-type (WT) cells by the matrix metalloproteinase inhibitor BB94 (Fig. 2, A and C) resulted in a phenotype similar to *iRhom2*$^{-/-}$ macrophages. Together, these data imply that loss of iRhom2 does not interfere with the induction or intracellular trafficking of TNF but instead suggests a shedding defect. We tested this hypothesis directly. Although TACE levels were normal in both WT and mutant macrophages (Fig. 2D), loss of iRhom2 led to a complete abolition of activity of immunoprecipitated TACE (Fig. 2E and fig. S2B). This result explains the loss of TNF shedding in mutant mice and macrophages.

Like TNF, TACE has been the focus of major pharmaceutical interest: Not only does it regulate inflammation through TNF, but it is also implicated in cancer by activating EGF receptor ligands (*16*); furthermore, it is a point of integration for a wide range of incoming signals (*17*). Despite this intense spotlight, TACE regulation remains poorly understood. Several lines of evidence suggest the trafficking of enzyme to the plasma membrane is important, but other work implies that, at least in some contexts, the rate-limiting step may be activation of molecules already at the cell surface (*5*–*7*, *18*, *19*). Because most evidence agrees that the plasma membrane is the primary site of TACE activity, we tested

[1]Medical Research Council Laboratory of Molecular Biology, Hills Road, Cambridge CB2 0QH, UK. [2]Cambridge Research Institute, Cancer Research UK, Li Ka Shing Centre, Robinson Way, Cambridge CB2 0RE, UK.

*Present address: Boehringer Ingelheim, NBE Discovery, Dr. Boehringer-Gasse 5-11, A-1121 Wien, Austria.
†These authors contributed equally to this work.
‡To whom correspondence should be addressed. E-mail: MF1@mrc-lmb.cam.ac.uk

whether TACE was present at the cell surface of *iRhom2*$^{-/-}$ cells. In contrast to WT cells, no TACE was found on the surface of *iRhom2*$^{-/-}$ macrophages (Fig. 3, A and B), which implies that the cause of TACE inactivity is a fundamental defect in its intracellular trafficking.

Endoglycosidase-H (endo-H)–sensitive *N*-glycans are added to TACE in the ER. The sugars are then elaborated in the Golgi apparatus, becoming resistant to endo-H. Later in the trans-Golgi network (TGN), the inhibitory N-terminal prodomain is removed by furin (*20*). These modifications can be used to track the progress of TACE from the ER to the plasma membrane (see fig. S2, C and D, for an overview). Consistent with previous reports (*7*, *20*), we found the majority of endogenous TACE to be endo-H–sensitive and, therefore, located in the ER in both WT and mutant cells (Fig. 3C). In the absence of iRhom2, however, TACE never became endo-H resistant, which demonstrated that it was unable to reach the site of addition of Golgi-specific glycans as it does in WT cells (Fig. 3C, bracket). Furthermore, furin cleavage of the prodomain was abolished in the KO cells (Fig. 3C, white arrowhead). We conclude that trafficking from the ER is a limiting step for TACE maturation and that iRhom2 is an essential component of the mechanism that releases it to the Golgi apparatus. Without iRhom2, therefore, TACE cannot reach the TGN to be activated.

Our results are consistent with iRhom2 being a rate-limiting factor in releasing TACE from the ER. To examine this directly, we expressed mouse *iRhom2* in human embryonic kidney (HEK) cells and assayed its effect on endogenous human TACE. Overexpression of *iRhom2* caused excess TACE to leave the ER, which resulted in more furin-processed TACE (Fig. 3D, white arrow), and this translated into an overall increase in TACE enzyme activity (Fig. 3E). This result demonstrates that iRhom2 is rate-limiting for TACE activity and also indicates conservation of human and mouse iRhom2 function. This was confirmed by showing that knockdown of human *iRhom2* expression by RNA interference (RNAi) inhibited the maturation of endogenous TACE in human cells (Fig. 3F).

How might iRhom2 control trafficking of TACE? Because most TACE resides in the ER, which is also where the bulk of iRhom2 is detected in COS cells (*11*), we asked whether they can bind to each other directly. Indeed, when coexpressed in HEK cells, mouse iRhom2 efficiently immunoprecipitated tagged mouse TACE (Fig. 4A and fig. S3A), whereas multiple control transmembrane proteins showed no interaction with iRhom2 (Fig. 4, A and F; and fig. S3, A and B). Conversely, tagged iRhom2 was immunoprecipitated by endogenous TACE (fig. S3C). Moreover, we found that both endogenous TACE and iRhom2 proteins could coimmunoprecipitate one another in macrophages (Fig. 4, B and C). iRhom2 interacts with both endogenous full-length TACE and the mature form (Fig. 4A; black and white arrowheads, respectively), although by increasing the stringency of the binding and washing conditions, we found that the interaction is weaker once the TACE prodomain is removed (Fig. 4D; immature and mature TACE indicated by black and white arrowheads, respectively). We also tested whether iRhom2 interacts with ADAM10, TACE's closest relative (*16*). In contrast to TACE, no interaction (Fig. 4A) or effect on ADAM10 trafficking (Fig. 4E) was detected, which indicated a high level of specificity of iRhom2 for potential client proteins.

The membrane-permeable chemical cross-linker dithiobis(succinimidyl propionate) (DSP) could cross-link iRhom2 to both full-length and mature TACE (Fig. 4F; black and white arrowheads, respectively) in living HEK cells, which implied that the interaction occurs in vivo and that the two proteins are less than 12 Å apart. Therefore, the binding is probably direct. Together, these data make a strong case that iRhom2 binds directly to TACE and so regulates its trafficking from the ER. We envisage two alternative models to explain these results. Either iRhom2 is required in the ER for the folding and/or maturation of TACE, or it acts like a cargo receptor to assist the onward trafficking of TACE. In support of the latter model, we find that iRhom2 in macrophages carries endo-H–resistant, Golgi-

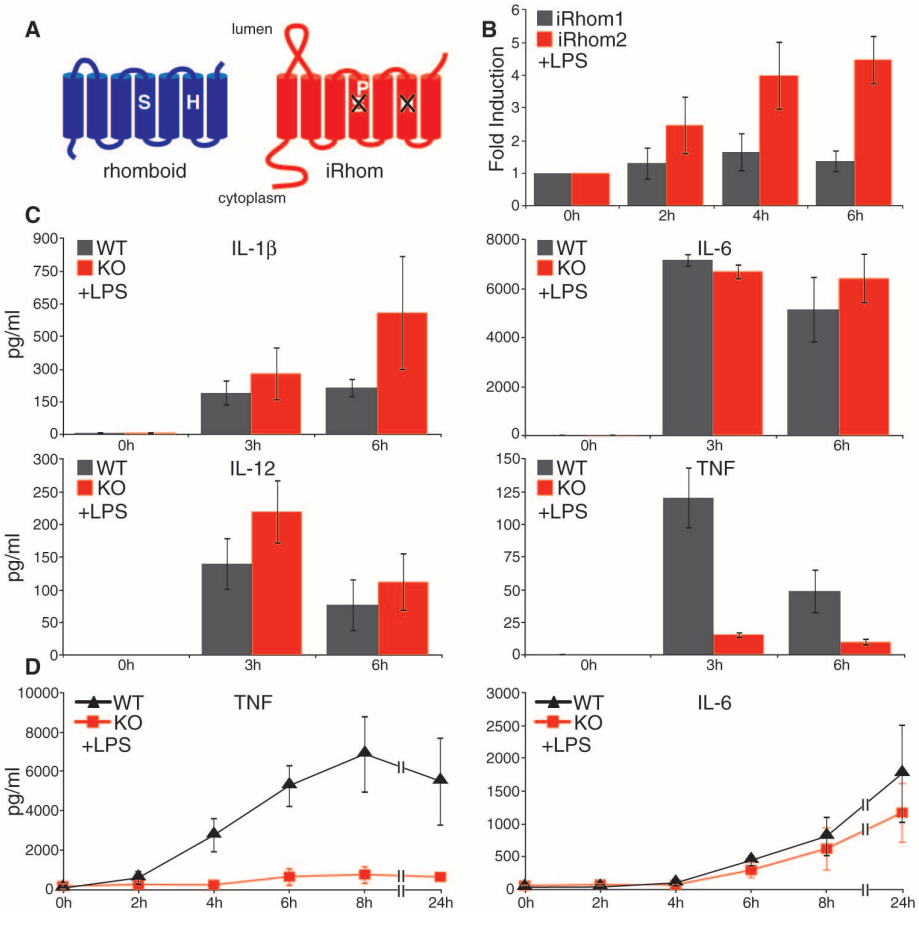

Fig. 1. iRhom2 is essential for LPS-induced TNF shedding. (**A**) Comparison of an active rhomboid protease and iRhom. (**B**) Fold induction of *iRhom2* mRNA in response to LPS in WT macrophages (mean of three experiments ± SD), as measured by quantitative polymerase chain reaction. mRNA levels were normalized to endogenous actin. (**C**) Serum concentrations of the indicated cytokines in WT and *iRhom2*$^{-/-}$ (KO) mice in response to LPS (mean of five experiments ± SD), as measured by multianalyte cytokine profiling. (**D**) TNF and IL-6 production by LPS-stimulated BMDMs [WT and *iRhom2*$^{-/-}$ (KO); mean of three experiments ± SD], as measured by enzyme-linked immunosorbent assay (ELISA). All graphs show means ± SD.

specific glycans (Fig. 4G), which implies that at least some iRhom2 is trafficked beyond the ER. This is consistent with the observed binding in vivo of iRhom2 to both full-length and mature TACE. The reduction in affinity once the prodomain is removed suggests possible release of TACE from iRhom2 once activated by furin (although we emphasize that this last interpretation is speculative). In further support of our model, and as an argument against TACE folding being substantially disrupted, catalytically inactive TACE immunoprecipitated from *iRhom2* KO cells (Fig. 2E) can be made active by incubation with recombinant furin (Fig. 4H). This indicates that lack of access to furin is the primary cause of TACE inactivity.

These data, along with our previous results (*11*), suggest that iRhoms are polytopic membrane proteins that bind to single-pass transmembrane proteins in the ER and so regulate their subsequent trafficking (Fig. 4I). Depending on the specific iRhom, the client, and/or the cellular context, iRhoms can promote exit from ER, or degradation (*11*). The ER exit of some Toll-like receptors, which also have a single transmembrane domain (TMD), depends on an unrelated polytopic membrane protein, Unc93b1 (*21*). Perhaps trafficking assistance for proteins with single TMDs is common; they may require specific cargo reception machinery, or alternatively, TMD chaperones may prevent nonspecific TMD interactions. There is a family of other nonproteolytic rhomboidlike proteins that also lack defining features of iRhoms, including, very distantly, derlins (*10*, *22*). It is possible that this wider group of rhomboidlike membrane proteins may also interact with, and regulate, the fate of single-pass transmembrane proteins.

This work provides a mechanistic explanation for why TNF production is abolished in *iRhom2* KO mice. Note that *iRhom2* expression is itself

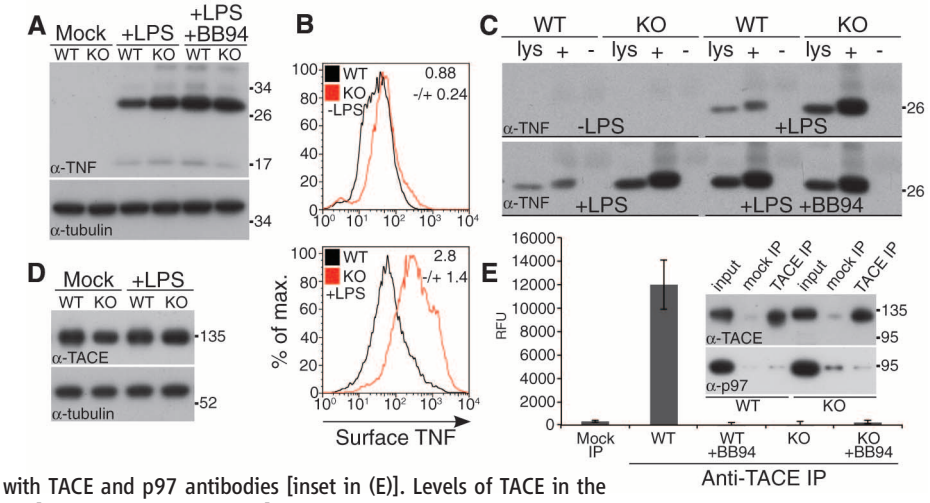

Fig. 2. TNF biogenesis is normal, but TACE proteolytic activity is defective in *iRhom2*$^{-/-}$ cells. (**A**) Immunoblots for TNF of extracts from mock, LPS-, or LPS- and BB94-treated macrophages. Antibody against tubulin was used to determine equal loading throughout. (**B**) Flow cytometric analysis of surface TNF on CD11b+ WT and *iRhom2*$^{-/-}$ (KO) macrophages 3 hours after LPS treatment. The fold change in mean fluorescent intensity (KO/WT) is indicated in each graph (mean of three experiments ± SD). (**C**) Whole-cell lysate (lys) versus cell surface biotinylated (+) or mock-treated (–) proteins bound to NeutrAvidin resin from WT or KO macrophages were immunoblotted as indicated. (**D**) Immunoblot of TACE expression in BMDMs. (**E**) Immunoprecipitates (IPs) from *iRhom2*$^{-/-}$ macrophages subjected to a fluorogenic cleavage assay (mean of three experiments ±SD). Specificity of the TACE antibody is demonstrated by probing IPs with TACE and p97 antibodies [inset in (E)]. Levels of TACE in the activity assay were equal in WT and KO macrophages [inset in (E) and fig. S2B].

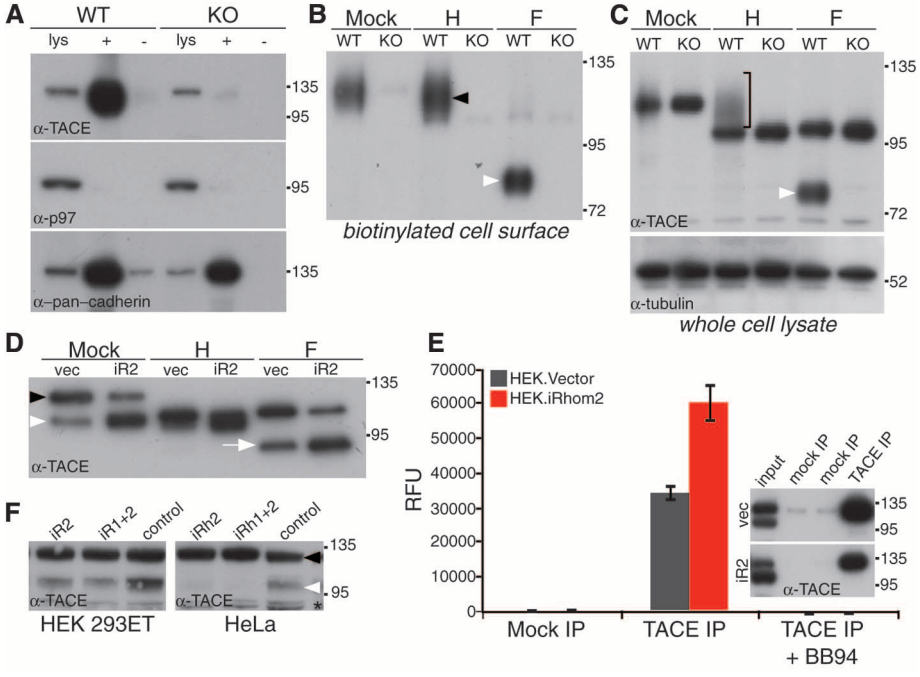

Fig. 3. iRhom2 is essential for ER exit and activation of TACE. (**A**) Cell surface biotinylation was used to detect TACE at the plasma membrane in WT and *iRhom2*$^{-/-}$ (KO) macrophages: whole-cell lysates (lys); NeutrAvidin captured cell surface proteins (+); mock-treated (–). Cytoplasmic protein p97 was used as a negative control for cell surface biotinylation; surface levels of cadherin are comparable in WT and KO cells. (**B**) Biotinylated cell surface proteins were deglycosylated with endo-H (H), which cleaves ER, but not Golgi, *N*-glycans, or *N*-glycosidase F (PNGase F) (F), which removes both. Cell surface TACE is endo-H–resistant (black arrowhead). TACE matures by acquiring Golgi *N*-glycans and by furin-catalyzed removal of the prodomain. PNGase F treatment of cell surface TACE generates a lower molecular weight polypeptide corresponding to the furin-cleaved species (white arrowhead; see also fig. S2, B and C). (**C**) TACE immunoblot of whole-cell lysates treated with endo-H (H) or PNGase F (F) Bracket, endo-H–resistant mature TACE. For PNGase F–treated lysates: the upper band is ER resident, immature TACE, and the lower band is furin-cleaved TACE (white arrowhead; see also Fig. 3B and fig. S2, C and D). (**D**) Cell extracts from HEK cells stably expressing mouse iRhom2 were deglycosylated with endo-H (H) or PNGase F (F) and immunoblotted for TACE. Unlike mouse BMDM-derived TACE, human TACE can be detected as two species in lysates without prior deglycosylation (immature, black arrowhead; mature, white arrowhead). (**E**) Activity of TACE IPs from HEK cells expressing iRhom2 (mean of three experiments ± SD); specificity of the IP was confirmed by Western blot (inset). (**F**) The effect of small interfering RNA knockdown of human *iRhom2* (and combined *iRhom1/2*) on the expression of endogenous mature TACE (white arrowhead; black arrowhead indicates immature TACE) in human HEK 293T and HeLa cells. As a control, an unrelated member of the rhomboid family (RHBDL2) was knocked down. The asterisk denotes a nonspecific band.

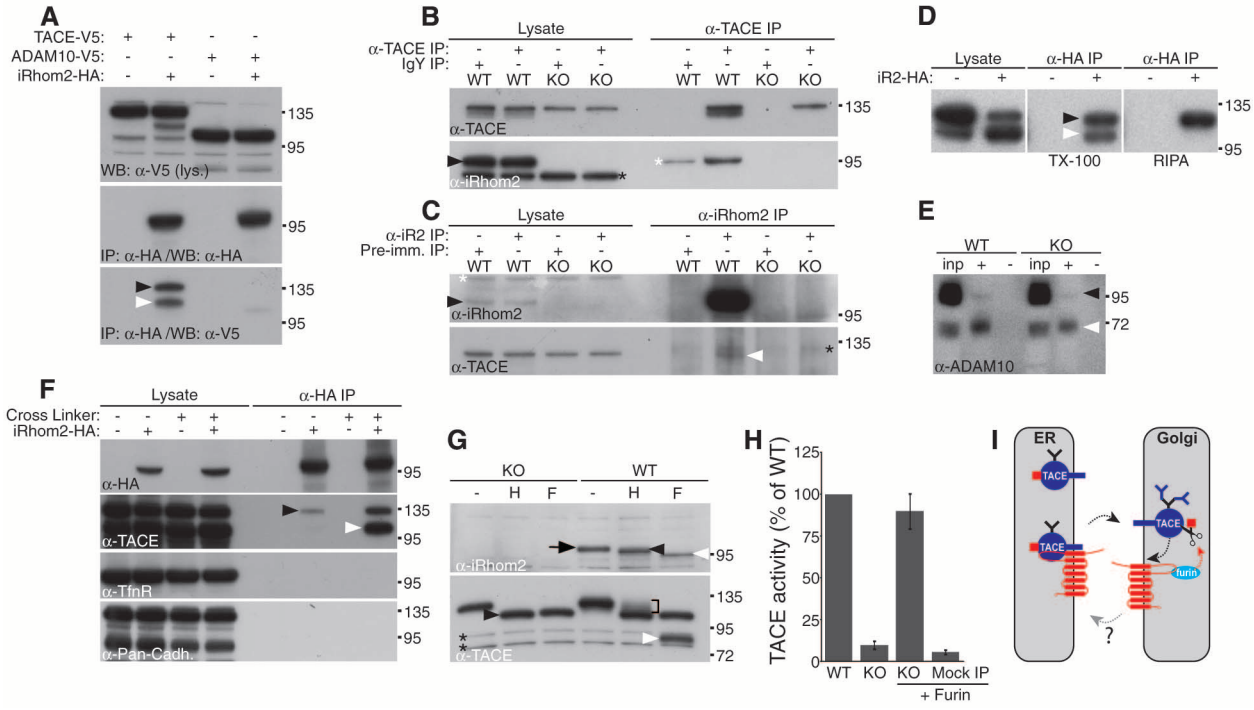

Fig. 4. iRhom2 interacts with TACE and leaves the ER. (**A**) HEK cells or HEK cells stably expressing iRhom2-HA were transfected with TACE-V5 or ADAM10-V5. Lysates were immunoprecipitated with HA-specific antibody and immunoblotted with V5 and HA antibodies. Coimmunoprecipitation of immature and mature TACE is indicated by black and white arrowheads, respectively. (**B**) Macrophage lysates were immunoprecipitated with antibody against TACE and immunoblotted for iRhom2 or TACE. Arrowhead, endogenous iRhom2; black asterisk, a nonspecific band detected in both KO and WT; white asterisk, background binding of iRhom2 to the resin. (**C**) Macrophage lysates were immunoprecipitated with anti-iRhom2 and immunoblotted for iRhom2 or TACE. White arrowhead, endogenous TACE; black arrowhead, endogenous iRhom; white asterisk, original TACE signal detected following reprobing; black asterisk, a nonspecific band in all IP lanes. (**D**) HEK cells expressing iRhom2-HA were immunoprecipitated with HA-specific antibody and immunoblotted for TACE. Immature and mature TACE are indicated by black and white arrowheads, respectively. Immunoprecipitations were performed under mild (Triton X-100 detergent) and more stringent [radioimmunoprecipitation assay (RIPA) buffer] conditions. (**E**) Complete input extracts (inp) and surface biotinylated proteins (+) from WT and iRhom2 KO macrophages immunoblotted for ADAM10. Black arrowhead, immature ADAM10; white arrowhead, mature ADAM10. (**F**) IPs (in RIPA buffer) of iRhom2-HA from HEK cells; precipitates were done +/– the cross-linker DSP. IPs were immunoblotted for TACE; immature and mature TACE are indicated by black and white arrowheads, respectively. Transferrin receptor and pan-cadherin immunoblots were used as negative controls. (**G**) Lysates from LPS-treated WT or KO macrophages were treated with endo-H (H) or PNGase-F (F) and immunoblotted for iRhom2. Arrow, fully glycosylated iRhom2; black and white arrowheads, endo-H–resistant single glycan form and unmodified polypeptide, respectively (iRhom2 has two predicted N-linked glycosylation sites; only one is modified in the Golgi). (Bottom) TACE in the same lysates as control. Black arrowhead, endo-H–sensitive TACE; bracket, endo-H–resistant TACE; white arrowhead, mature TACE; asterisks, nonspecific bands. (**H**) TACE IPs were preincubated –/+ 100 nM recombinant furin before TACE activity was measured. (**I**) Model of iRhom2 function in macrophages.

up-regulated by TNF signaling (*23*), which implies a positive-feedback loop: TNF up-regulates the mechanism that promotes its own activation. Positive feedback can sharpen physiological signaling responses—but can also promote hyperactivity if normal regulation is disrupted—and underlies a variety of inflammatory and oncogenic pathologies (*24*). The further medical implication of this work is the potential of interfering with iRhom2 or its binding to TACE as a strategy to block TNF signaling. Although TNF blockade is already licensed as a therapeutic strategy, its use is hampered by side effects. The specificity, expression, and the mouse phenotype we report implies that pharmacological disruption of the interaction between iRhom2 and TACE should block specifically macrophage release of TNF.

References and Notes

1. M. Gooz, *Crit. Rev. Biochem. Mol. Biol.* **45**, 146 (2010).
2. J. J. Peschon *et al.*, *Science* **282**, 1281 (1998).
3. D. Tracey, L. Klareskog, E. H. Sasso, J. G. Salfeld, P. P. Tak, *Pharmacol. Ther.* **117**, 244 (2008).
4. R. A. Black *et al.*, *Nature* **385**, 729 (1997).
5. S. M. Le Gall *et al.*, *J. Cell Sci.* **123**, 3913 (2010).
6. P. Xu, R. Derynck, *Mol. Cell* **37**, 551 (2010).
7. S. M. Soond, B. Everson, D. W. Riches, G. Murphy, *J. Cell Sci.* **118**, 2371 (2005).
8. S. D. Ha *et al.*, *J. Immunol.* **181**, 690 (2008).
9. Z. Z. Lieu *et al.*, *Proc. Natl. Acad. Sci. U.S.A.* **105**, 3351 (2008).
10. M. K. Lemberg, M. Freeman, *Genome Res.* **17**, 1634 (2007).
11. M. Zettl, C. Adrain, K. Strisovsky, V. Lastun, M. Freeman, *Cell* **145**, 79 (2011).
12. Materials and methods are presented as supporting material on *Science* Online.
13. A. I. Su *et al.*, *Proc. Natl. Acad. Sci. U.S.A.* **101**, 6062 (2004).
14. BioGPS, mouse RHBDF2 gene atlas data sets MOE430 and GNF1M, www.biogps.org/#goto=genereport&id=79651.
15. D. R. McIlwain *et al.*, *Science* **335**, 229 (2012).
16. P. Saftig, K. Reiss, *Eur. J. Cell Biol.* **90**, 527 (2011).
17. G. Murphy, *Semin. Cell Dev. Biol.* **20**, 138 (2009).
18. S. M. Le Gall *et al.*, *Mol. Biol. Cell* **20**, 1785 (2009).
19. S. Rousseau *et al.*, *J. Cell Sci.* **121**, 149 (2008).
20. J. Schlöndorff, J. D. Becherer, C. P. Blobel, *Biochem. J.* **347**, 131 (2000).
21. Y. M. Kim, M. M. Brinkmann, M. E. Paquet, H. L. Ploegh, *Nature* **452**, 234 (2008).
22. E. J. Greenblatt, J. A. Olzmann, R. R. Kopito, *Nat. Struct. Mol. Biol.* **18**, 1147 (2011).
23. Gene Expression Omnibus, profile GDS1543, www.ncbi.nlm.nih.gov/geoprofiles?term=GDS1543[ACCN]+nm_024599.
24. M. Freeman, *Nature* **408**, 313 (2000).

Acknowledgments: We thank C. Blobel, R. Hegde, G. Murphy, S. Munro, V. Lastun, C. Luginsland, and K. Strisovsky for their advice and generously sharing unpublished reagents. We are grateful to R. Pannell for help with the mouse knockout and to members of the animal facility for their assistance. The data presented in this paper are reported in the main paper and in the Supporting Online Material. C.A. was supported by a long-term fellowship from The International Human Frontier Science Program Organization and was the recipient of an EMBO Long-Term Fellowship. M.Z. was supported by Erwin-Schrödinger fellowship from the Austrian Science Fund (FWF), and an APART fellowship from the Austrian Academy of Science. This work was supported by the Medical Research Council programme number U105178780.

Supporting Online Material

www.sciencemag.org/cgi/content/full/335/6065/225/DC1
Materials and Methods
Figs. S1 to S3
References (*25*–*27*)

23 September 2011; accepted 10 November 2011
10.1126/science.1214400

iRhom2 Regulation of TACE Controls TNF-Mediated Protection Against *Listeria* and Responses to LPS

David R. McIlwain,[1,2]* Philipp A. Lang,[1,3]* Thorsten Maretzky,[4] Koichi Hamada,[5] Kazuhito Ohishi,[6] Sathish Kumar Maney,[3] Thorsten Berger,[1] Aditya Murthy,[7] Gordon Duncan,[1] Haifeng C. Xu,[1,3] Karl S. Lang,[3,8] Dieter Häussinger,[3] Andrew Wakeham,[1] Annick Itie-Youten,[1] Rama Khokha,[7] Pamela S. Ohashi,[1,2] Carl P. Blobel,[4,9] Tak W. Mak[1,2]†

Innate immune responses are vital for pathogen defense but can result in septic shock when excessive. A key mediator of septic shock is tumor necrosis factor–α (TNFα), which is shed from the plasma membrane after cleavage by the TNFα convertase (TACE). We report that the rhomboid family member iRhom2 interacted with TACE and regulated TNFα shedding. iRhom2 was critical for TACE maturation and trafficking to the cell surface in hematopoietic cells. Gene-targeted iRhom2-deficient mice showed reduced serum TNFα in response to lipopolysaccharide (LPS) and could survive a lethal LPS dose. Furthermore, iRhom2-deficient mice failed to control the replication of *Listeria monocytogenes*. Our study has identified iRhom2 as a regulator of innate immunity that may be an important target for modulating sepsis and pathogen defense.

Tumor necrosis factor–α (TNFα) is both crucial for effective innate immunity and a pathologic contributor to inflammatory diseases, including sepsis and rheumatoid arthritis (*1*–*4*). How TNFα signaling is regulated, however, is still not fully understood. To identify new molecules involved in regulating TNFα signaling, we performed an unbiased cyclic packaging rescue screen (*5*) to isolate cDNAs conferring TNFα resistance. One such candidate was a short cDNA (iRhom2*) derived from the gene encoding iRhom2 (Rhbdf2) (fig. S1), which is a largely uncharacterized member of the rhomboid protein family (*6*–*8*). Stable overexpression of iRhom2* in L929 cells revealed its localization in the endoplasmic reticulum (ER), consistent with previous studies of iRhoms (*8*–*10*), and partial localization in the Golgi apparatus (fig. S2). iRhom2* overexpression protected L929 cells from TNFα-induced apoptosis (Fig. 1A). Experiments using the metalloprotease (MP) inhibitor BB-2516 suggested that this TNFα resistance was the result of MP-dependent release of TNFα receptors (TNFRs) from the cell surface (Fig. 1, B and C). Because TNFR shedding is mediated by TNFα convertase (TACE) [also known as a disintegrin and MP (ADAM) 17] (*11*), we investigated whether iRhom2 interacts with TACE. Mature TACE is generated after processing of its prodomain in the Golgi (*12*, *13*). By preparing cell lysates in the presence of MP inhibitors to prevent autocatalytic degradation of mature TACE (*12*) and by performing concanavalin A (Con A) lectin purification, we were able to use immunoblotting to clearly distinguish immature (or pro-TACE) from the active mature form of TACE (fig. S3). Immunoprecipitation of lysates of iRhom2-overexpressing fibroblasts followed by immunoblotting revealed a physical association between tagged iRhom2 and both pro- and mature forms of TACE, which suggested that iRhom2 and TACE are associated through multiple stages of the secretory pathway (Fig. 1D). This interaction appears specific, as no such association with other ADAM family members, including ADAM9 and ADAM15, could be detected

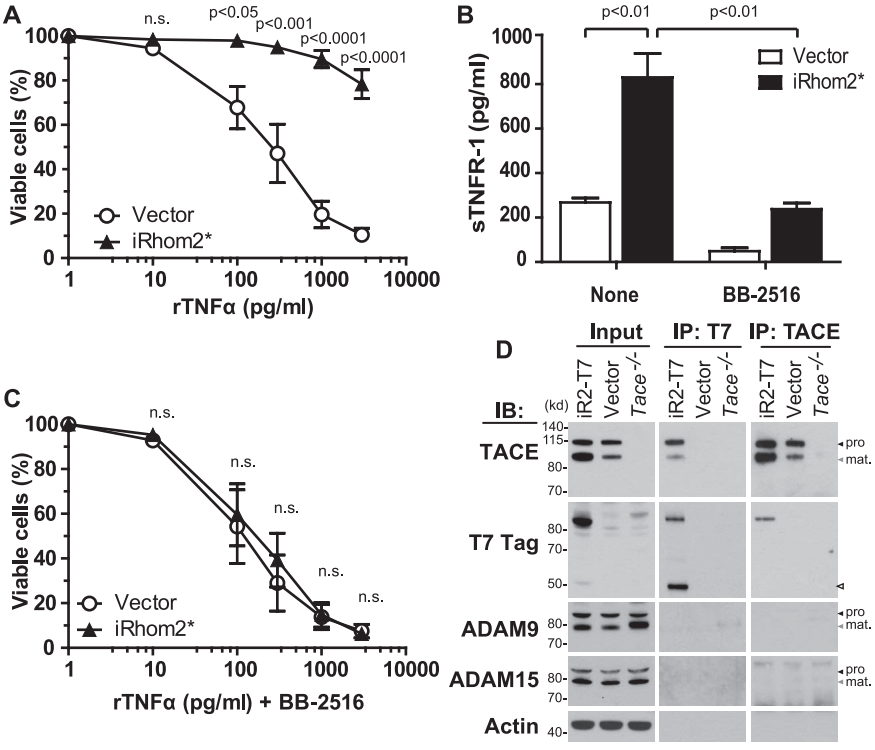

Fig. 1. iRhom2 confers resistance to TNFα in a MP-dependent manner and interacts with TACE. (**A**) L929 cells stably overexpressing iRhom2* or control vector were treated with recombinant TNFα (rTNFα) at the indicated concentrations, and percent viability was determined by Annexin-7AAD exclusion (means ± SEM; $n = 4$ experiments). (**B**) Untreated cells from (A) were cultured with or without MP inhibitor BB-2516 (20 μM) for 24 hours. Soluble TNFR1 in the culture supernatant was measured by enzyme-linked immunosorbent assay (ELISA) (means ± SEM; $n = 3$ experiments). (**C**) Cells from (A) were treated for 24 hours with TNFα at the indicated concentrations plus 20 μM BB-2516, and viability was assessed as in (A) (means ± SEM; $n = 4$ experiments). (**D**) WT immortalized mouse embryonic fibroblasts (MEFs) stably overexpressing T7-tagged iRhom2 (iR2-T7) or control vector and *Adam17*$^{-/-}$ (*Tace*$^{-/-}$) MEFs (negative control) were immunoprecipitated (IP) by using antibodies against T7 or TACE followed by immunoblotting (IB) to detect T7 or TACE. ADAM9 and ADAM15 were specificity controls; actin, loading control. Black arrowheads indicate immature proforms, whereas gray arrowheads indicate mature forms, of TACE and other ADAMs (for all figures). Empty arrowhead is likely a processed form of iRhom2. Con A purification was used to enhance detection of TACE in input lanes (unpurified input appears in fig. S3). Results are representative of three trials.

[1]Campell Family Institute for Breast Cancer Research, Ontario Cancer Institute, University Health Network (UHN), 620 University Avenue, Toronto, Ontario M5G 2C1, Canada. [2]Department of Medical Biophysics, University of Toronto, 1 King's Circle, Toronto, Ontario M5S 1A8, Canada. [3]Department of Gastroenterology, Hepatology and Infectious Diseases, University of Düsseldorf, Universitätsstrasse 1, 40225 Düsseldorf, Germany. [4]Arthritis and Tissue Degeneration Program, Hospital for Special Surgery, New York, NY 10021, USA. [5]Okada Projects at the Center for AIDS Research, Kumamoto University, 2-2-1 Honjo, Kumamoto 860-0811, Japan. [6]Department of Pathology, Graduate School of Medicine, Osaka University, 2-2 Yamada-oka, Suita, Osaka 565-0871, Japan. [7]Ontario Cancer Institute, UHN, Toronto, Ontario, M5G 2M9, Canada. [8]Institute for Immunology, University of Essen, Hufelandstrasse 55, 45147 Essen, Germany [9]Departments of Medicine and of Physiology, Biophysics and Systems Biology, Weill Medical College of Cornell University, New York, NY 10021, USA.

*These authors contributed equally to this work.
†To whom correspondence should be addressed. E-mail: tmak@uhnresearch.ca

(Fig. 1D). These data suggested that association with iRhom2 might be important for regulating TACE activity.

To investigate whether the relation between iRhom2 and TACE was physiologically relevant, we generated mice deficient for the gene that encodes iRhom2 (*iRhom2*$^{-/-}$) in which exons 4 to 14 of the *iRhom2* gene were deleted, which abolished expression of *iRhom2* mRNA (fig. S4). *iRhom2*$^{-/-}$ mice are viable and fertile, show no obvious defects, have a normal life-span, and exhibit a normal immune cell distribution (table S1). Because TACE is classically known to be the enzyme responsible for production of soluble TNFα through surface shedding (*14*, *15*), we analyzed TNFα production by macrophages. When thioglycollate-elicited peritoneal macrophages (TGEMs) were isolated from control (*iRhom2*$^{+/+}$ or *iRhom*$^{+/-}$) mice and stimulated in vitro with the Toll-like receptor (TLR) 4 ligand lipopolysaccharide (LPS), the mRNA levels of iRhom2, TACE, and TNFα were all increased (fig. S5, A to C). TACE and TNFα mRNA levels were comparably up-regulated in LPS-stimulated *iRhom2*$^{-/-}$ TGEMs (fig. S5, B and C), but significantly less TNFα protein was shed into mutant cell culture supernatants than into control supernatants (Fig. 2A). Consistent with a block in membrane-bound TNFα cleavage (*16*) in the absence of iRhom2, LPS-treated *iRhom2*$^{-/-}$ TGEMs accumulated higher expression of

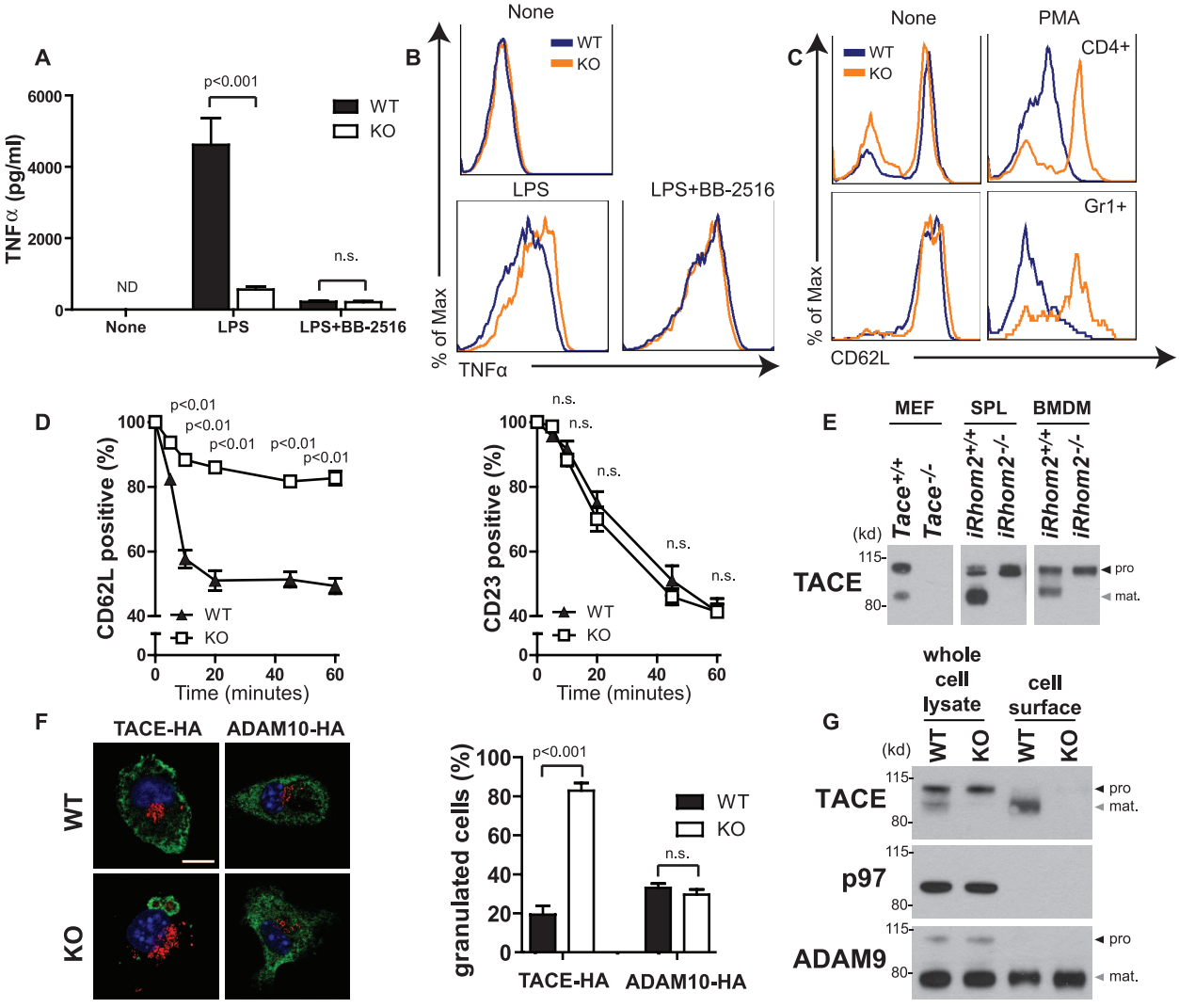

Fig. 2. iRhom2 deficiency reduces TACE activity in vitro. (**A** and **B**) WT and *iRhom2*$^{-/-}$ TGEMs were stimulated in vitro with 1 μg/ml LPS, with or without 20 μM BB-2516. (A) TNFα in culture supernatants was determined by ELISA after 24 hours of treatment (means ± SEM of triplicates). (B) Membrane-bound TNFα was assayed by flow cytometry after 3 hours of treatment. Results are representative of three trials. (**C**) Isolated WT and *iRhom2*$^{-/-}$ total splenocytes were stimulated in vitro with 25 ng/ml PMA for 3 hours, and CD62L expression on CD4$^+$ T cells and Gr1$^+$ granulocytes was determined by flow cytometry. Results are representative of three trials. (**D**) WT and *iRhom2*$^{-/-}$ total splenocytes were stimulated with 2 mM BzATP for the indicated times, and surface–levels of CD62L and CD23 (ADAM10 substrate) on B220$^+$CD3$^-$ B cells were determined by flow cytometry (means ± SEM; n = 3 mice per group). (**E**) Con A–purified lysates of control and *iRhom2*$^{-/-}$ splenocytes (SPL) or BMDMs were immunoblotted to detect pro- (black arrowhead) and mature (gray arrowhead) TACE. *Adam17*$^{-/-}$ *(TaCE*$^{-/-}$*)* MEFs, negative control. Additional controls appear in fig. S6A. Results are representative of three trials. (**F**) (Left) Control and *iRhom2*$^{-/-}$ BMDMs were transfected with vectors expressing TACE-HA or ADAM10-HA (green), stimulated with LPS, and visualized by confocal immunofluorescence microscopy. Giantin (red) and 4′,6′-diamidino-2-phenylindole (DAPI) stain (blue). Scale bar, 10 μm. (Right) Percentages of control and *iRhom2*$^{-/-}$ BMDMs that exhibited granulated vesicular appearance of TACE or ADAM10 localization (means ± SEM; n = 4 to 6 experiments). (**G**) (Top) Immunoblot to detect pro- (black arrowhead) and mature (gray arrowhead) TACE in whole-cell lysates and purified cell surface fractions of control and *iRhom2*$^{-/-}$ BMDMs. (Middle) P97, intracellular protein (negative control). (Bottom) Pro- (black arrowhead) and mature (gray arrowhead) ADAM9 (positive control). Results are representative of three trials.

membrane-bound TNFα than controls (Fig. 2B, left). Treatment with BB-2516 mimicked iRhom2 deficiency, as it increased levels of membrane-bound TNFα on LPS-stimulated wild-type (WT) TGEMs to levels observed on untreated *iRhom2*$^{-/-}$ TGEMs (Fig. 2B, right). No difference in the secretion of other LPS-induced cytokines, such as interleukin-6 (IL-6) or IL-12, was observed (fig. S5, D and E). Although a mechanism of triggering IL-12 production involving processing of the TNFα intracellular domain has been described (*17*), proficient IL-12 production in *iRhom2*$^{-/-}$ macrophages after LPS is consistent with other mouse models incapable of producing soluble TNFα (*18*).

TACE is also crucial for the stimulus-dependent cleavage of other substrates from the surfaces of immune cells, including L-selectin (CD62L) (*11*). Granulocytes and CD4^{+} T cells that were isolated from *iRhom2*$^{-/-}$

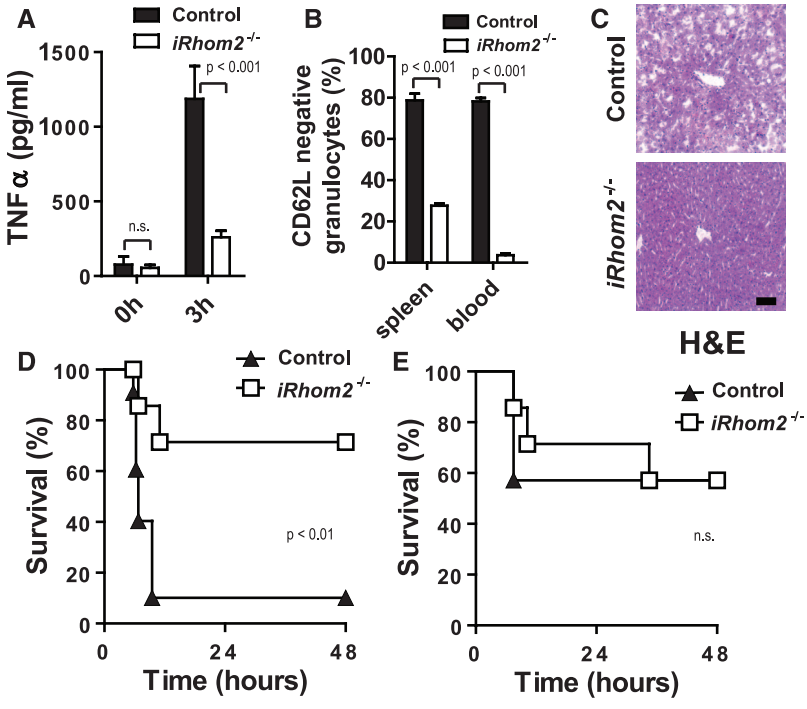

Fig. 3. iRhom2 deficiency prevents LPS-induced liver pathology by inhibiting TNFα shedding. (**A** and **B**) Control and *iRhom2*$^{-/-}$ mice (n = 4 per group) were intravenously injected with 0.14 mg per mouse LPS O111:B4. Serum TNFα (A) and CD62L^{-}Gr1^{+}CD11b^{+} cells in spleen and blood (B) were measured 3 hours after injection by ELISA or flow cytometry, respectively. (**C**) Control (n = 7) and *iRhom2*$^{-/-}$ (n = 8) mice were intraperitoneally injected with 10 mg GalN, followed 20 min later by intravenous injection of 0.05 mg LPS O111:B4. Livers were snap-frozen 6 hours after injection and sections stained with hematoxylin and eosin (H&E). Control panel is representative for six out of seven samples. *iRhom2*$^{-/-}$ panel is representative for five out of eight samples. Scale bar, 100 μm. (**D**) Control and *iRhom2*$^{-/-}$ mice (n = 10 to 11 per group) were injected with GalN and LPS as for (C), and survival was monitored for 48 hours. (**E**) Control and *iRhom2*$^{-/-}$ mice (n = 7 per group) were intraperitoneally injected with 10 mg GalN, followed 20 min later by intravenous injection of 0.15 μg rTNFα. Survival was monitored for 48 hours.

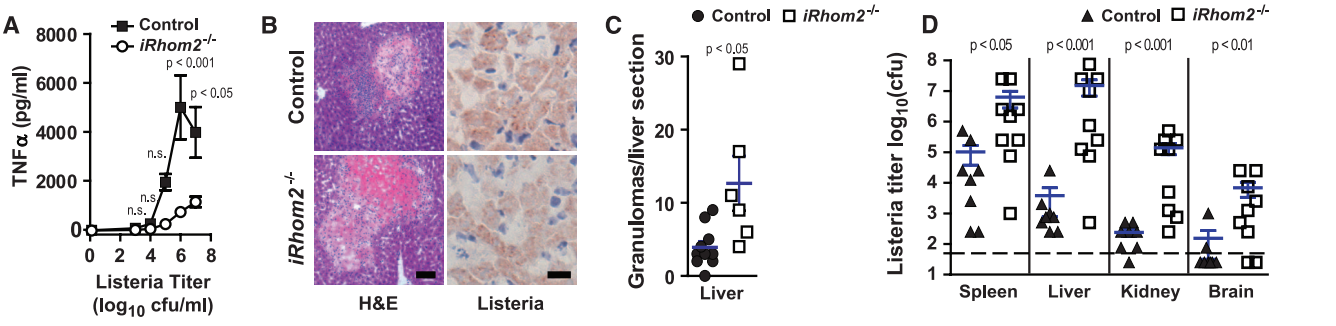

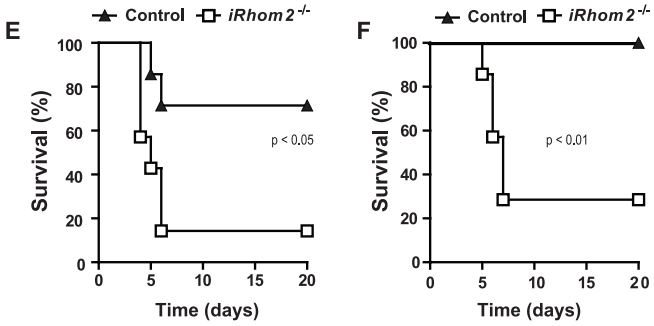

Fig. 4. iRhom2 is crucial for control of *L. monocytogenes*. (**A**) TGEMs (10^5) isolated from control or *iRhom2*$^{-/-}$ mice (n = 5 to 8 per group) were exposed to the indicated titers of *L. monocytogenes* for 24 hours. TNFα in culture supernatants was determined by ELISA (means ± SEM). (**B**) Control and *iRhom2*$^{-/-}$ mice (n = 6 to 10 per group) were infected with 10^4 colony-forming units (CFU) *L. monocytogenes*. Livers were isolated on day 4 after infection, sectioned, and stained with H&E (left) or with antibody against *Listeria* (right). Scale bars: left, 100 μm; right, 20 μm. (**C**) Granulomas were counted in F4/80-stained liver sections (not shown) from the mice in (B). Data points are granulomas per liver section of individual mice. Blue lines, means ± SEM (n = 6 to 10 per group). (**D**) Control and *iRhom2*$^{-/-}$ mice (n = 8 to 9 mice per group) were infected with 10^5 CFU *L. monocytogenes*, and bacterial titers were determined in spleen, liver, kidney, and brain on day 4 after infection. Data points are titers of individual mice. Dashed line, limit of detection. Blue lines, means ± SEM. (**E** and **F**) Control and *iRhom2*$^{-/-}$ mice (n = 7 per group) were infected with 5×10^4 CFU (E) or 5×10^3 CFU (F) *L. monocytogenes*, and mouse survival was monitored for 20 days.

mice and stimulated in vitro with phorbol-12-myristate-13-acetate (PMA) to activate TACE (*11*) showed impaired CD62L surface down-regulation compared with controls (Fig. 2C). Similarly, when WT and *iRhom2*$^{-/-}$ B cells were stimulated with the nucleotide analog 2′(3′)-*O*-(4-benzoyl)benzoyl adenosine 5′-triphosphate (BzATP) to induce shedding of both CD62L and CD23 (an ADAM10 substrate), only CD62L shedding was inhibited in *iRhom2*$^{-/-}$ B cells (Fig. 2D). We also detected elevated surface expression of another TACE substrate, intercellular adhesion molecule–1 (*19*), on *iRhom2*$^{-/-}$ TGEMs (fig. S5F). Taken together, these results suggest that iRhom2 is specifically required for TACE-mediated shedding of multiple surface molecules, including TNFα, from immune cell surfaces.

To determine potential mechanisms by which iRhom2 might control TACE activity, we examined the status of TACE maturation in the absence of iRhom2. Using immunoblotting, we readily detected both the inactive pro- and active mature forms of TACE in splenocytes and bone marrow–derived macrophages (BMDMs) from control mice. However, *iRhom2*$^{-/-}$ splenocytes and BMDMs exhibited only pro-TACE expression (Fig. 2E and fig. S6A). When we analyzed the subcellular localization of hemagglutinin (HA)–tagged TACE (TACE-HA) in WT BMDMs by immunofluorescence microscopy, TACE was broadly distributed, which included prominence in the cell periphery. In contrast, TACE appeared mislocalized in *iRhom2*$^{-/-}$ BMDMs, as it was restricted to granular vesicular compartments. (Fig. 2F and fig. S6, B and C). No discernible differences were observed in ADAM10-HA localization between WT and *iRhom2*$^{-/-}$ BMDMs (Fig. 2F and fig. S6B). To examine if this phenotype held true for endogenous TACE, we isolated cell surface proteins from BMDMs by biotinylation and probed for endogenous TACE by immunoblotting. Consistent with our microscopy data, mature TACE was correctly localized in cell surface fractions of WT BMDMs, whereas *iRhom2*$^{-/-}$ BMDMs exclusively expressed only minute quantities of pro-TACE at the cell surface (Fig. 2G). These data suggest that iRhom2 is critical for triggering TACE maturation and trafficking to the cell surface and may explain why iRhom2 is necessary for TACE activity in immune cells.

To examine the consequences of iRhom2-mediated regulation of TACE maturation in vivo, we injected control and *iRhom2*$^{-/-}$ mice with LPS and determined serum TNFα levels. The mutants showed dramatically less serum TNFα than controls (Fig. 3A), and granulocytes isolated from these animals exhibited decreased LPS-stimulated down-regulation of CD62L (Fig. 3B and fig. S7A). A well-known model of TNFα-mediated septic shock and liver damage involves the combined injection of LPS and D-galactosamine (GalN) (*4*). When we injected control and *iRhom2*$^{-/-}$ mice with LPS and GalN, serum TNFα was reduced in the mutants, whereas IL-6, IL-12, and interferon-γ (IFNγ) levels were comparable with those in controls (fig. S7B). Examination of liver histology 6 hours after injection showed that 87% of LPS- and GalN-treated control mice had disrupted liver architecture, compared with only 35% of LPS- and GalN-treated *iRhom2*$^{-/-}$ mice (Fig. 3C). In terms of lethality, whereas most LPS- and GalN-treated control mice died within 24 hours, most LPS- and GalN-treated *iRhom2*$^{-/-}$ mice survived beyond the 48 hours of the experiment (Fig. 3D). However, treatment of control and *iRhom2*$^{-/-}$ mice with recombinant TNFα and GalN led to similar rates of death (Fig. 3E and fig. S7, C and D). Thus, although in vivo responses to exogenous TNFα are normal in *iRhom2*$^{-/-}$ mice, endogenous production of soluble TNFα is impaired, such that these mutants are resistant to LPS lethality.

TNFα and TNFR1 are crucial for defense against bacterial infections (*4*, *16*, *20*, *21*). To determine whether iRhom2 is required for TNFα-mediated antibacterial activity, we infected TGEMs from untreated control and *iRhom2*$^{-/-}$ mice with the intracellular bacterium, *L. monocytogenes*. Little TNFα was detected in the supernatants of infected *iRhom2*$^{-/-}$ TGEM cultures (Fig. 4A). When control and *iRhom2*$^{-/-}$ mice were infected with *L. monocytogenes*, serum levels of IL-6, IL-12, and IFNγ were comparable (fig. S8A), and no differences in granulocyte infiltration were observed in spleen or liver (fig. S8B). Although granuloma formation and intracellular *L. monocytogenes* were detected in liver tissues of both control and *iRhom2*$^{-/-}$ mice (Fig. 4B), more granulomas were present in infected *iRhom2*$^{-/-}$ liver than in the control (Fig. 4C). In addition, *L. monocytogenes* titers in spleen, liver, kidney, and brain were all significantly higher in *iRhom2*$^{-/-}$ mice than in controls 4 days after infection (Fig. 4D). As a result, *iRhom2*$^{-/-}$ mice rapidly succumbed to the infection (Fig. 4E), a pattern that held true even at bacterial doses that were nonlethal for control mice (Fig. 4F). Thus, iRhom2 is critical for defense against *L. monocytogenes*.

Our data support a role of iRhom2 as an essential factor for the activity and trafficking of TACE in hematopoietic cells and are supported by the results presented in the accompanying manuscript by Adrain *et al.* (*22*). Mice with a myeloid cell–specific deletion in TACE, are similar to *iRhom2*$^{-/-}$ mice in that both are resistant to LPS-induced septic shock and defective in generating soluble TNFα (*23*). Unlike what we observed in the *iRhom2*$^{-/-}$ mice, TACE-deficient (*Adam17*$^{-/-}$) mice often die perinatally (*11*). These differences may be the result of cell-, or context-specific effects of iRhom2 function. The inhibition of iRhom2 may represent a potential new therapeutic approach for treating TNFα-mediated diseases.

References and Notes

1. D. L. Scott, G. H. Kingsley, *N. Engl. J. Med.* **355**, 704 (2006).
2. M. A. Palladino, F. R. Bahjat, E. A. Theodorakis, L. L. Moldawer, *Nat. Rev. Drug Discov.* **2**, 736 (2003).
3. M. Feldmann, *Nat. Rev. Immunol.* **2**, 364 (2002).
4. K. Pfeffer *et al.*, *Cell* **73**, 457 (1993).
5. D. Bhattacharya, E. C. Logue, S. Bakkour, J. DeGregori, W. C. Sha, *Proc. Natl. Acad. Sci. U.S.A.* **99**, 8838 (2002).
6. E. V. Koonin *et al.*, *Genome Biol.* **4**, R19 (2003).
7. M. K. Lemberg, M. Freeman, *Genome Res.* **17**, 1634 (2007).
8. M. Zettl, C. Adrain, K. Strisovsky, V. Lastun, M. Freeman, *Cell* **145**, 79 (2011).
9. H. Zou *et al.*, *FASEB J.* **23**, 425 (2009).
10. T. Nakagawa *et al.*, *Dev. Dyn.* **233**, 1315 (2005).
11. J. J. Peschon *et al.*, *Science* **282**, 1281 (1998).
12. J. Schlöndorff, J. D. Becherer, C. P. Blobel, *Biochem. J.* **347**, 131 (2000).
13. K. Reiss, P. Saftig, *Semin. Cell Dev. Biol.* **20**, 126 (2009).
14. R. A. Black *et al.*, *Nature* **385**, 729 (1997).
15. M. L. Moss *et al.*, *Nature* **385**, 733 (1997).
16. L. Alexopoulou *et al.*, *Eur. J. Immunol.* **36**, 2768 (2006).
17. E. Friedmann *et al.*, *Nat. Cell Biol.* **8**, 843 (2006).
18. D. Torres *et al.*, *Am. J. Pathol.* **167**, 1677 (2005).
19. N. L. Tsakadze *et al.*, *J. Biol. Chem.* **281**, 3157 (2006).
20. M. Pasparakis, L. Alexopoulou, V. Episkopou, G. Kollias, *J. Exp. Med.* **184**, 1397 (1996).
21. J. Rothe *et al.*, *Nature* **364**, 798 (1993).
22. C. Adrain, M. Zettl, Y. Christova, N. Taylor, M. Freeman, *Science* **335**, 225 (2012).
23. K. Horiuchi *et al.*, *J. Immunol.* **179**, 2686 (2007).

Acknowledgments: The authors thank S. Le Gall, S. McCracken, A. Elia, E. Arpaia, and J. Height for experimental assistance and M. Saunders for scientific editing. The data reported in this manuscript are tabulated in the main paper and in the Supporting Online Material. P.A.L. was supported by the Sofja Kovalevskaja Award 2010 of the Alexander von Humboldt Foundation and the Strategic Research Fund of the Heinrich Heine University. K.S.L. was funded by the Sofja Kovalevskaja Award 2008 of the Alexander von Humboldt Foundation; Deutsche Forschungsgemeinschaft grant LA1419/3-1; and the Molecules of Infection Center, Manchot Graduate School (Jürgen Manchot Foundation). This study was supported by the Collaborative Research Center 575 (SFB575: Experimental Hepatology; Coordinator: D.H.). C.P.B. was supported by NIH GM64750, and T.M. by the Emerald Foundation. K.O. was supported in part by the Naito Foundation; the Mochida Memorial Foundation for Medical and Pharmaceutical Research; the Senri Life Science Foundation; and the Ministry of Education, Culture, Sports, Science and Technology of Japan. T.W.M., D.R.M., and K.O. have filed U.S. Patent Application 61/426,396 regarding the use of iRhom2 for regulating innate immunity. This work was generously supported by funding from the Canadian Institutes of Health Research and the Terry Fox Foundation.

Supporting Online Material

www.sciencemag.org/cgi/content/full/335/6065/229/DC1
Materials and Methods
Figs. S1 to S8
Table S1
References (*24*–*33*)

26 September 2011; accepted 9 November 2011
10.1126/science.1214448

Widespread Genetic Switches and Toxicity Resistance Proteins for Fluoride

Jenny L. Baker,[1]* Narasimhan Sudarsan,[2,3]* Zasha Weinberg,[2,3] Adam Roth,[2,3] Randy B. Stockbridge,[4] Ronald R. Breaker[2,3,5]†

Most riboswitches are metabolite-binding RNA structures located in bacterial messenger RNAs where they control gene expression. We have discovered a riboswitch class in many bacterial and archaeal species whose members are selectively triggered by fluoride but reject other small anions, including chloride. These fluoride riboswitches activate expression of genes that encode putative fluoride transporters, enzymes that are known to be inhibited by fluoride, and additional proteins of unknown function. Our findings indicate that most organisms are naturally exposed to toxic levels of fluoride and that many species use fluoride-sensing RNAs to control the expression of proteins that alleviate the deleterious effects of this anion.

Fluoride has been widely used as an additive in oral hygiene products and water since the 1950s because of its usefulness in preventing tooth decay. Fluoride ions present at millimolar concentrations in bacterial culture media inhibit cell growth (*1*–*3*), and this has been proposed as one of the mechanisms for its efficacy (*4*–*7*). However, little has been reported on how organisms respond to toxic levels of fluoride.

We identified a fluoride-responsive riboswitch class by analyzing a group of noncoding RNA structures that carry a conserved domain called the *crcB* motif (Fig. 1A) (*8*, *9*). *crcB* motif RNAs are located upstream of genes encoding proteins of diverse functions and presumably regulate these genes. Some of the gene products are annotated as ion transporters (for example, chloride, sodium, proton) and some others are involved in various physiological (e.g., universal stress adaptation, DNA repair) or metabolic (e.g., enolase, formate-hydrogen lyase) processes (fig. S1).

We used a method called in-line probing (*10*, *11*) to assess the binding of various possible metabolites, which unexpectedly revealed that fluoride contaminating a commercial compound sample caused extensive conformational changes in *crcB* RNAs (fig. S2). Using a 78-nucleotide RNA called 78 Psy that encompasses the *crcB* motif from *Pseudomonas syringae* (Fig. 1B and table S1), we determined that the most highly conserved nucleotides of this RNA class undergo structural change on addition of NaF (Fig. 1C), which suggests that these nucleotides help form a ligand-binding aptamer for fluoride. The pattern of products resulting from in-line probing at various fluoride concentrations reveals an apparent dissociation constant (K_D) of ~60 μM (Fig. 1D). We obtained similar K_D values with *crcB* motif RNAs from other organisms (fig. S3).

Ca^{2+} forms a strong complex with fluoride ions (*12*), and the addition of Ca^{2+} in excess over fluoride precludes RNA structure changes (fig. S4). This demonstrates that free fluoride is important for binding by the RNA. The 78 Psy RNA rejects other halogen anions (chloride, bromide, iodide), even when they are added at high concentrations (fig. S5). Likewise, hydroxide ions (up to pH 9.7) and carbon monoxide and nitric oxide as dissolved gasses do not induce RNA folding changes.

Mutations that alter the aptamer's conserved substructures (fig. S6) or conserved nucleotides (fig. S7) adversely affect fluoride binding, indi-

[1]Department of Chemistry, Yale University, Box 208103, New Haven, CT 06520, USA. [2]Howard Hughes Medical Institute, Yale University, Box 208103, New Haven, CT 06520, USA. [3]Department of Molecular, Cellular, and Developmental Biology, Yale University, Box 208103, New Haven, CT 06520, USA. [4]Department of Biochemistry and Howard Hughes Medical Institute, Brandeis University, Waltham, MA 02454, USA. [5]Department of Molecular Biophysics and Biochemistry, Yale University, Box 208103, New Haven, CT 06520, USA.

*These authors contributed equally to this work.
†To whom correspondence should be addressed. E-mail: ronald.breaker@yale.edu

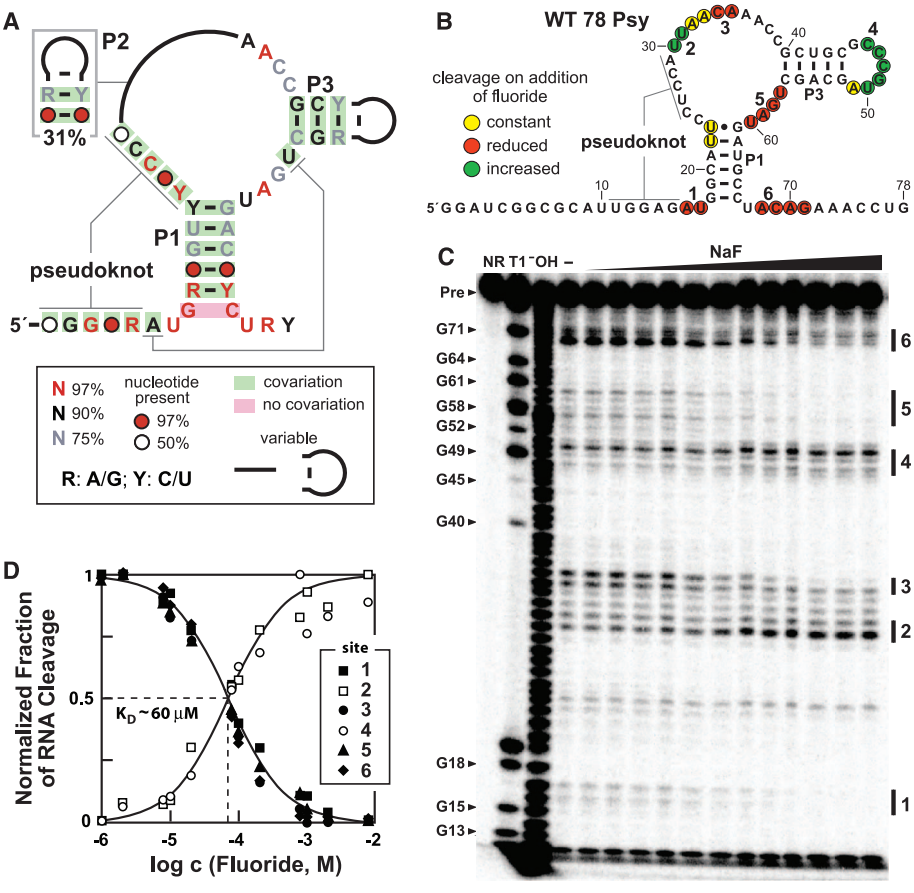

Fig. 1. Fluoride binding by *crcB* motif RNAs. (**A**) Consensus sequence and structural model for *crcB* RNAs based on 2188 representatives from bacterial and archaeal species. P1, P2, P3 and pseudoknot labels identify extended base-paired substructures. (**B**) Sequence and secondary structure model for the WT 78 Psy RNA from *P. syringae*. Colored circles summarize the in-line probing results presented in (C). The two G residues preceding nucleotide 1 were added to facilitate RNA production. (**C**) Polyacrylamide gel electrophoresis analysis of an in-line probing assay with 78 Psy RNA and various amounts of fluoride. NR, T1, and ⁻OH designate no reaction, partial digestion with RNase T1 (cleaves after guanosines), or partial digestion with hydroxide ions (cleaves after any nucleotide), respectively. Precursor RNA (Pre) band and some RNase T1 product bands are labeled (left). Locations of fluoride-mediated spontaneous RNA cleavage suppression (regions 1, 3, 5, 6) and enhancement (regions 2, 4) are identified by vertical bars. (**D**) Plot of the normalized fraction of RNA cleavage versus fluoride ion concentration from the data in (C). Curves represent those expected for one-to-one binding with a K_D of 60 μM.

cating that the features common to all *crcB* motif RNAs are necessary for the selective recognition of fluoride. Certain RNAs are known to directly bind chloride ions (*13*), and therefore it seems conceivable that RNA could form a fluoride-specific pocket without the use of a cofactor. Selectivity could be based on the ionic radius of fluoride (0.133 nm), which is smaller than those of other chemical species tested, including chloride (0.181 nm); also, fluoride has unique hydrogen-bonding abilities (*9*). Alternatively, the polyanionic *crcB* motif RNAs may exploit one or more Mg^{2+} ions to form bridging contacts between anionic fluoride and nucleotides.

A reporter construct was created by joining a representative *crcB* motif RNA from the *Bacillus cereus crcB* gene to a *lacZ* gene (transcriptional fusion). The observed activation in *B. subtilis* of the reporter gene by fluoride (figs. S8 and S9) and additional in-line probing experiments (fig. S10) indicate that this representative is a fluoride-responsive riboswitch that operates by controlling the formation of an intrinsic transcription terminator stem.

The homologous fluoride riboswitch from a *P. syringae eriC* gene was joined (translational fusion) to *lacZ*, and the plasmid-based construct was transformed into an *Escherichia coli* strain with its natural *lacZ* gene disabled. High expression occurred when cells were grown on a medium supplemented with 50 mM fluoride, whereas lower fluoride concentrations resulted in little or no expression (Fig. 2A, left side). Results of mutational analysis of this representative (fig. S11) also are consistent with our hypothesis that the *crcB* motif RNA from *P. syringae* is a fluoride-responsive riboswitch that controls gene expression by regulating translation initiation.

The *crcB* genes, which are most commonly associated with fluoride riboswitches, have previously been implicated in chromosome condensation and camphor resistance (*14*). However, *crcB* genes are predicted to code for membrane proteins (*15*) belonging to a superfamily that is predominantly composed of transporters (*16*). Therefore, we speculated that CrcB proteins might function as fluoride transporters to reduce cellular concentrations of this anion. An *E. coli* strain carrying a genetic knockout (KO) of its *crcB* gene could not grow at 50 mM fluoride and exhibited high reporter gene expression even at low (for example, 0.2 mM) fluoride concentrations (Fig. 2A, right side).

We recorded a series of growth curves for wild-type (WT) and KO cells at various fluoride concentrations in liquid media to assess whether there is a correlation between cell growth and reporter gene activity as fluoride concentrations in the medium are increased. For WT *E. coli* cells, growth was noticeably reduced at 30 mM NaF, and the minimum inhibitory concentration (MIC) for fluoride was ~200 mM (Fig. 3A and fig. S12A). In contrast, the growth of the *E. coli crcB* KO strain is inhibited by micromolar amounts of fluoride and exhibits an MIC of slightly higher than 1 mM (Fig. 3B and fig. S12A). Fluoride sensitivities of both strains are heightened under acidic conditions (fig. S12B) due to the increased membrane permeability of hydrogen fluoride.

A comparison of the growth curves (Fig. 3 and fig. S12) with the reporter gene expression driven by fluoride riboswitches (Fig. 2) indicates that reporter expression increases in proportion to the amount of fluoride in the culture media until the anion concentration becomes toxic to cells. Both growth inhibition (Fig. 3B) and reporter gene expression (Fig. 2B) phenotypes are similarly shifted to lower fluoride concentrations in

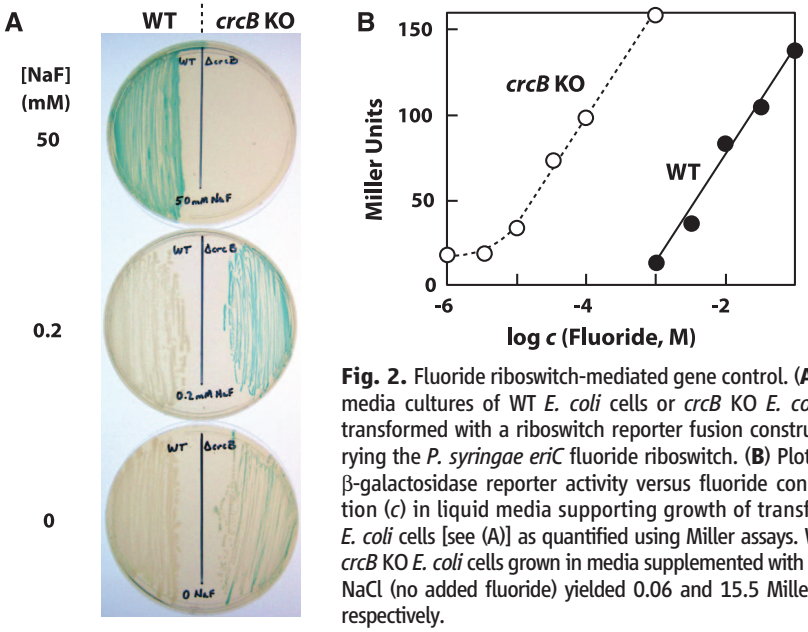

Fig. 2. Fluoride riboswitch-mediated gene control. (**A**) Solid media cultures of WT *E. coli* cells or *crcB* KO *E. coli* cells transformed with a riboswitch reporter fusion construct carrying the *P. syringae eriC* fluoride riboswitch. (**B**) Plot of the β-galactosidase reporter activity versus fluoride concentration (*c*) in liquid media supporting growth of transformed *E. coli* cells [see (A)] as quantified using Miller assays. WT and *crcB* KO *E. coli* cells grown in media supplemented with 50 mM NaCl (no added fluoride) yielded 0.06 and 15.5 Miller units, respectively.

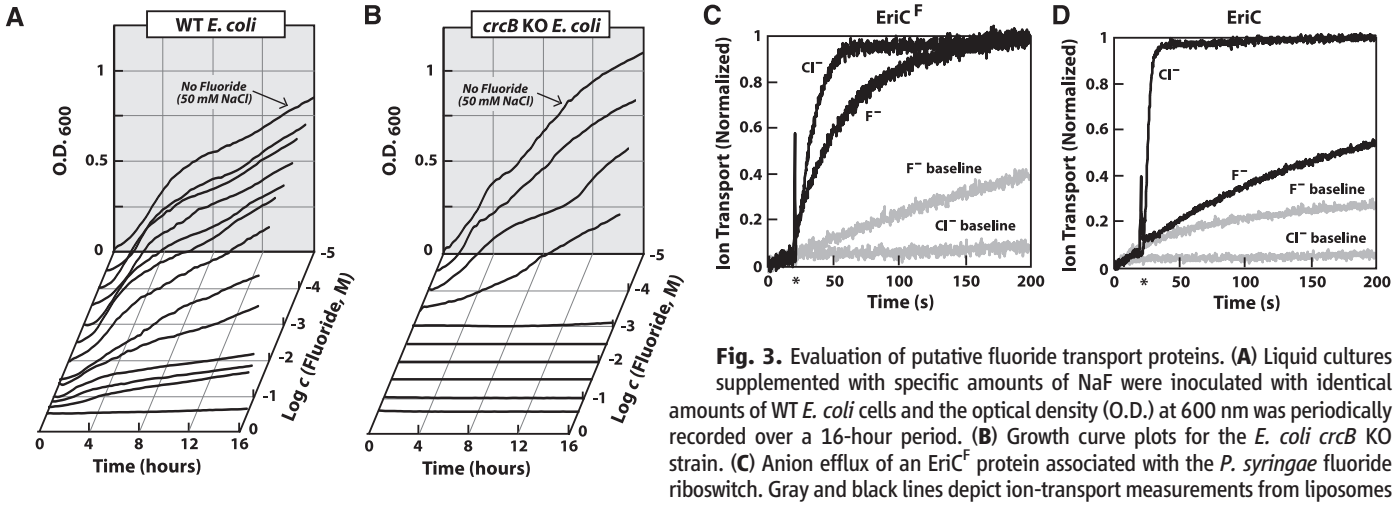

Fig. 3. Evaluation of putative fluoride transport proteins. (**A**) Liquid cultures supplemented with specific amounts of NaF were inoculated with identical amounts of WT *E. coli* cells and the optical density (O.D.) at 600 nm was periodically recorded over a 16-hour period. (**B**) Growth curve plots for the *E. coli crcB* KO strain. (**C**) Anion efflux of an $EriC^F$ protein associated with the *P. syringae* fluoride riboswitch. Gray and black lines depict ion-transport measurements from liposomes in the absence or presence of protein, respectively. The high fluoride baseline is due to the relative membrane permeability of HF (pK_a of 3.4) compared with chloride (pK_a of −7). Asterisks in (C) and (D) identify the times at which protein-mediated anion transport is initiated. (**D**) Anion efflux by an EriC protein from *E. coli* that is known to serve as a chloride transporter.

crcB KO cells. These findings suggest that CrcB protein is important for reducing fluoride concentrations in cells, thus reducing its toxicity.

Another gene family commonly associated with fluoride riboswitches is a distinct subset of highly related *eriC* genes (hereafter called *eriC*^{F}) coding for ClC-type ion channel proteins. The prototypic *eriC* representatives exhibit specificity for chloride (fig. S13) (*17*–*19*). However, EriC^F protein homologs commonly associated with fluoride riboswitches carry a distinct set of amino acids in their putative channels compared with validated chloride-specific EriC proteins (fig. S14). This finding suggests that members of the EriC^F subgroup could be channels for fluoride anions. Anion flux assays conducted with the EriC^F protein from *P. syringae* reveal similar efficiency for chloride and fluoride transport (Fig. 3C), whereas a typical EriC protein from *E. coli* greatly favors chloride over fluoride (Fig. 3D).

We assessed the biological function of the EriC^F variant from *P. syringae* by expressing the protein in the *E. coli* strain lacking the CrcB protein. Consistent with fluoride transport activity, the *P. syringae eriC*^{F} gene rescues growth of the *E. coli crcB* KO strain to yield cells with restored resistance to high fluoride concentrations in both liquid and solid media (fig. S15). The functional equivalency of EriC^F and CrcB proteins is likewise suggested by their distributions among bacterial species (fig. S16). The genes for these putative fluoride transport proteins are rarely observed in the same species under the control of fluoride riboswitches, suggesting that their biochemical roles may be identical.

crcB genes associated with fluoride riboswitches are distributed broadly among bacteria and archaea (fig. S16). Riboswitches are associated with genes for CrcB proteins that vary greatly in amino acid sequence (fig. S17), suggesting that all CrcB proteins might have the same function in mitigating fluoride toxicity. If true, a surprisingly large number of organisms are predicted to contend with fluoride toxicity, including eukaryotic lineages such as fungi and plants. Moreover, the bacterium *Streptococcus mutans* (a causative agent of dental caries) encodes EriC^F proteins in the same genomic location where other *Streptococcus* species encode CrcB proteins (fig. S18). This arrangement again supports the hypothesis that the proteins are functionally equivalent and reveals the importance of fluoride toxicity resistance for *S. mutans*.

Though the vast majority of species encode at most 2 fluoride riboswitches, the bacterium *Methylobacterium extorquens* DM4 encodes at least 10 fluoride riboswitches in its genome. This organism, known for its ability to consume halogenated hydrocarbons as a food source (*20*), has been shown to survive on dichloromethane. The pertinent halogenase enzyme can catalyze the degradation of dibromomethane (*21*), suggesting that this organism also might degrade fluorinated hydrocarbons, which would generate fluoride anions and require a more robust fluoride sensor and toxicity mitigation response system for rapid growth on fluorinated food sources.

Our findings resolve a long-standing mystery regarding why some species carry sensor and mitigation systems for toxic metals such as arsenic, cadmium, lead, and silver, whereas an analogous fluoride-specific system had been notably absent (*22*). The pervasive occurrence of these fluoride toxicity mitigation systems is consistent with the fact that fluorine is the 13th most abundant element in Earth's crust. Given their wide distributions, fluoride-specific riboswitches and commonly associated proteins such as CrcB may represent components of an ancient system by which cells have contended with toxic levels of this anion.

References and Notes

1. R. J. Lesher, G. R. Bender, R. E. Marquis, *Antimicrob. Agents Chemother.* **12**, 339 (1977).
2. M. Maltz, C. G. Emilson, *J. Dent. Res.* **61**, 786 (1982).
3. R. E. Marquis, S. A. Clock, M. Mota-Meira, *FEMS Microbiol. Rev.* **26**, 493 (2003).
4. R. S. Levine, *Br. Dent. J.* **140**, 9 (1976).
5. H. Koo, *Adv. Dent. Res.* **20**, 17 (2008).
6. I. R. Hamilton, *J. Dent. Res.* **69**, spec. no. 660, discussion 682 (1990).
7. C. Van Loveren, *Caries Res.* **35**, 65 (2001).
8. Z. Weinberg *et al.*, *Genome Biol.* **11**, R31 (2010).
9. Supporting text and materials and methods are available as supporting material on *Science* Online.
10. G. A. Soukup, R. R. Breaker, *RNA* **5**, 1308 (1999).
11. E. E. Regulski, R. R. Breaker, *Methods Mol. Biol.* **419**, 53 (2008).
12. J. T. Dobbins, H. A. Ljung, *J. Chem. Educ.* **12**, 586 (1935).
13. P. Auffinger, L. Bielecki, E. Westhof, *Structure* **12**, 379 (2004).
14. K. H. Hu *et al.*, *Genetics* **143**, 1521 (1996).
15. M. Rapp, E. Granseth, S. Seppälä, G. von Heijne, *Nat. Struct. Mol. Biol.* **13**, 112 (2006).
16. R. D. Finn *et al.*, *Nucleic Acids Res.* **38**, D211 (2010).
17. K. Matulef, M. Maduke, *Mol. Membr. Biol.* **24**, 342 (2007).
18. R. Dutzler, E. B. Campbell, M. Cadene, B. T. Chait, R. MacKinnon, *Nature* **415**, 287 (2002).
19. A. Accardi, C. Miller, *Nature* **427**, 803 (2004).
20. R. Gälli, T. Leisinger, *Conserv. Recy.* **8**, 91 (1985).
21. S. Vuilleumier, H. Sorribas, T. Leisinger, *Biochem. Biophys. Res. Commun.* **238**, 452 (1997).
22. S. Silver, *Gene* **179**, 9 (1996).

Acknowledgments: We thank members of the Breaker laboratory for helpful discussions and G. L. Ryan at Oligos Etc. for information on synthetic dinucleotide preparations. Ion channel flux experiments were conducted by R.B.S. in the laboratory of C. Miller, Brandeis Univ., and we thank him for his support of this project. We also thank N. Carriero and R. Bjornson for assisting our use of the Yale Life Sciences High Performance Computing Center (NIH grant RR19895-02). This work was supported by NIH (grant GM022778) and by the Howard Hughes Medical Institute. R.R.B. is a cofounder of and consults for BioRelix, a biotechnology company that has licensed intellectual property on riboswitches from Yale University Yale University has filed for patent protection on aspects of the *crcB* motif and fluoride riboswitches.

Supporting Online Material

www.sciencemag.org/cgi/content/full/science.1215063/DC1
Materials and Methods
SOM Text
Figs. S1 to S18
Table S1
References (*23*–*82*)

10 October 2011; accepted 2 December 2011
Published online 22 December 2011;
10.1126/science.1215063

Erasure of a Spinal Memory Trace of Pain by a Brief, High-Dose Opioid Administration

Ruth Drdla-Schutting, Justus Benrath,* Gabriele Wunderbaldinger, Jürgen Sandkühler†

Painful stimuli activate nociceptive C fibers and induce synaptic long-term potentiation (LTP) at their spinal terminals. LTP at C-fiber synapses represents a cellular model for pain amplification (hyperalgesia) and for a memory trace of pain. μ-Opioid receptor agonists exert a powerful but reversible depression at C-fiber synapses that renders the continuous application of low opioid doses the gold standard in pain therapy. We discovered that brief application of a high opioid dose reversed various forms of activity-dependent LTP at C-fiber synapses. Depotentiation involved Ca^{2+}-dependent signaling and normalization of the phosphorylation state of α-amino-3-hydroxy-5-methyl-4-isoxazolepropionic acid receptors. This also reversed hyperalgesia in behaving animals. Opioids thus not only temporarily dampen pain but may also erase a spinal memory trace of pain.

μ-Opioid receptors (MORs) are expressed on spinal terminals of nociceptive C-fiber afferents and mediate the acute and quickly reversible presynaptic depression by opioids, mainly via inhibition of N- and P/Q-type voltage-gated calcium channels (*1*). In addition, brief activation of postsynaptic MORs triggers a rise in postsynaptic Ca^{2+} levels by increasing Ca^{2+} influx through *N*-methyl-D-aspartate (NMDA)–receptor channels (*2*) and by releasing Ca^{2+} from ryanodine-sensitive intracellular Ca^{2+} stores (*3*).

The acute synaptic depression and the prevention of synaptic plasticity by opioids have been studied extensively (*4*–*6*). In contrast, surprisingly little is known about the potential induction of Ca^{2+}-dependent synaptic plasticity by opioids.

Synaptic long-term potentiation (LTP) is a cellular model for learning and memory formation. The reversal of LTP, that is, synaptic depotentiation, is a potential mechanism of memory erasure (*7*). Depotentiation involves Ca^{2+}-dependent signaling (*8*) and may reverse LTP-associated changes in the phosphorylation state of α-amino-3-hydroxy-5-methyl-4-isoxazolepropionic acid receptors (AMPARs) (*9*). We tested the hypothesis that brief application of a MOR agonist reverses LTP at C-fiber synapses in superficial lumbar dorsal horn by Ca^{2+}-dependent signaling pathways, which normalize the phosphorylation state of AMPAR subunits.

In adult rats, conditioning low-frequency stimulation (LFS) of sciatic nerve fibers at C-fiber intensity induced LTP of spinal C fiber–evoked field potentials (*10*) (Fig. 1A). Brief intravenous infusion of a high dose of the ultrashort-acting MOR agonist remifentanil (450 $\mu g \cdot kg^{-1} \cdot hour^{-1}$) acutely depressed potentiated responses. Upon termination of the remifentanil infusion, C fiber–evoked field potentials did not return to the elevated predrug levels but were significantly depotentiated from 188 ± 11% to 128 ± 14% of control values before LFS (n = 25, P < 0.001, Fig. 1B). This is in contrast to the potentiation of C fiber–evoked field potentials upon wash-out of remifentanil in naïve animals (*3*, *11*) and thus cannot be explained by an incomplete wash-out of the opioid. A second application of remifentanil given 1 hour later fully reversed LTP [depotentiation from 180 ± 11% (mean ± SEM) to 128 ± 16% of control after the first application, P = 0.001; and to 76 ± 14% after second application, P < 0.001; n = 6, Fig. 1C]. A lower dose of remifentanil (225 $\mu g \cdot kg^{-1} \cdot hour^{-1}$) was, however, ineffective (196 ± 22% versus 194 ± 12% of control, n = 5, P = 1, Fig. 1D).

Our previous study revealed that abrupt but not tapered withdrawal from remifentanil induces LTP at naïve synapses (*3*). Here, the same tapering regimen had, in contrast, no effect on the efficacy of opioid-induced depotentiation (OID; depotentiation from 180 ± 13% to 123 ± 10%, n = 6, P = 0.002; fig. S1A).

OID was unaffected by blockade of spinal γ-aminobutyric acid type A ($GABA_A$) receptors with picrotoxin (depotentiation from 216 ± 19% to 151 ± 22% of control, n = 7, P = 0.001; fig. S1B), indicating that an enhanced inhibition via $GABA_A$ receptors is not involved.

Acute depression and OID were fully blocked by intravenous application of the opioid receptor antagonist naloxone (fig. S1C) and by spinal application of the selective MOR antagonist D-Phe-Cys-Tyr-D-Trp-Orn-Thr-Pen-Thr-NH_2 (CTOP, Fig. 2A), demonstrating that activation of spinal MORs is essential for both effects.

Withdrawal from opioids may trigger the release of glutamate and the activation of Ca^{2+}-permeable glutamate receptors of the NMDA subtype (*12*). The activation of group I metabotropic glutamate receptors (group I mGluRs) may lead to an additional rise in free cytosolic Ca^{2+} by Ca^{2+} release from intracellular stores. Blockade of Ca^{2+} entry through spinal NMDA receptors (Fig. 2B), blockade of group I mGluRs (Fig. 2C), or blockade of Ca^{2+} release from ryanodine-sensitive intracellular stores with dantrolene (Fig. 2D) all abolished OID but not the acute depression by the opioid.

LTP at the first synaptic relay in nociceptive pathways requires activation of Ca^{2+}/calmodulin-dependent protein kinase II and protein kinase C (PKC) (*13*, *14*), which phosphorylate the GluR1 subunit of the AMPA receptor at Ser^{831} (*15*, *16*). Interestingly, the time course of Ser^{831} phosphorylation in spinal dorsal horn parallels post-injury pain amplification (*17*) and is located to the superficial spinal dorsal horn (*18*), where C fibers terminate. Here, LFS-induced LTP was also associated with changes in the phosphorylation state of AMPARs, and we speculated that OID may reverse these changes. LFS caused enhanced phosphorylation of surface GluR1 subunits of AMPARs at Ser^{831} (S831-p; ratio of S831-p to total GluR1 protein levels was increased to 304 ± 60% of control, n = 12, P = 0.006). Remifentanil fully reversed this phosphorylation (ratio of S831-p to total GluR1 protein levels was 118 ± 21% of control, n = 12, P = 0.41 compared to control, P = 0.007 compared to LFS group; Fig. 3A). Dephosphorylation of spinal AMPARs at Ser^{831}, for example, by protein phosphatase 1 (PP1), reduces single-channel conductance and may thereby normalize synaptic strength (*9*). Accordingly, OID was completely prevented by blockade of PP1 (Fig. 2E).

LFS also induced a dephosphorylation of GluR2 subunits of AMPARs at Ser^{880} (S880-p) in the spinal dorsal horn (ratio of S880-p to total GluR2 protein levels was reduced to 67 ± 10% of control, n = 12, P = 0.007; Fig. 3B). After the opioid application, Ser^{880} was rephosphorylated (ratio of S880-p to total GluR2 protein levels

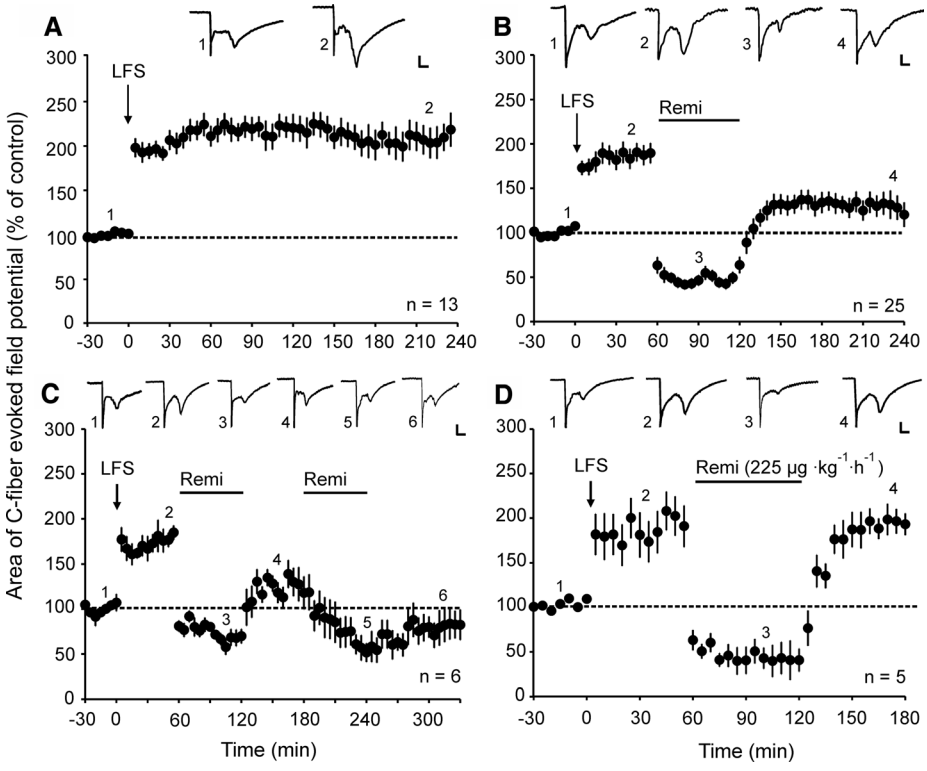

Fig. 1. Acute opioid administration induces depotentiation of spinal LTP. Area of C fiber–evoked field potentials was normalized to baseline values before LTP induction (dotted lines) and plotted versus time (min). Data are expressed as mean ± 1 SEM. Insets show original traces of field potentials recorded at indicated time points; calibration bars indicate 50 ms and 0.2 mV. (**A**) Mean time course of LTP of C fiber–evoked field potentials. LFS (time point zero, arrow) induced LTP in all animals tested (n = 13, P < 0.001). (**B**) Sixty min post-LFS, a high-dose remifentanil infusion [450 $\mu g \cdot kg^{-1} \cdot hour^{-1}$ intravenously (i.v.)] was started by bolus injection (30 $\mu g \cdot kg^{-1}$) and continuously infused for 1 hour (black horizontal bar). After wash-out of the drug, LTP was depotentiated (n = 25, P < 0.001). (**C**) A second infusion of high-dose remifentanil, which was started 60 min after the first one, abolished LTP after wash-out of the opioid (n = 6, P < 0.001). (**D**) Remifentanil infusion at a low dose (225 $\mu g \cdot kg^{-1} \cdot hour^{-1}$ i.v.) did not depotentiate LTP (n = 5, P = 1) after wash-out of the drug. In all graphs, statistical significance was determined by using one-way repeated measures analysis of variance (RM ANOVA).

Department of Neurophysiology, Center for Brain Research, Medical University of Vienna, A-1090 Vienna, Austria.

*Present address: Centre of Pain Therapy, Clinic of Anaesthesia and Intensive Care, University Medical Centre Mannheim, Medical Faculty Heidelberg University, D-68167 Mannheim, Germany.

†To whom correspondence should be addressed. E-mail: juergen.sandkuehler@meduniwien.ac.at

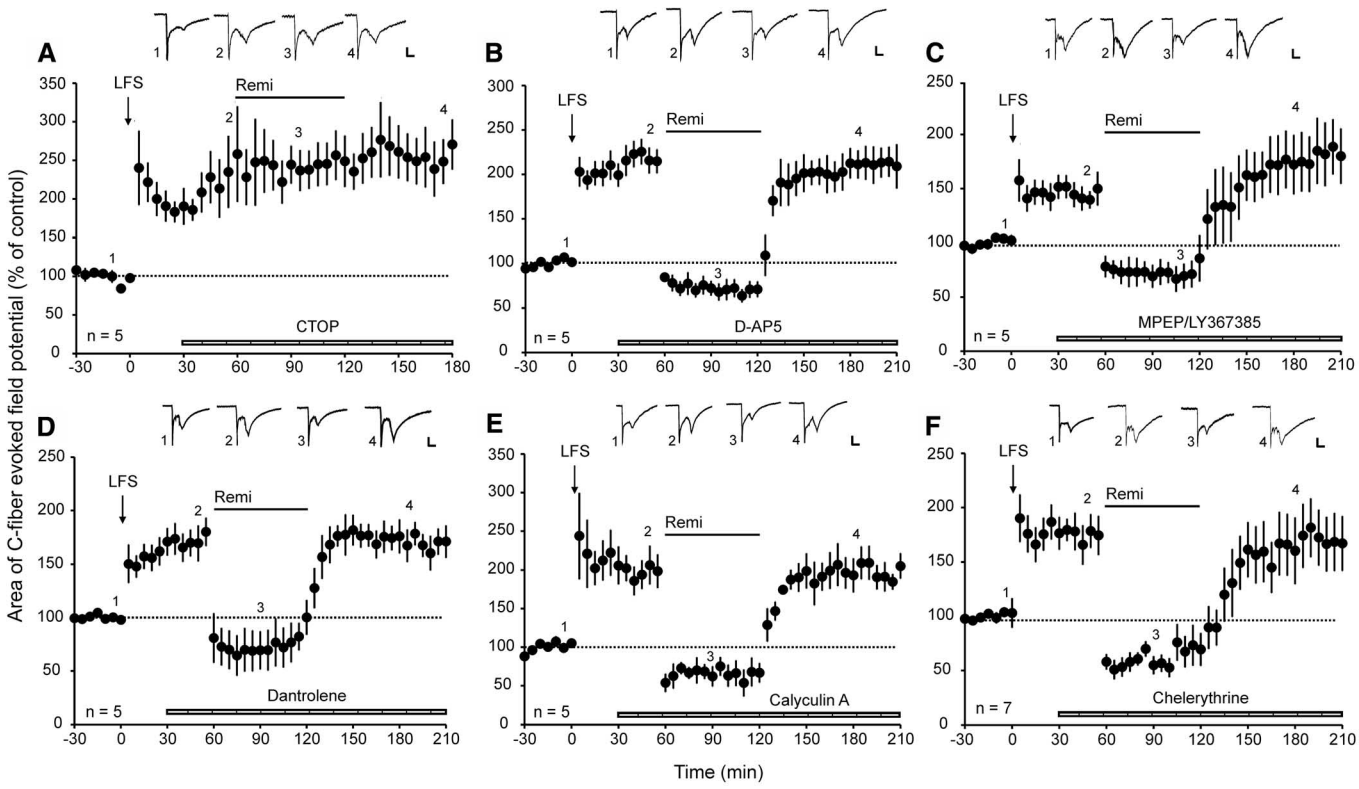

Fig. 2. Signaling pathways involved in opioid-induced depotentiation. LTP induction and remifentanil application as in Fig. 1. Different blockers were applied directly onto the spinal cord at the recording segment (dashed horizontal bars). Insets show original traces of field potentials recorded at indicated time points; calibration bars, 50 ms and 0.2 mV. (**A**) Spinal superfusion with the MOR antagonist CTOP (10 μM) abolished acute depression and depotentiation in all animals tested ($n = 5$, $P = 1$). (**B** to **F**), OID was prevented by topical application of the NMDA receptor antagonist D-AP5 (100 μM, $n = 5$, $P = 1$), the mGluR antagonists MPEP (100 μM) and LY367385 (300 μM, $n = 5$, $P = 0.6$), the ryanodine receptor blocker dantrolene (500 μM, $n = 5$, $P = 1$), the PP1 inhibitor calyculin A (300 nM, $n = 5$, $P = 1$), or the PKC blocker chelerythrine (800 μM, $n = 7$, $P = 1$). In all experiments, statistical significance was determined by using a one-way RM ANOVA.

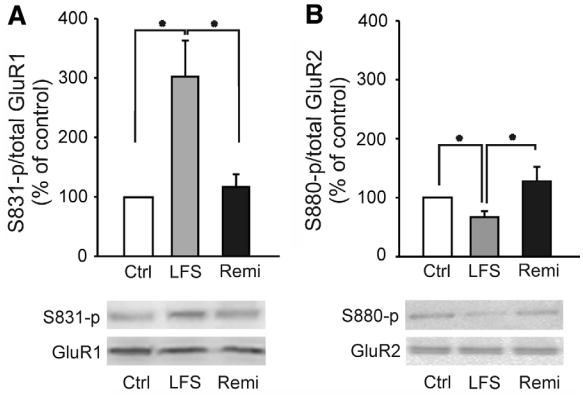

Fig. 3. Quantitative analysis of phosphorylation of surface AMPAR subunits after LFS and opioid treatment. Bar graphs summarize the ratio of phospho-GluR1-Ser^{831} (S831-p) with total GluR1 (A) and ratio of phospho-GluR2-Ser^{880} (S880-p) with total GluR2 (B). Data are expressed as mean + 1 SEM. Tissue samples were taken from naïve animals (Ctrl, $n = 12$), from animals 180 min post-LFS (LFS, $n = 12$), or from animals 180 min post-LFS with an additional 60-min remifentanil infusion (Remi, $n = 12$). Representative, corresponding Western blots are shown at the bottom. *$P < 0.05$. (**A**) LFS induced phosphorylation of AMPAR GluR1 subunits at Ser^{831}, which was reversed by opioid treatment. (**B**) LFS dephosphorylated AMPAR GluR2 subunits at Ser^{880}, whereas remifentanil induced rephosphorylation at this site.

was 127 ± 23% of control, $n = 12$, $P = 0.028$; Fig. 3B). PKC phosphorylates GluR2 subunit at Ser^{880}. This reduces glutamatergic synaptic transmission by promoting receptor endocytosis (*19*). Consistently, blockade of PKC fully prevented OID without affecting acute depression (Fig. 2F). We found no evidence for significant changes in the phosphorylation state of GluR1 subunit of the AMPAR at Ser^{845} after LFS (ratio of S845-p to total GluR1 protein levels was 160 ± 38% of control, $n = 12$, $P = 0.142$) or after opioid application (93 ± 17% of control, $n = 12$, $P = 0.706$). The above described changes in the phosphorylation state of the AMPAR after LFS may enhance glutamatergic synaptic transmission (*9*), and their reversal may thus lead to OID.

The induction phase of spinal LTP, which lasts for 1 to 3 hours, involves posttranslational modifications, including changes in the phosphorylation state of synaptic proteins. The maintenance phase of LTP [>3 hours in spinal cord (*20*) and brain (*21*)] may in addition also involve de novo protein synthesis. We thus asked whether LTP in the maintenance phase can also be depotentiated by opioids. When remifentanil was given 4 hours after LTP induction, OID was as effective (depotentiation from 193 ± 22% to 131 ± 14%, $n = 10$, $P = 0.028$; fig. S2, A and B) as when given after 1 hour. The reversal of late-phase LTP by remifentanil was, in contrast to that of early-phase LTP, not blocked by the PP1 inhibitor calyculin A (220 ± 22% versus 156 ± 20%, $n = 10$, $P = 0.024$; fig. S2C).

The persistently active protein kinase Mζ (PKMζ) is required in the spinal cord for maintaining tactile allodynia after intraplantar injection of interleukin-6 (*22*). We thus asked whether PKMζ in spinal cord also plays a role for the maintenance phase of LTP (*22*, *23*) after LFS. PKMζ inhibitor ZIP had, however, no obvious

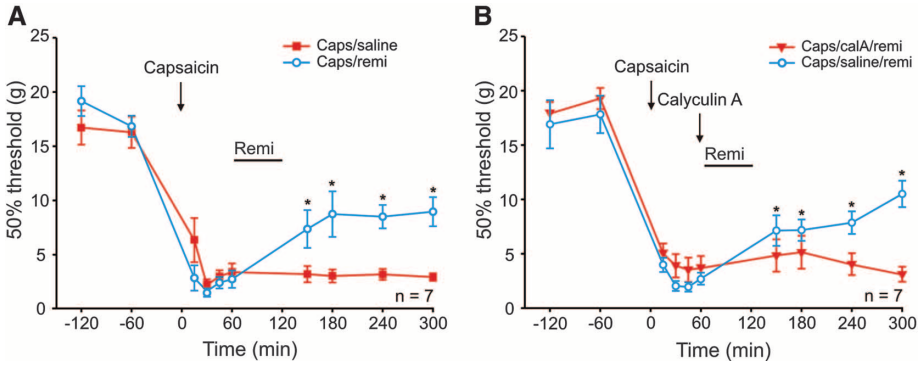

Fig. 4. Capsaicin-induced mechanical hyperalgesia is reduced after opioid administration. Capsaicin injection (time point zero, arrow) significantly reduced mechanical withdrawal thresholds in the ipsilateral paw of awake, drug-free rats. (**A**) One group of animals received a 1-hour high-dose remifentanil infusion (horizontal bar) 60 min after capsaicin injection (blue circles, $n = 7$). A control group was treated with an intravenous saline infusion (red squares, $n = 7$). After wash-out of the opioid, mechanical thresholds were elevated significantly compared with thresholds before opioid treatment at 150 min ($P = 0.05$), 180 min ($P = 0.003$), 240 min ($P = 0.004$), and 300 min ($P = 0.002$), indicating partial reversal of hyperalgesia. (**B**) Opioid-induced reduction of mechanical hyperalgesia is blocked by the PP1 inhibitor calyculin A. After capsaicin injection, calyculin A (300 nM, 10 μl) was injected intrathecally 10 min before a 1-hour high-dose remifentanil infusion (red triangles, $n = 7$). Intrathecal injections of saline served as control (blue circles, $n = 7$). After wash-out of the opioid, mechanical thresholds were elevated significantly compared with thresholds before opioid treatment in the control group at 150 min ($P = 0.021$), 180 min ($P = 0.019$), 240 min ($P = 0.003$), and 300 min ($P < 0.001$). No effect of the opioid treatment on mechanical thresholds could be observed in the calyculin A–treated group ($P = 0.523$). One-way RM ANOVA or RM ANOVA on ranks was used for statistical comparisons.

effect on the maintenance of LFS-induced LTP within the observation period of 6 hours (fig. S2D).

Depending on the type of conditioning stimulation, distinct forms of LTP are induced at C-fiber synapses, which affect different groups of postsynaptic neurons (*13*, *24*) and involve signaling pathways that overlap only partially (*13*, *24*, *25*). We therefore tested whether OID can also be achieved for other forms of established spinal LTP. We induced LTP by conditioning high-frequency stimulation (HFS, 100 Hz; fig. S3A) of sciatic nerve fibers or by subcutaneous capsaicin injections (fig. S3C). The latter selectively activates nociceptive nerve fibers, which express the transient receptor potential channel subfamily V member 1 (TRPV1). Remifentanil also fully reversed these forms of LTP (after HFS, depotentiation was from 158 ± 8% to 99 ± 9%, $n = 12$, $P < 0.001$; after capsaicin, depotentiation was from 170 ± 16% to 100 ± 13%, $n = 5$, $P < 0.001$; fig. S3, B and D), demonstrating that OID applies to various forms of activity-dependent LTP at C-fiber synapses.

LTP is a synaptic model for some forms of hyperalgesia (*26*). We therefore asked whether OID has any relevance for behaving animals. Subcutaneous injections of capsaicin quickly led to mechanical hyperalgesia at the injected hindpaw (Fig. 4). The same dosage regimen of remifentanil that caused OID significantly attenuated capsaicin-induced hyperalgesia (Fig. 4A). Not surprisingly, the behavioral hyperalgesia was reversed only partially by the opioid treatment because additional peripheral and central mechanisms contribute to capsaicin-induced hyperalgesia (*27*, *28*). PP1 inhibitor calyculin A fully blocked the attenuation of hyperalgesia by remifentanil (Fig. 4B), suggesting that depotentiation at nociceptive C fibers may erase a memory trace of pain. LTP is expressed in ascending nociceptive pathways, which are relevant for the aversive components of pain. It will thus be interesting to explore whether opioids may also reverse the tonic-aversive state of pain (*29*).

Taken together, the present and our previous data (*3*) demonstrate that activation of spinal MORs triggers distinct, bidirectional, and state-dependent synaptic plasticity in naïve versus potentiated C-fiber synapses. Remifentanil activates Ca^{2+}-dependent signaling pathways, leading to activation of PP1 and PKC. At potentiated synapses, this normalizes the phosphorylation state of GluR1 at Ser^{831} and that of GluR2 at Ser^{880} and thereby depotentiates synaptic strength in C fibers. The presently identified reversal of synaptic LTP in nociceptive pathways provides a rationale for novel therapeutic strategies to cure rather than to temporarily dampen some forms of pain with opioids.

References and Notes

1. B. Heinke, E. Gingl, J. Sandkühler, *J. Neurosci.* **31**, 1313 (2011).
2. L. Chen, L.-Y. M. Huang, *Neuron* **7**, 319 (1991).
3. R. Drdla, M. Gassner, E. Gingl, J. Sandkühler, *Science* **325**, 207 (2009).
4. G. W. Terman, C. L. Eastman, C. Chavkin, *J. Neurophysiol.* **85**, 485 (2001).
5. F. S. Nugent, E. C. Penick, J. A. Kauer, *Nature* **446**, 1086 (2007).
6. M. H. Ossipov, G. O. Dussor, F. Porreca, *J. Clin. Investig.* **120**, 3779 (2010).
7. M. Zhuo *et al.*, *Proc. Natl. Acad. Sci. U.S.A.* **96**, 4650 (1999).
8. C.-C. Huang, Y.-C. Liang, K.-S. Hsu, *J. Biol. Chem.* **276**, 48108 (2001).
9. H.-K. Lee, M. Barbarosie, K. Kameyama, M. F. Bear, R. L. Huganir, *Nature* **405**, 955 (2000).
10. Materials and methods are available as supporting online material at *Science* Online.
11. C. Heinl, R. Drdla-Schutting, D. N. Xanthos, J. Sandkühler, *J. Neurosci.* **31**, 16748 (2011).
12. K. H. Jhamandas, M. Marsala, T. Ibuki, T. L. Yaksh, *J. Neurosci.* **16**, 2758 (1996).
13. H. Ikeda *et al.*, *Science* **312**, 1659 (2006).
14. H.-W. Yang *et al.*, *J. Neurophysiol.* **91**, 1122 (2004).
15. A. Barria, D. Muller, V. Derkach, L. C. Griffith, T. R. Soderling, *Science* **276**, 2042 (1997).
16. K. W. Roche, R. J. O'Brien, A. L. Mammen, J. Bernhardt, R. L. Huganir, *Neuron* **16**, 1179 (1996).
17. Y. Wang *et al.*, *Neurochem. Res.* **36**, 170 (2011).
18. L. Fang, J. Wu, X. Zhang, Q. Lin, W. D. Willis, *Neuroscience* **122**, 237 (2003).
19. H. J. Chung, J. Xia, R. H. Scannevin, X. Zhang, R. L. Huganir, *J. Neurosci.* **20**, 7258 (2000).
20. N.-W. Hu *et al.*, *J. Neurophysiol.* **89**, 2354 (2003).
21. P. V. Nguyen, T. Abel, E. R. Kandel, *Science* **265**, 1104 (1994).
22. M. N. Asiedu *et al.*, *J. Neurosci.* **31**, 6646 (2011).
23. T. C. Sacktor, *Nat. Rev. Neurosci.* **12**, 9 (2011).
24. H. Ikeda, B. Heinke, R. Ruscheweyh, J. Sandkühler, *Science* **299**, 1237 (2003).
25. R. Drdla, J. Sandkühler, *Mol. Pain* **4**, 18 (2008).
26. J. Sandkühler, *Physiol. Rev.* **89**, 707 (2009).
27. W. D. Willis Jr., *Exp. Brain Res.* **196**, 5 (2009).
28. D. Julius, A. I. Basbaum, *Nature* **413**, 203 (2001).
29. T. King *et al.*, *Nat. Neurosci.* **12**, 1364 (2009).

Acknowledgments: This work was supported by grant no. LS07-040 from the Vienna Science and Technology Fund, Austria, to J.S. Remifentanil was kindly provided by GlaxoSmithKline, Austria. The authors declare no conflicts of interest.

Supporting Online Material

www.sciencemag.org/cgi/content/full/335/6065/235/DC1
Materials and Methods
Figs. S1 to S3
References (*30*, *31*)

26 July 2011; accepted 2 December 2011
10.1126/science.1211726

HIGH-SPEED FLUORESCENCE IMAGING CAMERA

The Rolera Bolt Scientific CMOS camera is a high-speed imaging alternative that is less than half the cost of most scientific complementary metal oxide semiconductor (CMOS) and charge-coupled device (CCD) cameras. Designed for low-light imaging, the Rolera Bolt is especially suited for biomedical imaging as more research moves toward live-cell and whole-organism studies at video frame rates. This includes motility studies in which dynamic events need to be captured with high spatial and temporal resolution in order to provide the maximum amount of information to the researcher. The camera's technical features include a high quantum efficiency 1.3 megapixel sensor (3.63 μm × 3.63 μm pixel size) combined with low read noise (~3e⁻) and high-speed (30 frames per second full resolution) simultaneous readout. Using new Pixel-Freeze Technology, dark current is reduced to nearly undetectable levels, eliminating the need for an expensive Peltier cooling system. This allows for a lightweight, compact design with minimal power requirements.

QImaging
For info: 800-874-9789 | www.qimaging.com

HIGH CONTENT SCREENING SYSTEM

Incorporating state-of-the-art detector and illumination technologies, the ImageXpress Micro XL System can capture cellular resolution images using a single field that encompasses one 384 well, maximizing content up to twofold of what is acquired with standard camera HCS systems. This generous increase in field of view allows users to image twice the number of objects per image, minimizing the need to tile when capturing sizeable objects that span across the sample. The new MetaXpress 4 Software complements the ImageXpress Micro XL System by increasing image analysis speed 100%, allowing acquisition and analysis of greater than 10 million cells per hour. Maintaining extensive sample and objective compatibility, combined with the longevity of a 10,000+ hour light source, the ImageXpress Micro XL System offers researchers an extremely flexible widefield high content screening system that can grow with expanding applications.
Molecular Devices
For info: 800-635-5577 | www.moleculardevices.com

ACOUSTIC BIOSENSOR

The samX acoustic biosensor features eight analysis channels and adaptable routing that expands the workflow options available for increased power and flexibility. The new system uses Surface Acoustic Wave technology to detect mass binding and protein conformational changes on whole cells. Unlike many similar detection platforms, the range of sam acoustic biosensors do not require complex labelling methods, are real-time rather than equilibrium, and can be used to investigate living cells rather than fixed cells or purified proteins. The new samX has two sensor chips for higher-end users, increasing the number of channels to eight, further facilitating the parallel processing of samples. Using sophisticated fluidics, each channel can be utilized independently or via sequential combinations of 4 x 2, 2 x 4, or 1 x 8 channels. This optimizes user workflow, regardless of whether discrete or common reagents need to be delivered to particular sensor chip positions.
SAW Instruments GmbH
For info: +49-(0)-228-812876-0 | www.saw-instruments.de

DNA BARCODES

The NEXTflex-96 DNA Barcodes reduce the costs associated with next generation sequencing by increasing throughput using barcoded indices. This allows the user to pool multiple library preparations in a single flow cell lane. The NEXTflex-96 DNA Barcodes accomplish this by providing 96 indexed adapters, each of which contains a unique eight-nucleotide sequence. The indices are designed to be error resistant and allowing for proper differentiation between samples. Using the NEXTflex-96 DNA Barcodes, the index is added to the sample during the adapter ligation step, allowing polymerase chain reaction (PCR) amplification to be reduced or eliminated, thus minimizing amplification-based bias and preventing poor reads from single base errors introduced during PCR. These barcodes can be used to multiplex genomic DNA, RNA, and ChIP sequencing libraries.
Bioo Scientific
For info: 888-208-2246 | www.biooscientific.com

ELECTRONIC MICROPLATE SEALER

Designed for convenience, the compact MiniSeal only requires plugging into a single electrical outlet to operate. This eliminates the need to place your thermal sealer near a compressed air source or buy a dedicated compressor. Unlike hand-operated manual thermal sealers, the MiniSeal uses a preset sealing pressure to deliver highly reproducible plate seals time after time. To complement its ease of use and high-quality plate sealing, the MiniSeal ensures operator safety with its unique twin-button operation. The MiniSeal offers researchers a reliable and productive sealing tool for maintaining the integrity of their samples while in storage. The versatile device is capable of producing an accurate and tight seal on any standard, deep-well, or polymerase chain reaction (PCR) microplate from 3 to 62 mm in height. Offering adjustable temperature heat-sealing from 50°C up to 200°C, MiniSeal is able to operate optimally with most foil and film seals.
Porvair Sciences
For info: +44-(0)-1372-824290 | www.porvair-sciences.com

STEROID/DRUG/COMPOUND IMMOBILIZATION KIT

The SDC (Steroid/Drug/Compound) Immobilization Kit generates affinity resins by immobilizing steroids, drugs, and other chemical compounds. Immobilization is preformed through active hydrogens, eliminating the need for primary amines, sulfhydryls, carbonyls, and other common coupling groups. The coupling uses the Mannich reaction, described as the condensation of formaldehyde with ammonia in the form of its salt, and another compound containing active hydrogen. The SDC Immobilization kit replaces the ammonia with the primary amine on the DADPA and the active hydrogen is supplied by the steroid, drug, or chemical compound to be coupled. The SDC Immobilization Kit is ideal for the generation of five 2 mL affinity columns.
G-Biosciences
For info: 800-628-7730 | www.gbiosciences.com

Electronically submit your new product description or product literature information! Go to **www.sciencemag.org/products/newproducts.dtl** for more information.

Newly offered instrumentation, apparatus, and laboratory materials of interest to researchers in all disciplines in academic, industrial, and governmental organizations are featured in this space. Emphasis is given to purpose, chief characteristics, and availability of products and materials. Endorsement by *Science* or AAAS of any products or materials mentioned is not implied. Additional information may be obtained from the manufacturer or supplier.

POSITIONS OPEN

ASSOCIATE DEAN for Research and Graduate Education

The University of South Carolina School of Medicine in Columbia, South Carolina, invites applications for the position of Associate Dean for Research and Graduate Education. The Associate Dean for Research and Graduate Education is a senior-level faculty position reporting directly to the Dean. The candidate who fills this faculty position will provide vision and leadership around the School's research mission as it builds its extramural funding base and expands its reputation for scholarly excellence. Internally, the position works closely with the Dean, Dean's staff, departmental chairpersons and administrators, and the central administration of the University. Externally, the position works closely with the leadership of the School of Medicine's affiliated hospitals and agencies, and with the various funding, regulatory, and accrediting bodies of the School of Medicine. Additionally, the position will oversee and coordinate the graduate programs in the School of Medicine. A successful candidate must qualify for a faculty appointment at the rank of **PROFESSOR.**

Outline of Desired Qualifications: M.D./Ph.D. or M.D./D.O. with a record of federally funded research, or Ph.D. with significant clinical trials research; National recognition as a scholar; Proven success as an extramurally funded researcher; Extensive experience with federal funding agencies and regulatory compliance; Management experience in an academic environment; Commitment to promoting a culture that nurtures diverse forms of inquiry and scholarship; Demonstrated evidence of strong interpersonal and communications skills; Experience planning, implementing, and sustaining comprehensive research centers or programs is highly desirable; Strong commitment towards cultural diversity and equal opportunity.

An outline of the job responsibilities is available at **website: http://hr.sc.edu/employ.html, Requisition #004321.** Applications will be accepted until the position is filled. Applicants should send a letter of interest and a curriculum vitae, and request three letters of reference to be sent under separate cover (Adobe Acrobat PDF format) to **e-mail: lynn.heard@uscmed.sc.edu.** *The University of South Carolina is an Equal Opportunity Employer and specifically invites and encourages applications from women and minorities.*

FACULTY POSITION
Cell Biology with Expertise in Quantitative Imaging

The Department of Biological Sciences at Wellesley College invites applications for a tenure-track faculty position at the rank of **ASSISTANT PROFESSOR** to start in August 2012. The position requires expertise in the use of quantitative imaging techniques to address fundamental questions in eukaryotic cellular/molecular biology. We seek broadly trained biologists who are strongly committed to excellence in both teaching and research in a liberal arts college environment. In addition to teaching in our cellular biology core curriculum, successful candidates would be expected to offer advanced courses in their specialty, and to develop an active research program that involves undergraduates. A Ph.D. and postdoctoral experience are required. Applications should include a cover letter, curriculum vitae, statements of teaching and research interests, a statement describing the candidate's training and experience with quantitative imaging techniques, and three letters of recommendation (the online application will request name and e-mail address in order for recommenders or dossier services to submit letters directly). Materials should be submitted by visiting our application **website: https://career.wellesley.edu.** If circumstances make it impossible to submit materials online, please electronically send to **e-mail: working@wellesley.edu.** The deadline for receipt of all application materials is February 17, 2012.

Wellesley College is an Affirmative Action/Equal Opportunity Employer and we are committed to increasing the diversity of the college community and the curriculum. Candidates who believe they can contribute to that goal are encouraged to apply.

POSITIONS OPEN

PROFESSOR OF NEUROBIOLOGY
Boston University

The Biology Department invites applications for a tenured faculty appointment in neurobiology at the rank of full professor. We are particularly interested in innovative researchers who integrate cell and molecular neurobiology with systems neuroscience to study basic questions in signaling, synaptic function, development or learning and memory, and their connections to organismal phenotypes. We seek a colleague with an international reputation and an outstanding record of research accomplishment who will serve as a leader in the future development of neurobiology in the department and the broader neuroscience community at Boston University (BU). Responsibilities include training graduate students as part of a vigorous research program with extramural funding and participation in undergraduate and graduate instruction. The successful candidate will be offered laboratory facilities in our new interdisciplinary Life Science & Engineering Building, a competitive salary, and generous startup funding. Review of applications will begin 15 February 2012 and continue until the position is filled. Please use AcademicJobsOnline (**website: https://academicjobsonline.org/ajo/jobs/1368**) to submit your application. Inquiries can be addressed to **Michael Baum** (**e-mail: baum@bu.edu**), Chair, Neurobiology Search Committee, or **Michael Sorenson** (**e-mail: msoren@bu.edu**), Chair, Department of Biology. Please visit the following websites for additional information about the Biology Department (**website: http://www.bu.edu/biology/**) and BU's interdisciplinary programs in Neuroscience (**website: http://www.bu.edu/neuro/**). *Boston University is an Equal Opportunity/Affirmative Action Employer.*

THE METHODIST HOSPITAL RESEARCH INSTITUTE
Weill Cornell Medical College

The Molecular Imaging Program at the Department of Translational Imaging develops novel agents and new technologies to image molecular processes and treat diseases. The research focuses on cancer, cardiovascular disease, neurodegeneration, cell therapy, and nanomedicine. Several **POSTDOCTORAL FELLOW** positions are currently open for application. Self-motivated scientists with expertise in peptides, nanotechnology, radiochemistry, photodynamic therapy, cell biology, and animal model are encouraged to join our dynamic research team. Please e-mail curriculum vitae and contact information of three references to **Dr. Ching H. Tung** at **e-mail: ctung@tmhs.org.** The Methodist Hospital Research Institute is centrally located in the world largest medical center in Houston, Texas.

POSTDOCTORAL POSITION

Full-time postdoctoral position available at the Loyola University Chicago Cardinal Bernadin Cancer Center. Candidates must hold M.D. or Ph.D. and have experience with methodologies relating to molecular biology and background in genitourinary oncology. Please forward curriculum vitae and cover letter to **Gopal Gupta,** M.D. via **e-mail: gogupta@lumc.edu.** *Loyola University Health System is an Affirmative Action/Equal Opportunity Educator and Employer. The University undertakes affirmative action to assure equal employment opportunity for underrepresented minorities, women, and persons with disabilities.*

DIRECTOR

U.S. Geological Survey Western Fisheries Research Center, Seattle. Molecular to ecosystem scale fisheries research throughout the Western U.S.; six laboratory locations support genetic, conservation, habitat, climate change, and other investigations. Competitive salary and federal benefits. Apply at **website: http://www.usajobs.gov.** Title: Western Fisheries Research Center Director, GS-0401/0482-15. *The federal government is an Equal Opportunity Employer.*

Director, Office for Policy in Clinical Research Operations, Division of AIDS

The National Institute of Allergy and Infectious Diseases (NIAID) is seeking an exceptional and visionary leader to take on the role of the director, Office for Policy in Clinical Research Operations (OPCRO) in the Division of AIDS (DAIDS). The OPCRO director is responsible for oversight of a number of critical functions to ensure 1) the sound conduct of clinical trials; 2) compliance with applicable regulations, standards, and good practice guidelines; 3) study participant safety and welfare; and 4) study quality and integrity. The OPCRO director oversees four branches composed of 20 federal employees as well as a number of on-site contractors. The OPCRO director also serves as a key advisor to the DAIDS director and to scientific programs on all clinical research oversight issues; provides objective, experience-based guidance and oversight; and is responsible for identifying and resolving a variety of complex clinical trials management, policy, and administrative issues. These issues require close coordination and interfacing with other programs within NIAID, NIH, other federal agencies, pharmaceutical companies, and patient advocacy and community groups.

NIAID

National Institute of Allergy and Infectious Diseases

Qualifications: Applicants must possess an M.D. or equivalent degree with specialization in internal medicine, infectious diseases, or any other medical specialty that will lead to expertise in infectious diseases research with a focus on HIV/AIDS. In addition, the candidate must have demonstrated skills in 1) working both independently and collaboratively in planning, organizing, and conducting/overseeing clinical trials; 2) serving effectively in clinical research program administration; and 3) effective communications and collaborations.

Application Process: Provide curriculum vitae, bibliography, and a three-page summary explaining 1) your vision for HIV/AIDS clinical research; 2) your reasons for being interested in the position; and 3) the specific leadership skills and experience you would bring to the HIV/AIDS clinical research programs at NIAID. Submit application package to Mr. Robert Gulakowski, Office of the Director, DAIDS, NIAID, 6700-B Rockledge Drive, Room 4140, Bethesda, MD 20892-7620, and reference announcement number DAIDS-11-33.

The deadline for receipt of applications is January 31, 2012. Direct any inquiries to Mr. Gulakowski at rgulakow@niaid.nih.gov or 301-496-0545. All information provided by applicants will remain confidential and will be reviewed only by authorized NIAID officials.

The successful candidate will be appointed under the Title 42(f) authority at a salary commensurate with experience. The maximum annual base salary is $230,000, with a maximum total annual compensation limit of $240,000. A full package of benefits is also available, including retirement; health, life, and long-term care insurance; annual and sick leave; and a thrift savings plan (401K equivalent). This position is subject to financial disclosure requirements.

To learn more about NIAID and how you can play a role in this exciting and dynamic research organization, visit us on the Web at www.niaid.nih.gov/careers/dtc1.

Institute of Molecular Medicine, Peking University

The Institute of Molecular Medicine (IMM) is an autonomous research and educational institute at Peking University (PKU), focusing on basic and translational study of cardiovascular and metabolic diseases. Inaugurated in 2005, IMM has now blossomed into an international and leading research institute in cardiovascular science, demonstrated by its excellent track record of scientific discoveries, public service, and training of future leaders in biomedicine and biotechnology.

Located by Wei-Ming Lake and Bo-Ya Tower, IMM houses eleven interdisciplinary laboratories and several comprehensive core technology facilities including a world-class nonhuman primate platform. With strong support from the Chinese National 985 Program, IMM laboratories receive generous institutional funding for personnel, laboratory consumables and equipment, and competitive employment benefits. Moreover, through the newly-established joint program with the National Center for Cardiovascular Diseases (FuWai Hospital), participating IMM laboratories are entitled to additional financial support and have access to abundant clinical resources.

IMM always values challenging and longer-term research initiatives, deep collaboration, and innovation through integration. After six years' development, we are now ready for a significant expansion. Applications are cordially invited for positions at the **Principal Investigator (PI), Co-Principal Investigator (Co-PI)** and **Postdoc** levels.

PI positions: We are recruiting up to 10 outstanding scientists seeking to establish independent research programs in areas including, but not limited to, **cardiovascular stem cell biology and regenerative medicine, cardiometabolic proteomics and genomics, mitochondrial biomedicine, GPCR signaling,** and **RNA therapeutics.** Competitive candidates are especially encouraged to apply for the national "**Thousand Talents Program** (type A, full-time)" and the national "**Thousand Young Talents Program**". Successful applicants who participate in the aforementioned IMM-FuWai joint program will have the choice of primary appointment in either institute. Applicants with demonstrated academic excellence and leadership in their respective fields should submit a CV, a statement of research interests (past and future), and the contact details of three academic referees in PDF format by email to **imm_recruit@pku.edu.cn**.

Non-independent Co-PI positions: We are looking for young and promising scientists (M.D. or Ph.D.) who will take up co-PI positions in the Laboratories of Nucleic Acid Technology (Dr. Zicai Liang), Cellular Biophysics (Dr. Zhuan Zhou), Calcium Signaling and Mitochondrial Biomedicine (Dr. Heping Cheng), Human Population Genetics (Dr. Xiaoli Tian), Molecular Pharmacology (Dr. Yuchun Gu), and Cell Secretion and Metabolism (Dr. Liangyi Chen). Successful applicants are expected to team up with their respective PIs to run scientific programs, mentor graduate students, and supervise technicians in the laboratory. The applicants should submit a CV, a statement of research interests, and the contact details of three academic referees by email to **imm_recruit@pku.edu.cn** and state the name of the intended laboratory in the cover letter.

Postdoc positions: Please directly contact the PIs of the laboratories in which you are interested. Competitive candidates may apply for additional support from the postdoctoral fellowships established by the Peking University-Tsinghua University Joint Center for Life Sciences.

You can learn more about IMM, individual laboratories, and this recruitment at **www.imm.pku.edu.cn** and **www.imm.pku.edu.cn/recruit_2012**. The deadline for application is July 15th, 2012, or until filled.

NDSU

THREE ASSISTANT PROFESSOR FACULTY POSITIONS
Department of Veterinary and Microbiological Sciences
North Dakota State University
Fargo, North Dakota 58108

The Department of Veterinary and Microbiological Sciences is seeking three, tenure-track faculty members at the Assistant Professor level.

Infectious Disease and Public Health (http://jobs.ndsu.edu/postings/1666): We invite applications from scientists with research and/or teaching interests that focus on the impact of infectious diseases on public health. These interests could include, but are not limited to, the ecology, evolution, and epidemiology of infectious diseases.

Microbial Pathogenesis (http://jobs.ndsu.edu/postings/1604): We invite applications from scientists with research interests in microbial pathogenesis of human and/or animal diseases. Broadly defined, this includes, but is not limited to, the disciplines of bacteriology, virology, mycology, parasitology, and immunology.

Foodborne Disease Pathogenesis (http://jobs.ndsu.edu/postings/1665): We invite applications from scientists with research interests that focus on the mechanisms by which foodborne pathogens cause disease in humans.

For further information about these positions, please visit **www.ndsu.edu/vetandmicro/facultypositions/**. Review of applications will begin **February 24, 2012** and positions will remain open until filled. Positions will be available beginning July or August, 2012. If you have questions or need additional information contact **Dr. Penelope Gibbs** at **(701) 231 6726** or **penelope.gibbs@ndsu.edu**.

Women and other members of traditionally underrepresented groups are encouraged to apply. North Dakota State University is an Equal Opportunity/Affirmative Action Employer. NDSU is an NSF ADVANCE and Carnegie Very High Research Activity Institution. These positions are exempt from North Dakota Veterans' Preference requirements.

FELLOWSHIPS

John Innes Centre

INDEPENDENT RESEARCH FELLOWSHIPS

The John Innes Centre (JIC), Norwich, UK is a world leading centre of excellence in plant and microbial sciences based on the Norwich Research Park. We are inviting applications from outstanding researchers who either hold, or wish to apply for Independent Research Fellowships, to attend a Conference at the JIC on 30th April/1st May 2012. At the meeting you will be able to present a talk about your proposed area of research and to discuss your proposals, the development of your group and your future career plans in depth with senior JIC Scientists.

After the Conference we will select and mentor outstanding candidates in writing Fellowship applications and/or offer the opportunity to move existing Fellowships to the JIC.

Further details and particulars can be found at
http://www.jic.ac.uk/corporate/opportunities/vacancies/fellows.htm

Please e-mail a 2-page summary of your research plan, a copy of your CV and arrange for three letters of recommendation to be emailed to dawn.barrett@jic.ac.uk by Friday 16th March 2012

The John Innes Centre is a registered charity (No223852) grant-aided by the Biotechnology and Biological Sciences Research Council and is an Equal Opportunities Employer.

Georgia Health Sciences University

Tenure Track Faculty Positions

The Section of Experimental Medicine in the Department of Medicine at Georgia Health Sciences University is recruiting tenure track faculty at the Assistant, Associate, or Professor level (academic rank commensurate with experience). The successful candidates will have an earned Ph.D., M.D. or M.D./Ph.D. degree. They will join an active group of extramurally-funded research faculty currently supported by two Program Project Grants and numerous other national level awards focused on hypertension, diabetes, and/or kidney disease. The mission of the Section of Experimental Medicine is to foster and initiate basic and clinical research in a translational fashion. We are specifically dedicated to growth and development of clinically relevant research programs in collaboration with other sections of the department in recently renovated laboratories utilizing state-of-the-art equipment. The candidates are expected to develop an active, extramurally-funded research program in basic or clinical aspects of cardiology, nephrology, or endocrinology. A particular interest in translational research and the willingness and ability to collaborate with clinical investigators is required. They will have the opportunity to participate in a NIH-funded T32 institutional training program in Integrative Cardiovascular Biology. Participation in educational and service activities within the university is also expected. Highly competitive salary and start-up package, commensurate with prior experience, will be provided. Interested individuals should apply for this position through our website at: **http://www.georgiahealth.edu/facultyjobs/**, MCG-Experimental requisition **5837**. Application materials should include a detailed CV, statement of research goals and contact information for three references. Applications will be reviewed beginning in late February and remain open until filled.

For more information about the position please contact: **David M. Pollock, Ph.D., Regents Professor and Chief, Section of Experimental Medicine, Department of Medicine, Georgia Health Sciences University, Augusta, GA 30912; dpollock@georgiahealth.edu.**

Georgia Health Sciences University is an Equal Opportunity and Equal Access Institution. Applications from women and underrepresented minorities are particularly encouraged.

FAU
FLORIDA ATLANTIC UNIVERSITY

Professor of Neuroscience

Florida Atlantic University seeks to hire a neuroscientist at the rank of full professor who will join a new neuroscience initiative on the university's MacArthur campus located in in Jupiter, Florida. We are interested in candidates with a well-established research program who will complement existing strengths at FAU in the Biology and Psychology Departments. Although all applicants with an interest in the neurosciences will be considered, applicants with an exceptional record of accomplishment in molecular and/or cellular neuroscience are strongly encouraged to apply. The Max Planck Florida Institute (MPFI) and The Scripps Research Institute (Scripps Florida) have recently established new research facilities on the MacArthur campus adjacent to the FAU-Life Science buildings that will house the neuroscience program. Ample opportunities exist for interaction and collaboration with their scientists, and as an initial step in this collaboration, a joint graduate program between FAU and MPFI has been established and admitted its first students this year (see **http://www.science.fau.edu/neuroscience/iban/**). A competitive start-up package will be available.

Interested applicants for this position should go to **https://jobs.fau.edu** and search postings for position **#991114**. Applications must be filed electronically and should include a cover letter stating your interest and a personal statement of research and teaching interests, a full CV as well as names and contact information for three referees. Applications will be considered beginning January 1, 2012 and the position will remain open until a suitable candidate is hired. A background check is required for candidates selected for these positions. Questions about the search can be directed to **Dr. Rod Murphey, Search Chair and Chairman, Department of Biological Sciences, 777 Glades Rd., Boca Raton, FL 33431; rmurphey@fau.edu; phone: (561) 297-0384**.

FAU is an Equal Opportunity/Equal Access Institution.

MMV 2012 10th Call for Proposals

MMV welcomes projects in the hits-to-lead stage for new families of molecules specifically addressing the key priorities of the malaria eradication agenda: transmission blocking and prevention of *P. vivax* relapse. Proposals for chemical series with the potential for *P. falciparum* chemoprevention or blood stage efficacy as a result of long-half lives are encouraged, though the project should already have initial confirmation of *in vivo* oral blood stage activity. Early target validation falls outside of our mandate.

In the clinical arena, MMV welcomes proposals for the clinical development of new chemical entities. We have a strong pipeline of new molecules, and so welcome applications regarding capacity building to develop new sites for first-in-patient testing of these new molecules, including both blood stage, transmission blocking and vivax anti-relapse capabilities.

Templates for the 3-page Letter of Interest to apply for the above Call can be found at **www.mmv.org**.

In addition, to celebrate the release of the MMV Malaria Box **www.mmv.org/malariabox**. MMV will be offering up to ten Challenge Grants of USD 50,000. Proposals are expected to be at the concept stage (i.e. no prior experimental work is required) and to last no more than a year. These Challenge Grants will be prioritized based on scientific merit and according to the MMV strategy, and can constitute:

i) Screening: testing the MMV Malaria Box against malaria and other parasitological assays
ii) Medicinal Chemistry: perform hit-to-lead or optimization chemistry on any anti-malarial series
iii) Translational and Clinical Development: new methods to study or validate the inhibition of P.vivax relapses or the interruption of transmission

It is envisaged that applications for the MMV Challenge Grants shall be reviewed and awarded by May 2012. A 1-page template to apply can be found at **www.mmv.org**.

All applications using the specified templates should be sent electronically to **proposals@mmv.org** by **12 noon CET March 15th 2012**. More details of the call can be found at **www.mmv.org**.

Get a Career Plan that Works.

An exceptional career requires insightful planning and management. That's where *Science* Careers comes in. From job search to career enhancement, *Science* Careers has the tools and resources to help you achieve your goals. Get yourself on the right track today and get a real career plan that works. Visit **ScienceCareers.org**.

Science Careers
From the journal *Science* AAAS

ScienceCareers.org

Download your free copy today.

ScienceCareers.org/booklets

Polish the critical skills you need for a successful job search.

Science Careers is offering a booklet of career advice on topics including choosing a career path, getting the most from a career fair, effective networking, marketing yourself to potential employers, and acing your job interview.

To download the booklet, just sign up for a free *Science* Careers job seeker account by visiting ScienceCareers.org/booklet. Already have an account? Just login and click the link from the "My *Science* Account" page.

Science Careers
From the journal *Science* AAAS

Webinar

The Hunt for Missing Heritability

Challenges and Opportunities for Novel Locus Discovery in Non-European Populations

TUESDAY, JANUARY 31, 2012

12 noon Eastern • 9 a.m. Pacific • 5 p.m. UK

Characterizing the genetics of complex diseases has, to date, focused on common variants and predominantly on populations of European descent. GWAS methodologies have been successful in uncovering novel susceptibility loci for common disorders but the heritability of many disorders remains to be explained. Now, a growing number of investigators are looking beyond European cohorts to study common and rare variants in populations around the world, including African, Asian, and other ancestries in the hunt for novel susceptibility genes.

PARTICIPANTS:

Charles Rotimi, Ph.D.
National Institutes of Health
Bethesda, MD

Carlos Bustamante, Ph.D.
Stanford University School of Medicine
Stanford, CA

REGISTER NOW!
www.sciencemag.org/webinar

THE THOUGHT-LEADERS ON OUR WEBINAR PANEL WILL:

- Discuss how population genetics integrates with the genetics of complex disease to reveal novel disease genes
- Describe how the discovery of population-specific rare variants expands our understanding of complex diseases
- Explain the importance of population-optimized strategies and tools that account for differences in genetic diversity and population admixture
- Answer your questions live!

Webinar sponsored by

Affymetrix®
Revolutionize life

Science
AAAS

Brought to you by the *Science*/AAAS Custom Publishing Office

GE & Science Prize for Young Life Scientists

Congratulations to our 2011 winners!

Dr. Erez Lieberman Aiden

Grand Prize Winner and Regional Winner, North America

Essay: Zoom!

Dr. Eran Eden

Regional Winner, All Other Countries

Essay: Proteome Dynamics and Fate the of Individual Cancer Cells in Response to a Drug

Dr. Felipe Karam Teixeira

Regional Winner, Europe

Essay: Mechanisms of Transgenerational DNA Methylation Inheritance

Dr. Tatsuya Tsukahara

Regional Winner, Asia

Essay: CDK Directs the Chromosome Passenger Complex to Centromeres for Chromosome Bi-Orientation

www.gescienceprize.org

GE Healthcare

Science
AAAS

105

things you didn't (and 3 you probably shouldn't) know about some of your most respected colleagues.

One more data point on why you should spend more time at membercentral.aaas.org. There you can enjoy a feast of blogs, videos, webinars, discounts, and downloads created by and for the most insatiable brains around.

membercentral.aaas.org

AAAS MemberCentral

Science Mobile App Now Available for Android Phones

They say you never know when inspiration will strike. Download the *Science* mobile app for Android devices and be ready the next time you're inspired to read the latest news, research, and career advice from *Science* on your mobile phone.

To download the *Science* mobile app for Android visit **content.aaas.org/mobile**, visit the Android Market on your phone, or just scan this barcode.

Features include:

- Summaries and abstracts from *Science*, *Science Translational Medicine*, and *Science Signaling*.
- Ability to e-mail full-text links.
- The latest news from *Science*NOW.
- Career advice articles from *Science* Careers.
- Access to the *Science* weekly podcast and other multimedia.
- Content caching for reading without wi-fi access.

Science
AAAS

HIGH-SPEED FLUORESCENCE IMAGING CAMERA

The Rolera Bolt Scientific CMOS camera is a high-speed imaging alternative that is less than half the cost of most scientific complementary metal oxide semiconductor (CMOS) and charge-coupled device (CCD) cameras. Designed for low-light imaging, the Rolera Bolt is especially suited for biomedical imaging as more research moves toward live-cell and whole-organism studies at video frame rates. This includes motility studies in which dynamic events need to be captured with high spatial and temporal resolution in order to provide the maximum amount of information to the researcher. The camera's technical features include a high quantum efficiency 1.3 megapixel sensor (3.63 μm × 3.63 μm pixel size) combined with low read noise (~3e^-) and high-speed (30 frames per second full resolution) simultaneous readout. Using new Pixel-Freeze Technology, dark current is reduced to nearly undetectable levels, eliminating the need for an expensive Peltier cooling system. This allows for a lightweight, compact design with minimal power requirements.

QImaging
For info: 800-874-9789 | www.qimaging.com

HIGH CONTENT SCREENING SYSTEM

Incorporating state-of-the-art detector and illumination technologies, the ImageXpress Micro XL System can capture cellular resolution images using a single field that encompasses one 384 well, maximizing content up to twofold of what is acquired with standard camera HCS systems. This generous increase in field of view allows users to image twice the number of objects per image, minimizing the need to tile when capturing sizeable objects that span across the sample. The new MetaXpress 4 Software complements the ImageXpress Micro XL System by increasing image analysis speed 100%, allowing acquisition and analysis of greater than 10 million cells per hour. Maintaining extensive sample and objective compatibility, combined with the longevity of a 10,000+ hour light source, the ImageXpress Micro XL System offers researchers an extremely flexible widefield high content screening system that can grow with expanding applications.

Molecular Devices
For info: 800-635-5577 | www.moleculardevices.com

ACOUSTIC BIOSENSOR

The samX acoustic biosensor features eight analysis channels and adaptable routing that expands the workflow options available for increased power and flexibility. The new system uses Surface Acoustic Wave technology to detect mass binding and protein conformational changes on whole cells. Unlike many similar detection platforms, the range of sam acoustic biosensors do not require complex labelling methods, are real-time rather than equilibrium, and can be used to investigate living cells rather than fixed cells or purified proteins. The new samX has two sensor chips for higher-end users, increasing the number of channels to eight, further facilitating the parallel processing of samples. Using sophisticated fluidics, each channel can be utilized independently or via sequential combinations of 4 x 2, 2 x 4, or 1 x 8 channels. This optimizes user workflow, regardless of whether discrete or common reagents need to be delivered to particular sensor chip positions.

SAW Instruments GmbH
For info: +49-(0)-228-812876-0 | www.saw-instruments.de

DNA BARCODES

The NEXTflex-96 DNA Barcodes reduce the costs associated with next generation sequencing by increasing throughput using barcoded indices. This allows the user to pool multiple library preparations in a single flow cell lane. The NEXTflex-96 DNA Barcodes accomplish this by providing 96 indexed adapters, each of which contains a unique eight-nucleotide sequence. The indices are designed to be error resistant and allowing for proper differentiation between samples. Using the NEXTflex-96 DNA Barcodes, the index is added to the sample during the adapter ligation step, allowing polymerase chain reaction (PCR) amplification to be reduced or eliminated, thus minimizing amplification-based bias and preventing poor reads from single base errors introduced during PCR. These barcodes can be used to multiplex genomic DNA, RNA, and ChIP sequencing libraries.

Bioo Scientific
For info: 888-208-2246 | www.biooscientific.com

ELECTRONIC MICROPLATE SEALER

Designed for convenience, the compact MiniSeal only requires plugging into a single electrical outlet to operate. This eliminates the need to place your thermal sealer near a compressed air source or buy a dedicated compressor. Unlike hand-operated manual thermal sealers, the MiniSeal uses a preset sealing pressure to deliver highly reproducible plate seals time after time. To complement its ease of use and high-quality plate sealing, the MiniSeal ensures operator safety with its unique twin-button operation. The MiniSeal offers researchers a reliable and productive sealing tool for maintaining the integrity of their samples while in storage. The versatile device is capable of producing an accurate and tight seal on any standard, deep-well, or polymerase chain reaction (PCR) microplate from 3 to 62 mm in height. Offering adjustable temperature heat-sealing from 50°C up to 200°C, MiniSeal is able to operate optimally with most foil and film seals.

Porvair Sciences
For info: +44-(0)-1372-824290 | www.porvair-sciences.com

STEROID/DRUG/COMPOUND IMMOBILIZATION KIT

The SDC (Steroid/Drug/Compound) Immobilization Kit generates affinity resins by immobilizing steroids, drugs, and other chemical compounds. Immobilization is preformed through active hydrogens, eliminating the need for primary amines, sulfhydryls, carbonyls, and other common coupling groups. The coupling uses the Mannich reaction, described as the condensation of formaldehyde with ammonia in the form of its salt, and another compound containing active hydrogen. The SDC Immobilization kit replaces the ammonia with the primary amine on the DADPA and the active hydrogen is supplied by the steroid, drug, or chemical compound to be coupled. The SDC Immobilization Kit is ideal for the generation of five 2 mL affinity columns.

G-Biosciences
For info: 800-628-7730 | www.gbiosciences.com

Electronically submit your new product description or product literature information! Go to **www.sciencemag.org/products/newproducts.dtl** for more information.

Newly offered instrumentation, apparatus, and laboratory materials of interest to researchers in all disciplines in academic, industrial, and governmental organizations are featured in this space. Emphasis is given to purpose, chief characteristics, and availability of products and materials. Endorsement by *Science* or AAAS of any products or materials mentioned is not implied. Additional information may be obtained from the manufacturer or supplier.

2012 AAAS Annual Meeting

Flattening the World: Building a Global Knowledge Society

16-20 February, Vancouver

Act Now ... Rates Go Up on January 27th

Registration

Discounted advance registration rates are available until Thursday, 26 January 2012.

Take advantage of unlimited access to all symposia, seminars, topical lectures, plenary events, career workshops, the International Exhibition, and a variety of networking opportunities.

Professional: $295 Members/ $399 Non-Members
Postdoc: $235 Members/$335 Non-Members
K-12 Teacher: $235 Members/$335 Non-Members
Emeritus: $235 Members/$335 Non-Members
Student: $60 Members/$90 Non-Members

Housing

Special room rates and benefits are available to registrants.

Forecasts show that the U.S. dollar will hold its strength against the Canadian dollar in 2012.

Fairmont Hotel Vancouver
Rate: $189 CAD single/double

Fairmont Pacific Rim
Rate $225 CAD single/double

Fairmont Waterfront
Rate: $202 CAD single/double

Hyatt Regency Vancouver
Rate: $195 CAD single/double

Pan Pacific Vancouver
Rate: $208 CAD single/double

Vancouver Marriott Pinnacle Downtown Hotel
Rate: $195 CAD single/double

Westin Bayshore
Rate: $199 CAD single/double

Rooms are available on a first-come, first-served basis until 24 January 2012.

AAAS, publisher of *Science,* thanks the sponsors and supporters of the *2012 Annual Meeting*

Presenting sponsor

SUBARU

Gold

EUROPEAN COMMISSION
European Research Area

NSF

UBC a place of mind
THE UNIVERSITY OF BRITISH COLUMBIA

Silver

ACS Chemistry for Life
American Chemical Society

Canada

HELMHOLTZ ASSOCIATION

Bronze

Council of Canadian Academies
Conseil des académies canadiennes

AAAS thanks THE KAVLI FOUNDATION
for its generous support of the Science Journalism Awards

AAAS
ADVANCING SCIENCE, SERVING SOCIETY

For more information visit: **www.aaas.org/meetings.**

Proteins

Antibodies

ELISAs

Assay Services

MultiAnalyte Profiling

Activity Assays

Stem Cells

ELISpot Kits

Flow Cytometry

Cell Selection

R&D Systems Quantikine® ELISAs

The Most Referenced Immunoassays

A direct measure of product quality is the frequency of citations in the scientific literature. R&D Systems has more than 20 years of experience designing, testing, and optimizing the most cited ELISA kits in the world. Find out why scientists trust R&D Systems ELISAs more than any other brand.

R&D Systems is the Most Referenced ELISA Manufacturer

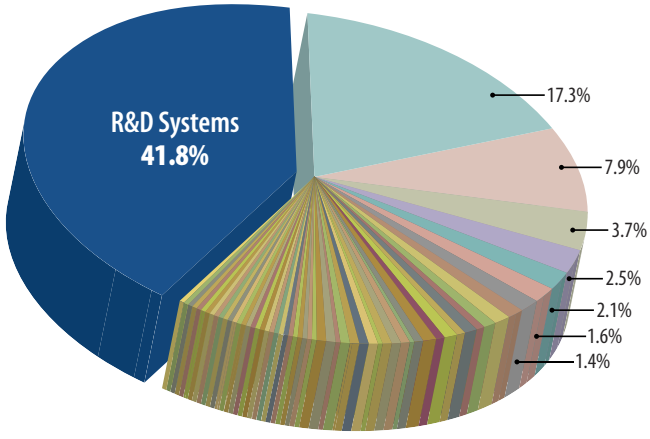

Approximately 42% of Referenced Immunoassays are Developed and Manufactured by R&D Systems. A survey of 860 manuscripts from 44 journals was conducted to compare the number of citations specifying the use of R&D Systems ELISAs to the number citing ELISAs from other commercial sources. A total of 433 ELISA citations referencing immunoassays from 66 different vendors were identified in the survey.

NEW Quantikine ELISA Kits

- α1-Acid Glycoprotein
- Angiopoietin-like 3
- Cathepsin V
- Clusterin
- Dkk-1
- EGF R/ErbB1
- EG-VEGF/PK1
- Fetuin A
- FGF-21
- Galectin-3
- Gas 6
- GDF-15
- IL-17A/F Heterodimer
- IL-19
- Lipocalin-2/NGAL
- MBL
- Proprotein Convertase 9/PCSK9
- Periostin/OSF-2
- Progranulin
- ST2/IL-1 R4
- Thrombomodulin/CD141
- Tie-1
- TIM-1/KIM-1

For more information visit our website at www.RnDSystems.com/go/ELISA

For research use only. Not for use in diagnostic procedures.

R&D Systems, Inc. www.RnDSystems.com

R&D Systems Europe, Ltd. www.RnDSystems.co.uk

R&D Systems China Co., Ltd. www.RnDSystemsChina.com.cn

R&D SYSTEMS®